THE UNIVERSITY OF QUEENSLAND

AUSTRALIA

Design Optimisation of an Australian EGS Power Plant Using a Natural Draft Dry Cooling Tower

Sam Duniam

A thesis submitted for the Degree of Master of Philosophy

The University of Queensland in 2015

School of Mechanical and Mining Engineering

Abstract

Enhanced Geothermal Systems (EGS) technology was successfully demonstrated in the Australian context with the operation of the Habanero 1MW pilot plant. This project aims to determine the optimum power plant design for the geothermal parameters found at the Habanero pilot plant. In order to achieve this, a techno-economic optimisation of an Organic Rankine Cycle (ORC) was undertaken.

The EGS conditions used in this work are a brine production well head temperature of 220 °C, and minimum brine temperature of 80°C in order to limit scaling formation in the brine heat exchanger(s). The production well head pressure is 35 MPa and the required reinjection pressure is 45 MPa in order to maintain the desired mass flow rate of 35 kg/s through the EGS resource.

A significant source of parasitic power consumption in ORC systems occurs in the condensing system. In order to avert this parasitic power consumption Natural Draft Dry Cooling Towers (NDDCTs) were investigated as the condenser for the ORC. A one dimensional NDDCT model was developed and integrated into the cycle design process to analyse and design for the coupled nature of NDDCT performance with the power cycle. As a base for comparison a one dimensional Mechanical Draft Air Cooled Tower (MDACT) model was developed and each cycle was also analysed with MDACT as the condenser.

A wide range of organic working fluids and several cycle configurations were evaluated in the preliminary analysis using a simplified NDDCT model. The cycles were optimised for maximum net power generation and the highest performing cycle configurations were progressed to the techno-economic design point optimisation stage. The cost of each of the major equipment items in the plant was estimated using cost correlations based on historical equipment cost data. The condensing system geometry for both NDDCT and MDACT, heat exchanger geometry and cycle parameters were optimised to find the lowest Specific Investment Cost (SIC) in AUD/kWe for each candidate cycle. The cycle configurations with the lowest SIC from the design point analysis were evaluated across the range of ambient temperatures expected at the site. The mean annual net power generation for each cycle was calculated based on site temperature data and this was used in determining the annualised SIC values, the measure by which the optimum plant configuration was selected.

The recuperated, regenerative and basic ORCs were found to be the cycles that obtained the highest net power generation in the preliminary analysis with butane, butene, isobutene, R152a, isobutane, R123 and isopentane the highest performing fluids. The highest net power generation found in the preliminary analysis was 2.688 MWe.

The NDDCT model developed in IPSEpro was investigated in isolation to find the optimum design configuration which gives the lowest SIC_{cd}, in AUD/kWth of heat rejected. The tower geometry ratios selected were: aspect ratio (tower height / base diameter) of 1.4, diameter ratio (outlet diameter / base diameter) of 0.7, and A_{fr}/A_3 (the proportion of heat exchanger coverage of the base of the tower) of 0.65. With these geometric ratios fixed, the effect of tower size on cycle performance was investigated in a basic cycle model, by varying the number of heat exchanger bundles, and it was found that an NDDCT of 52.5 m in height and 37.5 m in base diameter gave the lowest SIC for the cycle.

The detailed cycle design stage optimised the 15 cycle configurations selected from the preliminary analysis with both indirect NDDCT and direct MDACT condensers. The cycles were optimised for SIC and it was found in all cases that, despite their higher TCI, the NDDCT condensed cycles produced lower SIC values, due to the higher $\dot{W}_{net}$. The highest performing cycles in ascending order of SIC were the recuperated cycles with isobutene, butene and butane, basic butene, recuperated R152a and then the regenerative butene and regenerative butane cycles. These cycles were selected to progress to the annual performance analysis along with one of each cycle type with an MDACT condenser, in order to allow comparison of NDDCT and MDACT performance variation versus ambient temperature.

The selected cycles were first analysed across the range of ambient temperatures expected at the site, based on temperature data from the Australian Bureau of Meteorology. Next they were subject to a diurnal performance variation analysis for four sample cases for each of the seasons; significant variation of net power generation was found with variation of up to ∓20% from the mean on a daily basis and 25 to 35% change in the mean net power generation from summer to winter, depending on the cycle. Finally, the annual performance analysis used daily temperature data for 2012 to calculate the mean daily net power generation for each of the finalist cycles and this was used to find a mean annual net power generation. The NDDCT cycles were found to achieve 3% to 5% lower SIC than their respective MDACT condensed cycles. The optimum cycle according to the annualised SIC was found to be the recuperated supercritical butene ORC with an NDDCT.

Declaration by author

This thesis is composed of my original work, and contains no material previously published or written by another person except where due reference has been made in the text. I have clearly stated the contribution by others to jointly-authored works that I have included in my thesis.

I have clearly stated the contribution of others to my thesis as a whole, including statistical assistance, survey design, data analysis, significant technical procedures, professional editorial advice, and any other original research work used or reported in my thesis. The content of my thesis is the result of work I have carried out since the commencement of my research higher degree candidature and does not include a substantial part of work that has been submitted to qualify for the award of any other degree or diploma in any university or other tertiary institution. I have clearly stated which parts of my thesis, if any, have been submitted to qualify for another award.

I acknowledge that an electronic copy of my thesis must be lodged with the University Library and, subject to the General Award Rules of The University of Queensland, immediately made available for research and study in accordance with the *Copyright Act 1968*.

I acknowledge that copyright of all material contained in my thesis resides with the copyright holder(s) of that material. Where appropriate I have obtained copyright permission from the copyright holder to reproduce material in this thesis.

Publications During Candidature

None.

Publications Included in this Thesis

None.

Contributions by others

Prof. Hal Gurgenci contributed the thesis topic and provided ongoing guidance in developing the framework and scope of the thesis.

Suoying He provided his NDDCT model written in MATLAB which was referred to while developing the IPSEpro NDDCT model and was used to validate the results of the developed IPSEpro model.

Stephen Gwynne-Jones contributed the cost correlation used to estimate NDDCT cost and numerous discussions on techno-economic modelling.

Statement of parts of the thesis submitted to qualify for the award of another degree

None.

Acknowledgements

Keywords

Australian and New Zealand Standard Research Classifications (ANZSRC)

Fields of Research (FoR) Classification

Contents

List of Figures

XIV

List of Tables

XVIII

Nomenclature

a_B	Baumann factor [-]
A	Area [m^2]
$a_{i,k}$	An empirical constant used in calculating F_T [-]
b	Plate spacing [m]
c	Corrosion allowance [m]
c_p	Specific heat capacity [J/(kg K)]
C	Coefficient
C_p^0	Equipment base purchase cost [USD$_{reference\ year}$]
C_p	Equipment base purchase cost adjusted to 2015 AUD [AUD$_{2015}$]
d	Diameter [m]

$\dot{E}$	Exergy [W]
f	Friction factor [-]; tensile strength, design [MPa]
fpm	Fins per metre [1/m]
F	Correction factor [-]
Fr	Froude Number [-]
g	Gravitational acceleration [m/s^2]
G	Mass velocity [kg/(m^2 s)]
h	Heat transfer coefficient [W/m^2 K]
h	Specific enthalpy [J/kg]
h_{fg}	Latent heat [J/kg]
H	Height; elevation [m]
k	Thermal conductivity [W/(m K)]
K	Loss coefficient [-]
L	Length [m]
$\dot{m}$	Mass flow rate [kg/s]
n	Number [-]
Nc	Number of channels [-]
Nu	Nusselt number [-]
Ny	Characteristic heat transfer parameter [m^{-1}]
p	Pressure [Pa]
P	Tube pitch [m]
Pr	Prandtl number [-]
$\dot{Q}$	Heat transfer rate [W]
R	Gas constant [J/kgK]
r_a	Aspect ratio [-]
r_{am}	Mean diameter aspect ratio [-]
Re	Reynolds number [-]
Ry	Characteristic flow parameter [m^{-1}]
s	Specific entropy [kJ/kg.K]
S	Spacing [m]
SF	Safety factor
SIC	Specific Investment Cost [AUD/kWe]; [AUD/kWth]
t	Thickness [m]
T	Temperature [^{o}C]
U	Overall heat transfer coefficient [W/m^2 K]
v	Specific volume [m^3/kg]

$\dot{V}$	Volume flow rate [m³/s]
w	Fluid velocity [m/s]
$\dot{W}$	Power input/output [W]
x	Vapour quality [%]
y	Fraction of mass flow rate that goes to open feed fluid heater in regenerative cycle [-]

Greek Symbols

Δ	Differential
ε	Surface roughness [m]
η	Efficiency
θ	Angle [º]
μ	dynamic viscosity [Pa.s]
ν	Kinematic viscosity [m²/s]
ξ	Friction coefficient
ρ	Density [kg/m³]
σ	Area ratio
φ	Dimensionless temperature difference

Subscripts

_0_	Dead state
_1_	Relating to the ambient conditions at ground level outside of NDDCT, as per Figure 55
_3_	Relating to the inlet of NDDCT, as per Figure 55
_4_	Relating to the outlet of heat exchangers of NDDCT, as per Figure 55
_5_	Relating to the outlet/throat of NDDCT, as per Figure 55
_a_	Air; aspect
_a34_	Air property at mean temperature through heat exchanger.
amb	Ambient
_av_	Average
_BM_	Bare module
_bp_	Brine pump
bpm	Brine pump motor
_bt_	Bare tube
_c_	Cold
_cd_	Condensing; condensing system
_cf_	Cycle fluid; counterflow

ch	Chamber of tube inlets in STHE
cont	Contingency and contractors fee
cp	Cycle pump
cpm	Cycle pump motor
cr	Critical point
ct	Cooling tower
ctc	Cooling tower contraction
cte	Cooling tower expansion
cw	Cooling water
d	diameter
D	Darcy; drag; drop
DPI	Direct permanent investment
e	Effective
el	Electrical
ev	Evaporating
f	Saturated liquid, fin
fr	Frontal; fin root
ft	Fin thickness
d	Downstream loss
g	Saturated vapour
gb	Geothermal brine
gen	Generator
h	Hot; hydraulic
he	Heat exchanger
heθ	A-frame heat exchanger
hts	Heat transfer surface
in	Inlet
l	Laminar; length; longitudinal
land	Land (cost of)
latent	Latent (heat)
LM	Log mean
m	Mean; mechanical; motor
M	Material
MDACT	Mechanical draft air cooled tower
out	Outlet
p	Passes (tube); pressure

pp	Pinch point	
res	Reservoir	
rows	Tube rows	
royal	Royalties (cost of)	
Root	Fin root	
s	Isentropic; shell; staggered	
sat	Saturation	
sens	Sensible (heat)	
serv	Service facilities (cost of)	
site	Site preparation (cost of)	
startup	Plant startup (cost of)	
t	Tube; turbine	
tb	Tube bundle	
th	thermal	
to	Tower outlet	
tr	Transverse; transitional	
ts	Tower supports	
T	Temperature	
TBM	Total Bare Module	
TCI	Total Capital Investment	
TDC	Total Depreciable Cost	
TPI	Total Permanent Investment	
u	Utilisation	
UL	Upper limit	
wf	Working fluid	
WC	Working capital	

Acronyms and Abbreviations

BOM	Bureau of Meteorology, Australian Government
CEPCI	Chemical Engineering Plant Cost Indices
EGS	Enhanced Geothermal System
HDR	Hot Dry Rock
HSE	Health, Safety and Environmental
HPT	High Pressure Turbine
HTL	High Temperature Loop, refers to the dual fluid cycle

LMTD	Log Mean Temperature Difference
LPT	Low Pressure Turbine
LTL	Low Temperature Loop, refers to the dual fluid cycle
MTD	Mean Temperature Difference
MDACT	Mechanical Draft Air Cooled Tower
NIST	National Institute of Standards and Technology
NDDCT	Natural Draft Dry Cooling Tower
NPSH	Net Positive Suction Head
ODP	Ozone Depletion Potential
ORC	Organic Rankine Cycle
PHE	Plate Heat Exchanger
QGECE	Queensland Geothermal Centre of Excellence
SIC	Specific Investment Cost
STHE	Shell and Tube Heat Exchanger
REFPROP	Reference Fluid Thermodynamic and Transport Properties – by NIST
TCI	Total Capital Investment
WHR	Waste Heat Recovery

1. Introduction

1.1 Project Background

Population growth, continued industrialisation and the resulting growth in energy consumption, combined with the environmental impacts and depletion of fossil fuel resources and their environmental impacts are the drivers of a global search for renewable and clean energy sources. Enhanced Geothermal Systems (EGS) are a potentially viable source of renewable energy and the Organic Rankine Cycle (ORC) is widely recognised as the most promising methods of energy conversion for low to moderate temperature heat sources such as EGS.

Geothermal energy was first used on an industrial scale in Italy in 1912, was employed in New Zealand in the 1950s and, as shown in Figure 1, has steadily increased in usage since then (Bertani, 2015). The pioneering applications were generally from readily accessible near surface hot groundwater resources; at temperatures of around 100 ºC.
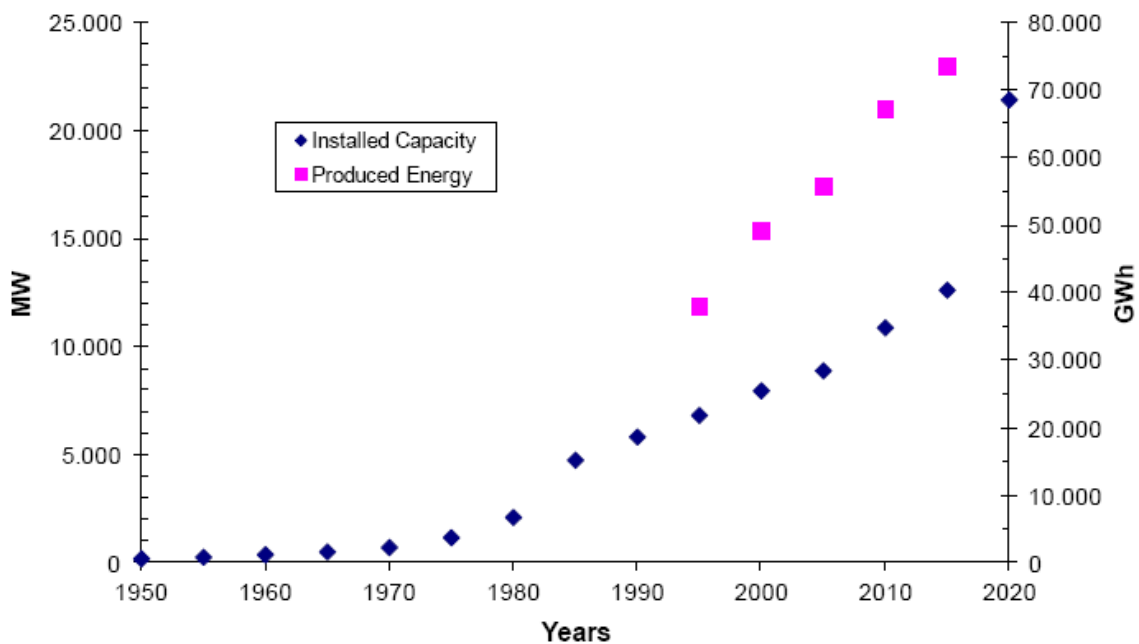
Figure 1: Cumulative installed capacity of geothermal worldwide (Bertani, 2015).

The EGS concept was first investigated in the 1970's. In 2013 the viability of EGS for Australian geothermal resources was demonstrated with the Habanero 1 MW pilot plant. The trial successfully ran for 160 days as scheduled in 2013 (Mills & Humphreys, 2013).

The power plant configuration used in the Habanero pilot plant was a simple brine flash plant. The design was deliberately kept simple to minimise the capital cost for the pilot plant.

After proving the viability of EGS in Australia, the next step is to develop the first commercial EGS power plant.

The aim of the current research project is to identify the most efficient power plant configuration for an Australian EGS power plant using a binary ORC. EGS is able to produce geothermal heat at a higher temperature than conventional geothermal wells, so this project aims to optimise the power plant for this temperature range.

EGS geothermal energy was first investigated to exploit the vast portions of the earth's crust that were expected to contain hot subsurface rock without fluid. Therefore these resources were first named Hot Dry Rock (HDR) and later started being called EGS. HDR or EGS resources are more abundant than conventional geothermal resources and more evenly distributed around the globe (Brown, 2009).

There is already an operational EGS plant in Landau, Germany, which was commissioned in 2007 (Clean Energy Action Project, 2012). It is the world's first commercially funded ORC EGS power plant. Landau is a Combined Heat and Power plant that utilises 155 $^\circ$C thermal water from a depth of 3000 m.

The current project is of commercial interest as it directly pertains to the conditions found at the Australian Habanero site. The project was conducted in collaboration with Geodynamics to the extent of using industry input where required and in order to develop an industry friendly plant design. The input conditions are provided by Geodynamics to facilitate comparison of the findings of this project to tender submissions by third parties.

The purpose of this project is to determine the power plant design that most cost effectively generates electrical power for the conditions found at the Habanero site, which are presented in Section 1.3. The overall objective of the project is to minimise the cost per kWe generated by the plant. There are several key aspects to determining the optimum plant design:

- Selection of the cycle working fluid and cycle configuration that work together synergistically to achieve the best thermodynamic performance. The cycle fluid thermodynamic properties can significantly affect the plant efficiency (Rayegan & Tao, 2010).
- Selection and design of the condensing system. Air-cooled geothermal power plants have conventionally used mechanical draft condensers, resulting in high parasitic

power consumption. The use of Natural Draft Dry Cooling Towers (NDDCT) would eliminate this source of efficiency reduction. The coupled modelling of NDDCT with the selected power cycle forms an integral part of this project.

- Heat exchanger selection and design. The heat exchangers are also a key focus in the design of the power plant, as they generally form a significant portion of the cost of the plant, especially in the pursuit of minimising exergy destruction. In binary geothermal power plants the heat transfer process is one of the key areas leading to high second law efficiencies (M. Kanoglu & Bolatturk, 2008). However, seeking to match the temperature profiles, thereby reducing exergy destruction requires a larger heat transfer surface area and therefore a more expensive heat exchanger.

- Holistic systems design approach to account for the interdependent nature of the power plant subsystems.

- Off-design analysis to allow prediction of plant performance in the range of expected ambient temperatures.

The key trade-off is between performance and cost. The drilling costs form a significant proportion of plant cost, reported by Kranz (2009) at up to 70% for resources of 2.5-5km depth.. It is deemed that the significantly larger cost of the geothermal wells makes the plant performance of greater importance to ensure that as much of the available energy is utilised as possible.

1.2 EGS Overview

This section will give a brief overview of the EGS process and how it differs from conventional geothermal systems. Gupta and Roy (2006) categorise the types of geothermal resources into the following groups:

1. Vapour-dominated,
2. Hot water,
3. Geopressured,
4. Hot dry rock (HDR), and
5. Magma.

The defining feature of EGS is that it utilises the heat from HDR resources. Conventional geothermal systems generally use either hot groundwater or vapour dominated resources. In both cases the heat is stored within the underground fluid that comprises the geothermal

resource. The source of the heat is often volcanic activity and is generally associated with seismically active regions (California Energy Commission, 2015). This geothermal water is more readily available and may even be accessible at the surface, for example via naturally occurring geysers. In such cases relatively little power is consumed in bringing the heat to the power plant at the surface. The EGS resource on the other hand, is located at depths of 3 to 5 km. Moreover, EGS operation requires substantial pumping power to generate the pressure required to maintain suitable water flow through the reservoir.

The following information is summarised from the Geodynamics Limited website (Geodynamics Limited, 2012) unless otherwise noted. The EGS resource consists of hot dry rocks, so a heat transfer fluid must be circulated to capture the heat and bring it to the surface; water is used for this function. Water is pumped down an injection well, then permeates through naturally pre-exiting cracks, which have been slightly opened up ("enhanced") by hydraulic stimulation to allow passage of the water. The injected fluid resurfaces via a production well on the other side at a significantly higher temperature. This process is illustrated in Figure 2.
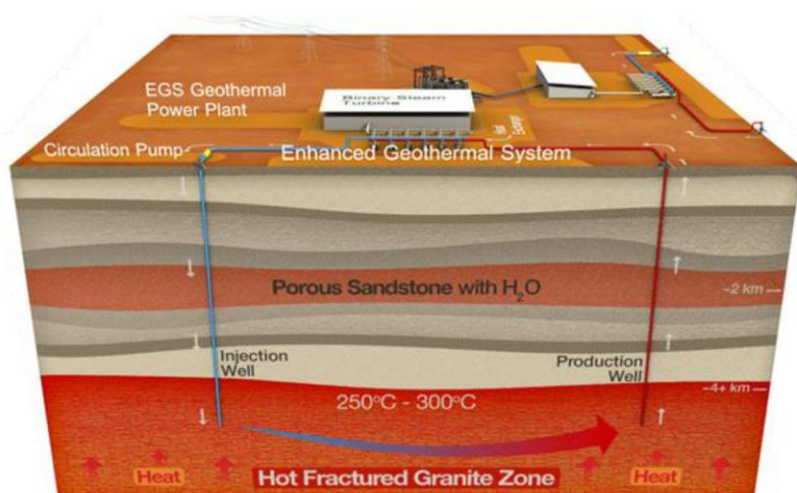
Figure 2: Overview of EGS process (Mills & Humphreys, 2013).

The source of the heat in EGS resources is high heat producing rock formations, mainly granites, which contain small quantities of naturally occurring radiogenic minerals such as isotopes of potassium, uranium and thorium. Through radiogenic decay, these minerals generate heat in the granite. Various layers of insulating sedimentary rock formations occur above the heat producing granite, which trap the heat and cause it to build up in the granite basin.

1.3 Site Conditions

The site conditions used in this project are those of the Innamincka site in the Cooper Basin in South Australia, as shown in Figure 3.
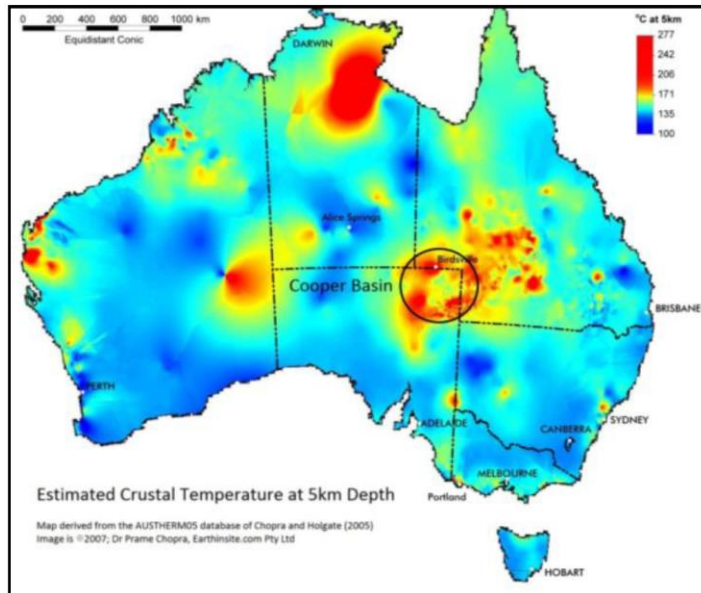
Figure 3: Location of the Cooper Basin EGS resource on a map of estimated crust temperatures at 5km depth (Mills & Humphreys, 2013).

The site parameters used for this project are presented in Table 1. The thermodynamic properties of water will be used for the geothermal brine properties.

Table 1: EGS conditions – those found at the Habanero site in the Cooper Basin in South Australia (Mills & Humphreys, 2013).

Parameter	Value
Brine production well head temperature	220 ºC
Minimum brine temperature	80 ºC
Brine mass flow rate	35 kg/s
Brine production wellhead pressure	35 MPa
Brine reinjection pressure	45 MPa
Minimum ambient temperature*	-1.4 ºC
Maximum ambient temperature*	49.1ºC
Average Annual rainfall*	206 mm

*Climate data taken from Bureau of Meterology (2015) for the period of 1972 to 1999

The high brine reinjection pressure is required in order to achieve the desired geothermal brine flow rate through the reservoir. The minimum brine reinjection temperature is constrained by the temperature below which the geothermal brine will start causing fouling

problems in the pipes and heat exchanger. Walraven, Laenen, and D'haeseleer (2013) found that constraint of the brine outlet temperature from the heat exchangers greatly decreases the mechanical power output of the system.

Historical climate data from the Australian Bureau of Meteorology will be used; the closest available climate data for the site is that for Moomba, SA.
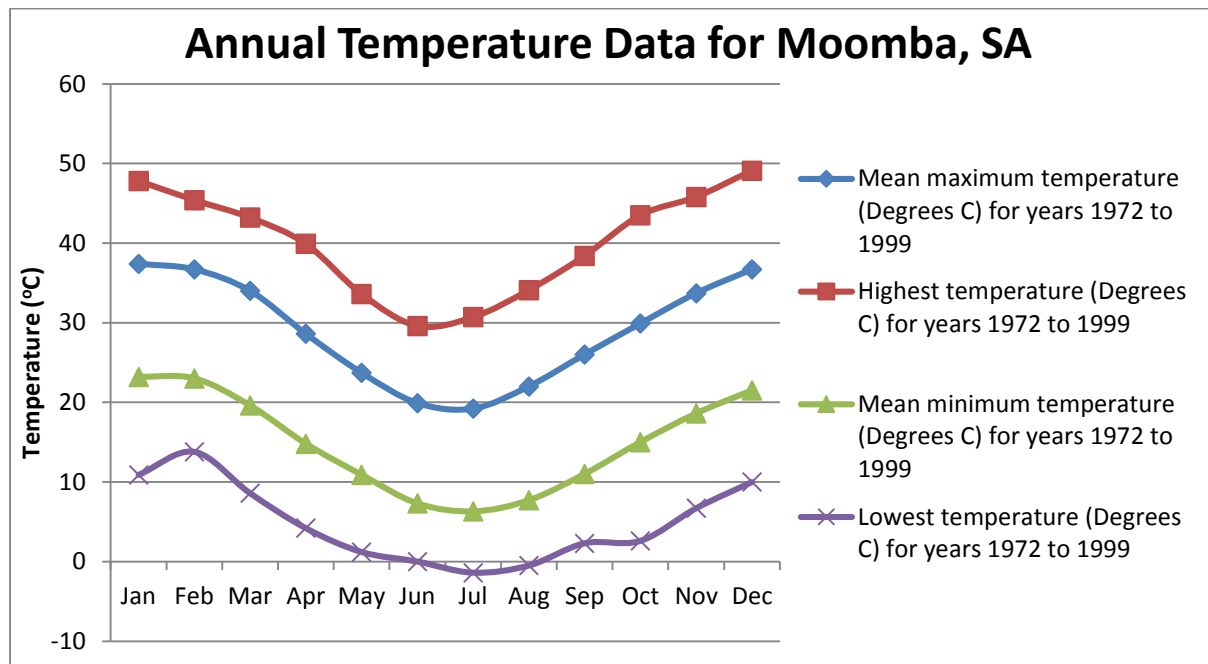
Figure 4: Annual ambient temperature range for Moomba, SA (Bureau of Meterology, 2015).

Figure 4 shows summary data for Moomba for the period of 1972 to 1999. As can be seen from Figure 4 there is a significant potential for temperature variation in this region, potentially over a short period of time, so it is important to account for this in the design for the power plant.

1.4 Project Structure Overview

The aim of this project is to determine the optimum ORC power plant configuration to utilise the EGS resource identified at Innamincka, South Australia. This is performed over several stages, starting with a literature review to determine potential cycle configurations and a candidate fluid search in REFPROP (Lemmon, Huber, & McLinden, 2013). Then each cycle and fluid are analysed in turn using a set of simplifying assumptions suitable to a preliminary, screening analysis. The highest performing cycles in the preliminary analysis are selected to progress to the detailed design stage.

Concurrently, detailed NDDCT, MDACT and shell and tube heat exchangers models are developed. The behaviour of the NDDCT model is explored in a trade-off analysis to identify the most cost effective NDDCT size and configuration.

Using these more detailed models and with plant cost correlations the cycles selected from the preliminary analysis are developed to a detailed cycle design stage in which they are optimised for minimum specific investment cost (SIC), which is defined as total investment cost per net power generation to give a value in AUD/kWe.

There appears to be a gap in the literature around the relative techno-economic performances of NDDCT and MDACT condensed ORCs. This project seeks to explore this issue and determine which is the more cost effective option in terms of SIC.

The cycles with the lowest SIC in the detailed cycle design stage progress to the diurnal and annual performance analysis stage, along with one cycle of each type using an MDACT as a condenser to allow for comparison. The cycles are analysed at a range of ambient temperatures and this data together with site climate data is used to calculate an annualised SIC value, from which the optimum cycle configuration is selected.

2. ORC Design Considerations

Three major types of power plants are used today to generate electricity from geothermal resources: dry-steam, flash steam, and binary. Guzovic, Raskovic, and Blatari (2014) provide the following general circumstances for when each is used: dry-steam plants are used for high temperature (>235 ℃), vapour dominant, hydrothermal resources; flash steam power plants are used for liquid dominated, hydrothermal resources (>180 ℃); binary is used for any other scenario. One of the most common binary cycle type is the Organic Rankine Cycle (ORC). There are several arguments for using an ORC for this project, despite the resource temperature being in the domain of flash steam power plants according to the above guidelines. The main relevant arguments for binary ORC over binary steam Rankine cycles, or the direct steam power plants mentioned above are:

- Component size, ORC components can be much smaller due to the higher density of organic fluids than steam at operating pressure (Quoilin, Van den Broek, Declaye, Dewallef, & Lemort, 2013).

- Plant configuration simplicity, ORC can achieve a comparable efficiency with a simple plant configuration, in terms of number of components (Quoilin et al., 2013).

- Separation of geothermal fluid from power conversion loop components. This limits the scaling issue and the associated performance degradation and resulting higher maintenance requirements to only the hot side of the heat exchanger, rather than right through the turbine(s), condenser and pump(s). As is the case for flash steam power plants which utilise the geothermal fluid directly as the working fluid (DiPippo, 2012).

- No liquid droplet formation in turbines, due to the range of fluids available and the different shapes of their T-s diagrams, ORC can be easily designed to have dry expansion process (Quoilin et al., 2013).

- Condensing pressure, to achieve a low condensing temperature, one approaching ambient temperature, steam cycles must condense at below ambient pressure and as such risks ingress of air to the system (Quoilin et al., 2013). This can cause problems such as system performance degradation and pump damage. The majority of ORC fluids have condensing pressure above atmospheric pressure.

- For geothermal resources with geofluid as pressurised liquid DiPippo (2012) states that it is not thermodynamically wise to flash the fluid in surface vessels and use it in

8

a flash steam plant. This is particularly applicable for this case where minimal water consumption is permissible, meaning the water must be used in a closed loop as the heat transfer fluid. Furthermore it simplifies the brine handling process in that the brine passes through the heat exchanger and remains in liquid form and is easily repressurised in the down-well pump for reinjection (DiPippo, 2012). EGS incurs a significant pressure loss in maintaining flow through the reservoir.

- Turbine design considerations also favour the choice of ORC. Steam cycles operate at a higher pressure ratio and enthalpy drop than ORC. As a result, turbines with several stages are generally used in contrast with the single or two stage turbines used for ORC (Quoilin et al., 2013).

The organic Rankine cycle (ORC) is comprised of the same main components as the conventional steam Rankine cycle: heat exchangers, expander, condenser and pumps. The difference however is that ORC uses organic fluids which have a much lower critical temperature and pressure, and lower specific heat of vaporisation. The various organic fluids have a wide range of thermodynamic properties and this allows the ORC to be designed to match any heat source characteristics.

Compared to conventional coal-fired thermal power plants which operate at high boiler temperatures, one of the major drawbacks of low temperature power applications is that they require a much larger relative heat rejection to condense the working fluid compared to steam power plants. Hence the efficiency of the condensing process can have a significant impact on the overall system performance. Therefore special attention is required in selecting and designing the condensing system.

The brine heat is transferred to the pressurised organic cycle fluid via heat exchangers. The cycle fluid is then expanded through a turbine after which it is condensed, and finally repressurised in the cycle pump then fed back through the heat exchangers. This process is shown schematically in Figure 5 and on a pressure-enthalpy diagram in Figure 6.
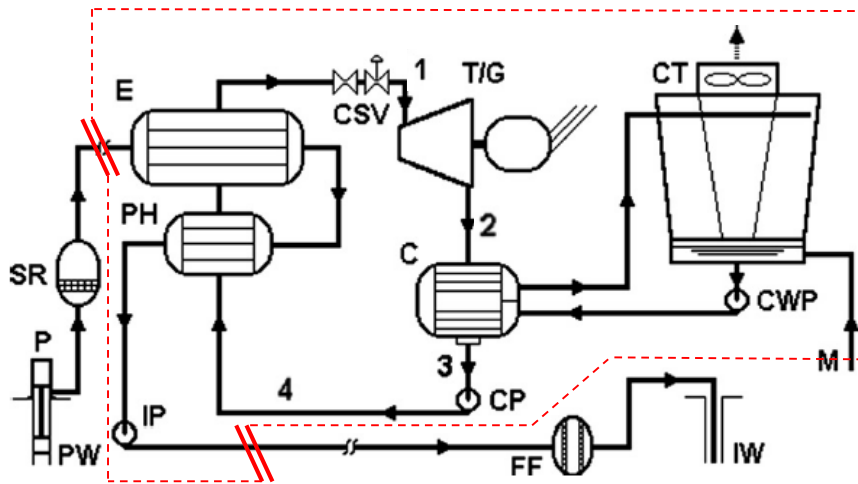
Figure 5: Basic binary ORC, where the dashed red line denotes the scope boundary for this project. ORC is shown here with a separate cooling fluid loop a mechanical draft air cooled tower (CT), preheater (PH), evaporator (E), turbine/generator (T/G), condenser (C), cooling water pump (CWP), cycle pump (CP) and injection pump (IP) (DiPippo, 2012). State point numbers added to diagram for consistency.

The scope of this project is the design of the power generation cycle only, so the limits of the scope are at the brine heat exchanger water side inlet, and at the injection pump outlet, as is depicted in Figure 5.
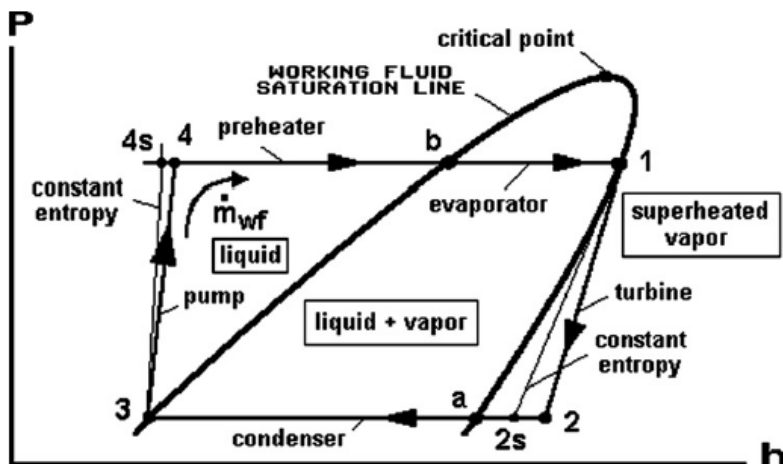
Figure 6: P-h diagram for a basic binary ORC plant (DiPippo, 2012).

Exergy analysis is a powerful tool for analysis of energy systems (Mehmet Kanoglu, 2002) and can be used identify where process efficiency improvements might be obtained. The following table presents the source of exergy destruction of several existing binary geothermal power plants, according to the references given in the column headings.

	Mehmet Kanoglu (2002)	Yildirim and Ozgener (2012)		Ganjehsarabi, Gungor, and Dincer (2012)	M. Kanoglu and Bolatturk (2008)	Jalilinasrabady, Itoi, Valdimarsson, Fujii, and Tanaka (2011)
Plant	Stillwater, NV, USA	DORA I, Turkey	DORA II, Turkey	DORA II, Turkey	Reno NV, USA, 27MW	Iran, 17MW
Commissioning Year	1989	2006	2010	2010	Unspecified	Proposed design
Brine Reinjection	14.8%	22.9%	31.7%	32%	35.3%	33.36%
Turbine and Pump losses	14.1%	15.9%	9.5%	12%	7.2%	8.84%
Heat Exchanger Losses	13%	13.2%	7.9%	8%	12.6%	8.95%
Condenser losses	22.6%	13.3%	19.7%	15%	18.9%	12.13%
Parasitic losses	6.4%	-	-	-	4.3%	2.36%
Net Power	29.1%	34.7%	31.2%	30%	21.7%	34.37%

The brine reinjection losses are constrained by the minimum brine temperature limit to prevent excessive fouling in the heat exchangers. Pump detailed design process is generally well established so there is little improvement that can be gained from that and turbine detailed design is beyond the scope of this project. The effect of cycle fluid selection and the cycle configuration is not represented in Table 2; Rayegan and Tao (2010) report that these can significantly affect cycle efficiency, this is discussed in more detail in Section 2.2. Quoilin et al. (2013) showed that fluid selection also influences the pump power consumption, this is discussed in further detail in Section 2.7.1.

The exergy flow diagram in Figure 7 shows the data in Table 2 graphically for the DORA II binary ORC plant.
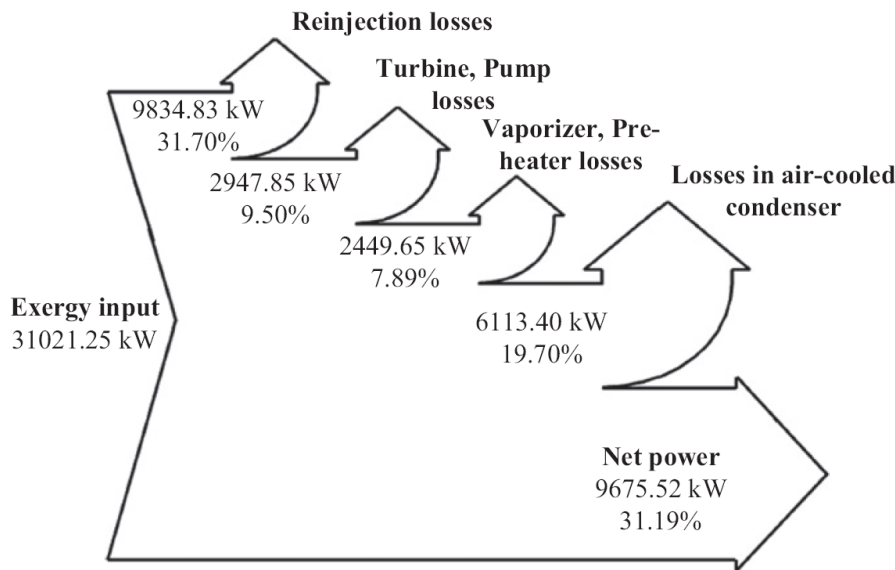
Figure 7: Exergy flow diagram of the DORA 2 plant in Turkey (Yildirim & Ozgener, 2012). Note figure not to scale.

As shown above in Table 2 and Figure 7, a significant portion of the exergy destruction occurs in the condenser. While the majority of this exergy destruction is the unavoidable exergy loss through latent heat transfer required to condense the cycle fluid, a portion of this is attributed to the parasitic power consumption in the condenser. The parasitic power consumption in forced draft condensing systems can account for 10% to 12% of gross power, under ideal conditions, and as much as 40-50% for ambient temperatures approaching condensing temperature (Franco & Villani, 2009). Utilising an NDDCT instead of a forced draft cooling tower eliminates this source of parasitic power consumption. This may, however, come at the expense of higher capital investment in the condensing system due to the larger heat transfer surface area required.

This gives the following main focus points in the ORC design approach for this project:

- Cycle configuration,
- Cycle fluid selection,
- Condensing system design, and
- Heat exchanger design.

These aspects of the project will be discussed in more detail in the following sections.

2.1 Overall Cycle Analysis

In this section some of the overall cycle analysis principles used in this project will be covered. The objective of this project is to find the cycle with the lowest cost per kWe net

power generation. The net power generation is given by the electrical power output at the generator less the electrical work input to the pump motors:

$$\dot{W}_{net,cycle} = \dot{W}_{gen} - \dot{W}_{cpm} - \dot{W}_{cd}$$

Equation 1

where $\dot{W}_{cpm}$ refers to the power required by the cycle pump motor and $\dot{W}_{cd}$ refers to power consumed in the condensing system. This gives the cycle net power output, which is distinguished from the plant net power output which also accounts for the non-negligible brine pump power consumption. The overall plant net power generation is given by

$$\dot{W}_{net} = \dot{W}_{gen} - \dot{W}_{cpm} - \dot{W}_{cd} - \dot{W}_{bpm}$$

Equation 2

There may be numerous other auxiliary parasitic loads such as station lighting etc., which are not considered in the plant thermal efficiency. The cycle First Law efficiency is calculated using the thermal efficiency, which is given by

$$\eta_{th,cycle} = \frac{\dot{W}_{net,cycle}}{\dot{Q}_{in}}$$

Equation 3

or for overall plant thermal efficiency

$$\eta_{th} = \frac{\dot{W}_{net}}{\dot{Q}_{in}}$$

Equation 4

Another useful measure of cycle and plant performance is the exergy efficiency or Second Law efficiency, which is obtained in the form of the utilisation efficiency, which DiPippo (2008) defines as the ratio of the actual net plant power to the maximum theoretical power obtainable from the geothermal fluid:

$$\eta_u = \frac{\dot{W}_{net}}{\dot{E}_{res}} = \frac{\dot{W}_{net}}{\dot{m}_{gb}[(h_{res} - h_0) - T_0(s_{res} - s_0)]}$$

Equation 5

where T_0 refers to the dead-state temperature, or the ambient temperature and h_0 and s_0 are the enthalpy and entropy of the geothermal fluid evaluated at the dead state pressure and temperature, and the subscript res denotes resource properties, which in this case is the brine inlet properties.

It is worth clarifying the difference in the meaning of these efficiency measures. Thermal efficiency provides a measure of how efficiently the energy input is used, regardless of the temperature range. While the utilisation efficiency is the measure of how efficiently the

available energy is used regardless of how much is extracted from the heat source, since the available energy of the heat source is only dependent on the resource temperature and the dead state conditions.

There may be a case where a cycle extracts less energy from the heat source, and in doing so is able to achieve a higher thermal efficiency, while generating less net power. This would however result in decreased utilisation efficiency. Thermal efficiency, while not necessarily the best indicator of plant performance in this case, is a commonly used method to compare different processes and hence should still be calculated for each cycle.

2.2 Fluid Selection

The selection of the working fluid for an ORC and the cycle configuration can significantly affect efficiency (Rayegan & Tao, 2010). There are many factors to consider in selecting the cycle fluid for an ORC plant, such as the fluid physical properties in the temperature range of the plant, the cost and availability, and the health, safety and environmental properties of the fluid (Rettig et al., 2011).

2.2.1 Fluid Selection Criteria

Due to the wide variety of applications, each requiring different working conditions, and priorities for objective function there is no single optimum fluid, the study of optimum working fluids should therefore be integrated into the ORC design process (Quoilin et al., 2013). The fluid selection criteria are comprehensively presented by Quoilin et al. (2013):

1) High vapour density, this leads to lower volume flow rates and smaller components.
2) Low viscosity, this leads to high heat transfer coefficients and lower friction losses in heat exchangers.
3) High thermal conductivity, this results in higher heat transfer coefficients.
4) The thermal stability of each candidate fluid also needs to be analysed in the operating range of the plant and the chemical compatibility with the materials used in the plant (Invernizzi, 2013).
5) Acceptable evaporating pressure, higher pressures usually lead to high investment costs and increased complexity.
6) Positive condensing gauge pressure to prevent ingress of air into the cycle as sealing of turbines and pumps are generally designed to minimise egress, not prevent ingress.

7) The fluid melting point should be lower than the lowest ambient temperature to avoid freezing of the cycle fluid.

8) Acceptable safety level; the two main safety parameters are flammability and toxicity.

9) Low Ozone Depletion potential (ODP).

10) Low Greenhouse Warming Potential (GWP).

11) Good availability and cost.

Selecting fluids for acceptable evaporating pressure is a reasonable objective. This objective is however at odds with the observation by Bao and Zhao (2013) that decreasing the heat of vaporisation decreases irreversibilities in the heat transfer process, as shown in Figure 8. For a given fluid the latent heat of vaporisation can be reduced by increasing pressure, so it can be seen how these objectives are somewhat conflicting and sticking firmly to a set of fluid selection criteria may not result in the optimum outcome.
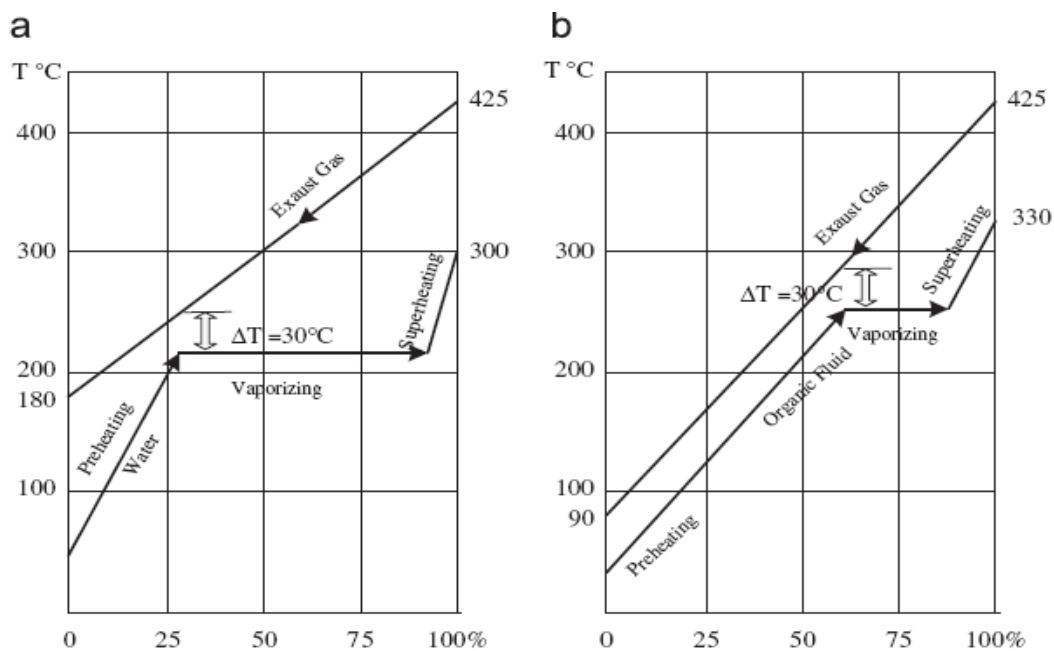
Figure 8: The effects of latent heat of vaporisation on the heat transfer process (Bao & Zhao, 2013).

At this stage no fluids will be ruled out based on health, safety or environmental (HSE) attributes; these attributes are being presented in order to consider them alongside performance. If a toxic, flammable liquid were significantly more efficient than any other fluid, the cost of the additional safety measures required to utilise such a fluid would need to be quantified and considered in the final decision making process.

Quoilin, Declaye, Tchanche, and Lemort (2011) studied the optimum evaporation temperature for subcritical ORC based on a thermoeconomic ORC model and found that the optimum evaporating temperature is usually far below the heat source temperature.

2.2.2 Fluid Types

One of the key methods of categorizing ORC fluids is by the shape of the T-s diagram (Bao & Zhao, 2013). The shape of the T-s diagram determines the types of cycle the fluid is compatible with and affects the cycle efficiency (Hung, 2001). The defining aspect of the T-s diagram is the gradient of the saturated vapour portion of the saturation curve. Figure 9 shows the three main types of fluids based on T-s diagram shapes: isentropic, wet and dry. The naming convention is based on the description of the expansion process with no superheating.
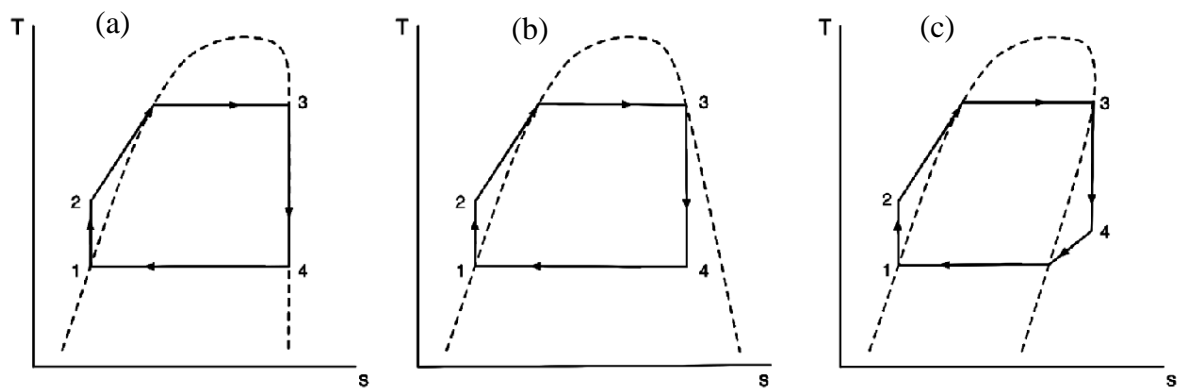
Figure 9: Comparison of the three types of organic fluids (a) isentropic, (b) wet, and (c) dry (Mago, Chamra, Srinivasan, & Somayaji, 2007).

The location of the critical temperature relative to the brine inlet temperature dictates whether the fluid is best suited to subcritical cycles or supercritical cycles, or whether both are possible. Subcritical versus supercritical cycles will be discussed further in Section 2.2.3.1. J. Xu and Liu (2013) showed that fluids with critical temperature approaching the heat source inlet temperature results in better exergy and thermal efficiencies. Quoilin et al. (2013) showed that the higher the fluid critical temperature, the lower the Back Work Ratio (BWR), which leads to lower pump power consumption relative to the turbine power generation. The BWR is discussed further in Section 2.7.1.

Based on the above a preliminary a range of potential fluids were collated; Figure 10 shows the T-s diagram shapes of some of the likely candidate fluids.
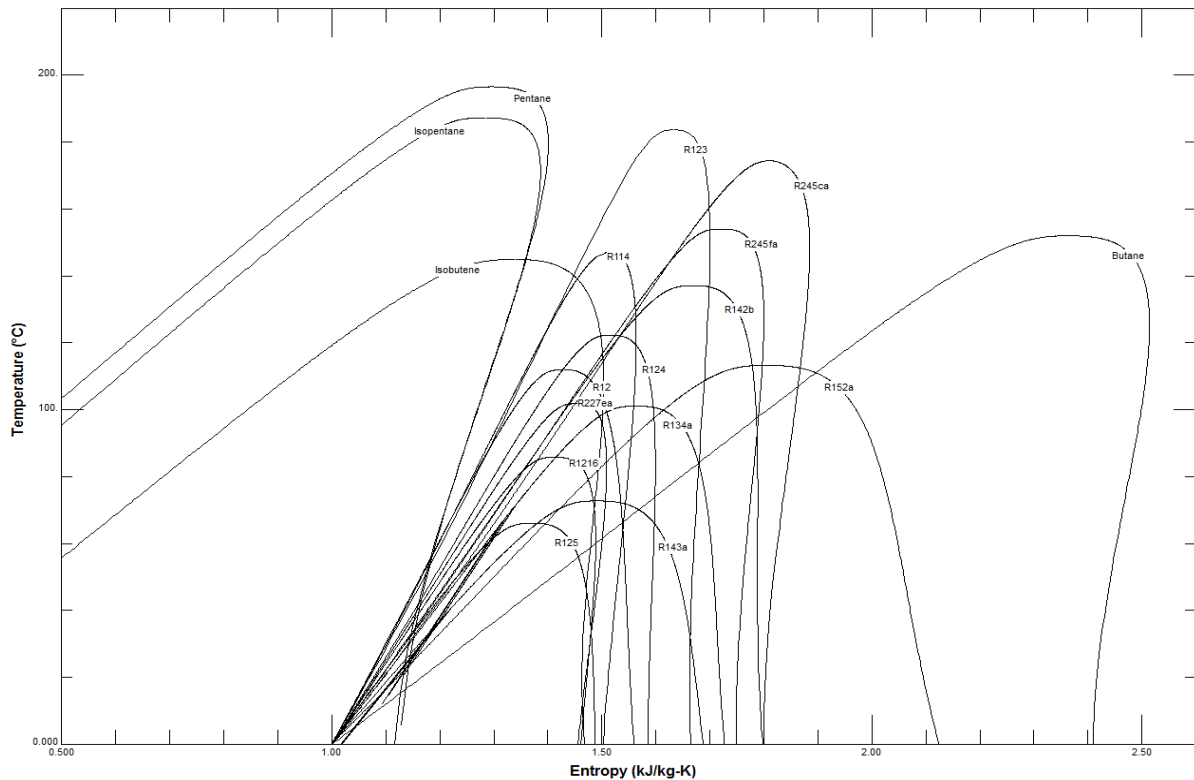
Figure 10: T-s Diagram comparison of some candidate fluids, compiled from REFPROP (Lemmon et al., 2013).

Several studies have found that multicomponent mixtures may provide efficiency improvements (Angelino & Colonna di Paliano, 1998; Huijuan Chen, D. Yogi Goswami, Muhammad M. Rahman, & Stefanakos, 2010). Mixtures evaporate at variable temperature, unlike pure fluids, so this allows better temperature matching to the brine heat curve (DiPippo, 2012). This benefit may not be comparable to the improvement gained by supercritical heat transfer. For this project only pure fluids will be considered.

2.2.3 Fluid Based Cycle Design Considerations

2.2.3.1 Subcritical vs Supercritical ORC

Subcritical and supercritical cycles each have their advantages. Subcritical cycles have long been used and can operate at lower pressures, reducing capital costs for lower pressure rating equipment, pipes and fittings, whereas supercritical cycles can better match the temperature profiles between the brine and the cycle fluid resulting in a more efficient and effective heat transfer process. The efficiency benefits of supercritical cycles have been shown in a number of studies (Gu & Sato, 2001, 2002; Karellas & Schuster, 2008; Vetter, Wiemer, & Kuhn, 2013; J. Xu & Liu, 2013).
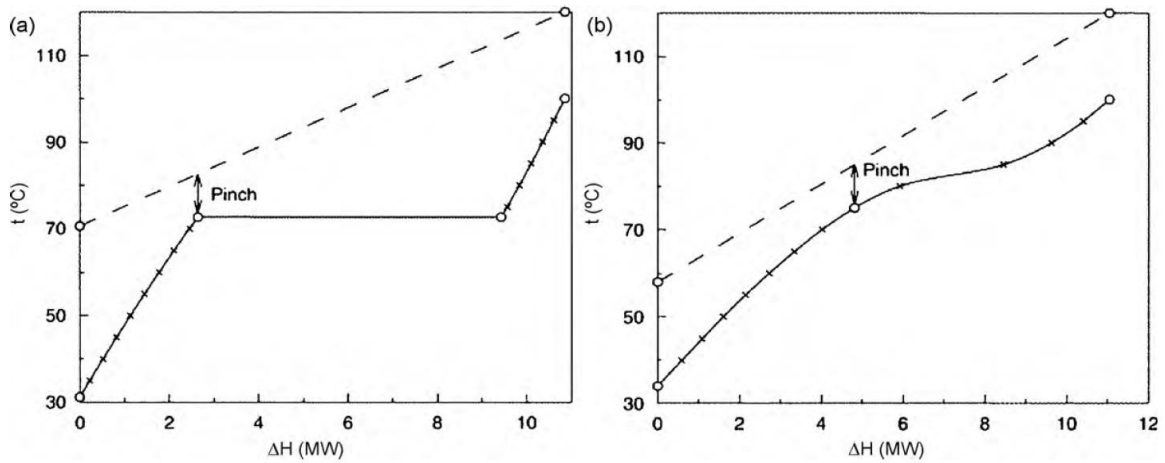
Figure 11: Illustrates the difference between (a) subcritical heat transfer and (b) supercritical heat transfer (Chen, Goswami, & Stefanakos, 2010).

Figure 11 shows how the supercritical cycle provides a better match in the heat transfer profiles. The pinch point is less pronounced and the mean temperature difference is lower, which results in less exergy destruction due to finite temperature difference.
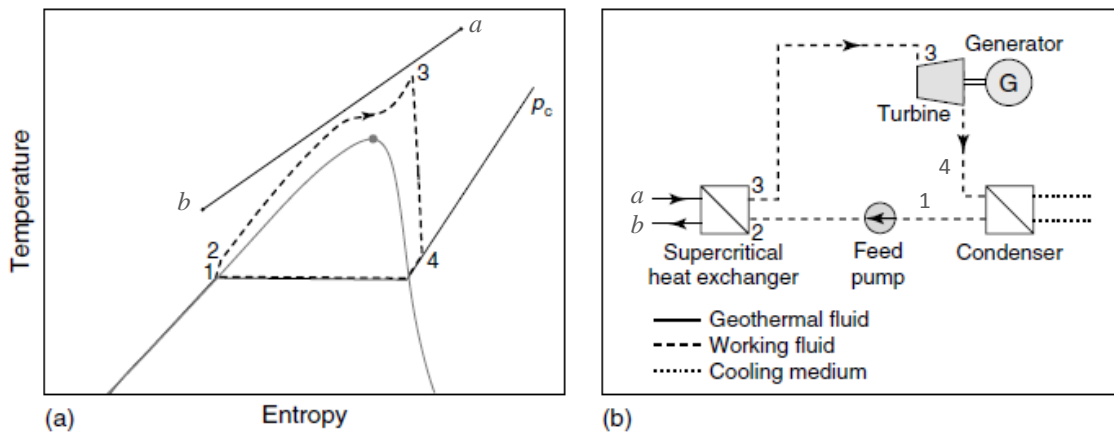
Figure 12: (a) T-s diagram and (b) simplified schematic of a supercritical binary ORC, taken from Saadat, Frick, Kranz, and Regenspurg (2010) with state point numbering modified for consistency.

The supercritical cycle also approaches the triangular cycle, which DiPippo (2012) argues is a more realistic ideal cycle for a geothermal binary plant than the Carnot cycle, due to the non-isothermal nature of the heat source. Note also that supercritical heat transfer can be achieved with a single heat exchanger due to the indistinct transition from liquid to vapour.

All of the ORC configurations considered in this project can be utilised as either subcritical or supercritical cycles. The more appropriate choice depends on the critical temperature of the cycle fluid being considered and the purpose of the cycle configuration.

2.2.3.2 Critical Conditions Approach Limit

Near critical temperature and pressure the small changes in temperature result in large changes in pressure so the system can become unstable resulting in unpredictable system behaviour (Bao & Zhao, 2013; Rayegan & Tao, 2010). It is therefore pertinent to set a limit for how close cycle pressure and temperature are allowed relative to critical conditions. There are differing limits used in the literature:

- Drescher and Brüggemann (2006) suggested a minimum of 0.1 MPa difference between maximum operating pressure and critical pressure.
- Heberle and Brüggemann (2010) used a maximum cycle pressure of 90% of the critical pressure.
- Delgado-Torres and García-Rodríguez (2007) used a limit of 10-15 °C.
- Rayegan and Tao (2010) argued that using a set interval for the limit is not a consistent method. Instead they developed a more elaborate method of limiting cycle high pressure, which only applies to dry and isentropic fluids with no superheating of the fluid. Their approach consists of restricting the vapour quality at point C, in Figure 13, to 1%, thus maximum pressure is Ph_2.
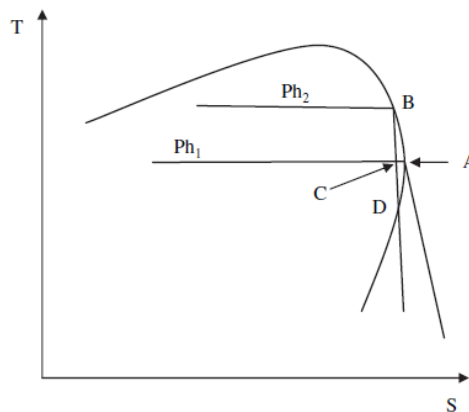
Figure 13: High pressure limit of the ORC, method used by Rayegan and Tao (2010).

The approach used by Rayegan and Tao (2010) is based on the general observation that superheating beyond the saturation line may increase the thermal efficiency but decreases the exergy efficiency. This method is dependent on the shape of the saturation envelope between the critical point and point A of Figure 13. This can result in a significant variation of limit that is further than is necessary from the critical point. For example, by this method Acetone has an interval of 1.321 MPa and 21.9 °C from critical conditions of 4.700 MPa and 234.9 °C, whereas Isopentane has an interval of 0.509 MPa and 10.2 °C from the critical point of 3.396

MPa and 187.2 °C. This method is also based on liquid droplet formation in the turbine by not exceeding Ph$_2$, rather than preventing encroachment on the variable properties zone around the critical point.

For the sake of simplicity and applicability to all fluid types a combination of Drescher and Brüggemann (2006) and Delgado-Torres and García-Rodríguez (2007) methods will be used with limits of 0.2 MPa or 10 °C, whichever comes first.

2.2.3.3 Effectiveness of Superheating

Superheating is an essential aspect of steam Rankine cycles, this is due to the wet fluid shape of the T-s diagram of water. However superheating is not necessarily beneficial for ORC and in some cases superheating negatively affects cycle efficiency (Chen et al., 2010; Vélez et al., 2012). Chen et al. (2010) summarised that superheating is necessary for wet fluids, as seen in Figure 14, but has little effect on isentropic fluids, and may negatively affect dry fluids.
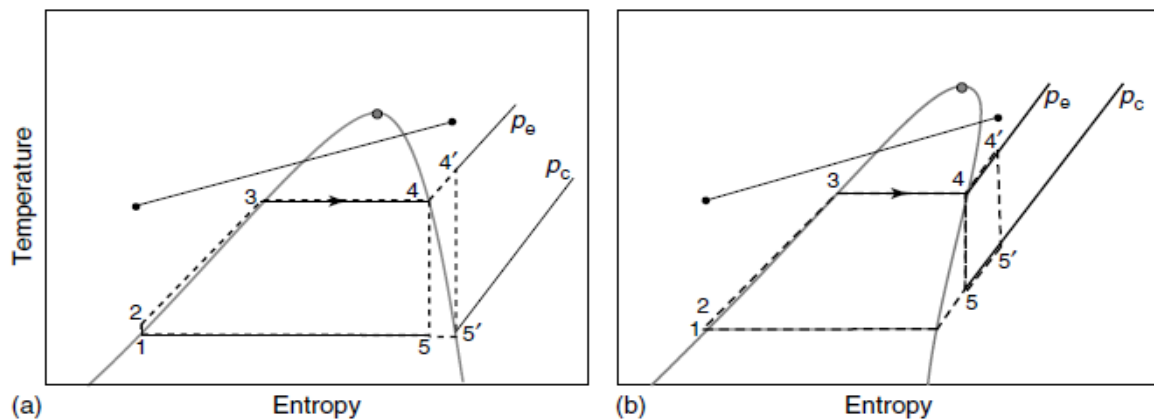
Figure 14: T-s diagrams showing heat transfer profile and comparing the effectiveness of superheating for (a) a wet fluid, and (b) a dry fluid (Saadat et al., 2010).

Figure 15 illustrates how superheating beyond the saturation envelope for dry fluids does not necessarily increase Δh, but it increase the sensible heat that needs to be rejected in the condenser due to displacing point 5 to 5' as shown in Figure 14 (b).
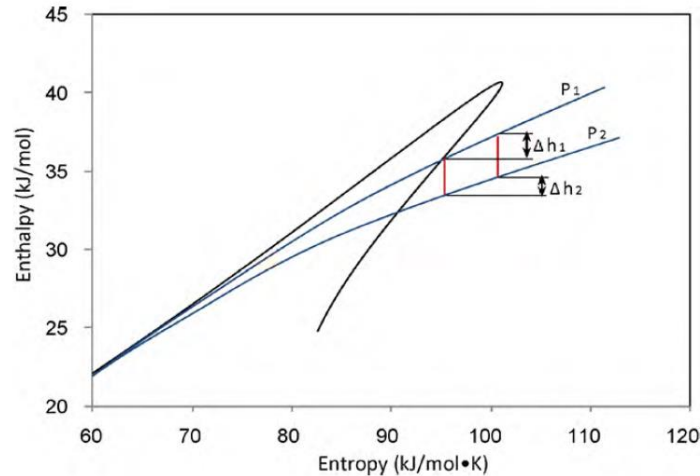
Figure 15:T-s diagram of pentane demonstrating that there is little benefit from superheating dry fluids (Chen et al., 2010).

Vélez et al. (2012) found that for ORC increasing the turbine pressure ratio resulted in much larger improvement in cycle efficiency than increasing the turbine inlet temperature.

2.3 ORC Cycle Variants

When considering the more advanced cycles another factor for consideration arises, the degree of complication of the plant. The more complicated cycles will need to provide a significant performance benefit in order to compensate for the additional components and complication in operational control. If a more complicated cycle arrangement only provides a marginal benefit then the simpler plant may still be the more favourable option.

2.3.1 Recuperated ORC

The basic binary cycle is effective for isentropic or dry fluids where the turbine outlet temperature is near the condensing temperature. However if there is significant recoverable heat at the turbine outlet this can be captured using a recuperator as shown below in Figure 16 (a).
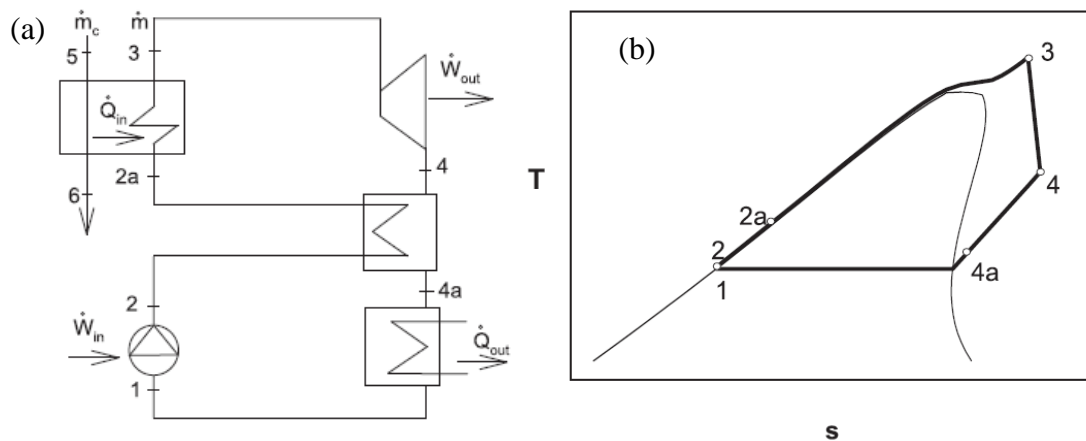
Figure 16: ORC with Recuperator (a) simplified schematic and (b) T-s Diagram, shown here as a supercritical cycle (Lai, Wendland, & Fischer, 2011).

The cycle fluid is pre-heated from 2 to 2a from the turbine exhaust via a recuperator, which reduces $\dot{Q}_{out}$ and also means the cycle mass flow rate can be increased from the basic binary mass flow rate due to the lower ΔT_{2a-3} for the same available $\dot{Q}_{in}$. This may, however, limit the brine outlet temperature from the heat exchanger because of the higher T_{2a}, this will depend on the cycle parameters.

Walraven, Laenen, and D'haeseleer (2014) showed that adding a recuperator to an ORC is only beneficial when the heat source outlet temperature is constrained to a temperature much higher than the condensing temperature. In the preliminary analysis the condensing temperature is 50 °C and the brine outlet temperature is 80 °C; this may or may not be high enough to draw benefit from a recuperator.

2.3.2 Dual Pressure ORC

The dual pressure cycle, shown in Figure 17, was developed to reduce thermodynamic losses in subcritical cycles by minimising irreversibilities in the heat exchangers caused by a large finite temperature difference (DiPippo, 2012).
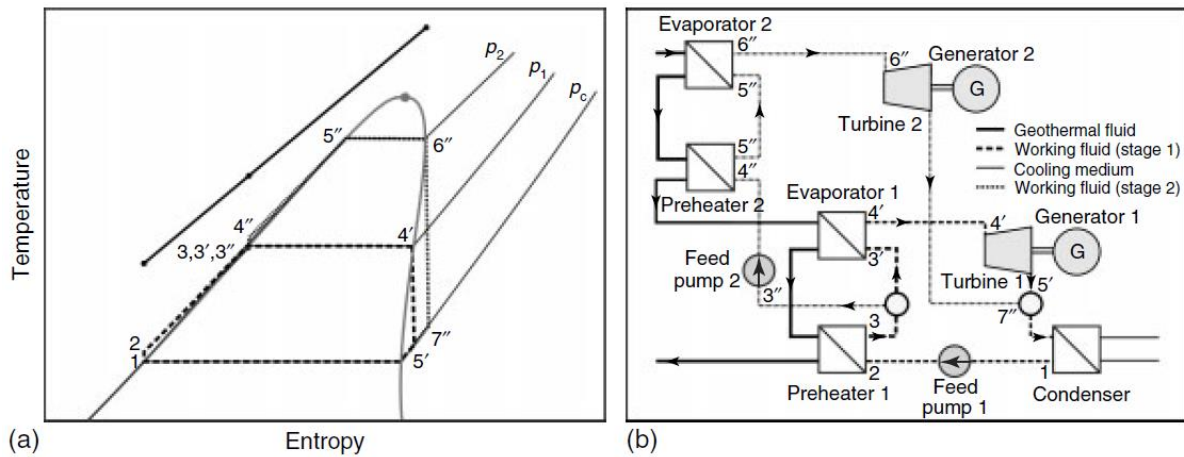
Figure 17: Dual pressure cycle (a) T-s diagram and (b) schematic configuration (Saadat et al., 2010).

A variation of the dual pressure cycle is the one used in the Stillwater binary geothermal power plant where there are two separate loops operating at different evaporator pressures with isopentane as the working fluid in both loops (Mehmet Kanoglu, 2002).

T. L. Li, Wang, Zhu, Hu, and Fu (2015) and Guzovic et al. (2014) found that the dual pressure ORC could increase the net power generation over the basic ORC for geothermal application with geothermal water inlet temperatures of 90-120 ºC and 175 ºC respectively. Only a single fluid at subcritical pressures was considered in each case. There was no comparison to supercritical cycles. Walraven et al. (2014) found that the net power generation of the basic ORC could be increased using dual pressure ORC but that this was the result of enablement of further reducing the brine outlet temperature and that the cycle efficiency remains about the same.

The dual pressure cycle aims to improve the heat source to cycle fluid heat transfer profile match as shown below in Figure 18. This is only relevant to subcritical cycles as supercritical cycles already have an improved match between the working fluid heating curve and the brine cooling curve. Therefore, the dual pressure cycle will likely only be beneficial for fluids with critical temperature near or above the brine inlet temperature that are used at subcritical evaporation pressure.

23
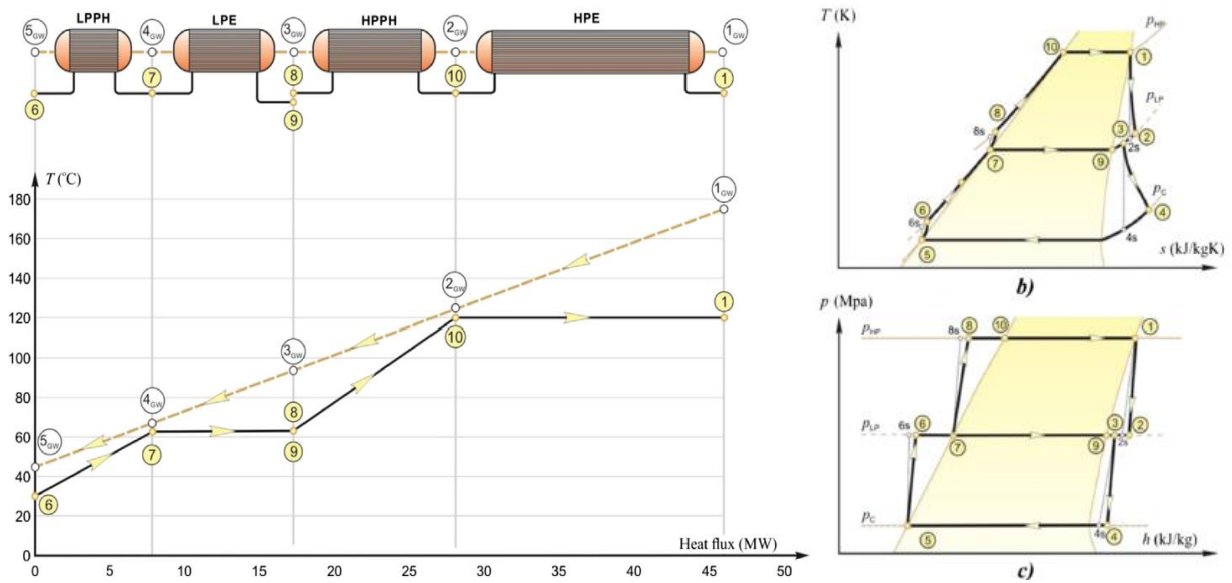
Figure 18: a) T-Q diagram for a dual pressure cycle illustrates how the temperature profiles can be better matched over a basic subcritical ORC, b) and c) T-s diagram and P-h diagram showing the process (Guzovic et al., 2014). LPPH: low pressure preheater; LPE: low pressure evaporator; HPPH: high pressure preheater; HPE: high pressure evaporator.

2.3.3 Reheat ORC

The reheat cycle was developed for wet fluids that would otherwise pass into the saturated mixture region during turbine expansion stage and is commonly used in steam power plants to extract more work from steam. In the reheat cycle, as shown below in Figure 19, the high pressure turbine exhaust fluid is reheated when it reaches the saturation envelope and is then further expanded through the low pressure turbine. The reheat cycle is shown below as a steam cycle with exhaust fluid from high pressure turbine being sent back to the same boiler as would be the case for coal power plants, but a binary geothermal plant would require a separate reheat heat exchanger.
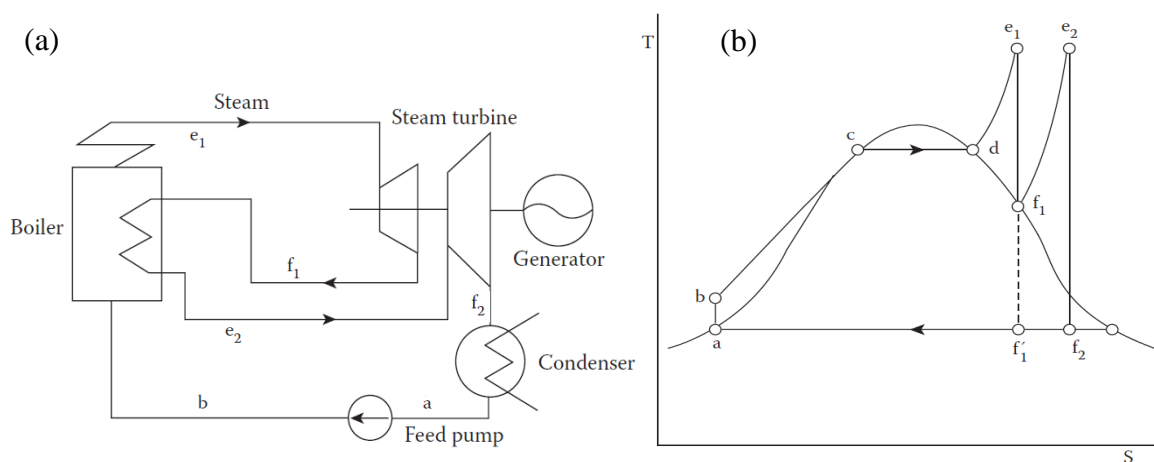
Figure 19: Reheat Rankine cycle (a) simplified schematic and (b) T-s diagram (Yasuo, 2009) (with state point notation added for consistency).

24

The reheat cycle is commonly used for steam cycles to make better use of the shape of the water T-s diagram. However, for ORC cycles, unlike steam cycles, where the cycle designer has a great deal of choice in the shape of the T-s diagram of the fluid selected the reheat cycle loses its attractiveness and benefit. Indeed, the reheat cycle is not generally mentioned in geothermal texts (DiPippo, 2012; Saadat et al., 2010; Watson, 2013) and it was found that the cycle efficiency was similar to the basic Rankine cycle (Mago et al., 2007).

The reheat cycle is effective for the steam cycle because with the cycle constrained to the heat source temperature the first stage of expansion will end up in the saturated mixture region by the end of expansion process, as shown in Figure 20. If, however, it is reheated the secondary expansion stage is pushed out to where the expansion process can remain in the dry vapour region for much longer. This illustrates the effectiveness and in some cases the necessity of the reheat cycle, but does not produce beneficial results for ORC because the flexibility in working fluid choice that ORC affords, renders the reheat cycle unnecessary for ORC.
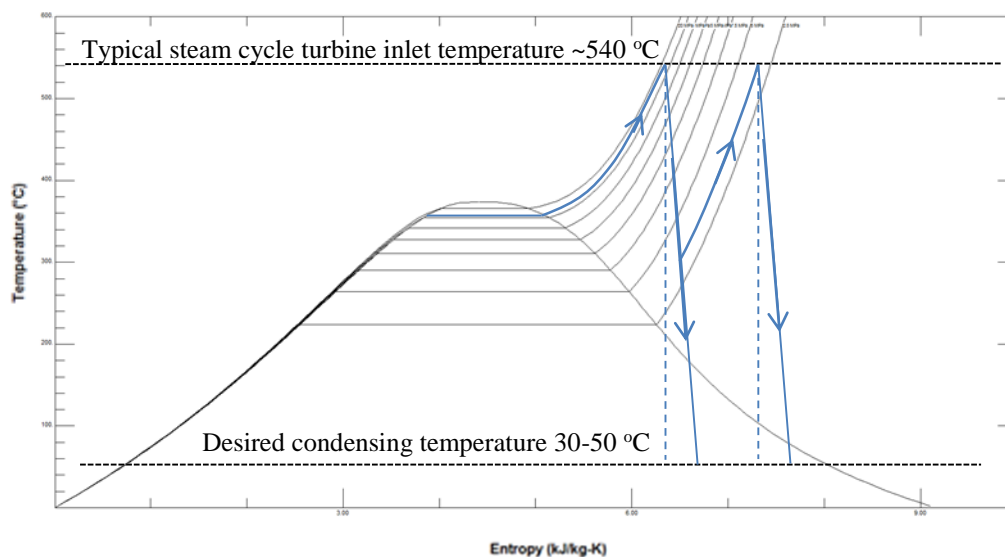
Figure 20: T-s diagram of the steam reheat cycle.

As can be seen from Figure 10 the majority of ORC fluids do not have the low negative gradient on the saturated vapour curve, which is the aspect of the water T-s diagram that motivates the use of the reheat cycle. Therefore the reheat cycle will not be analysed in this project.

2.3.4 Regenerative ORC

The purpose of the regenerative cycle is to decrease the energy rejected to the atmosphere in the condenser, $\dot{Q}_{out}$, while improving cycle efficiency (Yasuo, 2009) and similarly to the dual pressure cycle, to improve the temperature match in the heat exchanger. This is achieved by bleeding some of the cycle fluid after the high pressure turbine stage and using it to preheat the condensed fluid, by mixing it with the pump outlet stream in the open feed organic heater (OFOH), as shown below in Figure 21. This reduces the fluid mass flow rate through the condenser whilst improving cycle efficiency. The regenerative cycle is shown Figure 21 with a wet expansion turbine, with the cycle fluid expanding into the saturated mixture region. It is an objective to avoid this for the ORC design in this project.
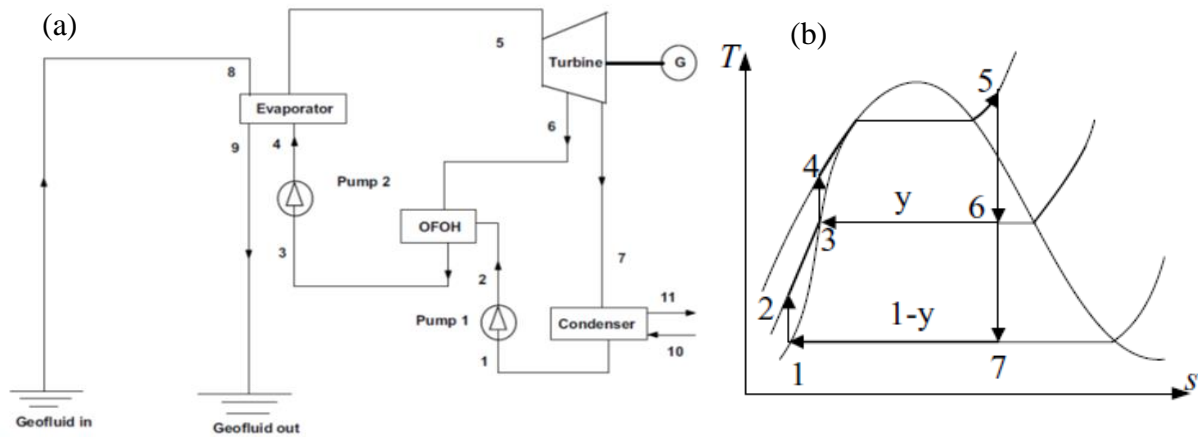
Figure 21: Regenerative ORC (a) simplified schematic (Yari, 2010) and (b) T-s Diagram (Massoud, 2005).

Mago et al. (2007), and R.-J. Xu and He (2011) found that the cycle thermal efficiency could be significantly improved for dry fluids using the regenerative cycle. It was also noted that use of the Regenerative ORC is not necessarily beneficial for all fluids in terms of thermal efficiency. As was discussed in Section 2.1, improving thermal efficiency does not necessarily meet the project objective of finding maximum net power generation; it is the utilisation efficiency that is more of interest then for assessing the regenerative cycle.

2.3.5 Dual Fluid ORC

The motivation for the dual fluid cycle is to create a better match between the brine and the cycle fluids in the heat exchangers (DiPippo, 2012) and to allow the heat exchange process to span a greater temperature range. This benefit may be offset by the irreversibilities of the additional heat transfer stages. The dual fluid cycle consists of two separate loops a high

temperature loop (HTL) and a low temperature loop (LTL), as shown below in Figure 22, where HTL and LTL are shown as fluid 1 and fluid 2 respectively.
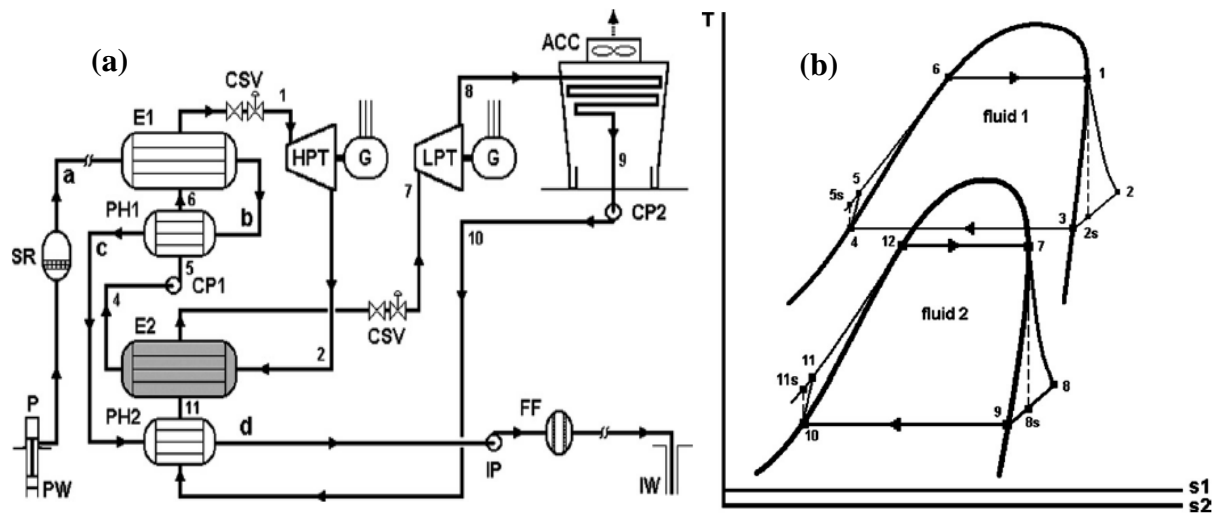
Figure 22: Dual fluid cascaded binary cycle (a) schematic configuration with heat exchanger E2 as the condenser for the HTL and the evaporator for the LTL and (b) T-s diagram (DiPippo, 2012). ACC: air-cooled condenser; CP: condensate pump; E: Evaporator; G: Generator; HPT: high pressure turbine; IP: injection pump; IW: injection well; LPT: low pressure turbine; P: Pump; PH: Preheater; PW: production well; SR: sand remover.

The fluids require careful selection such that they fit together to create synergy for the overall plant (DiPippo, 2012). Dual fluid cycles may also utilise a condenser for each cycle rather than using the condenser/evaporator E2, allowing the HTL condensing temperature to be lowered, increasing efficiency for the HTL.

2.3.6 Cycle-Fluid Type Compatibility Summary

The following table summarises which type of fluids are best suited to each cycle:

Table 3: Cycle-Fluid compatibility summary.

Cycle	Compatible Fluid Types
Basic ORC	All fluids – isentropic and dry are better.
Recuperated ORC	Any fluid that results in significant available heat for recuperation.
Dual Pressure ORC	Subcritical for any fluid type with critical temperature near or above the brine inlet temperature.
Reheat ORC	Wet fluids with low gradient on the saturated vapour curve – not applicable to ORC fluids.
Regenerative ORC	All fluids – dry and isentropic are better.
Dual Fluid ORC	Any two synergistic fluids, i.e., one high and one low critical temperature fluid.

Due to limited applicability of the dual pressure and reheat cycles, and since the regenerative provides similar benefits but is applicable to all fluid types, the dual pressure and reheat cycles will not be considered in the preliminary analysis. That leaves the following four cycle configurations to be considered in the preliminary analysis:

- Basic ORC,
- Recuperated ORC,
- Regenerative ORC, and
- Dual Fluid ORC.

2.4 Condensing System

Due to the relatively high proportion of heat rejection required for ORCs, the selection and design of the condensing system is of significant importance (Daniel Walraven, Ben Laenen, & William D'haeseleer, 2015). The condensing system parasitic power consumption can form a significant proportion of the system exergy loss. An appropriately selected and well-designed cooling system can also have a significant positive impact on plant profitability (Kröger, 2004). One of the key constraints for the condensing system in this project is the arid location, which means no cooling water is available and only dry cooling systems which reject heat to the atmosphere via air-cooled heat exchangers may be used.

The energy balance for the heat transfer from the condensing cycle fluid to the air, is given by

$$\dot{Q}_{cd} = \dot{m}_{cf}(h_{cf,i} - h_{cf,o}) = m_a c_{p,a}(h_{a,i} - h_{a,o})$$ **Equation 6**

The *UA* value is calculated via the log mean temperature difference (LMTD) method:

$$\dot{Q}_{in} = UAF_T \Delta T_{LM}$$ **Equation 7**

where U is the overall heat transfer coefficient, W/m^{2}K,

    A is the heat transfer surface area, m^2,

    F_T is the LMTD temperature correction factor to modify simple counterflow for various crossflow cases, and

    ΔT_{LM} is the log mean temperature difference (LMTD), ºC.

The LMTD may be approximated as:

$$\Delta T_{LM} = \frac{\Delta T_1 - \Delta T_2}{\ln(\Delta T_1/\Delta T_2)}$$ **Equation 8**

For counterflow $\Delta T_1 = T_{cf,o} - T_{a,i}$, and $\Delta T_2 = T_{cf,i} - T_{a,o}$.

There are two main types of air-cooled heat exchanger systems: MDACT and NDDCT.

General requirements of the condensing system are:

- Must be designed to operate across the range of possible ambient temperatures.
- The condensing system must ensure the working fluid at the outlet is subcooled liquid with a sufficient degree of subcooling to prevent cavitation in the pump. A minimum of 2 ℃ of subcooling is recommended by Greenhut et al. (2010).
- The heat transfer surface area required is inversely proportional to the desired temperature difference between the cooling fluid and the ambient air. Greenhut et al. (2010) recommend a minimum LMTD of 5 ℃ is used for preliminary calculations.

The VDI Heat Atlas (VDI, 2010) suggests that calculation of the overall heat transfer coefficient using average data is suitable for a preliminary estimate of the heat transfer area of a condenser. In the following sections the two types of condensing systems will be further investigated and compared.

2.4.1 NDDCT Overview

NDDCTs have been widely used in large commercial power plants, generally in the hundreds of megawatts scale. ORCs are generally applied in the kW to several MW scale such as in decentralised power generation applications and the use of NDDCTs on this scale is a relatively novel concept. Several studies have been performed considering smaller scale NDDCTs and have addressed some of the expected challenges associated with small scale NDDCTs, such as the susceptibility to performance degradation in cross-wind (Goodarzi, 2010; Y. Lu, Guan, Gurgenci, & Zou, 2013; Zhai & Fu, 2006).

NDDCTs generate the air flow through the heat exchangers via the effects of buoyancy of the air after heat transfer from the heat exchanger bundles. The transfer of heat to the surrounding air, increases the temperature and decreases the density. The air density inside the tower at the heat exchanger height is then lighter than the atmospheric air outside the tower at the same elevation. This generates a buoyancy force that causes the heated air to move up through the tower, drawing more air in through the bottom of the tower. The rate at which the air flows through the tower is dependent on the heat exchanger characteristics, the tower

geometry and the various flow resistances encountered (Kröger, 2004). An overview of a NDDCT is shown below in Figure 23.
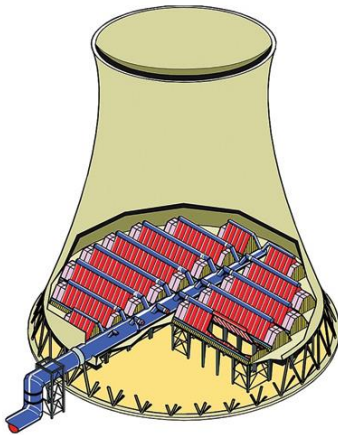
Figure 23: Overview of NDDCT shown here with A-frame heat exchangers (Wurtz & Peltier, 2008).

Analysis of NDDCT performance is through the use of the draft equation which equates this buoyancy force to the sum of the flow resistances through the tower to find the air flow rate. This is solved with an iterative procedure.

According to SPX Cooling Technologies (2014) concrete is used for the tower structure of large natural draft cooling towers for the following reasons; it is:

- Structurally stable,
- Durable,
- Fire resistant,
- Environmentally stable, and
- Readily available.

It is not uncommon for steel to be used for the tower shell material in locations of regular seismic activity. Steel is able to meet all of the above objectives, furthermore in this project only dry cooling systems are considered, steel becomes an even more attractive option as corrosion is not a major concern.

The NDDCT size being considered for this project is much smaller than is conventional for NDDCT, which is usually over 100m in height. Whereas the NDDCT required for the ~2.5 MWe scale geothermal plant considered in this project would be of the order of 30 to 50 m in height. Small NDDCTs have not yet gained widespread use largely due to concerns that negative cross-wind effects would be detrimental to performance at this small scale. However

there have been a number of numerical and experimental studies showing methods to minimise and even reverse this problem (Goodarzi, 2010; Goodarzi & Keimanesh, 2013; Y. Lu et al., 2013; Y. S. Lu et al., 2015; Y. S. Lu, Gurgenci, Guan, & He, 2014; Zhai & Fu, 2006). The Queensland Geothermal Energy Centre of Excellence (QGECE) has built an operational small NDDCT of about 20m height using this research.

One of the main reasons for the conventional hyperbolic shape of NDDCTs is for structural efficiency when building large towers with concrete. However, for smaller towers with the tower shell constructed of steel there is more flexibility in the design of the tower; thus tower design can be optimised for economic performance. An example of a small NDDCT constructed of steel, which is not of hyperbolic shape, is shown below in Figure 24.

Figure 24: Steel NDDCTs are not constrained to the conventional hyperbolic shape, the towers shown are at the Celsa Ostroweic Steelworks ("Cooling Towers: Overhaul of two natural draft cooling towers in celsa ostrowiec steelworks ", 2007) in Poland.

Another important consideration is the configuration of the heat exchangers. The main options are vertical circumferential, horizontal and A-frame heat exchanger bundle arrangements. In the vertical circumferential heat exchanger option the heat exchanger bundles are arranged vertically around the outside of tower base, whereas for horizontal and A-frame heat exchanger arrangements the heat exchanger bundles are within the tower inlet area as is shown above in Figure 23. According to Kroger (2004) the vertical circumferential arrangement is more sensitive to winds and results in reduced cooling capacity. Horizontal heat exchangers result in a lower pressure drop across the heat exchangers than A-frame, but require a larger tower inlet diameter for the same number of heat exchanger bundles. Y. Lu et al. (2013) use a horizontal heat exchanger arrangement in their analysis of small NDDCTs, as

small as 15 m in height. The horizontal heat exchanger arrangement will be used in this project.

Kröger (2004) states that technically and economically direct, natural-draft air-cooled condensers may offer an alternative option for large plants, but it seems implied that it is not something that is conventionally done. In this case the lower heat transfer coefficient for heat transfer from vapour would necessitate the use of more heat transfer surface area and therefore more bundles and a larger and therefore more expensive tower. Whether or not the capital costs saved from the eliminated components from utilising a direct condensing NDDCT system may be offset by the larger tower required. For this project only indirect NDDCT condensing systems will be considered.

2.4.2 MDACT Overview

Mechanical draft air-cooled towers utilise fans to provide the air-flow through the heat exchangers. There are a variety of potential configurations of MDACTs, they are generally categorised as one of the following two main options: forced-draft or induced-draft MDACTs. Referring to whether the fan is before or after the heat exchangers as shown in the figure below.
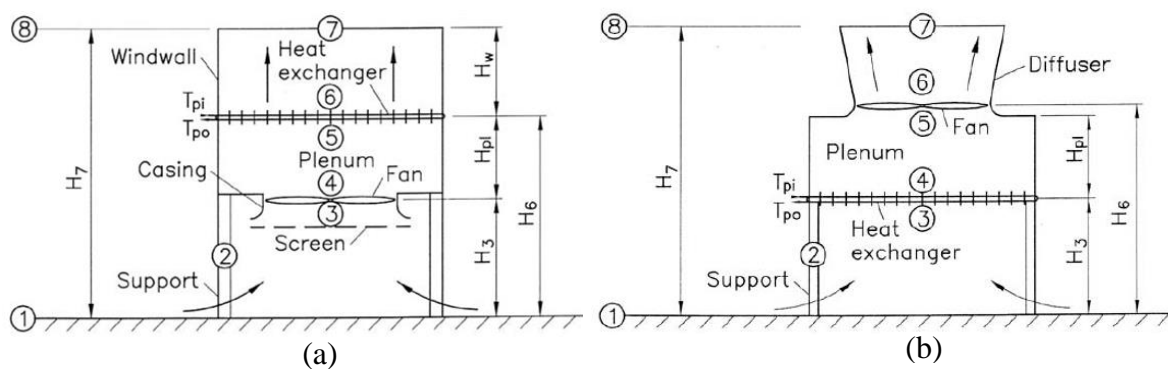
Figure 25: MDACT schematics, (a) forced-draft air-cooled heat exchanger, and (b) Induced-daft air-cooled heat exchanger (Kröger, 2004).

These particular configurations, with horizontal heat exchangers are generally used for liquid cooling applications; the typical configuration used for direct condensing is shown below in Figure 26. It employs an A-frame heat exchanger, to assist with condensate drainage, and reduce the required lengths of large bore vapour distribution ducts. However this comes at the expense of higher air-side pressure loss and therefore higher fan power consumption (Kröger, 2004).
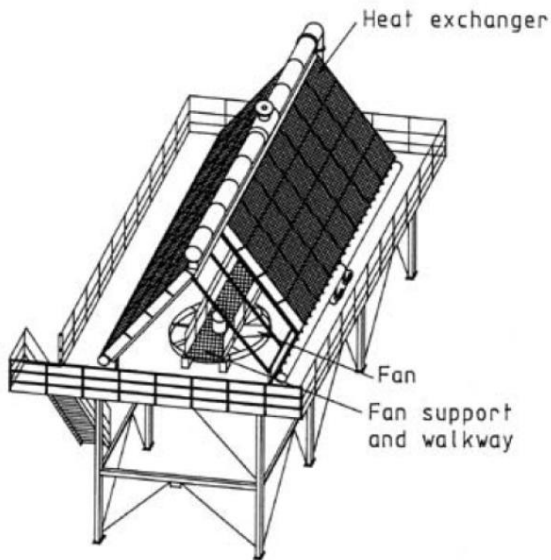
Figure 26: MDACT as a direct condenser usually employed in the A-frame forced-draft configuration (Kröger, 2004).

Conventional condensing system design methodology points towards the use of MDACT for small power generation capacities, however small NDDCTs provide an appealing alternative due to the elimination of the parasitic power consumption in the fans.

2.4.3 NDDCT vs. MDACT

In comparing NDDCT and MDACT for this project there are a number of pertinent considerations:

- Condensing system power consumption,
- Capital costs,
- Level of maintenance required,
- System performance in the range of ambient conditions at the site, and
- System controllability in the case of changing ambient conditions.

It is one of the aims of this project to develop quantitative comparison of these two systems for Australian EGS power generation.

2.5 Expanders

The performance of the ORC strongly depends on that of the turbine (Quoilin et al., 2013). There are a variety of different expander designs which can be separated into two main types: positive displacement and turbine, the choice of which depends on the application and scale. Positive displacement expanders are generally used for the kW scale applications. They are characterised by lower flow rates and higher pressure ratios, whereas turbines are typically

used for larger scale applications (Quoilin et al., 2013). The expander type selection will be discussed further below.

The turbine output shaft power is given by:

$$\dot{W}_t = \dot{m}_{cf}(h_i - h_o) = \dot{m}_{cf}\eta_t(h_i - h_{o,s})$$

<div align="right">Equation 9</div>

Where η_t = turbine isentropic efficiency

The electrical power output depends on the generator efficiency:

$$\dot{W}_{gen} = \eta_{gen}\dot{W}_t$$

<div align="right">Equation 10</div>

One of the main benefits of ORC is that it allows the use of dry and isentropic fluids that require minimal superheating to ensure a dry expansion process. However, there are some promising wet ORC fluids that are considered in this project. The method used to predict the performance in the case of moisture formation in the turbine is the Baumann rule, which penalises the turbine efficiency approximately 1% for each 1% of average moisture during the expansion (Augustine et al., 2009). The Baumann rule is given by (Petr & Kolovratnik, 2013):

$$\eta_t = \eta_{t,dry}\left(a_B\ \frac{x_i + x_o}{2}\right)$$

<div align="right">Equation 11</div>

Where $\eta_{t,dry}$ is the turbine isentropic efficiency for dry vapour expansion,

a_B is the Baumann factor, determined experimentally for each application; can vary from 0.4 to 2.5 but is generally assumed to be 1, and

x_i & x_o are the vapour quality at the inlet and outlet respectively.

Some manufacturers claim that the Bauman rule does not apply to radial turbines and the radial turbine isentropic efficiency stays constant until the vapour mass fraction drops below 80%. However, this is anecdotal information and no published data exist. Therefore the Baumann rule will be used, as this is the more conservative approach to take.

J. Xu and Liu (2013) use an upper limit of 10 MPa for the turbine inlet pressure due to the difficulties of manufacturing turbines for higher pressures. This limit will be adopted for this project. In the following sections the selection of expander type, efficiency and modelling will be discussed.

2.5.1 Expander Type Selection

Quoilin et al. (2013) presented the following plot illustrating the optimum operating range of expanders.
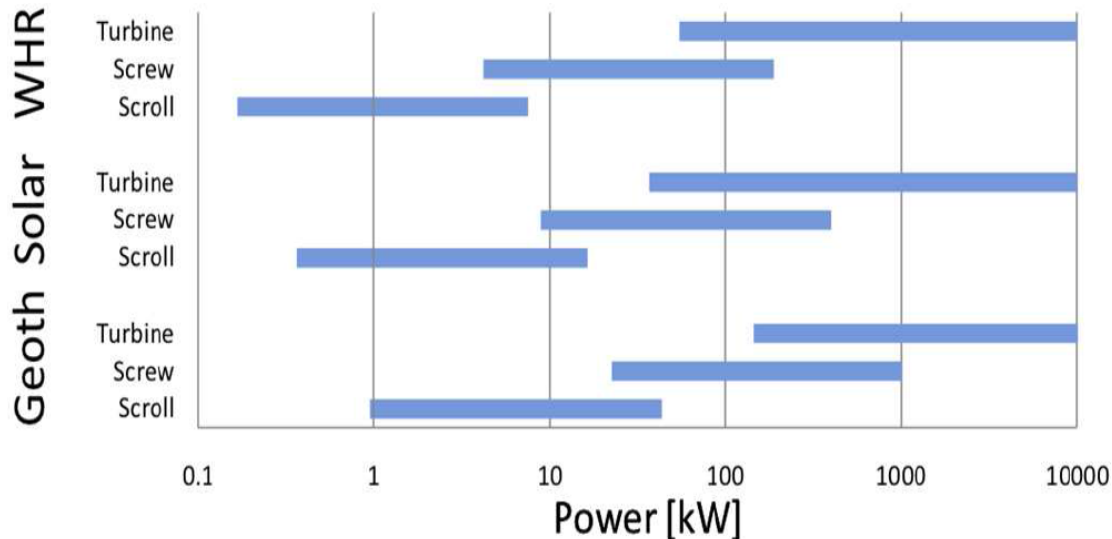
The turbine shaft power range for this project is approximately 3.5 MW to 4.5 MW, for this power range turbines are the best option according to Figure 27.

Bao and Zhao (2013) state that axial turbines are commonly used for high flow rates and low pressure ratios, whereas radial turbines are suitable for use with lower flow rates and higher pressure ratios, and that this makes them an attractive option for use with ORC systems. Bao and Zhao (2013) give the following as special characteristics of ORC turbines:

1) Typically have higher pressure ratio and smaller enthalpy drop than steam turbines. Especially for low grade heat sources.

2) Organic fluids have higher density than water so an equivalent power rating ORC turbine would have smaller overall dimensions than a steam turbine.

3) Availability of dry and isentropic organic fluids means that turbine exhaust vapour is generally still superheated, so there is no reduction in turbine efficiency due to moisture formation, and this may also extend the life of ORC turbines.

4) Some organic fluids are flammable, toxic or hazardous to the environment, so preventing fluid leakage is of critical importance. Hence, the sealing medium is typically gas and a double-faced seal is desired.

In summary radial inflow turbine is selected for this project.

2.5.1 Turbine Efficiency

The turbine efficiency greatly affects the cycle performance. There is a significant variation in radial turbine efficiencies used in published studies. The following table summarises the values used in a number of studies.

Table 4: Review of radial turbine and generator efficiencies stated in the literature.

Reference	ORC Turbine Isentropic Efficiency (%)	Source for Turbine Efficiency	Generator Efficiency (%)
Astolfi, Xodo, Romano, and Macchi (2011)	85% (ORC pump) 75% (brine injection pump)	Assumption	97.5
Augustine et al. (2009)	85 % (uses Baumann rule if liquid present)	Assumed	98
Erbas and Biyikoglu (2013)	79	Design for R134a by velocity triangle and loss calculator	-
Calise, Capuozzo, and Vanoli (2013)	80	Assumed	-
Campos Rodríguez et al. (2013)	85	Assumed	95
Gabbrielli (2012)	85	(Astolfi et al., 2011; Augustine et al., 2009; Greenhut et al., 2010)	98
Guzovic et al. (2014)	85	Assumed	-
Kang (2012)	Average: 78.7% Range: ~65% to ~90%	Experimental measurement of radial turbine with R245fa	-
Liu, Duan, and Yang (2013)	85% (isentropic) 98% (mechanical)	Assumed	97
(Madhawa Hettiarachchi, Golubovic, Worek, & Ikegami, 2007)	85	Assumed	96
Mago et al. (2007)	80	Assumed	-
Meinel, Wieland, and Spliethoff (2014)	80	Assumed	-
Muñoz de Escalona, Sánchez, Chacartegui, and Sánchez (2012)	87	Assumed	98
Sauret and Rowlands (2011)	85	Assumed for preliminary cycle analysis	-

Schuster, Karellas, and Aumann (2010)	80	Assumed	-
Tempesti and Fiaschi (2013)	80	-	-
J. Xu and Liu (2013)	85	(Franco & Villani, 2009; Zhang & Jiang, 2012)	-
Zarrouk and Moon (2014)	85	Typical for steam turbines in geothermal applications	95.7 to 99% from manufacturer data, depending on capacity
(Zhang & Jiang, 2012)	85	Assumed	-

The turbine efficiencies used in the studies considered above vary from 75 to 90%. The most commonly used efficiency value is 85% and the numerical average value presented above is 83%. So it is assumed for this project that at design point the turbine will achieve 85% efficiency.

The generator efficiencies used in the studies considered above vary from 95 to 98% with many cases neglecting generator efficiency, or assuming generator efficiency is incorporated in the turbine efficiency used. Zarrouk and Moon (2014) stated generator efficiency increases with size of the generator from 95.7 for small generators up to 99% for large generators. Since the scale of the generator required for this project is moderate, 97% will be used in this work.

Based on the above, 85% turbine isentropic efficiency and 97% generator efficiency are used, with a 10 MPa upper limit on turbine inlet pressure.

2.5.2 Off-Design Modelling

Most studies that consider ORC off-design performance assume that radial inflow turbines have minimal performance deterioration for a relatively wide range of off-design conditions. Sauret and Rowlands (2011) argue that radial turbines are able to maintain high efficiency at off-design conditions through the use of variable inlet guide vanes. Erbas and Biyikoglu (2013) conducted a numerical analysis of a radial turbine for R134a and found that the designed turbine maintains efficiency within 1% of peak efficiency from approximately 0.8 to 1.5 times design load, as shown in Figure 28, where turbine load is defined as the ratio of the power generated to the design power of the turbine.
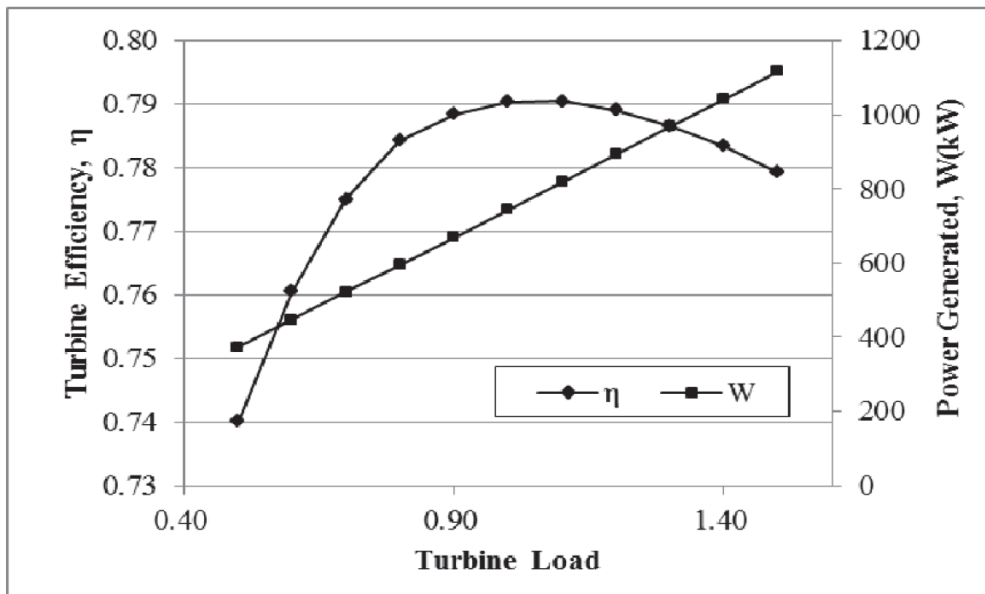
Figure 28: Turbine efficiency versus turbine load (Erbas & Biyikoglu, 2013).

Quoilin et al. (2012) presented the plot shown in Figure 29 of turbine efficiency against turbine specific speed. According to this plot a wide range of specific turbine speeds give a relatively small deviation in turbine efficiency.
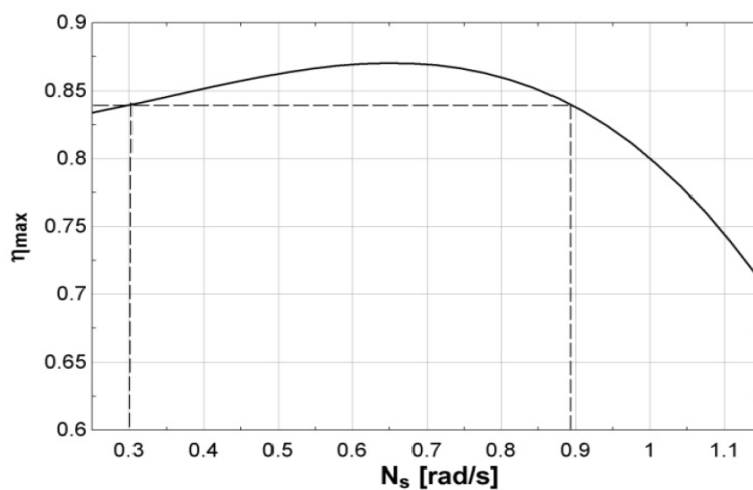
Figure 29: Maximum radial turbine efficiency as a function of the specific speed (Quoilin et al., 2012).

A review of previous literature finds little experimental data on ORC radial turbine off-design performance. As is illustrated in Figure 27 the lab scale is better serviced by positive displacement expanders and as such the few experimental studies use positive displacement expanders.

The experimental studies that are available show no useful correlation that could be used to predict turbine off-design performance. The experimental study by Kang (2012) of a radial

turbine in an ORC using R245fa shows no discernible trend in turbine performance, but does show a significant variation of values for varying turbine inlet conditions. M. Li, Wang, Hea, et al. (2013) studied the time dependence from start-up of an ORC and the performance variation of the turbine was associated with the gradual heating up of the heat exchangers and therefore the changing turbine inlet conditions.

So if the control strategy is used that the plant maintains turbine inlet temperature and pressure, varying only mass flow rate then according to Figure 28 and Figure 29 turbine efficiency should, to reasonable approximation, remain constant.

Therefore the planned control method for the plant is to, wherever possible, vary the mass flow rate of the cycle to control the turbine inlet temperature and pressure so that they can be maintained at the design point. In doing so turbine isentropic efficiency is assumed to be constant at off-design conditions.

2.6 Heat Exchangers

In binary geothermal power plants the heat exchangers (HE) are a significant source of exergy destruction and their performance considerably affects the overall plant efficiency (DiPippo, 2004; M. Kanoglu & Bolatturk, 2008). Heat exchangers can also form a significant portion of total plant cost; this is especially relevant for EGS with the high pressure geothermal fluid requiring high strength heat exchanger components.

The design of heat exchangers is well documented (Annaratone, 2010; Branan, 2005; Naterer, 2003; Shah & Sekulic, 2003; Thulukkanam, 2013; VDI, 2010). Additionally, most chemical engineering text books reserve at least a chapter for the design of heat exchangers. A common objective of industrial heat exchangers is to maximise heat transfer rate and minimise the heat transfer surface area, thereby minimising capital cost. However this comes at the expense of increased exergy destruction through the heat transfer process and therefore lower power generation capability. Hence this process needs to be incorporated into the system design process, to better account for the trade-off between heat exchanger capital cost and increased power generation due to improved heat transfer.

The energy balance across heat exchangers is given by:

$$\dot{Q}_{in} = \dot{m}_b\left(h_{b,i} - h_{b,o}\right) = \dot{m}_{cf}\left(h_{cf,i} - h_{cf,o}\right)$$

<div align="right">Equation 12</div>

The LMTD method is used for calculating the heat transfer surface area required for the heat transfer process, as described for the condensing system in Section 2.4.
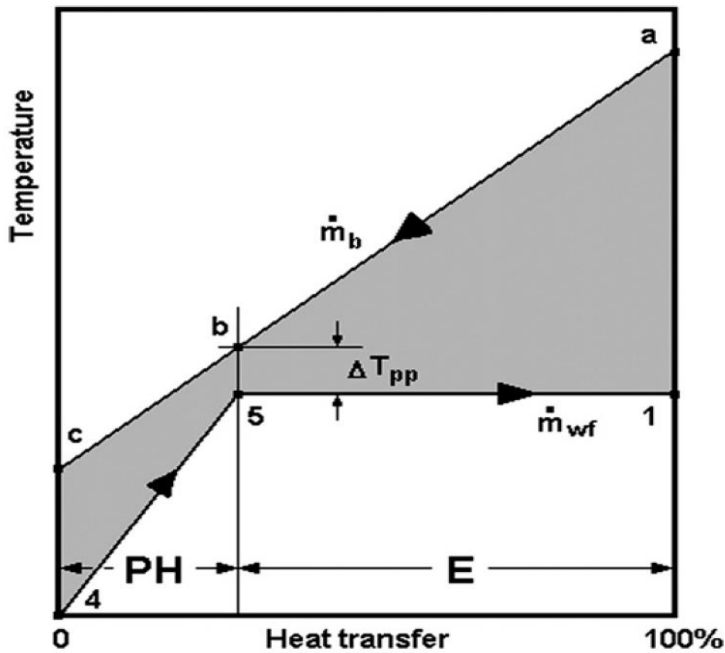
Figure 30: Temperature-Heat transfer diagram for the preheater and evaporator of a subcritical cycle, here the subscript wf refers to the working fluid, the subscript cf is used elsewhere in this work (DiPippo, 2012).

The two heat exchangers may be analysed separately, using the notation from Figure 30, as follows:

Preheater: $\dot{Q}_{in} = \dot{m}_b(h_b - h_c) = \dot{m}_{cf}(h_5 - h_4)$ Equation 13

Evaporator: $\dot{Q}_{in} = \dot{m}_b(h_a - h_b) = \dot{m}_{cf}(h_1 - h_5)$ Equation 14

The temperature difference at the evaporator inlet is known as the pinch point temperature difference, (ΔT_{pp}), and is a significant consideration in heat exchanger design.

2.6.1 Heat Exchanger Selection

In order to select the most suitable heat exchanger (HE) option, the basic design requirements for the HEs should be considered, these are presented below in Table 5.

	Preheater	Evaporator / Supercritical HE	Recuperator	Condenser (for indirect NDDCT cycle)
ΔP at cycle design point - between hot and cold side	~25 to 34 MPa	~25 to 30 MPa	1-10 MPa*	Up to ~1 MPa
ΔP_{max} at start-up/shut-down – between hot & cold side	35 MPa^	35 MPa^	Up to 10 MPa*	
Heat transfer from - to	Liquid – liquid	Liquid – two phase / supercritical fluid	Vapour – Liquid	2 phase – liquid
Fluids	Geothermal brine – cycle fluid	Geothermal brine – cycle fluid	Cycle fluid – cycle fluid	Cycle fluid – water
Flow direction	Counterflow preferred	Counterflow preferred	Counterflow preferred	Counterflow preferred
Cleaning requirement	Regular cleaning required on brine side	Regular cleaning required on brine side	Minimal fouling expected	Minimal fouling expected

^The high pressure rating in the preheater and evaporator /supercritical heat exchangers is due to the high geopressure in the brine side, as explained Section 1.3.

*The recuperator pressure depends on the cycle fluid and the turbine inlet pressure selected for the cycle, 10 MPa is the upper limit used for this project.

The two main options for HE selection for the brine HE are shell and tube heat exchangers (STHE) and plate heat exchangers (PHE). Each has their own advantages and disadvantages. Table 6 gives a comparison of each type of HE.

Table 6: Comparison between STHE, and PHE compiled from Thulukkanam (2013) unless otherwise noted.

	STHE	PHE	
		Gasketed PHE	Welded PHE*
Advantages	Flexible and robust design. Wide variety of design configurations possible Can handle aggressive media.	True counterflow, high turbulence, high heat transfer performance and close approach temperature. Low liquid volume and quick process control. Low cost.	Can handle aggressive media. True counterflow, high turbulence, high heat transfer performance and close approach temperature. Low liquid volume and quick process control. Low cost.
Disadvantages	Requires large footprint for	Maximum pressure and	High pressure loss.

	STHE	PHE	
		Gasketed PHE	**Welded PHE***
	installation. Construction is heavy. PHE may be cheaper for low pressure (< 1.6 MPa) and temperature (below 200 ºC).	temperature are limited by gasket material. Gaskets always increase the leakage risk. High pressure loss.	Difficult to clean - need to avoid fouling fluids.
Counter flow	Generally more cross-flow, with special design configurations may approach counterflow.	True counterflow can be achieved.	True counterflow can be achieved.
Maintenance	Mechanical cleaning possible tube side, but problematic for shell side, chemical cleaning is simple.	Simple and easy inspection and maintenance.	Chemical cleaning only as plates are welded together.
Maximum operating pressure	Up to 60 MPa	Standard design: 2.5 MPa with special design: 3 MPa	4.2 MPa
Maximum temperature	^ +600 ºC	Max temp: 160 ºC With special gaskets: 200 ºC	+400 ºC
Temperature approach	Varies greatly with configuration.	As close as 1 ºC	As close as 3 ºC
Heat Transfer Area Range	^3-1000 m^2	^ 1-2500 m^2	^ 1-2500 m^2

* AlfaLaval (n.d.) – laser welded plate heat exchanger

^ Peters, Timmerhaus, and West (2003)

The main issue with PHEs is the maximum operating pressure; the brine side is 35 MPa and the cycle fluid side will likely be of the order up to 10 MPa, which results in a large pressure difference. Therefore PHEs will not suffice for the brine heat exchanger. So STHEs will be used for the brine heat exchangers in a configuration that best approached counterflow. One STHE configuration that approaches counterflow is the STHE in E configuration (Shah & Sekulic, 2003) with single shell and double tube pass. This configuration is used in a number of ORC studies which utilise geometric models of heat exchangers for a more detailed analysis (Calise, Capuozzo, Carotenuto, & Vanoli, 2014; Calise et al., 2013; Walraven et al., 2014).

Schröder, Neumaier, Nagel, and Vetter (2014) conducted a detailed analysis of several heat exchanger configurations for use in a supercritical ORC for geothermal power generation. This study found the U-tube STHE type with two shell passes to be the preferred type for energy efficiency, cleaning purposes and investment costs. This configuration will be used in this project.

2.6.2 Heat Transfer Process Constraints for Preliminary Analysis

Heat exchangers can theoretically achieve 100% heat transfer with an infinitesimal temperature difference. However, the heat transfer surface area required to achieve this would be prohibitively expensive. So to make a realistic prediction of heat transfer performance in heat exchangers, realistic constraints are required. The following table summarises the constraints used in a number of ORC process studies.

Table 7: Review of heat exchanger parameters used in the literature.

Reference	ΔT_{pp} (ºC)	Heat loss	Pressure loss	Other
Astolfi et al. (2011)	3	3%	1-3% for various HEs	Effectiveness 0.9
Augustine et al. (2009)	5 ºC for evaporator ≥ 5 ºC for recuperator ≥ 10 ºC for condenser	-	-	LMTD ≥ 5 ºC for preheater LMTD = 10 ºC for supercritical HE
Calise et al. (2013)	Calculated heat transfer coefficient from geometric HE definition			
Campos Rodríguez et al. (2013)	3	-	-	-
Fernández, Prieto, and Suárez (2011)	≥ 15	-	-	-
Guzovic et al. (2014)	≥ 5	-	-	-
Gabbrielli (2012)	10	-	-	-
Le, Feidt, Kheiri, and Pelloux-Prayer (2014)	10 ºC for heat source HE 3 ºC for condenser	-	-	-
Liu et al. (2013)	5 ºC for recuperator & condenser 10 ºC for evaporator	-	-	-
Mago et al. (2007)	15	-	-	-
Meinel et al. (2014)	10	-	-	-
Muñoz de Escalona et al. (2012)	≥ 10 ºC for WHR HE ≥ 5 ºC for recuperator	5%	2%	-

Reference	ΔT_{pp} (ºC)	Heat loss	Pressure loss	Other
Schuster et al. (2010)	10	-	-	-
Sauret and Rowlands (2011)	10	-	-	-
Tempesti and Fiaschi (2013)	5	-	-	U and A specified for each heat exchanger
Vetter et al. (2013)	20	-	0.02 MPa	-
Wang, Yan, Zhao, and Dai (2014)	5	-	-	-
J. Xu and Liu (2013)	10	-	Assumes negligible ΔP	-
Zhang and Jiang (2012)	≥ 3	-	Assumes negligible ΔP	100% effectiveness, assumes perfect insulation

As can be seen from Table 7 there is a wide range of constraints that have been assumed in the literature. It is the aim of this section to select mean values for the key constraints. The following values will be used in analysing the heat exchangers in the preliminary cycle analysis.

Table 8: Heat Exchanger - parameters fixed for preliminary analysis.

Variable	Value	Unit
Pinch point temperature difference (ΔT_{pp})	≥ 5	ºC
ΔT_{LM} for supercritical heat exchangers (instead of ΔT_{pp} constraint)	≥ 10	ºC
Pressure Loss	0.02	MPa

Plate heat exchangers are very efficient, compact, and relatively cheap heat exchangers. For the same heat transfer surface area PHEs are significantly cheaper than STHEs, as shown below in Figure 31.
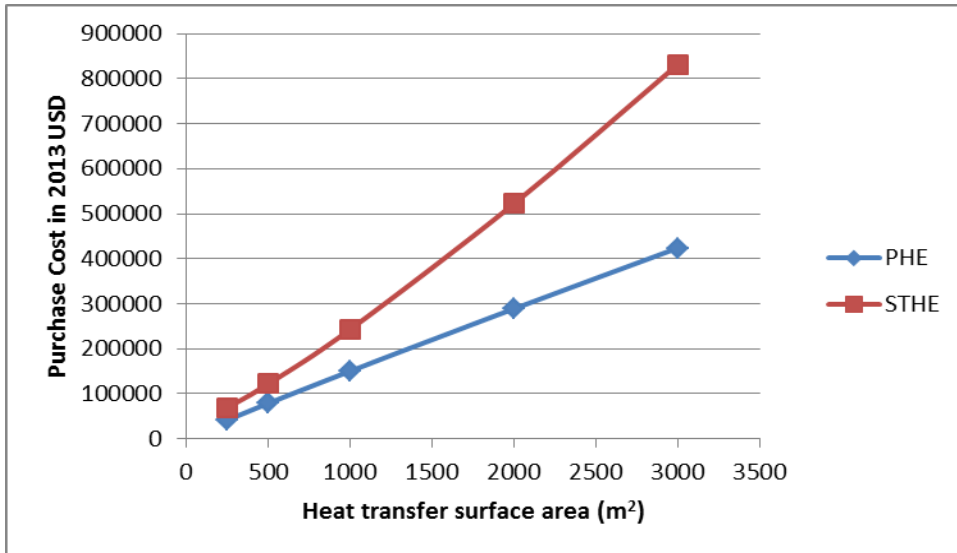
Figure 31: Comparison of purchase cost of PHEs and STHEs, based on purchase cost correlations presented in Towler and Sinnott (2013). This is for standard materials and standard operating pressures.

This motivates the use of PHEs wherever possible, the main restriction on the use of PHEs in this application is the pressure limitation of about 3 MPa. For this work PHEs could be used as the condenser in indirect cooling cycles.

2.6.3 Supercritical Heat Transfer

The thermodynamic properties of fluids near the critical point can vary significantly for small changes in temperature (Schröder et al., 2014), as shown below in Figure 32. This affects the heat transfer performance in heat exchangers, which becomes an issue for the detailed cycle analysis stage where this is calculated to determine the required heat transfer surface area, from which the cost of the heat exchanger is calculated.
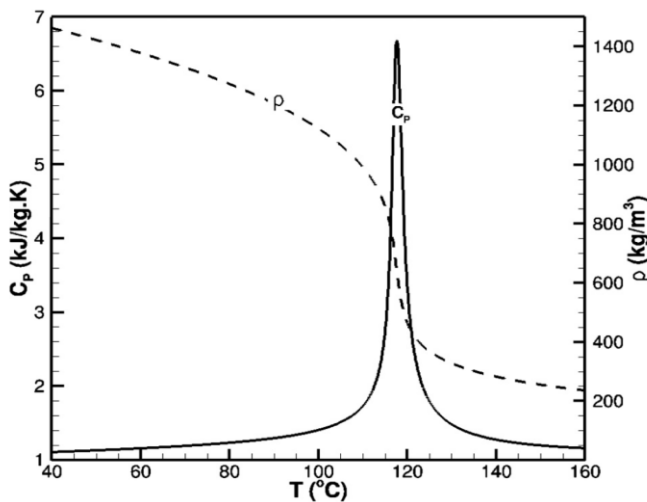
Figure 32: Variability of specific heat capacity and density vs. temperature near critical pressure, shows large changes in properties for small changes in temperature, for Perfluoro-butane (Molecular formula:C_4F_{10}) (Forooghi & Hooman, 2014).

45

Schröder et al. (2014) generated a similar plot, shown in Figure 33, of c_p vs. T at three pressures higher than the critical pressure. The fluid used was propane, with a critical temperature of 4.251 MPa, this shows the effect is still quite pronounced at almost 2 MPa above the critical pressure.
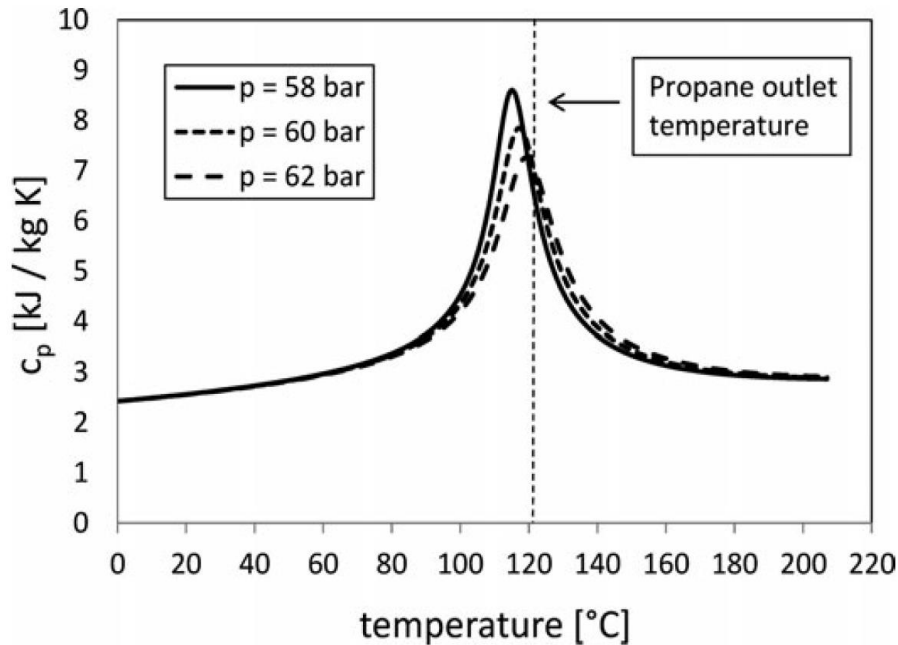
Figure 33: c_p-T plot showing the variability of c_p occurs even at ~2 MPa above the critical pressure (Schröder et al., 2014).

Schröder et al. (2014) performed a numerical study on supercritical heat exchangers with the purpose of improving the efficiency of geothermal power generation through the use of more efficient heat exchangers. Their approach consisted of accounting for the variations of fluid properties by applying a stepwise calculation of heat transfer coefficient using commonly used Nusselt number correlations.

The heat transfer coefficient is dependent on the Prandtl number, which is given by:

$$Pr = \frac{\mu \, c_p}{k}$$

<div align="right">**Equation 15**</div>

Schröder et al. (2014) plotted Prandtl number against temperature for propane for the same three pressures as above, this is presented below.
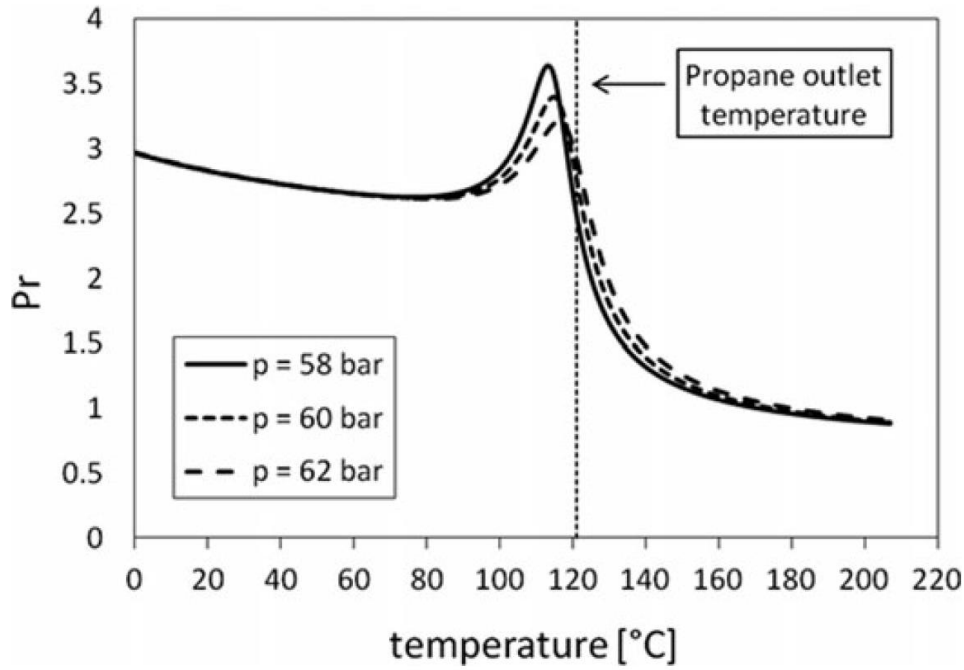
Figure 34: Prandtl number for propane plotted against temperature for three pressures near the critical pressure (Schröder et al., 2014).

As shown in Figure 34, the Prandtl number increases significantly as the temperature approaches the critical point and drops off sharply at temperatures above the critical temperature. The general approach for preliminary heat transfer coefficient calculation uses fluid properties at mean temperature through the heat exchanger. This approach for supercritical heat transfer may result in overestimation of the heat transfer coefficient. The method used to work around this issue, is to use the average of inlet and outlet properties, which should result in a more representative but conservative heat transfer coefficient. At the very least this method will not be skewed by abnormally high Prandtl numbers.

2.7 Pumps

The pump work input is described by the following:

$$\dot{W}_{cp} = \dot{m}(h_o - h_i)$$

<div align="right">**Equation 16**</div>

where the outlet enthalpy is calculated using the pump efficiency:

$$\eta_{cp} = \frac{h_{o,s} - h_i}{h_o - h_i}$$

<div align="right">**Equation 17**</div>

Finally the electrical power required by the pump motor is given by:

$$\dot{W}_{cpm} = \frac{\dot{W}_{cp}}{\eta_{cpm}}$$

<div align="right">**Equation 18**</div>

47

2.7.1 Efficiency

Steam Rankine cycles conventionally have very low pump power consumptions relative to the gross power generation. For ORC however, this relative pump power consumption is generally a more significant portion of the gross power generated. Quoilin et al. (2013) define the ratio of the pump power consumption to the turbine output as the back work ratio (BWR):

$$BWR = \frac{\dot{W}_p}{\dot{W}_t}$$

<div align="right">Equation 19</div>

Figure 35 shows the BWR for some fluids with a range of critical temperatures. Two conclusions Quoilin et al. (2013) drew from this figure are:

1) Higher critical temperature fluids tend to have a lower BWR. This elucidates the statement that steam Rankine cycles have a lower BWR than ORC.

2) BWR increases with T_{ev}, for each fluid and gets significantly high when operating near the critical point.
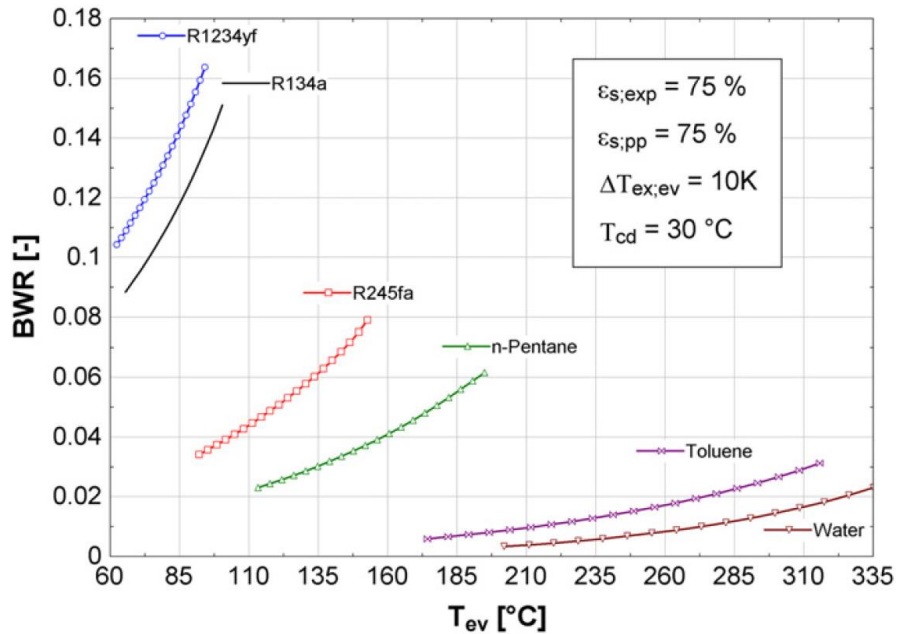
Figure 35: BWR as a function of evaporating temperature for various fluids (Quoilin et al., 2013).

Since the pump work is deducted from the turbine work to give the net work output for the cycle, it is important to have an accurate prediction of pump efficiency as this can have a significant impact on plant performance (DiPippo, 2012). A review of pump efficiencies used in the literature is summarised in Table 9.

Table 9: Review of pump and motor efficiencies stated in the literature.

Reference	Pump* Efficiency (%)	Source for pump efficiency	Motor Efficiency (%)
Astolfi et al. (2011)	80	Assumed	92.5 (electro-mechanical efficiency)
Augustine et al. (2009)	80	Assumed	-
Calise et al. (2014)	85% for ORC pump 80% for condenser feedwater pump	Assumed	-
Campos Rodríguez et al. (2013)	80	Assumed	-
Gabbrielli (2012)	80	Assumed	-
Guzovic, Raskovic, & Blatari, 2014)	75	Assumed	-
Le, Feidt, et al. (2014)	80	Assumed	90
Liu et al. (2013)	65	-	-
Madhawa Hettiarachchi et al. (2007)	75% for ORC pump 80% for brine pump	Assumed	-
Mago et al. (2007)	85	Assumed	-
(Meinel et al., 2014)	90	Assumed	-
Muñoz de Escalona et al. (2012)	80	Assumed	98
Sauret and Rowlands (2011)	65	Assumed	-
Schuster et al. (2010)	85	Assumed	-
Tempesti and Fiaschi (2013)	80	Assumed	-
Wang et al. (2014)	80	Assumed	96
J. Xu and Liu (2013)	85	(Franco & Villani, 2009; Zhang & Jiang, 2012)	-
Zhang and Jiang (2012)	85	Assumed	-

* Refers to ORC cycle pump unless stated otherwise

In some of these cases pump efficiency may refer to the combined efficiency of the pump and the motor. The studies that made separate motor efficiency assumptions used 80% for pump efficiency and the most commonly used efficiency value used is 80%. Peters et al. (2003) present the efficiency vs capacity relation (Figure 36) which gives the range of values that are suitable for design estimates of centrifugal pump efficiencies. According to preliminary calculations, the typical volume flow rates for an ORC with the constraints given in Table 1

is about 250-350 m^3/hr. A brine water mass flow rate of 35 kg/s at 35 MPa corresponds to a volume flow rate of about 128 m^3/hr, in both cases 80% pump efficiency is achievable according to Figure 36. Therefore 80% efficiency will be used for both ORC and water pumps.
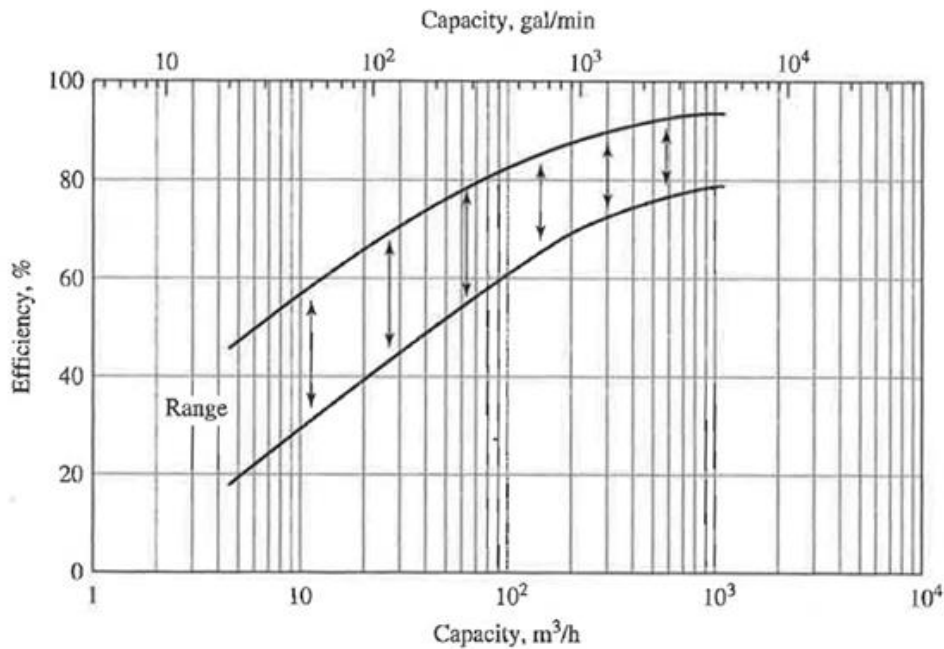
Figure 36: Efficiencies of centrifugal pumps (Peters et al., 2003).

Motor efficiency depends, similarly to generator efficiency, on capacity. With efficiency values ranging from 94% for single kW motor (Toshiba, n.d.) up to greater than 98% for motors over 10 MW. The expected motor power for this project will be in the hundreds of kW range, 96% is the assumed motor efficiency for this work.

2.7.2 Low Net Positive Suction Head (NPSH)

Cavitation is the major source of damage to pumps (Massoud, 2005). Cavitation occurs when the fluid reaches the boiling point within the pump due to localised pressure drop and results in the sudden formation and subsequent collapse of vapour bubbles in the pump. This localised pressure drop generally occurs at locations such as impeller tips, and cavitation will result in pitting damage to the impeller and can significantly reduce the life of the pump as well as causing immediate pump performance reduction on occurrence and potentially plant shut down.

As was mentioned in Section 2.4, a minimum subcooling of 2 °C is recommended at the condenser outlet. It is simpler to specify subcooling in IPSEpro in terms of vapour quality at

the outlet. Subcooling of 2 °C corresponds to approximately -1% vapour quality; this will be used as the minimum condenser outlet/pump inlet condition to ensure there is sufficient buffer accounted for to give pump reliability.

2.8 Economic Model

The objective of this project is to minimise cost per kWe generated. In order to meet this aim a cost model of the plant must be developed and integrated into an objective function which can be used to optimise the ORC. This cost model should incorporate the following criteria:

- Preliminary estimation of plant capital cost; this needs to be sufficiently accurate to compare different cycle configurations, needs consistency not necessarily precision.
- The method needs to be able to be numerically implemented within IPSEpro in the form of equations which estimate cost based on the component attributes available at the concept study design stage.

The components to be included in the cost model are:

- Heat Exchangers,
- Turbines,
- Cycle Pumps,
- Motors,
- Generators, and
- Condensing system: NDDCT and MDACT.

The cost of drilling and the heat source subsystem is assumed to be $20million across all scenarios. The brine pump cost is assumed to be covered under the heat source subsystem cost. Costs such as control systems, piping, cost of working fluid etc., are not considered at this stage, as attempting to quantify the relative cost of these for various fluids and cycle configurations may lead to erroneous results.

2.8.1 ORC Economic Model

There are numerous cost estimation methods that are used in the literature, which are summarised below in Table 10.

Reference	Method used
Tempesti and Fiaschi (2013)	Investment and O&M costs analysed for each component
Lecompte, Huisseune, van den Broek, De Schampheleire, and De Paepe (2013)	Simple objective function for Specific Investment Cost = total investment / net power generation
Astolfi et al. (2011)	Minimises Levelised cost of electricity. Slightly more involved cost estimation than is necessary for the purpose of this project.
Calise et al. (2014)	Minimises total cost function. Neglects cost of heat source subsystem, but includes operating cost and tariffs etc.
Quoilin et al. (2011)	SIC used for thermoeconomic optimisation. Performs SIC analysis for different fluids, also looking at T_{ev} vs SIC which shows a clear optimum region.
M. Li, Wang, Li, et al. (2013)	Computes overall capital cost of the cycle system, for transcritical CO_2 cycle & ORC
Yanga and Yeh (2015)	Optimises net power index (NPI) – which is just inverse of SIC, but uses purchase cost, doesn't account for labour/other costs.
Imran et al. (2014)	Use multivariable optimisation to minimise SIC and maximise thermal efficiency, comparing 5 different working fluids for 3 different cycle configurations.
Daniel Walraven et al. (2015)	Optimises NPV, using detailed heat exchanger models and a range of economic parameters

The SIC (Specific Investment Cost) method is a commonly used method in the literature and one that suits the objective of this project, which is to minimise cost per kWe generated. Only capital cost, not ongoing costs such as maintenance are being considered as it is assumed that for the candidate cycles that are being considered, the operating and maintenance demands will vary negligibly between cycles. Furthermore, the slight differences cannot be accurately quantified and to attempt to do so based on relative plant complexity may lead to erroneous results.

The plant SIC will be the objective function for the optimisation of cycle design when optimising at the detailed design stage.

$$SIC = \frac{total\ capital\ investment}{\dot{W}_{net}} = \frac{cost_{equipment} + cost_{installation} + cost_{heat\ source\ subsytem}}{\dot{W}_{net}} \qquad \text{Equation 20}$$

Total capital investment will be calculated as presented by Le, Kheiri, Feidt, and Pelloux-Prayer (2014), this is summarised in Table 11.

Variable	Equation	Eq No
Total equipment bare module cost, C_{TBM}	$C_{TBM} = \Sigma C_{BM} + C_{heat\ source\ subsystem}$	Equation 21
Cost of site preparation, C_{site}	$C_{site} = 0.05 C_{TBM}$	Equation 22
Cost of service facilities, C_{serv}	$C_{serv} = 0.05 C_{TBM}$	Equation 23
Total direct permanent investment, C_{DPI}	$C_{DPI} = C_{TBM} + C_{site} + C_{serv}$	Equation 24
Cost of contingencies and contractors fee, C_{cont}	$C_{cont} = 0.18 C_{DPI}$	Equation 25
Total depreciable capital, C_{TDC}	$C_{TDC} = C_{DPI} + C_{cont}$	Equation 26
Cost of land, C_{land}	$C_{land} = 0$	Equation 27
Cost of royalties, C_{royal}	$C_{royal} = 0$	Equation 28
Cost of plant startup, $C_{startup}$	$C_{startup} = 0.1 C_{TDC}$	Equation 29
Total permanent investment, C_{TPI}	$C_{TPI} = C_{TDC} + C_{land} + C_{royal} + C_{startup}$	Equation 30
Working capital, C_{WC}	$C_{WC} = 0$	Equation 31
Total Capital Investment, C_{TCI}	$C_{TCI} = C_{WC} + C_{TPI}$	Equation 32

In this project the cost of land, C_{land}, cost of royalties, C_{royal}, and working capital, C_{WC}, are assumed to be zero. The calculation of the bare module cost of equipment is covered in the following section.

2.8.2 Equipment Purchase Cost

There are a number of methods to calculate preliminary equipment cost estimates (Smith, 2005; Towler & Sinnott, 2013; Turton, Bailie, Whiting, & Shaeiwitz, 2009). The bare module cost method presented in (Turton et al., 2009) will be used in this project. In this method correlations based on historic data are used to calculate the base case purchased equipment cost. Following this the bare module factor is calculated which accounts for non-standard material and high operating pressure, where applicable. This is a useful method because it helps to account for factors such as the very high operating pressure of the brine heat exchanger and to more even-handedly compare the benefits of cycles which might achieve a higher net power output but require higher operating pressures in some equipment.

Equipment cost estimation methods are based on historical data, generally for the east coast of the U.S.A. as this is historically one of the main centres of the chemical industry. In order to develop reasonable, up to date installed plant cost estimates Towler and Sinnott (2013) recommend applying a number of correction factors to equipment purchase cost estimates:

Variable	Equation	Eq No
Equipment base purchase cost, C_p	$C_p = \left(\dfrac{AUD}{USD}\right)_{2014} \dfrac{CEPCI_{2014}}{CEPCI_{refyear}} C_p^0$	Equation 33
Equipment purchase cost, C_{BM}	$C_{BM} = F_{BM} C_p$	Equation 34
Bare module factor, F_{BM}	$F_{BM} = B_1 + B_2 F_M F_P$	Equation 35
Total bare module equipment cost, C_{TBM}	$C_{TBM} = \Sigma C_{BM}$	Equation 36

In Equation 33, C_p^0 is the base purchase cost in USD of the reference year, the correlations used for estimating C_p^0 for each equipment item is given in Table 13, and B_1 and B_2 are constants given in Table 14.

One particular aspect of the cost estimation that requires special attention is the cost correlation for the NDDCT structure, as it is a non-standard item and the results of the cost estimation are of significant importance for the outcome of this project. Stephen Gwynn-Jones of QGECE has developed the following cost estimation model for NDDCT tower structure in 2014 AUD:

$$C_P = 1392.2H_5^2 - 31937H_5 + 10^6 \qquad \text{Equation 37}$$

The developed cost model has been compared with good agreement against vendor quotes for building large NDDCTs in Australia. The cost model is for a concrete tower with aspect ratio of 1.2 and a diameter ratio of 1. The aspect ratio is defined as $r_a = H_5/d_3$, and diameter ratio is $r_d = d_5/d_3$, where the subscripts are as shown in Figure 55. As mentioned in Section 2.4.1 steel is being considered as the tower shell material in order to provide greater geometric design flexibility. It is assumed that this model should overestimate the costs of steel construction. If the aspect ratio of the tower is to be considered as a variable in the detailed design stage then the cost correlation should account for this. To this end, the following assumptions are made:

1. The tower shell cost is proportional to its surface area, i.e., for constant height, decreasing the diameter ratio decreases tower surface area and therefore tower shell cost, and
2. The tower surface area is approximated by that of a conical frustum, as shown in Figure 37, and is given by:

$$A = \pi \left(\frac{d_3 + d_5}{2}\right)(H_5 - H_3) = \pi d_m (H_5 - H_3)$$

If another form of the aspect ratio is defined, the mean diameter aspect ratio:

$$r_{am} = \frac{H_5}{d_m}$$

and the tower surface area is linearly proportional to the mean diameter, hence inversely proportional to the aspect ratio, then the cost correlation can be scaled by the mean diameter aspect ratio.
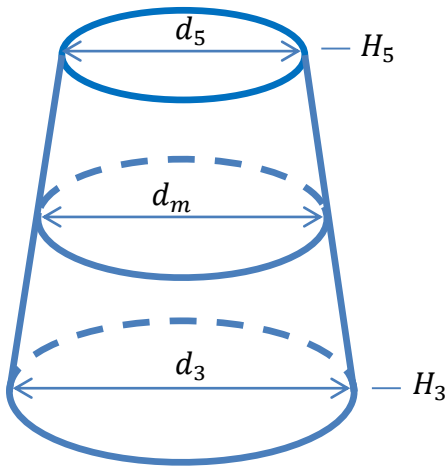
Figure 37: NDDCT geometry for tower surface area calculation.

From the above, the cost correlation is modified as follows:

$$C_p = \frac{1.2}{r_{am}}(1392.2H_5^2 - 31937H_5 + 10^6)$$

The correlations used for purchased cost of equipment are summarised in Table 13. These give the base case purchase cost for equipment made for typical pressure duty and from standard materials in USD of the year noted. These will be corrected to 2014 AUD using Equation 33. Cost factors are applied as per Equation 34 and Equation 35 where applicable to adjust for high operating pressure or non-standard materials.

Table 13: Cost correlations for ORC equipment, purchase cost, C_p^o, in **USD, except when noted.**

Component	Units for Size, S	Size Range	Equipment Purchase Cost, C_p^0	CEPCI / Year	Reference
Heat Exchanger – U tube STHE	A [m²]	10 - 1000	$28{,}000 + 54A^{1.2}$	532.9 / 2010	Towler and Sinnott (2013)

Component	Units for Size, S	Size Range	Equipment Purchase Cost, C_p^0	CEPCI / Year	Reference
Heat Exchanger – PHE	A [m²]	1.0 - 500	$1600 + 210A^{0.95}$	532.9 / 2010	Towler and Sinnott (2013)
Feed fluid heater (regenerative cycle)	$\dot{V}$ [L/s]	-	$\log C_p^0 = 4.2 - 0.204 \log(\dot{V})$ $+ 0.1245(\log(\dot{V}))^2$	397 / 2001	Imran et al. (2014)
Single stage centrifugal pump	$\dot{V}$ [L/s]	0.2 - 126	$8000 + 240\dot{V}^{0.9}$	532.9 / 2010	Towler and Sinnott (2013)
Motor - explosion proof	$\dot{W}_{motor}$ [kW]	1.0 - 2500	$-1100 + 2100\dot{W}^{0.6}$	532.9 / 2010	Towler and Sinnott (2013)
Turbine	$\dot{W}_{turbine}$ [kW]	1500 -	$115{,}791 + 78.53\,\dot{W}_{turbine}$	397 / 2001	See below
Generator	$\dot{W}_{gen}$	-	$60(\dot{W}_{gen})^{0.95}$	397 / 2001	Le, Kheiri, et al. (2014)
Air-cooled heat exchanger – used for MDACT & NDDCT	Bare-tube area, A [m²]	200 - 2000	$156{,}000\left(\dfrac{A}{200}\right)^{0.89}$	391 / 2000	Smith (2005)
MDACT Fan (including motor)	$\dot{W}_{fan}$ [kW]	50 - 200	$12{,}300\left(\dfrac{\dot{W}_{fan}}{50}\right)^{0.76}$	391 / 2000	Smith (2005)
MDACT tower structure	HE frontal area, A_{fr} [m²]	-	$448.96 A_{fr}$	564 / 2013	D. Walraven, B. Laenen, and W. D'haeseleer (2015)
NDDCT - Tower Structure, concrete tower	H_5 & r_{am} [m]	-	$\dfrac{1.2}{r_{am}}(1392.2 H_5^2 - 31937 H_5 + 10^6)$	AUD 2014	See above

The radial turbine cost correlation given in Turton et al. (2009) is only applicable up to 1500 kW, but the turbine sizes found in the preliminary analysis for the basic ORC are generally of the order of 3500-4500 kW. The shape of the cost curve is that of an increasing exponential decay, as shown in Figure 38. In order to estimate cost beyond the range of this correlation a linear extrapolation will be used from the final gradient of the cost curve.

$$C_p^0 = 115791 + 78.533 \, \dot{W}_{turbine}$$
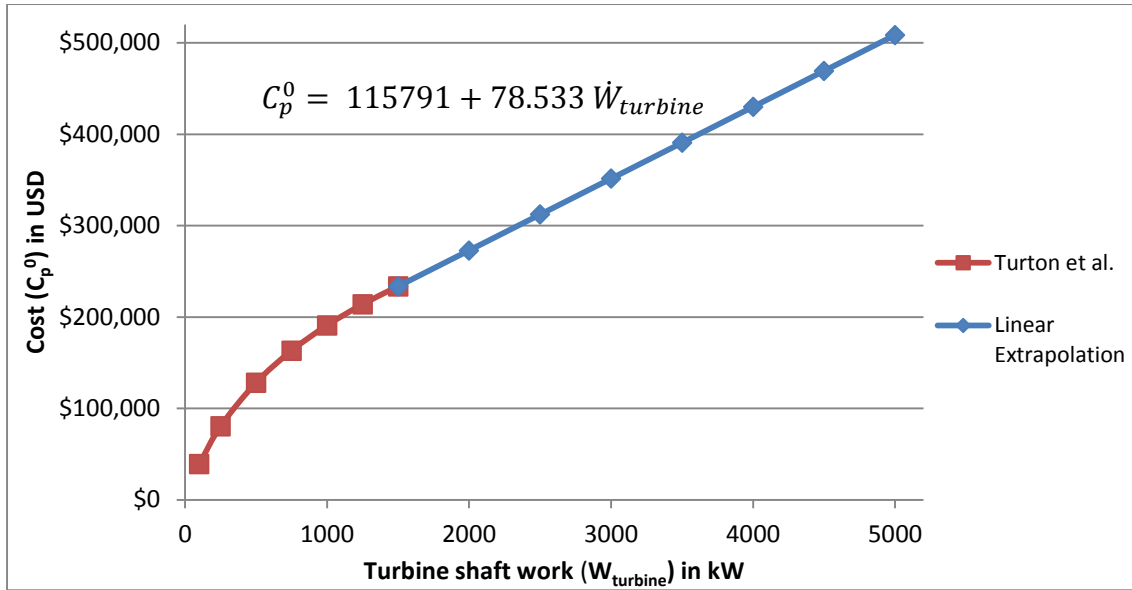
Figure 38: Linear Extrapolation of radial turbine cost correlation from Turton et al. (2009).

2.8.3 Equipment Bare Module Factors

The correlations provided above are the base purchase cost for equipment made from standard materials for typical operating pressure. Cost factors need to be applied to correct for high operating pressure and/or non-standard materials. The pressure factor, F_p, is calculated from the following general form

$$log_{10} F_p = C_1 + C_2 \, log_{10} p + C_3 (log_{10} p)^2 \qquad \text{Equation 41}$$

where P is the relative pressure in bar gauge and the constants C_1, C_2 and C_3 are given in Table 14. Turton et al. (2009) give the constants for the turbine pressure factor as being null, implying the turbine cost correlation already accounts for high operating pressure. Bare module factors are assigned for the turbine and generator to account for material.

Table 14: Constants for the calculation of the equipment bare module factor.

Equipment	C_1	C_2	C_3	B_1	B_2	F_m	F_{BM}	Reference
STHE	0.03881	-0.11272	0.08183	1.63	1.66	1.0	-	Le, Kheiri, et al. (2014)
Feed Heater	0.00	10.0	0.00	1.12	0.87	1.0	-	Imran et al. (2014)
Cycle pump	-0.3935	0.3957	-0.00226	1.89	1.35	1.0	-	Le, Kheiri, et al. (2014)
Generator	-	-	-	-	-	-	1.5	Le, Kheiri, et al. (2014)
Turbine	-	-	-	-	-	-	1.7	Atrens, Gurgenci, and Rudolph (2011)

3. Preliminary Cycle Analysis

3.1 Preliminary Analysis Methodology

The aim of this section is to perform a preliminary cycle analysis for the geothermal brine conditions given in Table 1. A number of standard simplifying assumptions are used for the preliminary analysis:

- Cycles are considered steady state adiabatic systems.
- Pipe and fitting pressure losses throughout the plant are neglected.
- Heat loss to surroundings in heat exchangers, turbines, pumps and pipes is neglected.
- Potential and kinetic energy of the fluids are neglected.

The minimum brine inlet temperature is 80 ºC to prevent scaling of the brine side of the heat exchangers due to silica, calcite and stibnite build-up, as was discussed in Section 1.3.

Assumed cycle component parameters are given in Table 15. The justification for the selection of these values is covered in the relevant parts of Chapter 2 - ORC Design Considerations.

Table 15: Parameters used for preliminary cycle analysis.

Variable	Value	Unit
Turbine isentropic efficiency	85	%
Pump efficiency	80	%
Generator efficiency	97	%
Motor efficiency	96	%
Condenser outlet temperature with -1% moisture, subcooling of ~2 ºC	50	ºC
Heat exchanger pinch point temperature difference (ΔT_{pp})	≥ 5	ºC
Heat exchanger ΔT_{LM}	≥ 10	ºC
Heat exchanger pressure loss	0.02	MPa

3.2 Candidate Fluid Selection

A candidate fluids search was performed using the Fluid Search function in REFPROP Version 9.1. The search criteria used was critical temperature between 50 ºC and 300 ºC, the results of which formed the initial candidate list. Next, the key Health, Safety and Environmental (HSE) information was collated, where available, for each fluid. No fluids

were filtered out at this stage based on their HSE properties, but these properties will be one of the key factors if there are several closely ranked high performing fluids, as having negative HSE attributes could significantly add to plant cost in the form of additional safety measures.

Organic fluids have an upper temperature and pressure limit beyond which they begin to chemically decompose. This temperature should be well above the geothermal fluid inlet temperature of 220 $^{\circ}$C. REFPROP provides a range of applicability for each fluid in its database. The upper limit stated is for the validity of the correlations used in the software, which is "usually near the point of decomposition" (Lemmon et al., 2013). Therefore, in some cases the fluid may actually be chemically stable beyond the stated limit. For example in REFPROP version 9.1 R245ca has a temperature upper limit, T_{UL}, of 176.85 $^{\circ}$C, whereas in version 9.0 the T_{UL} was stated as 226.85 $^{\circ}$C. The reason for this is that REFPROP 9.1 makes use of a more accurate correlation which has narrower validity limits.

In order to not prematurely eliminate any high potential fluids, all fluids are kept in contention and the T_{UL} in the .FLD files overridden so that the fluids can be analysed without limitation. If it is found that one of these fluids is a promising fluid, at that stage further investigation will be performed to ascertain a more accurate T_{UL} of the fluid. It should be noted that modifying the upper limits of the .FLD files means results are extrapolated beyond the applicability limits of the correlation. Hence there will be an increased uncertainty in the results obtained with this approach, and these results will need further verification. The fluids that meet the search criteria are presented in Table 16, along with their HSE and thermodynamic properties where data is available. Fluids with T_{UL} lower than the brine inlet temperature or P_{UL} of 10 MPa or lower are in bold.

Table 16: Health, safety and environmental, and thermodynamic properties of the candidate working fluids, significant figures are as per REPFROP version 9.1.

Fluid (name used in REFPROP)	Toxicity*	Flammability*	ODP*	GWP*	Fluid Type^	Available in IPSEpro LTP	Critical Temp. ^ (°C)	Critical Pressure^ (MPa)	REFPROP T_{UL}^ (°C)	REFPROP P_{UL}^ (MPa)
Butane	Low	High	0**	20	Dry	Y	151.98	3.796	301.85	200
Butene (1-Butene)	Low	High			Isentropic	Y	146.14	4.0051	251.85	70

Fluid (name used in REFPROP)	Toxicity*	Flammability*	ODP*	GWP*	Fluid Type^	Available in IPSEpro LTP	Critical Temp.^ (°C)	Critical Pressure^ (MPa)	REFPROP T_{UL}^ (°C)	REFPROP P_{UL}^ (MPa)
Cyclohexane					Dry	Y	280.45	4.0805	426.85	250
Cyclopentane					Dry	Y	238.57	4.5712	276.85	250
Cyclopropane			0**		Wet	Y	125.15	5.5797	**199.85**	250
Isobutane	Low	High	0^	4^	Dry	Y	134.66	3.629	301.85	35
Isobutene	Low	High			Dry	Y	144.94	4.0098	276.85	50
Isopentane	Low	High	0^	20	Dry	Y	187.2	3.378	226.85	1000
MDM					Dry	Y	290.94	1.415	399.85	30
MM					Dry	Y	245.6	1.939	399.85	30
Neopentane					Dry	Y	160.59	3.196	276.85	200
Pentane	Low	High			Dry	Y	196.55	3.37	326.85	100
Propane	Low	High	0^	20^	Wet	Y	96.74	4.2512	376.85	1000
R11			1	4750	Isentropic	N	197.96	4.4076	351.85	30
R12	Low	Non-flam	1	10900	Wet	N	111.97	4.1361	251.85	200
R21	Toxic	Non-flam	0.04*		Wet	N	178.33	5.1812	**199.85**	138
R22	Low	Non-flam	0.055	1810	Wet	N	96.145	4.99	276.85	60
R32			0	675	Wet	N	78.105	5.782	**161.85**	70
R40					Wet	N	143.15	6.6773	356.85	100
R41					Wet	N	44.13	5.897	**151.85**	70
R113			0.8	6130	Dry	N	214.06	3.3922	251.85	200
R114	Low	Non-flam	1	10000	Dry	N	145.68	3.257	233.85	21
R115			0.6	7370	Isentropic	N	79.95	3.129	276.85	60
R1216					Dry	N	85.75	3.1495	**126.85**	12
R123	Toxic	Non-flam	0.02	77	Dry	Y	183.68	3.6618	326.85	40
R1234yf					Isentropic	Y	94.7	3.3822	**136.85**	30
R1234ze					Isentropic	Y	109.36	3.6349	**146.85**	20
R124	Low	Non-flam	0.022	609	Isentropic	Y	122.28	3.6243	**196.85**	40
R125	Low	Non-flam	0	3500	Wet	Y	66.023	3.6177	226.85	60

Fluid (name used in REFPROP)	Toxicity*	Flammability*	ODP*	GWP*	Fluid Type^	Available in IPSEpro LTP	Critical Temp. ^ (°C)	Critical Pressure^ (MPa)	REFPROP T_{UL}^ (°C)	REFPROP P_{UL}^ (MPa)
R134a	Low	Non-flam	0	1430	Wet	Y	101.06	4.0593	**181.85**	70
R141b			0.11	725	Isentropic	N	204.35	4.212	226.85	400
R142b	Low	Low Flam	0.065	2310	Isentropic	Y	137.11	4.055	**196.85**	60
R143a	Low	Low Flam	0	4470	Wet	Y	72.707	3.761	376.85	100
R152a	Low	Low Flam	0	124	Wet	Y	113.26	4.5168	226.85	60
R161					Wet	N	102.1	5.01	**176.85**	**5.0**
R218			0	8830	Dry	N	71.87	2.64	**166.85**	20
R227ea			0	3220	Dry	Y	101.75	2.95	**201.85**	60
R236ea					Dry	Y	139.29	3.42	**138.85**	**6.0**
R236fa	Low	Non-flam	0	9810	Dry	Y	124.95	3.2	**126.85**	70
R245ca			0	693	Dry	Y	174.42	3.9407	**176.85**	**10.0**
R245fa	Toxic	Non-flam	0	1030	Dry	Y	154.01	3.651	**166.85**	200
R365mfc					Dry	N	186.85	3.266	226.85	35
RC318	Low	Non-flam			Dry	N	115.23	2.7775	349.85	60

* Toxicity, flammability, ODP, GWP from ASHRAE (2009).

^ Source of critical temperature and pressure and temperature upper limit: Lemmon et al. (2013).

There are a number of fluids within the search range, which are not available in IPSEpro and therefore cannot be analysed in this work.

All fluids will be assessed in the basic ORC, but following this it is useful to have guidelines for which fluids are appropriate for each cycle configuration. The ranges in Figure 39 were established using the findings of Section 2.2.3. Fluids with T_{cr} below, but near the brine inlet temperature are more likely to perform well in the basic ORC cycle and fluids with T_{cr} significantly below the brine inlet temperature are likely only effective as secondary fluids in the dual fluid cycle.
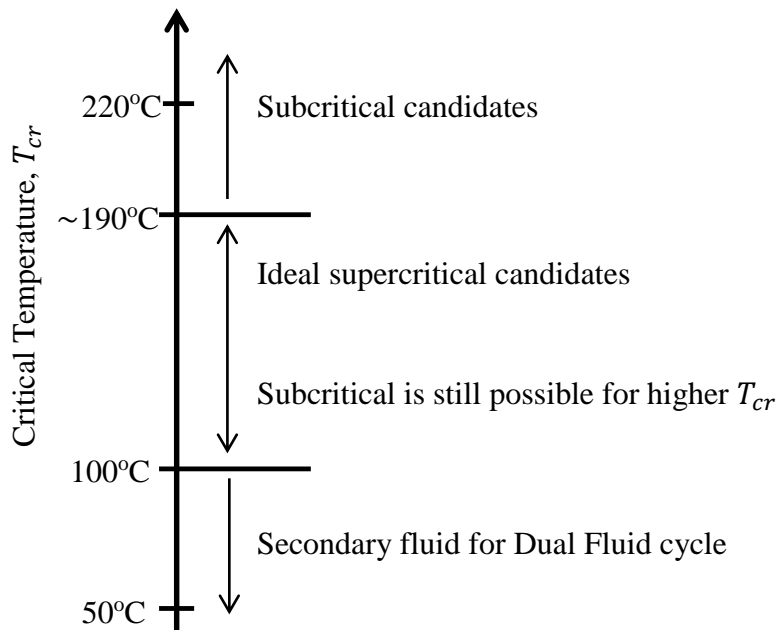
Figure 39: Approximate guideline temperatures used to classify candidate fluids based on their critical temperatures for cycle compatibility.

This is illustrated below in Figure 40 for R152a, with a T_{cr} of 113.26 °C, it is towards the lower end of the middle bracket in Figure 40.
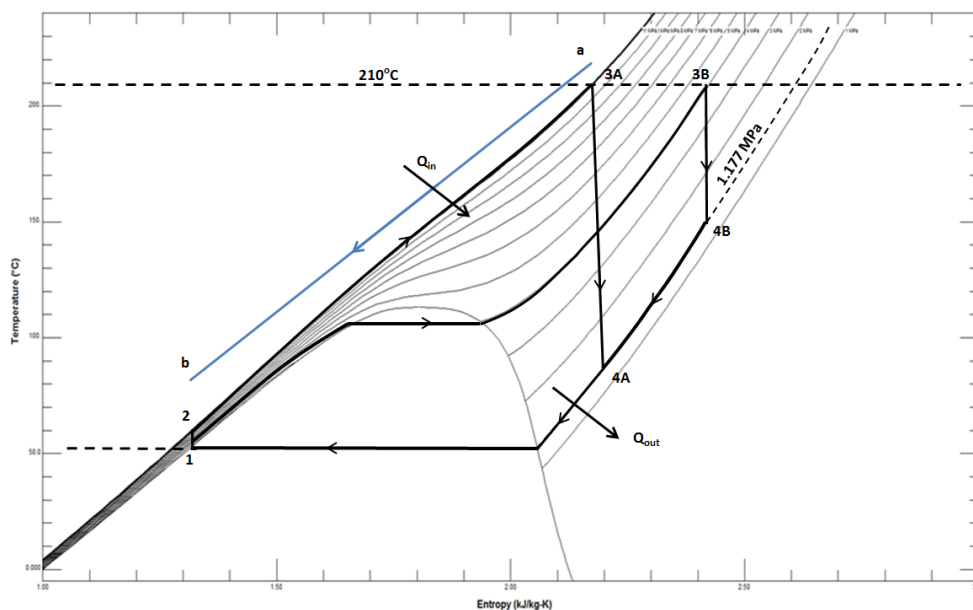
Figure 40: Cycle comparison on T-s diagram for R152a, T_{cr} = 113.26 °C, comparing supercritical and subcritical cycle feasibility.

The subcritical R152a cycle requires a high degree of superheating for a smaller pressure ratio and a higher heat rejection, $\dot{Q}_{out}$. Whereas the supercritical cycle for R152a shown in Figure 40 seems thermodynamically more promising with only moderate $\dot{Q}_{out}$ and a much better temperature profile match to the brine cooling curve.

3.3 Preliminary Analysis Results

All fluids are first analysed in the basic binary cycle to establish a baseline performance comparison between the fluids. The performance of each fluid in the basic ORC combined with Table 3 will inform the decision as to which fluids should be considered for subsequent cycles. Each of the candidate cycles will be addressed in sequence, and in each section the optimisation approach will be outlined. The optimisation objective throughout the preliminary analysis is to maximise the net power generation.

3.3.1 Basic ORC

The control variables used for the basic ORC are the turbine inlet temperature and pressure, and the condensing temperature, which is set to 50 ^{o}C. With constant specified brine inlet and outlet conditions the mass flow rate is the free variable that is solved for to satisfy the energy balance across the brine heat exchangers. The basic ORC model is shown below in Figure 41
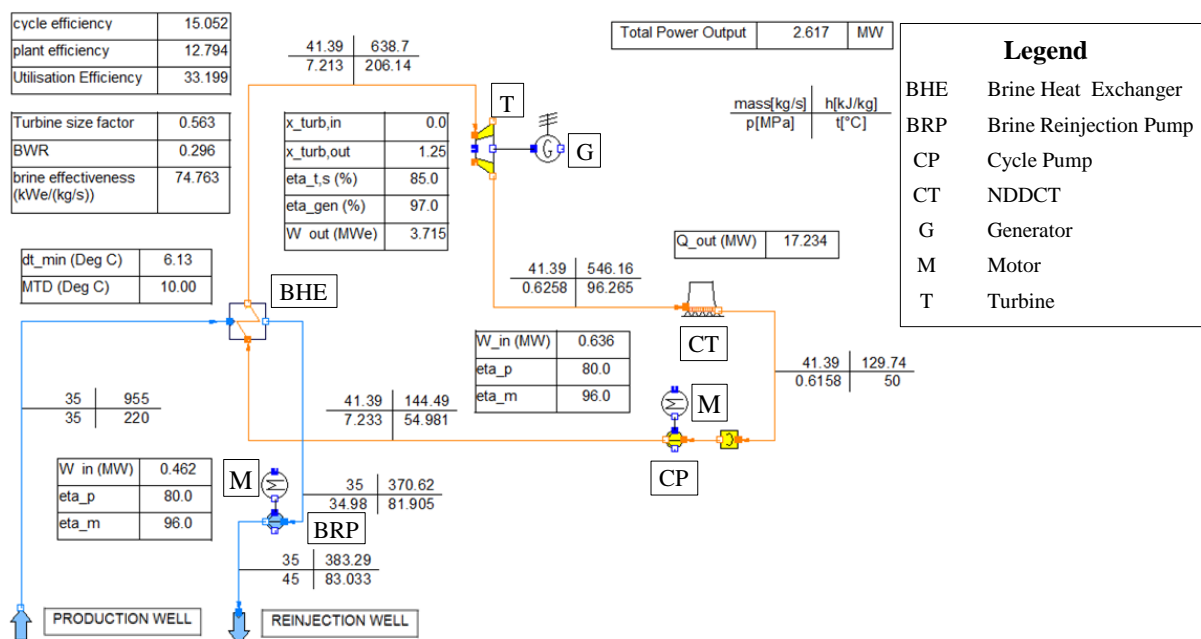
Figure 41: Screenshot of the basic ORC model in IPSEpro, shown here for supercritical isobutene.

Each of the basic ORCs have a peak net power generation range where the ratio of shaft work out of the turbine, $\dot{W}_{turb}$, to the work into the pump, $\dot{W}_{pump}$, is at an optimum and beyond which $\dot{W}_{turb}$ tapers off while $\dot{W}_{pump}$ continues to rise. This is shown below in Figure 42 for R152a.
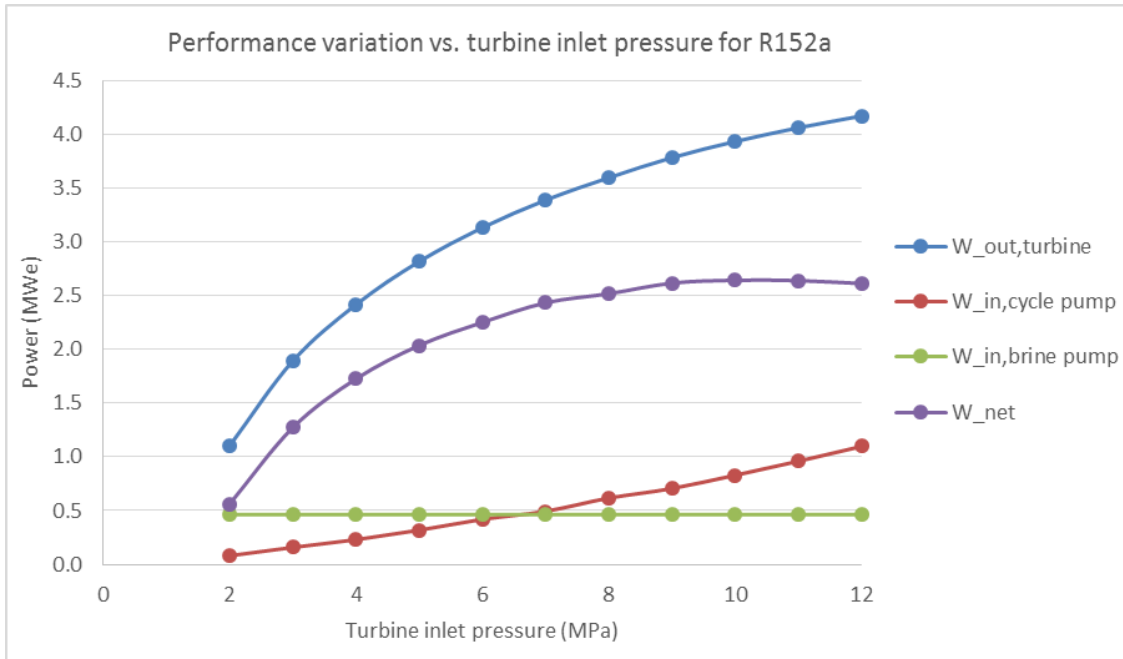
Figure 42: Cycle performance versus turbine inlet pressure for a basic ORC with working fluid R152a.

In order to find the optimum operating point for each cycle, the optimisation module in IPSEpro which uses the Genetic Algorithm was utilised. See Section 4.1.3 for details of this module and the approach taken.

It is not feasible for the Genetic Algorithm (GA) to cover the whole possible range for turbine inlet temperature and pressure while still maintaining a reasonable search interval and calculation time, for the number of calculations that would be required. In order to address this subcritical and supercritical cycles will be optimised separately, thereby reducing the range for each optimisation while also providing for the limitation on approach to critical temperature covered in Section 2.2.3.2.

In general, for the basic cycle optimisation a two stage optimisation was used. The first stage uses the broad search range, with the default ranges shown in Table 17 and Table 18 below, to find the region of the global optimum. Following this, a more targeted search range was used, in order to utilise a more refined search interval over a narrower search space. The decision variables for the first stage of optimisation are shown below in Table 17 for subcritical and Table 18 for supercritical. The specified Bit value determines the interval at which the optimisation searches across the range between the minimum and maximum; this is covered in further detail in Section 4.1.3.

64

Variable	Units	Minimum	Maximum	Bit / Interval
Turbine inlet temperature	ºC	150	200	7 / 0.39
Turbine inlet pressure	MPa	0.1	Fluid P_{cr} (typical 3-4 MPa)	6 / ~0.05
Brine reinjection temperature	ºC	80	90	6 / 0.156

Table 18: Default decision variables used for the optimisation of the supercritical basic ORC using a genetic algorithm.

Variable	Units	Minimum	Maximum	Bit / Interval
Turbine inlet temperature	ºC	170	215	7 / 0.273
Turbine inlet pressure	MPa	Fluid P_{cr} (typical 3-4 MPa)	10	6 / ~0.1
Brine reinjection temperature	ºC	80	90	6 / 0.156

These values are effective for the first stage optimisation for the majority of fluids considered, which are generally in the range of P_{cr} of 3-4 MPa and T_{cr} of 130-180 ºC. However, some fluids with critical conditions significantly outside of the typical range would not find a valid solution in the initial GA population when constrained to this area, at which point they are addressed on an individual basis. For example cyclopentane with T_{cr} of 238.57 ºC for the given brine inlet conditions and HE constraints can only reach a maximum of 133 ºC heat exchanger outlet temperature with evaporation pressure of 0.833 MPa. The parameters used for the GA optimisation are presented in Table 19. The GA and the significance of the parameters below are discussed in Section 4.1.3.

Table 19: Genetic Algorithm optimisation parameters used throughout the preliminary analyses.

Optimisation Parameter	Value
Population	60
Generations	15
Possibility of crossovers	0.6
Possibility of mutations	0.006

Table 20 lists the thermodynamic conditions found by the GA to maximise power generation for the basic cycle, subject to the constraints stated in Table 17 Table 19.

Cycle Fluid	Sub- or super-critical	$P_{t,in}$ (MPa)	$T_{t,in}$ (ºC)	$T_{t,out}$ (ºC)	$T_{gb,out}$ (ºC)	$\dot{m}_{cf}$ (kg/s)	BWR	$\dot{Q}_{out}$ (MWth)	$\eta_{th,cycle}$ (%)	η_u (%)	$\dot{W}_{net}$ (MWe)
Butane	Sub	3.70^	184.1	117.8	80.0	37.78	0.25	17.89	13.20	28.84	2.273
	Super	6.65	205.0	102.0	80.3	39.80	0.29	17.49	14.77	32.90	2.593
Butene	Super	3.90^	187.3	118.1	80.0	38.97	0.25	17.88	13.21	28.90	2.277
	Super	7.21	206.1	96.3	81.9	41.39	0.30	17.23	15.05	33.20	2.617
Cyclohexane	Sub	0.49	143.75	95.326	100.0	34.59	0.21	15.40	13.23	23.98	1.890
Cyclopentane	Sub	0.83	133.2	78.4	90.2	39.01	0.20	16.70	12.87	25.55	2.014
Cyclopropane*	Super	10.0^	199.4	90.2	80.0	40.31	0.39	17.61	14.87	30.62	2.368
Isobutane	Sub	3.50^	164.5	109.3	80.0	43.4	0.29	18.26	11.43	24.20	1.907
	Super	8.56	208.7	108.2	80.0	42.23	0.35	17.67	14.04	31.07	2.449
Isobutene	Sub	3.90^	189.2	123.1	80.0	37.97	0.25	17.94	12.94	28.16	2.219
	Super	8.00	206.5	92.5	80.0	42.64	0.31	17.51	14.82	33.12	2.611
Isopentane	Sub	3.20^	186.9	103.1	85.1	39.49	0.22	16.91	14.87	31.84	2.509
Neopentane	Sub	3.10^	167.6	103.2	80.0	46.35	0.26	17.98	12.75	27.66	2.180
	Super	5.67	207.9	117.1	80.0	42.37	0.29	17.70	13.99	30.94	2.439
Pentane	Sub	1.93	161.3	96.8	80.0	40.61	0.20	17.69	14.16	31.38	2.473
Propane	Sub	4.10^	155.5	118.7	80.0	43.17	0.40	19.04	7.79	14.64	1.154
	Super	10.00^	215.0	133.3	80.0	37.73	0.38	17.92	12.87	27.98	2.205
R123	Sub	2.47	162.2	78.4	80.0	97.05	0.21	17.61	14.53	32.35	2.550
	Super	4.22	195.2	100.3	81.6	100.28	0.26	17.54	13.88	11.63	2.383
R1234yf*	Sub	3.30^	215.0	185.86	80.0	68.86	0.40	19.25	6.87	12.21	0.962
	Super	10.00^	215.0	135.8	80.0	81.67	0.397	18.05	12.25	26.35	2.077
R1234ze*	Sub	3.50^	158.9	115.2	80.0	86.95	0.34	18.75	9.16	18.22	1.436
	Super	10.00^	215.0	122.7	80.0	79.52	0.36	17.80	13.42	29.44	2.320
R124*	Sub	3.55	170.2	117.8	80.0	96.73	0.30	18.43	10.65	22.14	1.745
	Super	8.00	199.5	103.7	80.0	100.02	0.34	17.79	13.51	29.66	2.338
R125	Super	10.00^	215.0	160.9	80.0	93.02	0.47	18.65	9.43	18.93	1.492
R134a*	Sub	3.90^	164.4	122.7	80.0	81.40	0.35	18.88	8.55	16.63	1.311
	Super	10.00^	215.0	127.1	80.0	75.30	0.35	17.83	13.32	29.16	2.299
R142b*	Sub	3.90^	192.9	124.9	80.0	69.25	0.25	17.99	12.68	27.50	2.167
	Super	6.92	196.0	86.7	80.0	76.69	0.30	17.59	14.50	32.28	2.544

Cycle Fluid	Sub- or super-critical	$P_{t,in}$ (MPa)	$T_{t,in}$ (ºC)	$T_{t,out}$ (ºC)	$T_{gb,out}$ (ºC)	$\dot{m}_{cf}$ (kg/s)	BWR	$\dot{Q}_{out}$ (MWth)	$\eta_{th,cycle}$ (%)	η_u (%)	$\dot{W}_{net}$ (MWe)
R143a	Super	10.00^	215.0	146.6	80.0	72.99	0.42	18.31	11.04	23.18	1.827
R152a	Sub	4.40^	215.0	156.6	80.0	46.86	0.28	18.37	10.95	22.94	1.808
	Super	10.00^	212.6	99.7	80.2	55.72	0.32	17.48	14.85	33.15	2.612
R227ea*	Super	10.00^	201.5	126.3	80.0	107.04	0.43	18.25	11.29	23.84	1.879
R236ea*	Sub	3.30^	215.0	164.1	80.0	71.30	0.26	18.28	11.38	24.06	1.896
	Super	10.00^	213.9	107.6	80.0	89.34	0.34	17.68	14.00	30.96	2.441
R236fa*	Sub	3.10	149.3	99.2	80.0	104.1	0.30	18.50	10.35	21.37	1.684
	Super	9.74	215.0	120.8	80.0	89.68	0.43	17.89	13.56	27.09	2.094
R245ca*	Sub	3.80^	184.3	100.1	80.0	73.01	0.22	17.58	14.65	32.67	2.575
	Super	6.46	207.7	85.5	80.2	77.32	0.26	17.42	15.23	34.15	2.692
R245fa*	Sub	3.50^	166.6	92.4	80.0	81.98	0.24	17.89	13.21	28.89	2.277
	Super	7.75	209.8	94.7	80.0	79.35	0.29	17.50	14.90	33.33	2.627

*Fluid T_{UL} specified as below 220 ºC in REFPROP 9.1, but with T_{UL} modified in REFPROP .FLD files to allow unhindered analysis. If T_{UL} limits stated are in fact the thermal stability limit, then the fluid would not be used for risk of hot spots in the heat exchanger leading to deterioration of the fluid. These results need further verification.

^Optimum solution found at limit of specified decision variable range for that optimisation, either from inefficient subcritical conditions with peak efficiency at upper limit before critical pressure, or due to reaching the 10 MPa pressure upper limit for supercritical cycles.

Note that all the highest performing cycles are supercritical cycles. The only fluids that had peak performance at a subcritical pressure were those that were unable to reach supercritical pressure due to constraint by a high critical temperature, such as pentane, isopentane and R123.

To illustrate this take R123, which achieved 15 % higher for subcritical than supercritical, with a critical temperature of 183.7 ºC, it is quite close to the brine inlet temperature and would seem to be a very promising fluid. However, the optimum solution found in the supercritical pressure range was significantly below the subcritical performance. As shown below in Figure 43, the operating point (a) is achievable within the heat transfer constraints, but results in excessive moisture formation in the turbine, and the turbine efficiency drops dramatically. Operating point (b) cannot be reached due to the curvature of the isobar resulting in a ΔT_{pp} which is too small. This only leaves a subcritical evaporating pressure such as point (c) as an achievable operating point for R123.
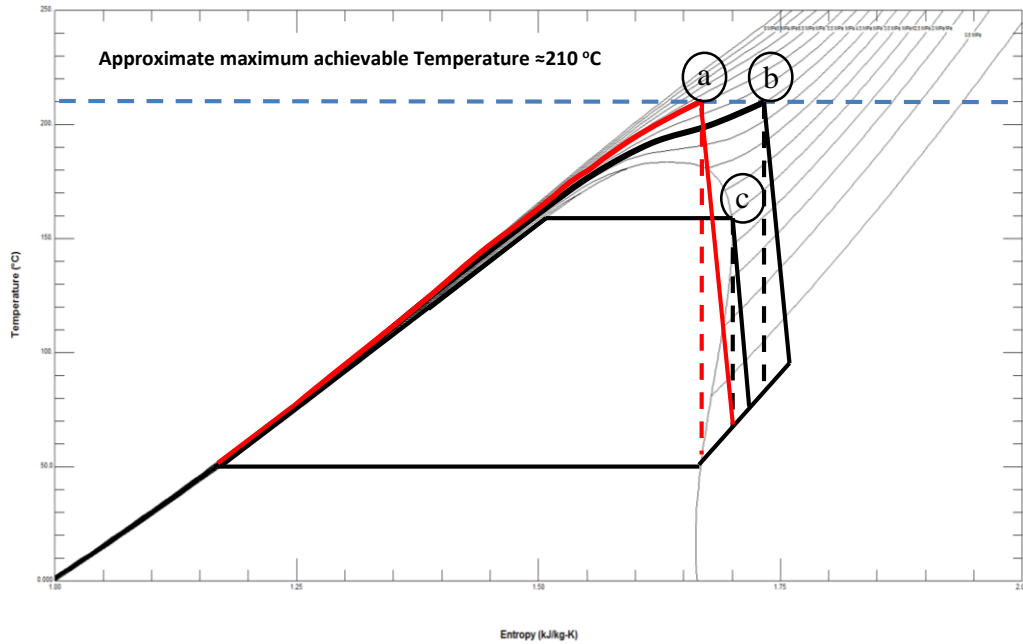
Figure 43: Fluids with critical temperature approaching the brine inlet temperature are restricted due to the proximity to the brine inlet temperature and the heat exchanger limits. This results in the supercritical pressures expanding into the saturated mixture region and resulting in undesirable moisture formation in the turbine and the associated performance degradation.

The cycles that have a turbine inlet temperature which is significantly less than brine inlet temperature have been limited by the location of the pinch point and the shape of the heat transfer profile. Subcritical cycles are more severely limited by this due to the shape of the isobar, this can be seen on the T-Q diagram below.
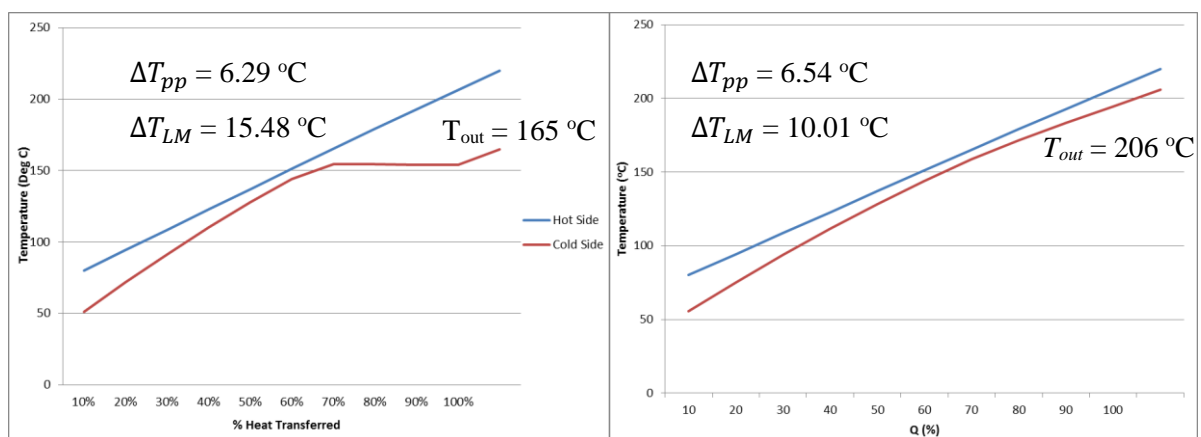
Figure 44: T-Q diagram comparison of isopentane at 2 MPa turbine inlet pressure (left) and supercritical butene with 7.7 MPa turbine inlet pressure (right).

Another observation is that cycles with a high turbine outlet temperature generally have a relatively low net power generation. Conversely, the higher performing cycles tend to have relatively low turbine outlet temperatures. This is in some cases an indication of unnecessary superheating. The reason the high performing cycles have a low turbine outlet temperature is

68

because the fluid T-s diagram shape is well matched to the brine heat transfer profile, as is illustrated with R152a in Figure 40, on page 62. To heat the working fluid at subcritical pressure to near the brine inlet temperature, with $T_{cr} = 113.26$ °C, a substantial degree of superheating is required and this results in a high turbine outlet temperature. This is reflected in the results for R152a with the subcritical cycle generating 1.808 kWe compared with the supercritical cycles 2.612 kWe.

One of the benefits of the ORC is the flexibility to select fluids with a T-s diagram shape that suit the heat source, thereby reducing or removing the need for superheating. This is beneficial as it removes or reduces the need for a super heater which can significantly increase system cost due to the need for a large heat transfer surface area to compensate for the low heat transfer coefficient when transferring heat to a vapour (Calise et al., 2014).

3.3.2 Recuperated ORC

The recuperated ORC uses the same constraints as the basic ORC: evaporator outlet temperature and pressure, condensing temperature and pump inlet vapour quality, with one additional constraint of the temperature at the pressurised liquid outlet side of the recuperator, which can be varied within the limits of the heat exchangers. The recuperated ORC model is shown below.
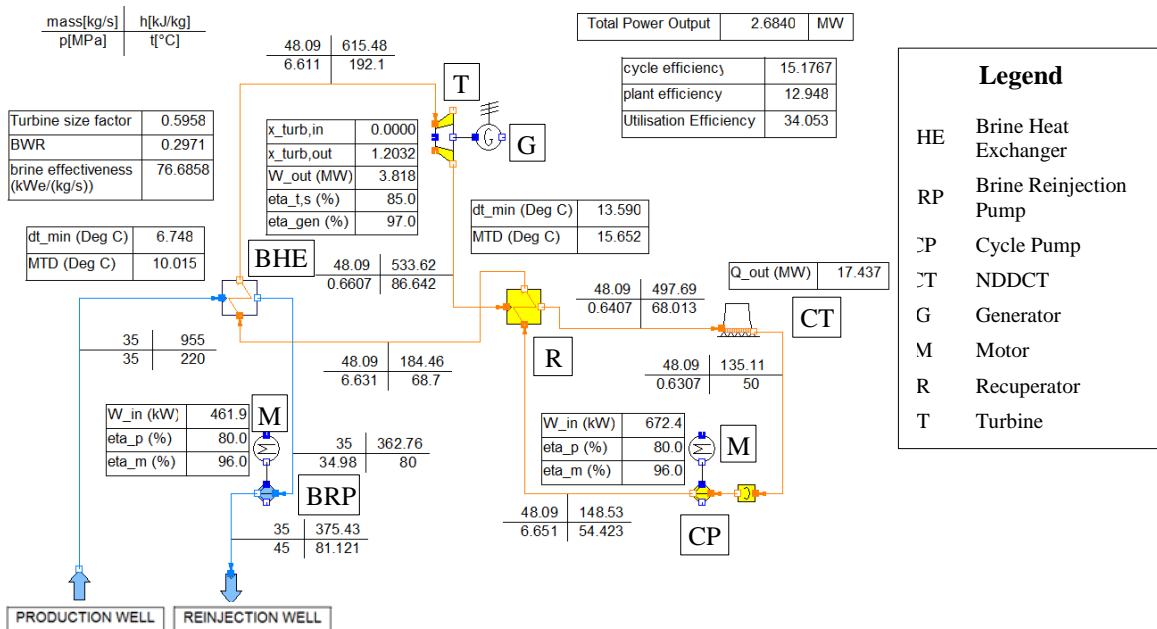
Figure 45: Screenshot of the recuperated ORC model in IPSEpro, shown here for supercritical isobutene.

69

The ranges used for the decision variables for the recuperated cycle were individually targeted to the optimum found in the basic cycle. The decision variables for the recuperated ORC are as below in Table 21:

Table 21: Default decision variables used for the optimisation of the Recuperated ORC using a genetic algorithm, the subscript opt,basic refers to the value found in the basic ORC analysis.

Variable	Units	Minimum	Maximum	Bit / Interval
Turbine inlet temperature	°C	$T_{opt,basic}$ - 15	$T_{opt,basic}$ + 15	7 / 0.234
Turbine inlet pressure	MPa	$P_{opt,basic}$ - 1	$P_{opt,basic}$ + 1	7 / 0.0156
Brine outlet temperature	°C	80	90	6 / 0.156
Recuperator liquid side outlet temperature	°C	60	80	7 / 0.156

Table 22 lists the thermodynamic conditions found by the GA to maximise power generation for the recuperated cycle. Only the higher performing fluids, those that achieve high $\dot{W}_{net}$, from the basic ORC analysis are considered here.

Table 22: Preliminary analysis results for the recuperated ORC optimised for each candidate fluid, for the conditions given in Table 1.

Cycle Fluid	Sub- or super-critical	$P_{t,in}$ (MPa)	$T_{t,in}$ (°C)	$\dot{m}_{cf}$ (kg/s)	$T_{gb,out}$ (°C)	$\dot{Q}_{out}$ (MWth)	$\eta_{th,cycle}$ (%)	η_u (%)	$\dot{W}_{net}$ (MWe)
Butane	Super	6.63	194.2	48.10	80.6	17.339	15.267	34.108	2.688
Butene	Super	6.45	192.8	47.69	80.0	17.437	15.185	34.074	2.686
Cyclopropane*	Super	9.91	196.2	42.17	80.8	17.361	15.063	33.541	2.644
Isobutane	Super	8.33	198.7	49.36	86.3	16.642	15.219	32.382	2.552
Isobutene	Super	6.61	192.1	48.05	80.0	17.442	15.154	33.992	2.679
Isopentane	Sub	2.80	175.3	44.03	80.0	17.635	14.390	31.983	2.521
Neopentane	Super	5.81	195.4	53.94	82.7	17.151	14.970	32.759	2.582
Pentane	Sub	1.79	157.0	41.93	87.94	16.687	14.283	29.591	2.332
Propane	Super	9.94	194.5	47.63	82.5	17.441	13.828	27.571	2.132
R123	Sub	2.74	170.4	91.65	88.8	16.483	14.732	30.469	2.402
R1234yf*	Super	8.03	203.0	46.67	80.0	17.464	15.009	33.611	2.649
R1234ze*	Super	9.56	194.7	101.20	81.1	17.461	14.311	31.482	2.481
R142b*	Super	7.02	196.1	85.38	85.4	17.315	15.302	34.156	2.692

Cycle Fluid	Sub- or super- critical	$P_{t,in}$ (MPa	$T_{t,in}$ (ºC)	$\dot{m}_{cf}$ (kg/s)	$T_{gb,out}$ (ºC)	$\dot{Q}_{out}$ (MWth)	$\eta_{th,cycle}$ (%)	η_u (%)	$\dot{W}_{net}$ (MW$_e$)
R143a	Super	10.00^	201.0	87.05	86.9	17.122	12.449	25.268	1.992
R152a	Super	9.76	198.2	65.19	80.0	17.433	15.134	33.955	2.676
R245ca	Super	5.37	197.5	82.18	81.3	17.298	15.370	32.005	2.475
R245fa	Super	6.41	195.8	91.65	83.2	17.016	15.650	32.177	2.488

*Fluid T_{UL} specified as below 220 ºC in REFPROP 9.1, but with T_{UL} modified in REFPROP .FLD files to allow unhindered analysis. If T_{UL} limits stated are in fact the thermal stability limit, then the fluid would not be used for risk of hot spots in the heat exchanger leading to deterioration of the fluid.

^Optimum solution found at upper limit of allowable range for that optimisation, either from inefficient subcritical conditions with peak efficiency at upper limit before critical pressure, or due to reaching the 10 MPa pressure upper limit for supercritical cycles.

The results from the recuperated ORC analysis given in Table 22 show an increase in $\dot{W}_{net}$ and η_{th} from the basic ORC cycle, to varying degrees. However, the increased brine heat exchanger inlet temperature results in a lower turbine inlet temperature because, as is shown below in Figure 46, the temperature profiles for the basic cycles are already well matched with ΔT_{pp} = 6.54 ºC and $LMTD$ = 10.0 ºC. To preheat the cycle fluid prior to inlet to the brine heat exchanger requires increasing the brine outlet temperature, and the decreasing the turbine inlet temperature in order to maintain to maintain the ΔT_{LM} and ΔT_{pp} constraints and, while it may improve cycle efficiency it provides little benefit to the net power generation.
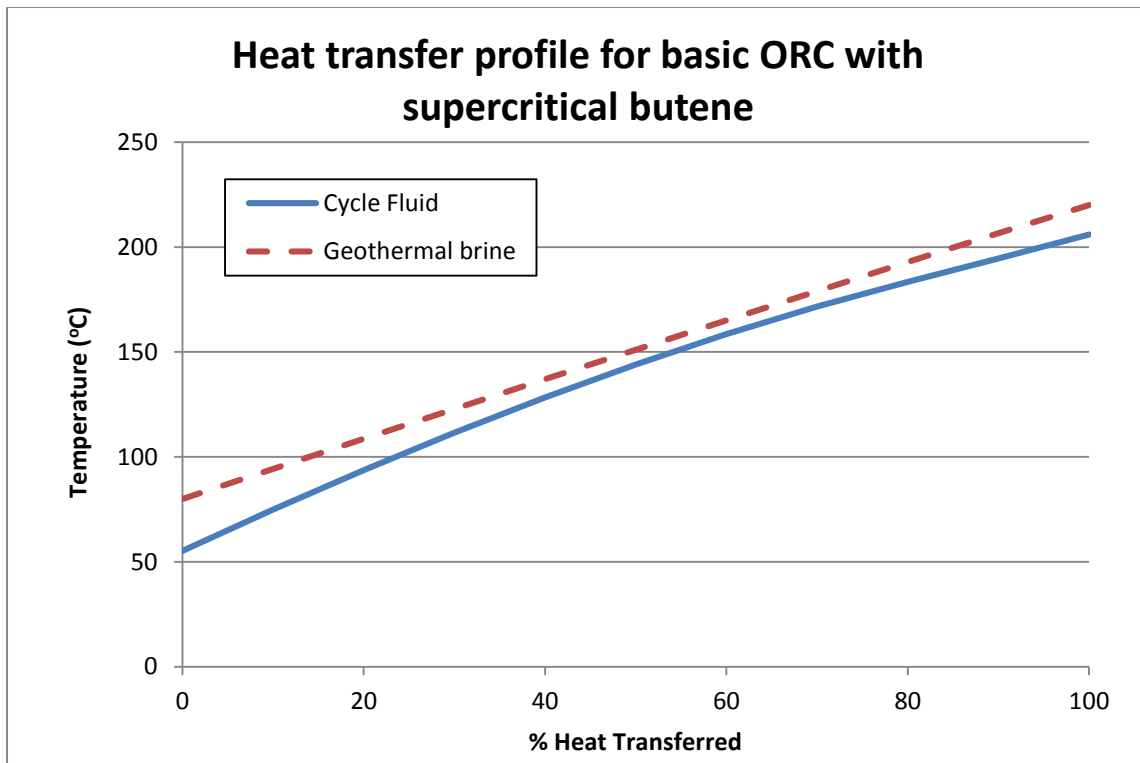
Figure 46: Q-T diagram of supercritical basic ORC with Butene.

The heat transfer process for the basic ORC is already very effective in most cases, particularly the supercritical cycles, with the majority of these being very close to the 10 ºC LMTD limitation, as illustrated in Figure 46. This shows that the fluid heat transfer profiles are already well matched in the basic ORC and adding a recuperator may require increasing the brine outlet temperature, or decreasing the turbine inlet temperature and / or pressure, which leads to a decrease in net power generation.

The recuperator provides varying degrees of benefit. This is because the benefit the recuperator can provide is limited by the amount of pre-heating the cycle fluid can utilise before it causes either ΔT_{pp} in the brine heat exchanger to be too small or a temperature cross over. To further utilise any more heat in the recuperator will result in extracting less heat from the brine and this would result in a lower utilisation efficiency.

3.3.3 Regenerative ORC

The characteristic aspect of the regenerative cycle is the addition of the open feed fluid heater, and the two stage expansion with a separate high pressure turbine (HPT) and low pressure turbine (LPT) as shown below in Figure 47. The cycle uses all the same constraints as for the basic ORC: evaporator outlet temperature and pressure, condensing temperature and pump inlet thermal subcooling with the following additional settings:

- Open feed fluid heater inlet pressures are equal. This pressure is set by the use of a free variable to represent pressure ratio between HPT and LPT inlet pressures. This is used as an optimisation variable.

- The regeneration rate y, which is the proportion of mass flow rate redirected, at the split between the HPT and LPTs, to the open feed fluid heater. This is also used as an optimisation variable.
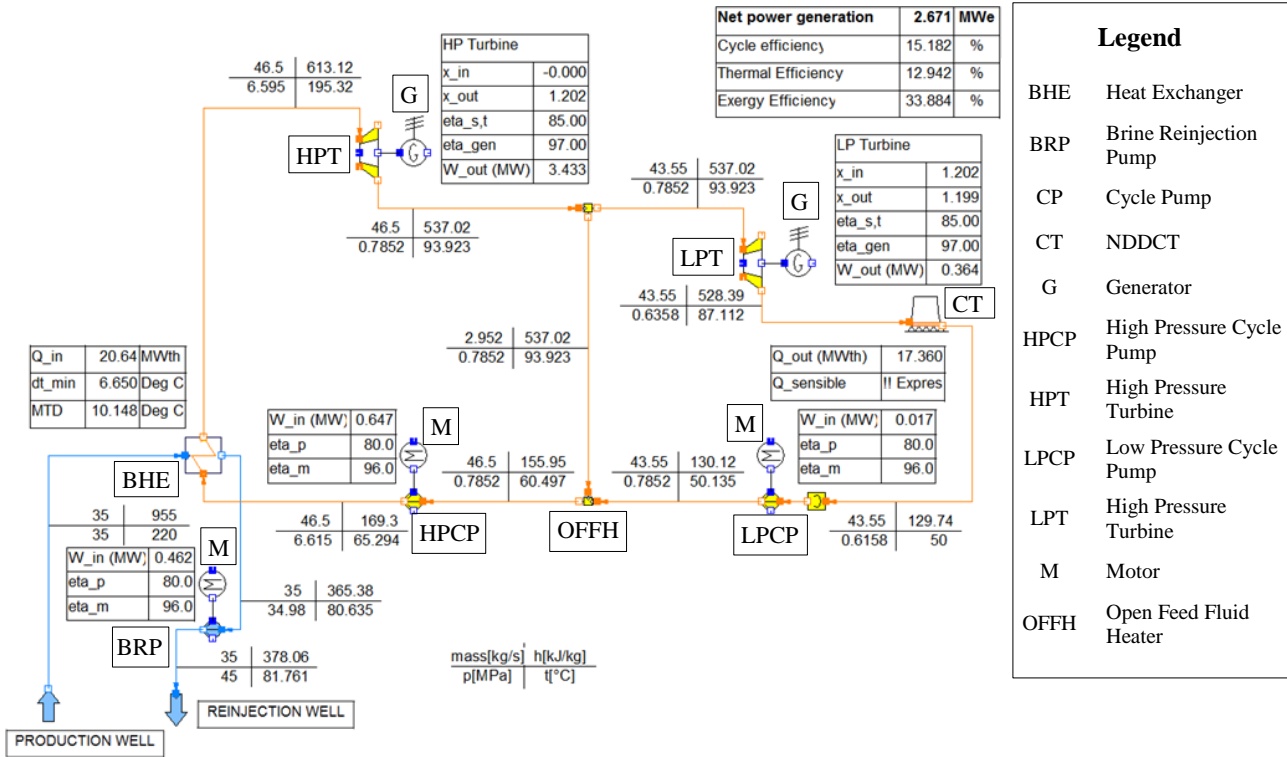
Figure 47: Regenerative ORC model in IPSEpro, shown here for supercritical butene.

The default decision variables for the optimisation of the regenerative ORC are presented in Table 23.

Table 23: Default decision variables used for the optimisation of the regenerative ORC using a genetic algorithm, the subscript opt,basic refers to the value found in the basic ORC analysis.

Variable	Units	Minimum	Maximum	Bit/Interval
Turbine inlet temperature	ºC	$T_{opt,basic}$ - 15	$T_{opt,basic}$ + 15	7 / 0.234
Turbine inlet pressure	MPa	$P_{opt,basic}$ - 1	$P_{opt,basic}$ + 1	7 / 0.0156
Pressure ratio between high and low pressure turbine inlet, r_p	--	0.1	0.3	6 / 0.00938
Split ratio mass flow rate, y	--	0.0	0.3	6 / 0.0078
Brine outlet temperature	ºC	80	90	7 / 0.1172

Initial analysis of the cycle using a maximum of 0.7 for r_p and y showed that all fluids had an optimum at less than 0.2 for both r_p and y. So an upper limit of 0.3 was used for all optimisations to allow an increase in resolution, as cycle performance is very sensitive to variation of these two variables. The same staged optimisation method as for the basic ORC was used.

Table 24 lists the thermodynamic conditions found by the GA to maximise power generation for the regenerative cycle. Again, only the higher performing fluids from the basic ORC analysis are considered here.

Table 24: Preliminary analysis results for the regenerative ORC optimised for each candidate fluid, for conditions given in Table 1.

Cycle Fluid	Sub- or super- critical	$P_{HPT,in}$ (MPa)	$T_{HPT,in}$ (ºC)	$\dot{m}_{cf,HPT}$ (kg/s)	$P_{LPT,in}$ (MPa)	$T_{LPT,in}$ (ºC)	$\dot{m}_{cf,LPT}$ (kg/s)	$T_{gb,out}$ (ºC)	$\eta_{th,cycle}$ (%)	η_u (%)	$\dot{W}_{net}$ (MWe)
Butane	Super	6.83	196.7	46.83	0.68	92.8	43.11	80.0	15.04	33.69	2.655
Butene	Super	6.60	195.3	46.50	0.79	93.92	43.55	80.6	15.18	33.88	2.671
Cyclopropane*	Super	9.94	199.8	40.40	2.16	111.4	39.43	81.3	15.07	33.41	2.633
Isobutane	Super	8.02	199.5	47.89	0.94	106.7	44.01	80.3	14.39	31.88	2.513
Isobutene	Super	8.15	204.1	45.35	0.93	98.6	43.33	80.9	15.02	33.39	2.631
Isopentane	Sub	2.49	167.9	44.95	0.39	108.3	42.03	80.7	14.57	32.27	2.544
Neopentane	Super	5.52	192.1	55.75	0.70	105.4	47.56	82.1	14.44	31.56	2.488
Pentane	Sub	1.88	159.7	41.22	0.30	107.2	39.51	83.7	14.15	30.36	2.393
Propane	Super	10.00^	200.7	44.59	2.43	128.8	41.05	80.0	13.15	28.71	2.263
R123	Sub	2.13	151.4	103.10	0.35	85.6	96.87	82.2	14.31	31.19	2.458
R1234yf*	Super	10.00^	207.9	91.01	1.73	135.4	84.94	80.1	12.57	27.17	2.141
R1234ze*	Super	9.84	209.1	86.53	1.38	125.3	79.94	82.9	13.87	29.89	2.356
R142b*	Super	6.73	193.2	86.63	0.97	95.5	79.62	80.0	15.13	33.92	2.674
R143a	Super	10.0^	209.9	80.90	2.86	149.2	74.76	80.0	11.39	24.09	1.899
R152a	Super	9.48	206.9	58.96	1.95	117.3	56.34	80.3	14.97	33.42	2.634
R245ca*	Super	6.48	208.1	76.52	0.80	112.0	75.29	83.3	15.25	33.31	2.625
R245fa*	Super	6.75	197.2	92.10	0.53	92.2	83.33	80.0	15.23	34.19	2.695

*Fluid T_{UL} specified as below 220 ºC in REFPROP 9.1, but with T_{UL} modified in REFPROP .FLD files to allow unhindered analysis. If T_{UL} limits stated are in fact the thermal stability limit, then the fluid would not be used for risk of hot spots in the heat exchanger leading to deterioration of the fluid.

^Optimum solution found at upper limit of allowable range for that optimisation, either from inefficient subcritical conditions with peak efficiency at upper limit before critical pressure, or due to reaching the 10 MPa pressure upper limit for supercritical cycles.

The majority of these results show an increase in $\dot{W}_{net}$ over the basic ORC results for the respective fluids.

3.3.4 Dual Fluid ORC

The combinations of working fluid selection are critical to finding high performance from the dual fluid cycle. The general approach outlined in Section 2.2, suggests that the ideal fluids for the high temperature loop (HTL) would be, as for the basic ORC, those with a T_{cr} approaching but below the brine inlet temperature. The condensing temperature of the HTL becomes a decision variable for optimisation and this is the target temperature for the T_{cr} of the low temperature loop (LTL) fluid. So it is be assumed that the condensing temperature should range between 70 ºC to 100 ºC, and then LTL evaporation temperature is slightly lower than that, as determined by the heat transfer process.
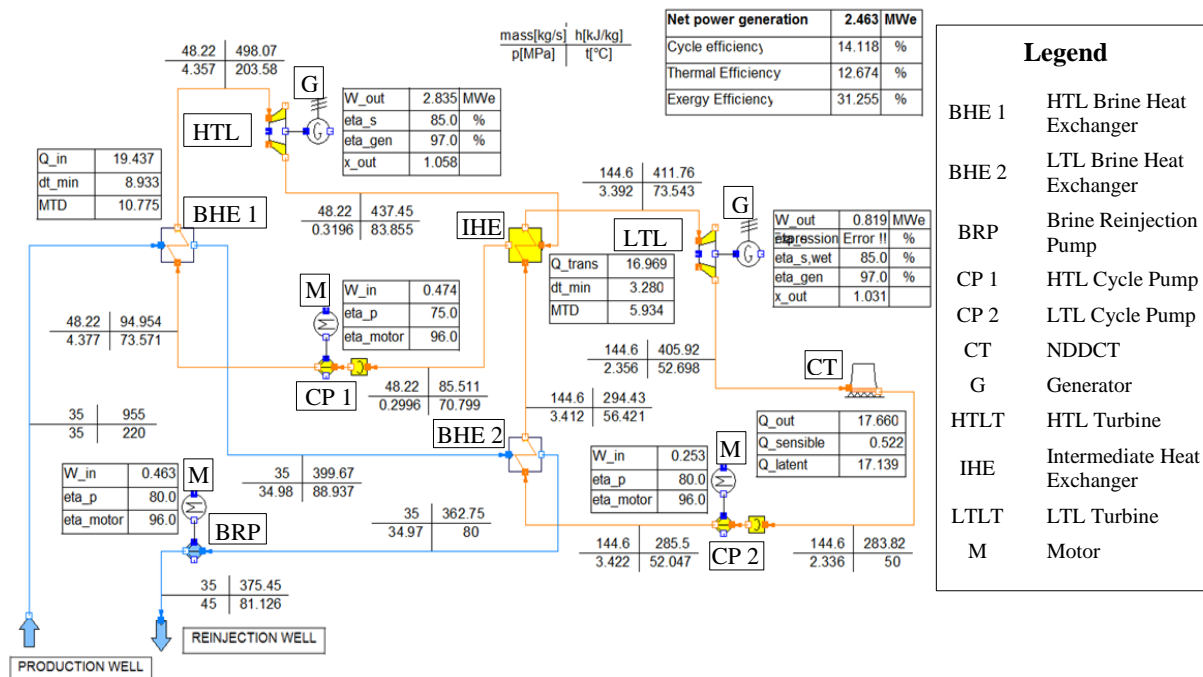
Figure 48: Dual fluid ORC configuration used in IPSEpro model, using a preheater in the secondary cycle to utilise the low temperature heat from the brine. Shown here with pentane in the HTL and R143a in the LTL.

There are a large number of potential fluid combinations that could be analysed for the dual fluid cycle. In order to better target the analysis the fluids are categorised according to suitability as HTL or LTL fluids. Fluid classifications are presented below in Table 25. These classifications are according to the critical temperature guidelines in Section 3.2, and fluids

are filtered according to their performance in the basic ORC analysis, only the higher potential fluids are selected for consideration here.

Table 25: Fluid classifications for dual fluid ORC according to critical temperature and fluid performance in basic ORC.

Higher T_{cr} suitable for HTL fluids	Lower T_{cr} suitable for LTL fluids
Pentane	R227ea
Isopentane	R134a
Butene	Propane
R152a	R1234yf
Isobutene	R143a
Butane	R125
Pentane	R227ea
R123	R152a

The HTL and LTL cycles are both constrained by turbine inlet temperature and pressure and the LTL condensing temperature is again set to 50 °C. The condenser for the HTL is to be the evaporator for the LTL, so the evaporating temperature of the HTL is used as a decision variable.

For the fluids considered the LTL evaporator operating pressures will be within the allowable range for PHEs, which allows the use of lower heat transfer process limits. The lower ΔT_{pp} and ΔT_{LM} of 3 °C and 8 °C respectively are used for this heat exchanger. The decision variables are summarised below in Table 26.

Table 26: Default decision variables used for the optimisation of the dual fluid ORC using a genetic algorithm, the subscript opt,basic refers to the values found in the basic ORC analysis.

Variable	Units	Minimum	Maximum	Bit/Interval
HTL turbine inlet pressure	MPa	$P_{opt,basic}$ - 1	$P_{opt,basic}$ + 1	7 / 0.0156
Turbine inlet temperature	°C	$T_{opt,basic}$ - 15	$T_{opt,basic}$ + 15	7 / 0.234
LTL turbine inlet pressure	MPa	P_{cd}	P_{cr}	7 / 0.0094
LTL turbine inlet temperature	°C	60	90	7 / 0.234
HTL condensing temperature	°C	70	100	7 / 0.234
Brine temperature between HTL evaporator and LTL preheater	°C	80	110	7 / 0.234

The thermodynamic conditions found by the GA to maximise power generation of the dual fluid ORC for selected fluids combinations are given below in Table 27.

Table 27: Preliminary analysis results for the dual fluid ORC optimised for each candidate fluid for conditions given in Table 1, where subscript HPT and LPT refer to high pressure turbine and low pressure turbine respectively.

HTL Cycle Fluid	LTL Cycle Fluid	$P_{HPT,in}$ (MPa)	$T_{HPT,in}$ (ºC)	$\dot{m}_{cf,HPT}$ (kg/s)	$P_{LPT,in}$ (MPa)	$T_{LPT,in}$ (ºC)	$\dot{m}_{cf,LPT}$ (kg/s)	$\eta_{th,HTL}$ (%)	$\eta_{u,LTL}$ (%)	$\eta_{th,cycle}$ (%)	η_u (%)	$\dot{W}_{net}$ (MWe)
Butane	R1234yf	6.04	198.7	41.5	2.08	87.9	120.5	11.48	3.83	13.72	30.21	2.38
Butane	R227ea	6.58	199.2	43.1	1.70	79.6	167.4	10.71	4.51	13.28	29.05	2.29
Butene	R125	7.21	198.2	47.1	2.87	63.2	203.6	12.85	0.87	13.35	29.22	2.30
Butene	R152a	6.25	194.5	45.2	1.70	68.0	72.3	11.60	2.96	13.31	29.11	2.29
Butene	R227ea	5.71	209.1	44.9	1.85	79.8	175.0	10.49	5.08	13.01	28.30	2.23
Isobutene	R134a	6.88	200.2	43.2	1.90	85.0	101.3	11.73	2.98	13.29	29.05	2.29
Isopentane	R227ea	2.75	174.3	43.5	1.84	87.6	158.9	10.28	5.06	13.26	28.98	2.28
Pentane	R125	1.93	161.2	41.1	3.65	69.9	240.0	11.55	2.53	12.79	27.77	2.19
Pentane	R143a	1.85	158.8	41.6	3.60	75.8	152.1	10.61	3.44	12.48	26.95	2.12
Pentane	R143a	2.55	178.5	36.1	4.40	87.9	152.5	10.69	4.60	12.24	26.33	2.08
Pentane	R143a	2.55	178.5	36.4	5.00	95.4	152.8	9.98	5.18	12.01	25.72	2.03
R123	Propane	2.93	175.2	86.7	2.40	72.5	59.8	12.23	3.05	12.98	28.26	2.23
R123	R227ea	2.87	170.9	94.8	1.59	76.5	168.9	11.46	4.08	13.32	29.15	2.30

The dual fluid cycle would appear to be a thermodynamically promising cycle configuration; however the results found here do not show an improvement over the basic cycle configuration in terms of net power generation.

The results shown in Table 27 appear to indicate that an increase in either HTL or LTL efficiency comes at the expense of reducing the efficiency of the other. This suggests that there may be a limit to the achievable overall thermal efficiency, which is restricted for the dual fluid cycle due to the exergy loss in the additional heat transfer process between the HTL and LTL.

Presumably, the benefit of dual fluid configuration may be better realised for a higher resource temperature, where other cycle configurations do not span the temperature range as effectively from resource temperature to ambient temperature as effectively as they do for the temperature range considered in this work.

3.4 Summary and Selection of Finalist Candidate Cycles

The following table presents a ranked list of the highest performing 30 cycles by net power generation.

Table 28: Overall ranking of cycles from preliminary analysis, for the geothermal brine inlet conditions given in Table 1.

Cycle Fluid	Cycle type	Sub- or Super-critical	$P_{turb,in}$ (MPa)	$T_{turb,in}$ (ºC)	$\dot{m}_{cf}$ (kg/s)	η_{th} (%)	η_u (%)	$\dot{W}_{net}$ (MWe)
R245fa*	Regenerative	Super	6.754 / 0.53	197.2 / 92.2	92.1 / 83.33	15.228	34.188	2.695
R245ca*	Basic	Super	6.46	207.7	77.32	15.23	34.15	2.692
R142b*	Recuperated	Super	7.02	196.1	85.38	15.302	34.156	2.692
Butane	Recuperated	Super	6.63	194.2	48.1	15.267	34.108	2.688
Butene	Recuperated	Super	6.45	192.8	47.69	15.185	34.074	2.686
Isobutene	Recuperated	Super	6.61	192.1	48.05	15.154	33.992	2.679
R152a	Recuperated	Super	9.764	198.2	65.19	15.134	33.955	2.676
R142b*	Regenerative	Super	6.73 / 0.97	193.2 / 95.5	86.63 / 79.62	15.13	33.92	2.674
Butene	Regenerative	Super	6.595 / 0.785	195.3 / 93.9	46.5 / 43.55	15.182	33.884	2.671
Butane	Regenerative	Super	6.825 / 0.683	196.7 / 92.8	46.83 / 43.11	15.038	33.689	2.655
R1234yf*	Recuperated	Super	8.03	203.0	46.67	15.009	33.611	2.649
Cyclopropane*	Recuperated	Super	9.91	196.2	42.17	15.063	33.541	2.644
R152a	Regenerative	Super	9.480 / 1.954	206.9 / 117.3	58.96 / 56.34	14.97	33.42	2.634
Cyclopropane*	Regenerative	Super	9.937 / 2.158	199.8 / 111.4	40.4 / 39.43	15.066	33.406	2.633
Isobutene	Regenerative	Super	8.151 / 0.9251	204.1 / 98.6	45.35 / 43.33	15.023	33.386	2.631
R245fa*	Basic	Super	7.75	209.8	79.35	14.9	33.33	2.627
R245ca*	Regenerative	Super	6.476 / 0.799	208.1 / 112.0	76.52 / 75.29	15.25	33.31	2.625
Butene	Basic	Super	7.21	206.1	41.39	15.05	33.2	2.617
R152a	Basic	Super	10.0^	212.6	55.72	14.85	33.15	2.612
Isobutene	Basic	Super	8	206.5	42.64	14.82	33.12	2.611

Cycle Fluid	Cycle type	Sub- or Super-critical	$P_{turb,in}$ (MPa)	$T_{turb,in}$ (°C)	$\dot{m}_{cf}$ (kg/s)	η_{th} (%)	η_u (%)	$\dot{W}_{net}$ (MW$_e$)
Butane	Basic	Super	6.65	205	39.8	14.77	32.9	2.593
Isobutane	Recuperated	Super	7.252	189.4	52.89	14.721	32.79	2.584
Neopentane	Recuperated	Super	5.811	195.4	53.9	14.97	32.759	2.582
R245ca*	Basic	Sub	3.8^	184.3	73.01	14.65	32.67	2.575
R123	Basic	Sub	2.47	162.2	97.05	14.53	32.53	2.550
Isopentane	Regenerative	Sub	2.493 / 0.385	167.9 / 108.3	44.9 / 42.0	14.57	32.27	2.544
R142b*	Basic	Super	6.92	196	76.69	14.5	32.28	2.544
Isopentane	Recuperated	Sub	2.8	175.3	44.03	14.39	31.983	2.521
Isobutane	Regenerative	Super	8.016 / 0.942	199.5 / 106.7	47.89 / 44.01	14.386	31.884	2.513
Isopentane	Basic	Sub	3.2^	186.9	39.49	14.87	31.84	2.509
Neopentane	Regenerative	Super	5.516 / 0.696	192.1 / 105.4	55.75 / 47.56	14.438	31.561	2.488

*Fluid T_{UL} specified as below 220 °C in REFPROP 9.1, but with T_{UL} modified in REFPROP .FLD files to allow unhindered analysis. If T_{UL} limits stated are in fact the thermal stability limit, then the fluid would not be used for risk of hot spots in the heat exchanger leading to deterioration of the fluid.

The highest performing cycles from the preliminary analysis are supercritical cycles, with the highest performing subcritical cycle generating about 5% less net power. The critical temperatures of the highest performing supercritical fluids are in the range of 110 °C to 170°C. The high performing subcritical fluids have higher critical temperatures, ranging from 170 °C to 190 °C.

A number of these top 30 cycles have T_{UL} that is, according to REFPROP, below the brine inlet temperature. These cycles are not further considered in this work as the T_{UL} should first be verified, before they can be investigated any further.

The five highest performing cycles of each type are selected from Table 28 to progress to the detailed design stage, giving 15 finalist cycles; these are shown presented below in Table 29.

Table 29: Cycles selected from the preliminary analysis results to progress to the detailed design stage, for the geothermal brine inlet conditions given in Table 1.

Cycle Fluid	Cycle type	Sub- or Super-critical	$P_{turb,in}$ (MPa)	$T_{turb,in}$ (ºC)	$\dot{m}_{cf}$ (kg/s)	$\eta_{th,cycle}$ (%)	η_u (%)	$\dot{W}_{net}$ (MW$_e$)
Butane	Recuperated	Super	6.63	194.2	48.10	15.267	34.108	2.688
Butene	Recuperated	Super	6.45	192.8	47.69	15.185	34.074	2.686
Isobutene	Recuperated	Super	6.61	192.1	48.05	15.154	33.992	2.679
R152a	Recuperated	Super	9.764	198.2	65.19	15.134	33.955	2.676
Butene	Regenerative	Super	6.595 / 0.785	195.3 / 93.9	46.50 / 43.55	15.182	33.884	2.671
Butane	Regenerative	Super	6.825 / 0.683	196.7 / 92.8	46.83 / 43.11	15.038	33.689	2.655
R152a	Regenerative	Super	9.480 / 1.954	206.9 / 117.3	58.96 / 56.34	14.97	33.42	2.634
Isobutene	Regenerative	Super	8.151 / 0.9251	204.1 / 98.6	45.35 / 43.33	15.023	33.386	2.631
Butene	Basic	Super	7.21	206.1	41.39	15.05	33.2	2.617
R152a	Basic	Super	10.0^	212.6	55.72	14.85	33.15	2.612
Isobutene	Basic	Super	8	206.5	42.64	14.82	33.12	2.611
Butane	Basic	Super	6.65	205	39.80	14.77	32.9	2.593
Isobutane	Recuperated	Super	7.252	189.4	52.89	14.721	32.79	2.584
R123	Basic	Sub	2.47	162.2	97.05	14.53	32.53	2.55
Isopentane	Regenerative	Sub	2.493 / 0.385	167.9 / 108.3	44.95 / 42.03	14.57	32.27	2.544

4. IPSEPro Model Development

In order to perform the detailed cycle analysis a number of changes are required from the standard models available in IPSEpro and some entirely new models developed. The structure, solving methods and language of the software need to be understood to effectively modify or create component models. In the following section a brief overview of the software is presented.

4.1 IPSEpro Overview

IPSEpro is an open-equation process modelling environment which allows the user to create an equipment model library from the ground up, or load a pre-engineered model library and modify it as necessary. For this project the Enginomix Low Temperature Process (LTP) library is used. The LTP library was designed for modelling low temperature energy conversion processes and it refers to the REFPROP application for fluid properties. The LTP library provides a suitable base level library for preliminary cycle design calculations. A comparison of IPSEpro with the LTP library against Aspen HYSYS is presented in Appendix C. The two modules of IPSEPro that are used in this project are the PSE and MDK modules. These two modules will be discussed in the following sections.

4.1.1 PSE Module

The Process Simulation Environment (PSE) is a module of IPSEpro which is used to create process models using a library of components created in the MDK module. It consists of a flow sheet editor with drag and drop functionality for creating process flows and connections. All process data can be entered into relevant components/streams on the flow sheet and results can be set up to display on the flow sheet and/or be exported to data files.

A two-phase approach is used in solving the system of equations: first is the system analysis and second is the numerical solution phase. The system analysis phase determines the order and grouping with which to solve the system of equations. The approach used to the solving system of equations representing the process is perhaps one of the most characteristic features of IPSEpro. The approach is similar to that which an engineer would use to solve it using paper and pen, by grouping equations in a way that allows them to be solved one group at a time, but also keeping the group size to a minimum. This approach allows the number of equations that must be solved simultaneously to be kept to a minimum. A group will often

consist of a single variable and a single equation. So this method of solving allows relatively straightforward locating of the problem equations in the case of convergence issues.

The default method used in the numerical solution phase is the undamped Newton-Raphson method, but the user may select to use the damped Newton-Raphson method.

There are three types of items used in IPSEpro: units, connections and globals. Units are equipment items with inlets and outlets and behaviour defined by equations. Connections could be fluid streams, which would carry a fluid composition/identity and the fluid properties at that state point from one component to the next, or they could be mechanical shafts which transfer work from one unit to another. Finally, globals can be a fluid composition type, which holds the functions for calculating fluid properties, or can be a set of properties used in several different components or the like.
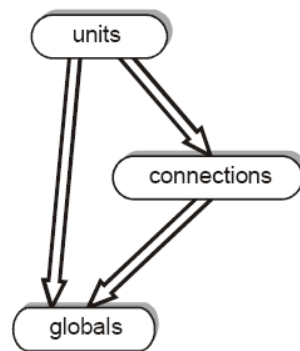
Figure 49: The hierarchy of model classes employed by IPSEpro (Simtech, 2014)

To illustrate, globals are not connected directly to any part of the process structure but can be referenced by any unit or connection. Units can access the inlet properties of a connection and then define outlet properties of a separate connection. Connections can refer to globals, for example to assign a fluid composition and then use the fluid property functions under that global.
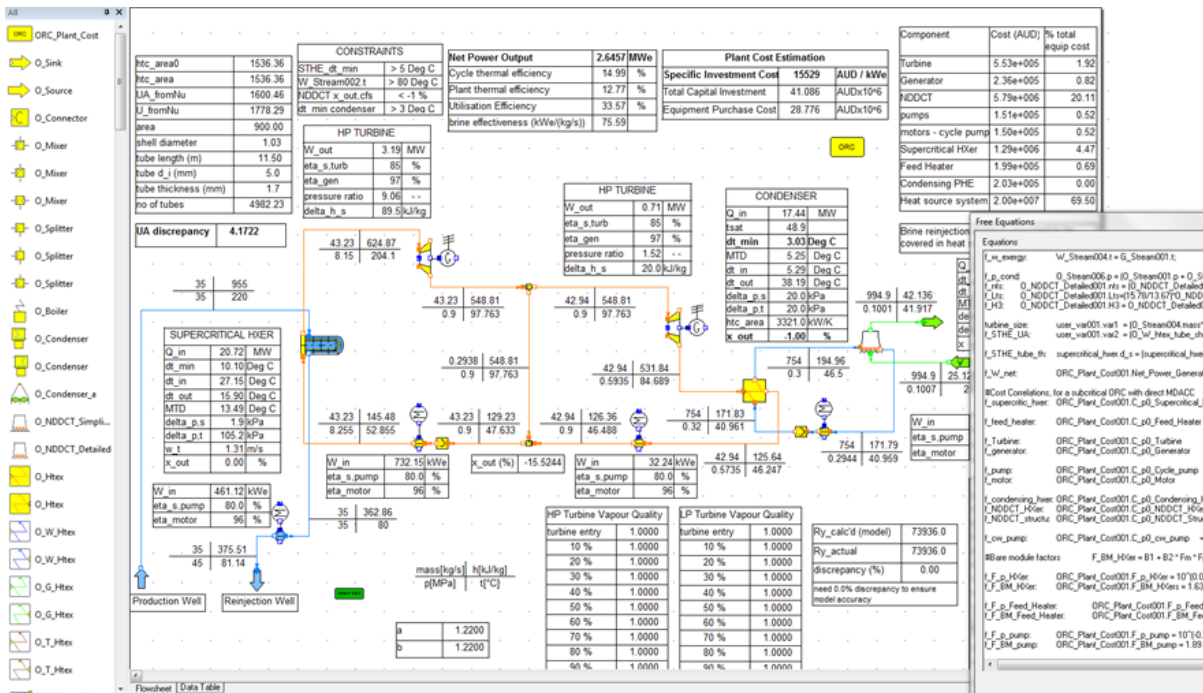
Figure 50: Screenshot of the PSE user interface, showing the free equations in the bottom right hand side.

Another useful feature of PSE is the free equations tool, which can be accessed and edited in the flow sheet to relate variables of any unit, connection, or global to any other unit, connection or global.

4.1.2 MDK Module

The Model Development Kit (MDK) module is used to build new model libraries or modify existing ones. The programming language used by IPSEpro MDK is the so called Model Description Language (MDL). MDL is a non-sequential equation oriented language. A model is defined by a block of equations and IPSEpro determines the optimum sequence to evaluate the equations. The user interface for MDK is shown below in Figure 51.

MDK does not require equations to be specified in terms of the variable to be solved for, since the variable being solved for may change depending on the configuration of specification of the process. However discontinuous equations can cause problems with divergence which can only be resolved by reformulating equations. For complex multi-variable equations this may not always be possible. There is one method that can be used to control convergence. MDK uses if statements to create branched equations, this is intended to be used to direct the solver to the relevant equations if a particular equation only applies within certain validity limits and another is used outside of those limits.
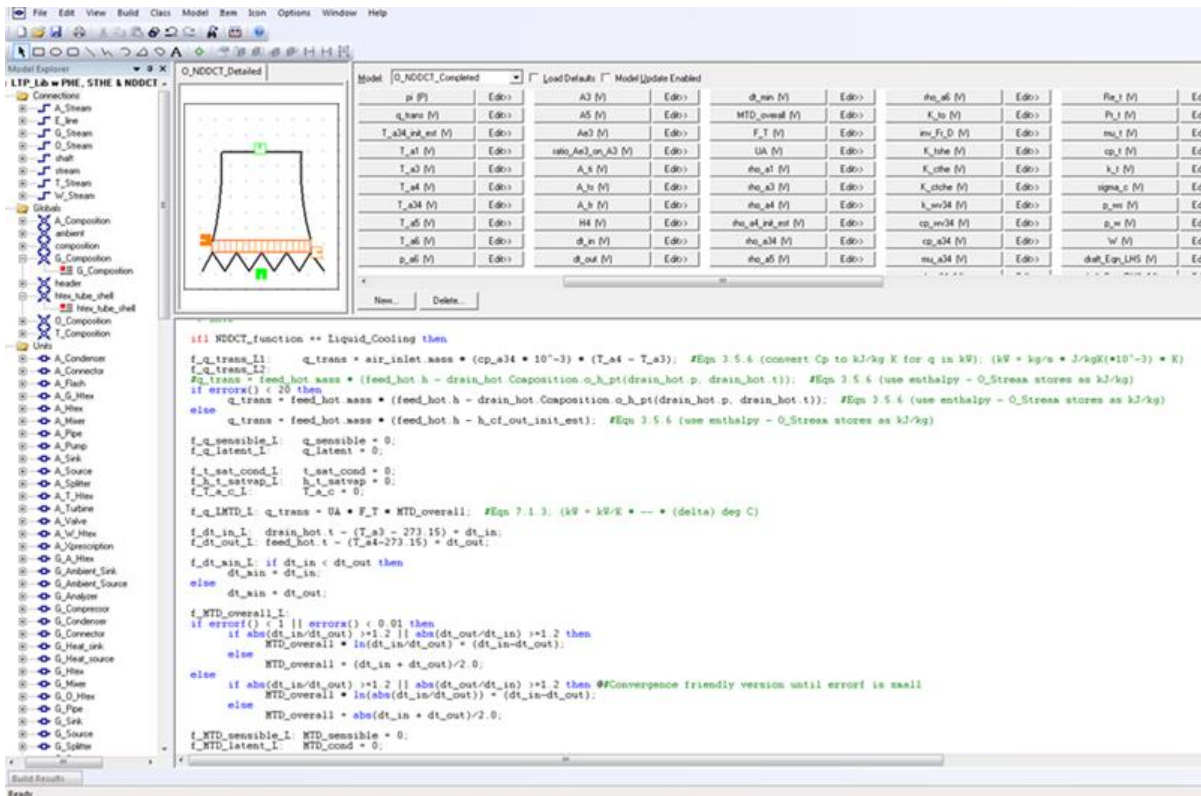
Figure 51: Screenshot of MDK user interface, showing user defined icon with inlet/outlets to connections, list of user declared variables and parameters, and description of equations in MDL.

IPSEpro uses system status functions for the norm of the error of the functions, and the variables, errorf and errorx. These status functions can be used to change the equation used as the system approaches a solution from a coarse to a more accurate function. This is useful in the above case, where a non-linear function is causing divergence issues. In the model testing phase, the problem equations can be identified and then this approach implemented and the threshold at which it switches functions can be calibrated by trial and error.

4.1.3 Process Optimisation with IPSEpro Using Genetic Algorithm

IPSEpro has an integrated optimisation module, PSOptimize, which minimises or maximises the nominated optimisation variable by varying selected decision variables within their specified range. PSOptimize uses the genetic algorithm (GA) optimisation technique. GAs are considered a more robust optimisation method than gradient based optimisation methods which can be misdirected by local optimum and discontinuous functions. GAs are more likely to find the global optimum in a given search space. The drawback of GAs is the relatively long calculation time. The PSOptimise Manual summarises the difference between GAs and classical optimisation methods as follows:

84

- Uses an initial population, randomly selected from across the solution space, rather than a single starting point,

- Selects solutions by the survival of the fittest, and

- Shows partly random behaviour instead of deterministic behaviour.

As a result of the process used, GAs generally produce slightly different solutions for separate runs for the same model.

There are a number of GA parameters that affect the effectiveness of the optimisation, they are population size, number of generations, probability of crossovers, and the probability of mutations.
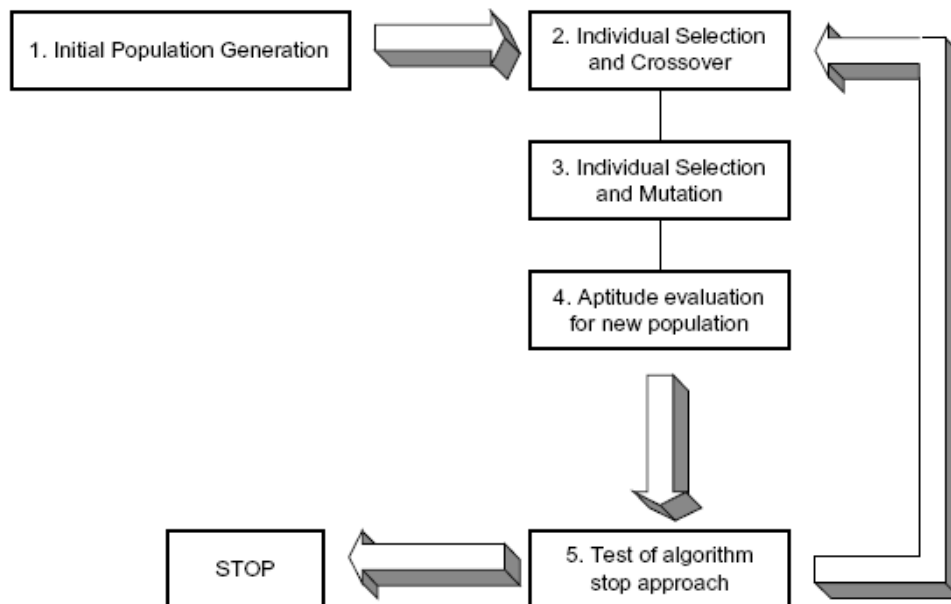
Figure 52: Diagram of GA operation for each generation (Ravagnani, Silva, Arroyo, & Constantino, 2005).

The values used for population and number of generations in this work depend on the stage of optimisation. In general, for preliminary stage optimisations a high population value and lower No. of generations is used to achieve wide coverage across the solution space. For more refined stages of optimisation reduced population size and higher number of generations is used over a narrower range of decisions variables. The default values of 0.6 and 0.002 are used for probability of crossovers and probability of mutations respectively.

For each decision variable the minimum and maximum values of the decision variable are prescribed. A bit value is also required, where the bit value determines the resolution to search within the specified range; the resolution is calculated using the following:

$$2^{bit} = No.\,of\,discrete\,values\,within\,specified\,range$$

The bit number is a significant consideration to ensure meaningful results for the optimisation. If the range is too wide and/or the bit rating is too small it will result in large intervals and a very coarse search across the solution space in that variable. To illustrate, a bit number of 4 gives 16 intervals across the specified range, whereas a bit number of 8 gives 256 intervals across the specified range. In preliminary optimisations lower bit numbers are used to find the approximate optimum for a given variable and in successive optimisations the range is narrowed and the bit number increased to increase the resolution.

4.2 NDDCT Model

4.2.1 Simplified NDDCT Model for Preliminary Analysis

This very simplified NDDCT model was developed to facilitate the preliminary analysis. It requires fully specified inlet and outlet conditions as well as a specified pressure drop to calculate the heat rejection load required for the cycle, at a specified condensing temperature.

$$\dot{Q}_{out} = \dot{m}_{cf}\left(h_{cf,i} - h_{cf,o}\right)$$
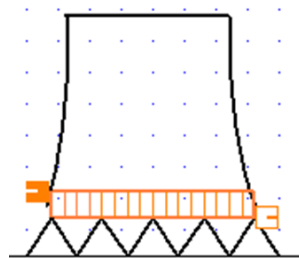
Figure 53: NDDCT model used in preliminary analysis, with only process fluid stream connections, no air stream inlet or outlet connections are used in this model.

In order to determine the influence of NDDCT performance on cycle performance, and to size the required tower a more detailed model was developed, which is presented in the following section.

4.2.2 Detailed Single Phase – Liquid Cooling NDDCT Model

This NDDCT model is based on the method of NDDCT analysis method presented by Kröger (2004). The model uses a one-dimensional analysis that balances the draft equation to determine the air flow rate and the cooling load based on the ambient conditions, the cycle fluid inlet conditions and the user specified NDDCT dimensions.
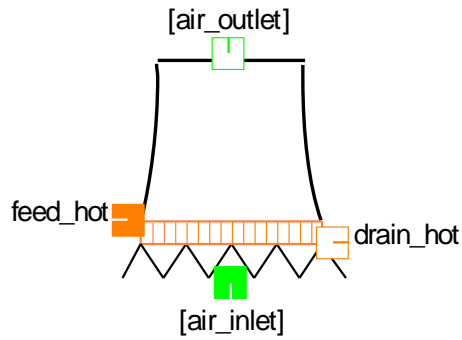
Figure 54: NDDCT model icon used in IPSEpro, with inlet and outlet streams for the cooling air flow.

The state point notation employed by Kroger (2004) is used and is shown below in Figure 55.
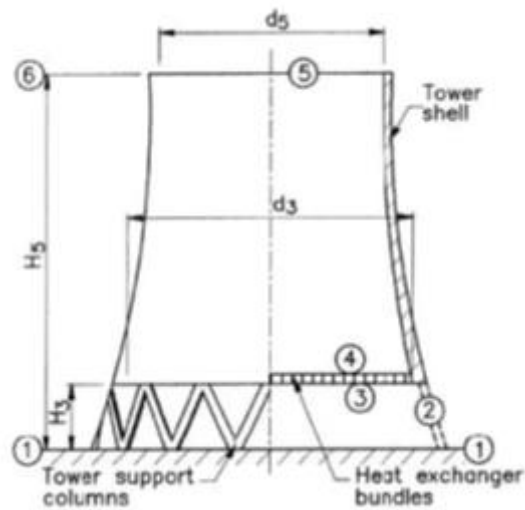
Figure 55: NDDCT schematic (Kröger, 2004).

The heat exchanger bundles used in this work are presented in Kroger (2004) and are characterised with experimental data. They are comprised of four rows of circular finned tubes with two fluid passes.
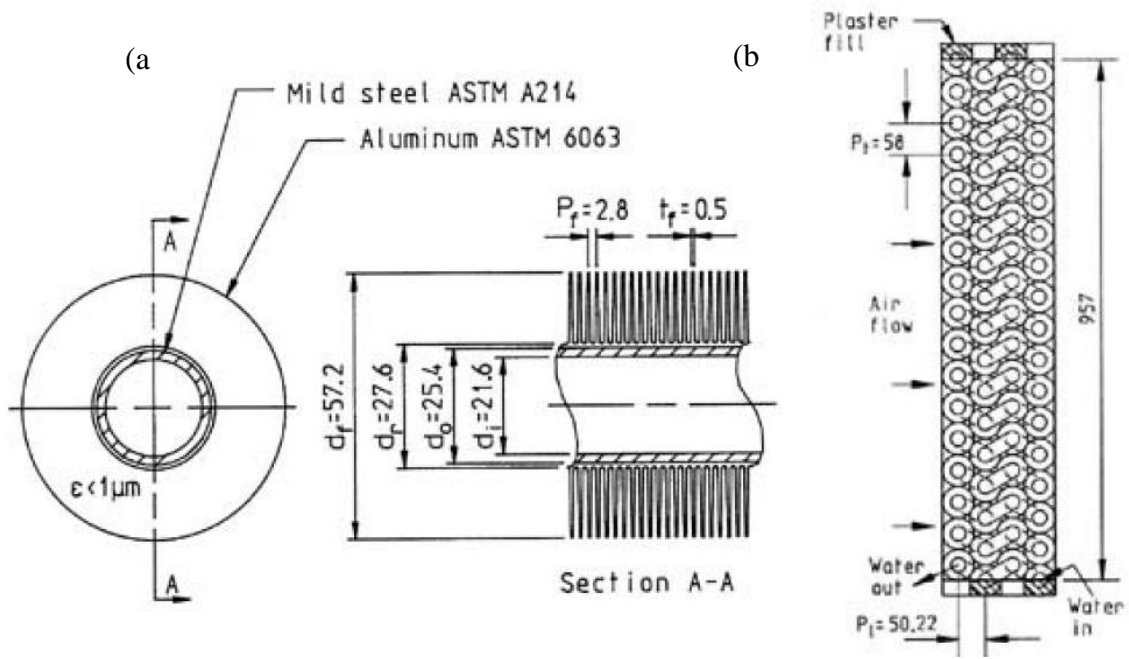
Figure 56: Heat exchanger bundle used in NDDCT analysis, (a) circular finned tube dimensions, and (b) heat exchanger bundle arrangement (Kroger 2004). All dimensions in mm.

The heat exchanger bundle geometry is summarised below in Table 30.

Table 30: Heat exchanger bundle and tube geometry (Kroger 2004)

Parameter	Value
Tube arrangement	Staggered
Number of tube rows, n_{rows}	4
Number of passes, n_p	2
Number of tubes per bundle, n_{tb}	154
Transversal tube pitch, P_{tr}	58 mm
Longitudinal tube pitch, P_l	50.22 mm
Length of finned tube, L_t	15 m
Effective length of finned tube, L_{te}	14.4 m
Effective frontal area per bundle, A_{frb}	32.573 m^2
Tube material	ASTM A214 mild steel
Fin Material	ASTM 6063 aluminium
Tube thermal conductivity, k_t	50 W/mK
Fin thermal conductivity, k_f	204 W/mK
Fin diameter, d_f	57.2 mm
Tube inner diameter, d_i	21.6 mm
Tube outer diameter, d_o	25.4 mm

Fin root diameter, d_r	27.6 mm
Fin tip thickness, t_{ft}	0.25 mm
Fin thickness (mean), t_f	0.5 mm
Fin root thickness, t_{fr}	0.75 mm
Fin pitch, P_f	2.80 mm
Fin surface roughness, ε_f	< 1 μm
Relative tube surface roughness, ε/d	5.24 x 10^{-4} m^2
Ratio of minimum to free stream flow area, σ	0.433

4.2.2.1 Draft Equation

The draft equation balances the buoyancy forces generated due to the heat transfer to the air, and the pressure drops of the air in the flow through the tower.

$$p_{a1}\left[\{1 - 0.00975(H_3 + H_4)/2T_{a1}\}^{3.5}\left\{1 - 0.00975\left(H_5 - \frac{H_3}{2} - \frac{H_4}{2}\right)/T_{a4}\right\}^{3.5}\right.$$

$$\left. - (1 - 0.00975H_5/T_{a1})^{3.5}\right]$$

$$= (K_{ts} + K_{ct} + K_{hes} + K_{ctc} + K_{he} + K_{cte})_{he}\left(\frac{\dot{m}_a}{A_{fr}}\right)^2\Big/(2\rho_{a34})\left[1\right.$$

$$\left. - 0.00975\left(H_5 - \frac{H_3}{2} - \frac{H_4}{2}\right)/T_{a4}\right]^{3.5} + (1 + K_{to})\left(\frac{\dot{m}_a}{A_5}\right)^2/2\rho_{a5}$$

Equation 44

where the K terms are the air side loss coefficients, evaluated at the mean density of the air flowing through the heat exchanger, ρ_{a34}, and are shown below in Figure 57.
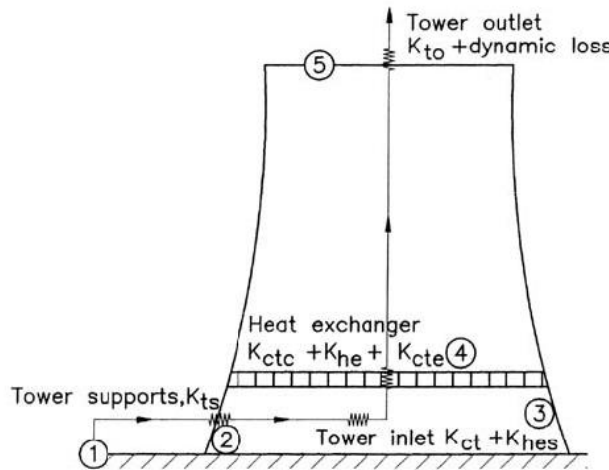
Figure 57: Diagram showing loss coefficients used in NDDCT analysis (Kröger, 2004).

The equations used to calculate these loss coefficients are summarised below in Table 31.

Table 31: Equations for calculation of air side loss coefficients for NDDCT (Kröger, 2004).

Loss coefficient for:	Equation	Eq No
Tower supports	$$K_{ts} = \frac{C_{Dts} L_{ts} d_{ts} n_{ts} A_{fr}^2}{(\pi d_3 H_3)^3}\left(\frac{\rho_{a34}}{\rho_{a1}}\right)$$	Equation 45
Inlet contraction	$$K_{ct} = 0.072\left(\frac{d_3}{H_3}\right)^2 - 0.34\left(\frac{d_3}{H_3}\right) + 1.7$$	Equation 46
Contraction at heat exchanger inlet	$$K_{ctc} = \left(1 - \frac{2}{\sigma_c} + \frac{1}{\sigma_c^2}\right)\left(\frac{\rho_{a34}}{\rho_{a3}}\right)\left(\frac{A_{fr}}{A_{e3}}\right)$$	Equation 47
Flow through heat exchanger	$$K_{he} = 1383.94795\left(\frac{\dot{m}_a}{\mu_{a34} A_{fr}}\right)^{-0.332458} + \frac{2}{\sigma^2}\frac{\rho_{a3} - \rho_{a4}}{\rho_{a3} + \rho_{a4}}$$	Equation 48
Expansion at heat exchanger outlet	$$K_{cte} = \left(1 - \frac{A_{fr}}{A_3}\right)^2\left(\frac{\rho_{a34}}{\rho_{a4}}\right)\left(\frac{A_{fr}}{A_{e3}}\right)^2$$	Equation 49
Tower outlet	$$K_{to} = -0.28\, Fr_D^{-1} + 0.04 Fr_D^{-1.5}$$	Equation 50

For horizontal heat exchangers $A_{fr} = A_{e3}$. The contraction coefficient, σ, refers to the contraction from the heat exchanger inlet area, to the minimum flow area through the heat exchanger. Fr_D is the densimetric Froude number, which is defined as $Fr_D = (\dot{m}_a/A_5)^2/[\rho_{a5}(\rho_{a6} - \rho_{a5})gd_5]$. The contraction coefficient σ_c refers to the contraction from the tower inlet area to the frontal area of the heat exchangers, and is given by

$$\sigma_c = 0.6144517 + 4.56493 \times 10^{-2}\left(\frac{A_{fr}}{A3}\right) - 0.336651\left(\frac{A_{fr}}{A3}\right)^2 + 0.4082743\left(\frac{A_{fr}}{A3}\right)^3$$
$$+ 2.670410\left(\frac{A_{fr}}{A3}\right)^4 - 5.963169\left(\frac{A_{fr}}{A3}\right)^5 + 3.558944\left(\frac{A_{fr}}{A3}\right)^6$$

Equation 51

4.2.2.2 Thermodynamics

The LMTD Method is used to determine the cooling water and air outlet temperature for the specified heat transfer surface area and calculated heat transfer coefficient, as described in Section 2.4. The temperature correction factor, F_T, is calculated for cross flow for a four row, two pass heat exchanger according to Kröger (2004).

$$F_T = 1 - \sum_{i=1}^{4}\sum_{k=1}^{4} a_{i,k}(1 - \varphi_{cf})^k \sin\left(2i\, arctan\frac{\varphi_h}{\varphi_c}\right)$$

Equation 52

Where φ_c and φ_h are dimensionless temperature changes of the cycle fluid and air, and φ_{cf} is a dimensionless form of mean temperature difference; these are given by

$$\varphi_h = \frac{T_{cf,i} - T_{cf,o}}{T_{cf,i} - T_{a,i}}$$

Equation 53

$$\varphi_c = \frac{T_{a,o} - T_{a,i}}{T_{cf,i} - T_{a,i}}$$

Equation 54

and

$$\varphi_{cf} = \frac{\Delta T_{LM}}{T_{cf,i} - T_{a,i}} = \frac{\varphi_h - \varphi_c}{\ln[(1 - \varphi_c)/(1 - \varphi_h)]}$$

Equation 55

The values for the empirical constant $a_{i,k}$ are given in below in Table 33.

Table 32: Values for empirical constant $a_{i,k}$ for cross flow for a two pass four row heat exchanger (Kröger, 2004).

$a_{i,k}$	$i = 1$	2	3	4
$k = 1$	-6.05 x 10^{-1}	2.31 x 10^{-2}	2.94 x 10^{-1}	1.98 x 10^{-2}
2	4.34 x 10^0	5.90 x 10^{-3}	-1.99 x 10^0	-3.05 x 10^{-1}
3	-9.72 x 10^0	-2.48 x 10^{-1}	4.32 x 10^0	8.97 x 10^{-1}
4	7.54 x 10^0	2.87 x 10^{-1}	-3.00 x 10^0	-7.31 x 10^{-1}

4.2.2.3 Heat transfer

The heat exchanger bundle used in this work is well defined by Kroger (2004) and the characteristic heat transfer parameter is presented based on experimental data. This is used in calculating the airside heat transfer performance. The product of the heat transfer area and the overall heat transfer coefficient is given by

$$\frac{1}{UA} = \frac{1}{h_{ae}A_a} + \frac{1}{h_{cw}A_{cw}}$$

Equation 56

The characteristic heat transfer parameter is defined by Kroger (2004) as:

$$Ny = \frac{h_e A}{k A_{fr} Pr^{0.333}}$$

Equation 57

Rearranging

$$h_e A = Ny k A_{fr} Pr^{0.333} \left(\frac{n_{tb,actual}}{n_{tb,maximum}} \right)$$

Equation 58

91

where $n_{tb,actual}/n_{tb,maximum}$ is to correct for the reduced effectiveness of the tubes at the bundle ends, as shown in Figure 56. Ny for normal non-isothermal flow through the specified heat exchanger bundles is given by

$$Ny = 383.617313\ Ry^{0.523761}$$

<div align="right">Equation 59</div>

where Ry is the characteristic flow parameter and is defined as:

$$Ry = \frac{\dot{m}_a}{\mu A_{fr}}$$

<div align="right">Equation 60</div>

The heat transfer coefficient inside the tubes is calculated via the correlation proposed by Gnielinski, as cited in Kroger (2004)

$$Nu = \frac{\frac{f_{Dt}}{8}(Re_{cw} - 1000)Pr_{cw}\left(1 + \frac{d_e}{L_{te}}\right)^{0.67}}{1 + 12.7\left(\frac{f_{Dt}}{8}\right)^{0.5}(Pr_{cw}^{0.67} - 1)}$$

<div align="right">Equation 61</div>

using the definition of the Nusselt number:

$$Nu = \frac{hd_e}{k}$$

<div align="right">Equation 62</div>

The friction factor inside the tubes, f_{Dt}, is calculated using the Colebrook equation

$$f_{Dt} = 0.3086\left[\log\left(\frac{6.9}{Re_{cw}} + \frac{\varepsilon/d}{3.7}\right)^{1.11}\right]^{-2}$$

<div align="right">Equation 63</div>

4.2.2.4 Pressure loss

The model used to calculate tube side pressure loss is adapted from the Enginomix STHE model in the EPP_Lib and is outlined in Section 4.4.2.2.

4.3 MDACT Model

The objective of modelling the MDACT in this project is to determine the electrical power input required to operate the fan(s), and to estimate the heat transfer area required to condense the fluid for use in the cost model.

4.3.1 Default MDACT Model

The default model uses the LMTD equation to determine the air flow rate required to achieve the specified cycle fluid outlet conditions. The model requires user specification of the air

side pressure drop, i.e., the pressure drop across heat exchanger and other flow resistances. The power consumption of the fan motor is highly sensitive to this value. However, this value depends entirely on the physical design of the MDACT and the heat exchangers and the assumption of a typical value would not provide a suitable degree of accuracy.
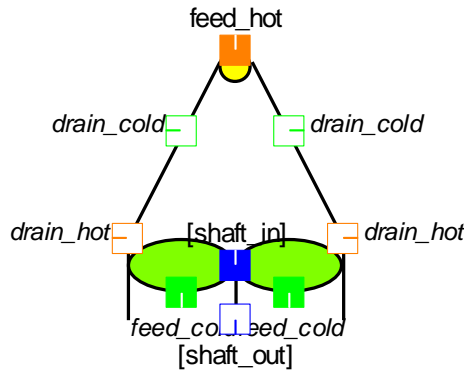
Figure 58: IPSEpro icon for air-cooled condenser.

In order to perform a meaningfully accurate analysis the pressure loss should be calculated for a specified heat exchanger design and the heat transfer performance of the heat exchanger design should be accounted for in the sizing design of the MDACT. The model used for this purpose is outlined in the following section.

4.3.2 Two-Phase Model of Direct Condensing MDACT

There are various arrangements available for MDACTs, the one used for this work is the single pass A-frame MDACT as shown below in Figure 59. The superheated vapour duct, labelled in the figure below as the steam header, distributes the cycle fluid vapour to the tubes and the condensate is collected in pipes at the bottom.
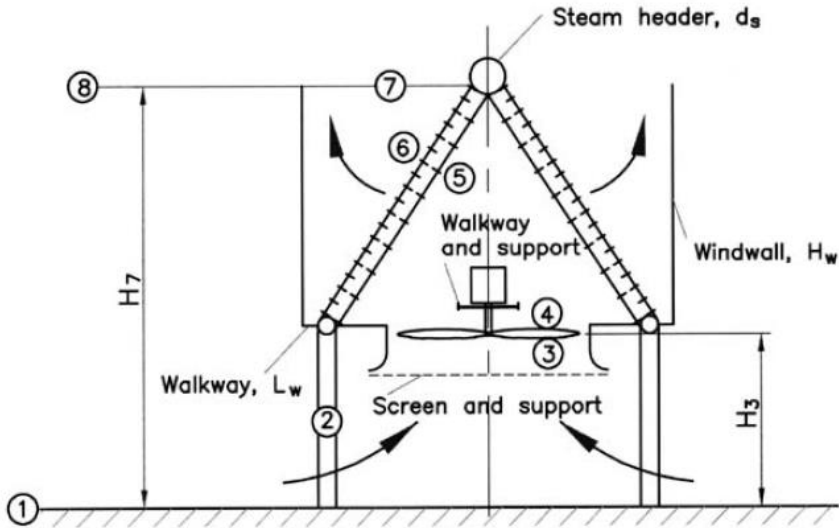
Figure 59: Mechanical draft air cooled condenser diagram (Kröger, 2004).

The heat exchanger is composed of several rows of staggered circular finned tubes as shown below in Figure 60.
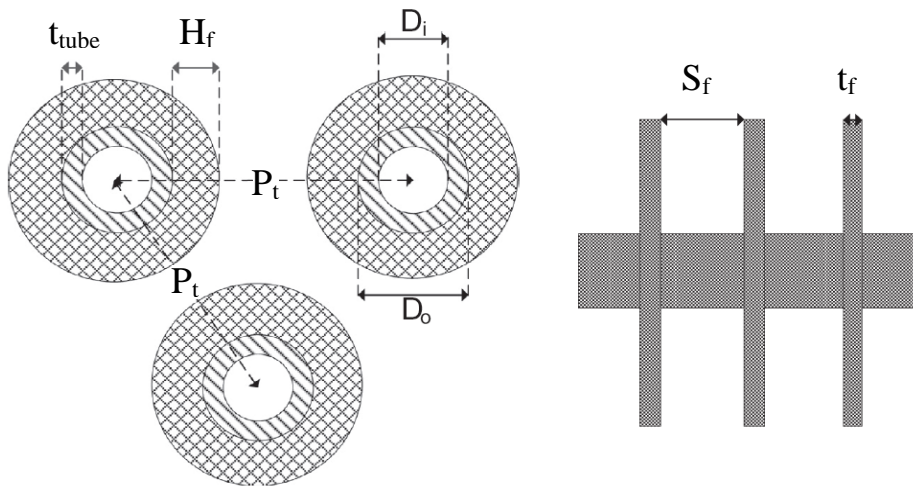
Figure 60: MDACT finned tube geometry, diagram taken from (Lecompte et al., 2013) with some notation modified for consistency, with the notation used in this work.

The internal surface area of the tubes is given by

$$A_i = n_t \, \pi d_i L_t$$

<div align="right">Equation 64</div>

The external surface area of the tubes is given by

$$A_o = \left(A_f + A_{root} \right) L_t n_t$$

<div align="right">Equation 65</div>

where L_t is the tube length, A_{fin} is the surface area of the fins per metre of tube and A_{root} is the free external tube surface area per metre of tube, and are given by

94

$$A_f = fpm \left(2\pi \left(\frac{d_o}{2} + H_f \right)^2 - \left(\frac{d_o}{2} \right)^2 + t_f \pi (d_o + 2H_f) \right)$$

<div align="right">**Equation 66**</div>

$$A_{root} = \pi \, d_o (1 - t_f fpm)$$

<div align="right">**Equation 67**</div>

where *fpm* is the fins per metre, the frontal area of the heat exchangers, which were used in calculating the pressure drop across the heat exchangers, is approximated by

$$A_{fr} = \frac{n_t}{n_{rows}} P_t L_t$$

<div align="right">**Equation 68**</div>

where P_t is the tube pitch. The bare tube surface area used for the cost estimation of the MDACT is given by

$$A_{bt} = n_t \, \pi d_o L_t$$

<div align="right">**Equation 69**</div>

4.3.2.1 Thermodynamics

There are two distinct regions of heat transfer in the MDACT, the sensible heat transfer region and the latent heat transfer region. This adds complication to the modelling of the process as compared to single phase heat exchangers.

It is difficult to accurately predict variation in vapour quality with length so average properties are used (Stewart, 2003). The use of average data for calculation of the condensation heat transfer coefficient is suitable for preliminary estimates of the required heat transfer area according to the VDI Heat Atlas (VDI, 2010).
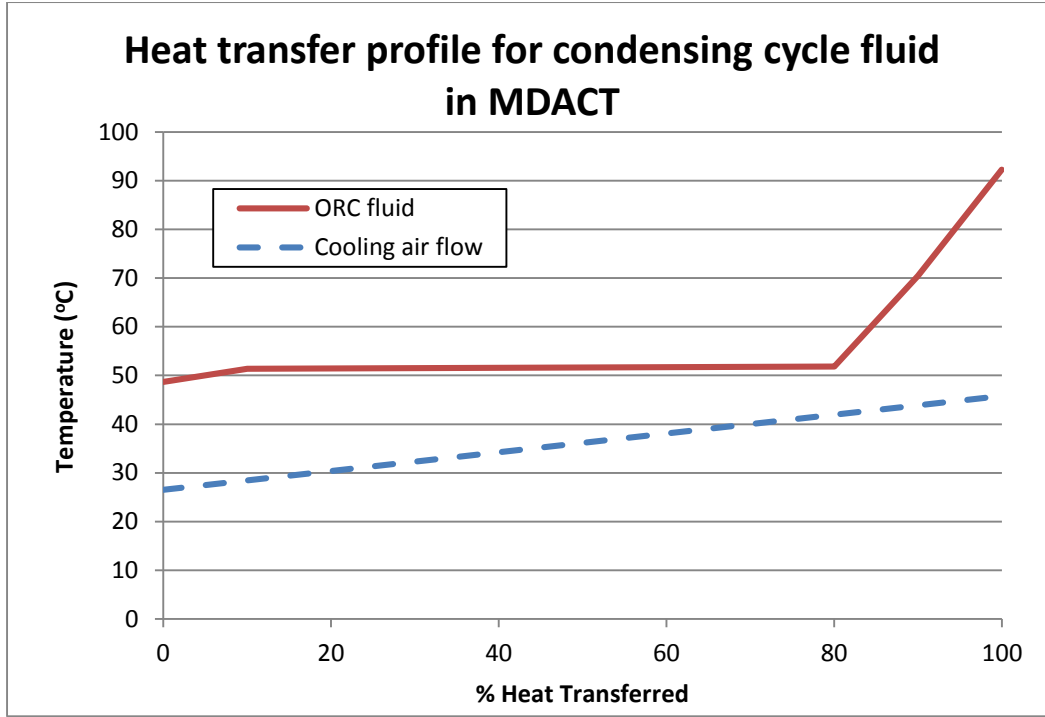
Figure 61: Heat transfer profile for a direct condensing MDACT.

The required air flow rate is found by applying an energy balance for specified air and cycle fluid inlet and outlet temperatures. The air-side heat transfer is given by:

$$\dot{Q} = \dot{m}_a c_{p,a}(T_{a6} - T_{a5})$$

<div align="right">Equation 70</div>

where T_{a5} is the air temperature at the fan outlet and $c_{p,a}$ is the average specific heat capacity of the air. The fan outlet conditions are determined via the isentropic compression efficiency of the fan, which is determined using the default model, based on an assumed value of fan isentropic efficiency:

$$\eta_s = \frac{h_{a,4} - h_{a,in}}{h_{a,4s} - h_{a,in}}$$

<div align="right">Equation 71</div>

The fan shaft power requirement is calculated as per the default IPSEpro model:

$$W_{in,fan} = m_a(h_{a,4} - h_{a,in}) = m_a \eta_s(h_{a,4s} - h_{a,in})$$

<div align="right">Equation 72</div>

The cycle fluid side heat transfer is given by

$$\dot{Q} = \dot{Q}_{sensible} + \dot{Q}_{latent} = \dot{m}_{cf}(h_{cf,in} - h_{cf,g}) + \dot{m}_{cf}(h_{cf,g} - h_{cf,out})$$

<div align="right">Equation 73</div>

The mean temperature difference is calculated using an IPSEpro function which calculates the temperature at a specified number of slices. The UA value required for the specified heat transfer process is found using the Log Mean Temperature Difference method as described in

<div align="center">96</div>

Section 2.4. F_T is calculated for cross flow with three or four row single pass tubes according to Kröger (2004).

The values for the empirical constant $a_{i,k}$ are given below in Table 33 and Table 34.

Table 33: Values for empirical constant $a_{i,k}$ for cross flow with three tube rows (Kröger, 2004).

$a_{i,k}$	$i = 1$	2	3	4
$k = 1$	-8.74 x 10^{-2}	-3.18 x 10^{-2}	-1.83 x 10^{-2}	7.1 x 10^{-3}
2	1.05	2.74 x 10^{-1}	1.23 x 10^{-1}	-4.99 x 10^{-2}
3	-2.45	-7.64 x 10^{-1}	-1.56 x 10^{-1}	1.09 x 10^{-1}
4	3.21	6.68 x 10^{-1}	6.17 x 10^{-2}	-7.46 x 10^{-2}

Table 34: Values for empirical constant $a_{i,k}$ for cross flow with four tube rows (Kröger, 2004).

$a_{i,k}$	$i = 1$	2	3	4
$k = 1$	-4.14 x 10^{-2}	-1.39 x 10^{-2}	-7.23 x 10^{-3}	6.10 x 10^{-3}
2	6.15 x 10^{-1}	1.23 x 10^{-1}	5.66 x 10^{-2}	-4.68 x 10^{-2}
3	-1.20	-3.45 x 10^{-1}	-4.37 x 10^{-2}	1.07 x 10^{-1}
4	2.06	3.18 x 10^{-1}	1.11 x 10^{-2}	-7.57 x 10^{-2}

4.3.2.2 Heat Transfer

The overall heat transfer coefficient is calculated, with reference to the tube inner diameter and neglecting fouling resistance, as:

$$\frac{1}{U} = \frac{t_t}{k_t} \frac{A_i \ln\left(\frac{d_o}{d_i}\right)}{2\pi L_t} + \frac{A_i}{h_a A_o \eta_o} + \frac{1}{h_{cf,av}}$$

Equation 74

Where k_t is the tube thermal conductivity,

h_a is the air side mean heat transfer coefficient,

η_o is the surface efficiency, and

$h_{cf,av}$ is the averaged heat transfer coefficient for the cycle fluid side.

The air side Nusselt number is calculated via the correlation proposed by Ganguli et al., as cited in (Kröger, 2004):

$$Nu_a = 0.38 \, Re_a^{0.6} \, Pr_a^{0.333} \left(\frac{A}{A_{root}}\right)^{-0.15}$$

Equation 75

Where A/A_{root} is the ratio of the total surface area to the exposed root surface area, Re_a and Pr_a are evaluated at mean air side properties and Reynolds number is given by:

$$Re_a = G_c d_r / \mu$$

<div align="right">Equation 76</div>

The mass velocity G_c is based on the minimum free flow area, A_c, which is given by:

$$A_c = A_{fr} - \frac{n_{tubes}}{n_{rows}} L_{te} fpm \left[t_f (d_o + 2H_f) + S_f d_o \right]$$

<div align="right">Equation 77</div>

The heat transfer correlations for the cycle fluid side sensible heat transfer region are from VDI Wärmeatlas (1988)   as presented in the STHE model in the Enginomix Power Plant Library for IPSEpro. The cycle fluid side Nusselt number for the sensible heat transfer region for $Re < 2300$ is given by

$$Nu_{cf,sens} = \left(3.66^3 + 1.61^3 \, Re_{cf,sens} \, Pr_{cf,sens} \frac{d_i}{L_{te}} \right)^{0.333}$$

<div align="right">Equation 78</div>

Where Re and Pr are evaluated at mean vapour properties. The Nusselt number for $Re > 2300$ is given by

$$Nu_{cf,sens} = \frac{\xi_{cf,sens}}{8} \left(Re_{cf,sens} - 1000 \right) Pr_{cf,sens} \frac{1 + \left(\frac{d_i}{L_{te}} \right)^{0.667}}{\left(1 + 12.7 * \sqrt{\frac{\xi_{cf,sens}}{8}} \left(Pr_{cf,sens}^{0.667} - 1 \right) \right)}$$

<div align="right">Equation 79</div>

Where the friction factor is $\xi_{cf,sens} = \left(1.82 \log(Re_{cf,sens}) - 1.64 \right)^{-2}$.

The Nusselt number in the latent heat transfer region is calculated using the correlation proposed by Akers and Rosson (1960):

$$Nu_{cf,latent} = 0.0265 \, Re_{latent}^{0.8} Pr_{latent}^{0.333}$$

<div align="right">Equation 80</div>

Where Re and Pr are evaluated at mean properties of the condensing region. The heat transfer coefficients are calculated using Equation 62 and the relevant Nusselt number.

4.3.2.3 Pressure Drop

The air-side pressure drop for normal flow through the heat exchangers is calculated with the correlation of Robinson and Briggs, as cited in Lecompte et al. (2013)

$$\Delta P_{he} = 18.03 \, n \frac{G_c^2}{\rho} Re_a^{-0.316} \left(\frac{p}{d_o}\right)^{-0.927}$$

Equation 81

where ρ and p are calculated at mean air properties through the heat exchanger.

Krogers relation for oblique flow through heat exchangers gives

$$\Delta P_{he\theta} = 0.5 \left(\frac{\dot{m}_a}{A_{fr}}\right) \left[\frac{K_{he}}{2}\left(\frac{1}{\rho_i}+\frac{1}{\rho_o}\right) + \frac{1}{\rho_i}\left(\frac{1}{\sin\theta_m}-1\right)\left(\left(\frac{1}{\sin\theta_m}-1\right) + 2K_{ci}^{0.5}\right) + \frac{K_d}{\rho_o}\right]$$

Equation 82

Where K_{he} is the loss coefficient for normal flow through the heat exchanger, K_{ci} is the inlet contraction coefficient and K_d is the downstream loss coefficient. K_{ci} is assumed to be 0.1, K_{he} and K_d are calculated as follows (Kröger, 2004):

$$K_{he} = \frac{\Delta p_{he}}{\rho_m w_m^2/2}$$

Equation 83

where Δp_{he} is given by Equation 81, ρ_m is the mean air velocity through the heat exchanger, and w_m is the mean velocity at the minimum flow area through the heat exchanger, i.e., $w_m = \dot{m}_a/\rho_a A_c$. K_d is calculated with the following empirical relation from Kroger (2004):

$$K_d = \exp(5.488405 - 0.2131209\theta + 3.533265 \times 10^{-3}\theta^2 - 0.2901016 \times 10^{-4}\theta^3)$$

Equation 84

where θ is the semi-apex angle in degrees.

There are a number of other flow losses that occur during the passage of air through the MDACT. These include losses due to tower supports, the upstream losses due to the safety screen and screen support beams, and downstream losses due to walkways and structural beams. Calculation of these losses require a degree of definition of the MDACT design which is beyond the scope of this project, so an assumed value will be used for these additional losses. In Kroger (2004) for a similar design problem these additional losses are approximately 40% of the heat exchanger losses. The total pressure drop through the MDACT used in this work is

$$\Delta p_{total} = 1.4 \times \Delta p_{he\theta}$$

Equation 85

This is the pressure rise required by the fan to force the required air flow rate through MDACT. The tube side pressure drop is calculated using the method presented in Section 4.4.2.2. This does not account for pressure drop in the distribution header.

4.4 Shell and Tube Heat Exchanger Model

4.4.1 Default Model

The default heat exchanger model in LTP_Lib uses the energy balance and log mean temperature difference (LMTD) equations as outlined in Section 2.6. The model solves the LMTD equation based on specified inlet and outlet conditions to give the required UA value for the heat transfer process. The ΔT_{LM} is calculated by default based on inlet and outlet conditions using Equation 8 but provides the option to calculate the mean temperature difference by calculating the temperature profile at a user specified number of slices via external functions stored in .dll files. This gives a more accurate value for the mean temperature difference, *MTD*, and ΔT_{pp}, which becomes quite significant for supercritical cycles, as the isobars deviate significantly from the idealised linear profile and calculation of the *MTD* based on inlet and outlet temperatures can significantly underestimate *MTD* and ΔT_{pp} values. The default model requires a user specified pressure drop for each fluid stream.

4.4.2 STHE Model

The Enginomix Power Plant Library (EPP_Lib) for IPSEpro, rather than the Low Temperature Process Library (LTP_Lib) which was used for this project, contains a detailed STHE model which calculates the heat transfer and pressure loss of the streams based on the geometric specification of the STHE. This model was adapted and used in LTP by converting the stream property notation to that used in LTP_Lib. At this stage the selection of which fluid goes on which side of the heat exchanger must be nominated. Geodynamics found during the pilot plant operation at Habanero that periodic chemical cleaning was effective to prevent scaling formation in the heat exchangers (Mills & Humphreys, 2013). It is assumed that chemical cleaning would also be effective on the shell side. Furthermore, modelling two phase heat transfer is more straightforward when the two phase fluid is in the tubes rather than in the shell. For these reasons the cycle fluid will be on the tube side and geothermal brine on the shell side.
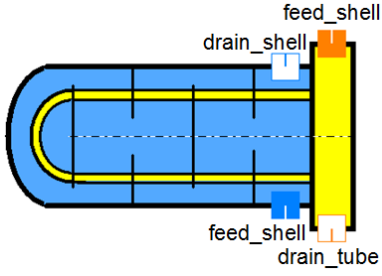
Figure 62: IPSEpro icon for STHE model, with connection naming as used in IPSEpro model.

The EPP_Lib STHE model uses only the specified inlet and outlet conditions to solve the LMTD equation. The calculate profile function from the default model is adapted to provide a more accurate value of the *MTD* and pinch point temperature difference. The key equations used in the STHE model are outlined in the following sections.

4.4.2.1 Heat Transfer

The tube side Nusselt number, Nu_t for single phase heat transfer if $Re < 2300$ is

$$Nu_t = \left(3.66^3 + +1.61^3 Re_t Pr_t \frac{d_t}{L_t}\right)^{0.333}$$

Equation 86

If Re > 2300 then Nu$_t$ is

$$Nu_t = \frac{\frac{\xi_t}{8}(Re_t - 1000)Pr_t\left(1 + \left(\frac{d_t}{L_t}\right)^{0.667}\right)}{1 + 12.7\sqrt{\frac{\xi_t}{8}}\left(Pr_t^{0.667} - 1\right)}$$

Equation 87

where ξ_t is the friction factor, and is given by

$$\xi_t = \frac{1}{(1.82\log(Re_t) - 1.64)^2}$$

Equation 88

The above Nusselt number correlations are cited in the Enginomix STHE model as being from the VDI Heat Atlas (VDI, 1988) as is the method of calculating the heat transfer coefficient for evaporation in the tubes

$$h_{t,ev} = h_{t,liquid} r_{2ph}$$

Equation 89

where r_{2ph} is the two phase multiplier and $h_{t,liquid}$ is the heat transfer coefficient for liquid flowing in the tube, and is given by

$$h_{t,liquid} = \frac{k_t}{d_t} 0.23 Re_t^{0.8} Pr_t^{0.4}$$

Equation 90

101

where k_t, Re_t and Pr_t are evaluated using the properties of saturated liquid at the inlet pressure. The two phase multiplier, r_{2ph}, is given by

$$r_{2ph} = \left(\left(\left((1 - x_{t,av}) + 1.2x_{t,av}(1 - x_{t,av})^{0.01}\left(\frac{v_{t,vapour}}{v_{t,liquid}}\right)^{.37}\right)^{-2.2}\right. \right.$$

$$\left.\left. + \left(\frac{h_{t,vapour}}{h_{t,liquid}}x_{t,av}^{0.01}\left(1 + 8(1 - x_{t,av})^{0.7}\left(\frac{v_{t,vapour}}{v_{t,liquid}}\right)^{0.67}\right)\right)^{-2}\right)\right)^{-0.5}$$

<div align="right">Equation 91</div>

where $x_{t,av}$ is the averaged vapour quality of the inlet and outlet vapour quality, and $v_{t,liquid}$ and $v_{t,vapour}$ are the saturated liquid and saturated vapour specific volumes at the inlet pressure. The heat transfer coefficient $h_{t,vapour}$ is calculated using Equation 68, with k_t, Re_t and Pr_t evaluated using the properties of saturated liquid at the inlet pressure.

4.4.2.2 Pressure Drop

The tube side pressure drop is calculated by summing the pressure losses from the various sources:

$$\Delta p_t = \Delta p_{fr} + \Delta p_{in,t} + \Delta p_{out,t} + \Delta p_{ch,in} + \Delta p_{ch,out}$$

<div align="right">Equation 92</div>

The tube side pressure loss terms are given below in Table 35.

Table 35: Equations used in the STHE model to calculate the components of pressure loss in the tube side of the heat exchanger, cited in the STHE model in the Enginomix EPP Library as being from (VDI, 1980).

Description	Equation	Equation No.
Pressure loss due to friction in tube	$\Delta p_p = \xi_t \dfrac{L_t}{2d_t} m_t^2 v_t$	Equation 93
Pressure loss at inlet of flow into tube	$\Delta p_{in,t} = 0.25\dfrac{w_t^2}{2v_t}$	Equation 94
Pressure loss at outlet of flow from tube	$\Delta p_{out,t} = \dfrac{w_t^2}{2v_t}$	Equation 95
Pressure loss at inlet of flow into chamber of tube inlets	$\Delta p_{in,ch} = 0.25\dfrac{w_{ch,in}^2}{2v_t}$	Equation 96
Pressure loss at outlet of flow from chamber of tube outlets	$\Delta p_{out,ch} = \dfrac{w_{ch,in}^2}{2v_t}$	Equation 97

where the mass flow density in the cross section of the tube is $m_t = w_t/v_t$, and the friction coefficient, and ξ_t is calculated using the Colebrook equation as cited in (Kröger, 2004), which is given by

$$1/\sqrt{\xi_t} = -2\log\left(\frac{2.51}{Re_t\sqrt{\xi_t}} + \frac{d_t}{\varepsilon_t}\right)$$

<div align="right">Equation 98</div>

where ε_t is the surface roughness of the inside of the tube. The mean velocity of flow into the chamber of tube inlets, $w_{ch,in}$, is given by

$$w_{ch,in} = \frac{4\,\dot{m}_{cf}\,v_t}{\pi D_{ch,in}^2}$$

<div align="right">Equation 99</div>

where $D_{ch,in}$ is the diameter of the chamber of tube inlets.

The following equations that are used to calculate the shellside pressure drop are again cited as being from VDI (1980). The shell side pressure drop is calculated from the following

$$\Delta p_s = \Delta p_{in,s} + \Delta p_{out,s} + \frac{\xi_s(N_{baffles} + 1)w_{s,max}^2}{2v_s}$$

<div align="right">Equation 100</div>

The pressure loss at inlet of flow into the shell is given by

<div align="right">Equation 101</div>

$$\Delta p_{in,s} = 0.25\frac{w_{s,in}^2}{2v_s}$$

and out pressure loss at outlet of flow from the shell is given by

<div align="right">Equation 102</div>

$$\Delta p_{out,s} = \frac{w_{s,in}^2}{2v_s}$$

The total friction coefficient in the shell for a staggered tube arrangement, ξ_s, for $Re_s > 10,000$ is given by $\xi_s = \xi_l + \xi_{tr}$, otherwise $\xi_s = \xi_l + \xi_{tr}\left(1 - e^{-(Re+200)/1000}\right)$, where $\xi_l = f_l/Re_{s,max}$ and $\xi_{tr} = f_{tr}/Re_{s,max}^{0.25}$, where the maximum shell side Reynolds number is calculated using mean shell side fluid properties, from

<div align="right">Equation 103</div>

$$Re_{s,max} = \frac{w_{s,max}d_{o,t}}{v_s\mu_s}$$

and the maximum shell side fluid velocity is given by

<div align="right">Equation 104</div>

$$w_{s,max} = \frac{\dot{m}_s v_s}{\sqrt{n_t}d_{o,t}(P_t - 1)}$$

4.4.3 Part-Load Modelling

Heat exchanger off-design analysis is performed using the above STHE model, since the actual heat transfer coefficient is calculated based on the specified heat transfer area; part-load correlations are not required. With the design point selected the heat exchanger geometry is fixed and the model calculates the UA value. As for the design point analysis it must be ensured that the calculated UA value is higher than the required UA value determined from the LMTD equation. So the only difference between design and off-design is that for off-design the STHE geometry is fixed. The only controls available to ensure sufficient UA is achieved is through modifying the specified inlet and outlet temperatures to change the ΔT_{LM}, or the mass flow rate, which will alter the U value.

4.5 Turbine Model

The default model uses the equations presented in Section 2.5 to model the turbine behaviour. This approach only considers inlet and outlet conditions, so there may be cases where, as shown below in Figure 63, inlet and outlets are in the dry vapour region, but during the expansion process, the fluid passes into the saturated mixture region and the user would have no indication of this.
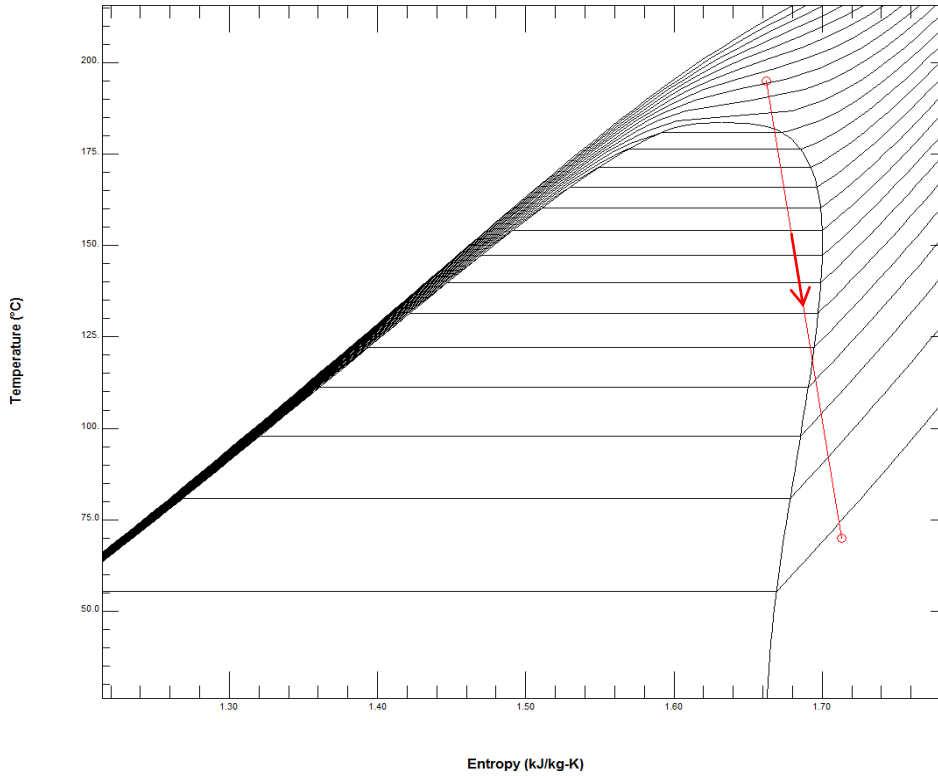
Figure 63: Expansion process for supercritical R123 to illustrate a case where the default model, according to inlet and outlet conditions, would appear to have a dry expansion process, but an expansion profile calculation would reveal that a portion of the expansion crosses the saturated vapour envelope.

To ensure the model accounts for this possibility, the vapour quality at points throughout the process is calculated. The inlet and outlet conditions, and the dry expansion isentropic turbine efficiency are known. The definition of vapour quality is

$$x = \frac{h - h_f}{h_g - h_f}$$

<div align="right">Equation 105</div>

where h_f is the saturated liquid specific enthalpy and h_g is the saturated vapour specific enthalpy. The specific enthalpy at some point part of the way through expansion, h_d, is calculated by interpolation. h_d is then substituted into Equation 105 and x_d becomes

$$x_d = \frac{\left(h_i - d\, \eta_{s_{dry}}(h_i - h_o)\right) - h_{f,d}}{h_{g,d} - h_{f,d}}$$

<div align="right">Equation 106</div>

where d is a value between 0 and 1 used to denote the percentage of the way through expansion the evaluated point is, $h_{f,d}$ and $h_{g,d}$ are the saturated liquid specific enthalpy and vapour specific enthalpy, evaluated at $P_d = P_i - d(P_i - P_o)$. From the calculated expansion

profile the mean vapour quality is calculated for use in Equation 11, to find the turbine isentropic efficiency according to the Baumann rule.

4.6 Plant Cost Modelling in IPSEpro

To facilitate incorporation of the cost modelling into the cycle design process, a new model was developed in MDK, ORC_Cost. Free equations were used to provide the required cost correlation to the model, while cost variables for components not present in the cycle are set to 0, as shown below in Figure 64.
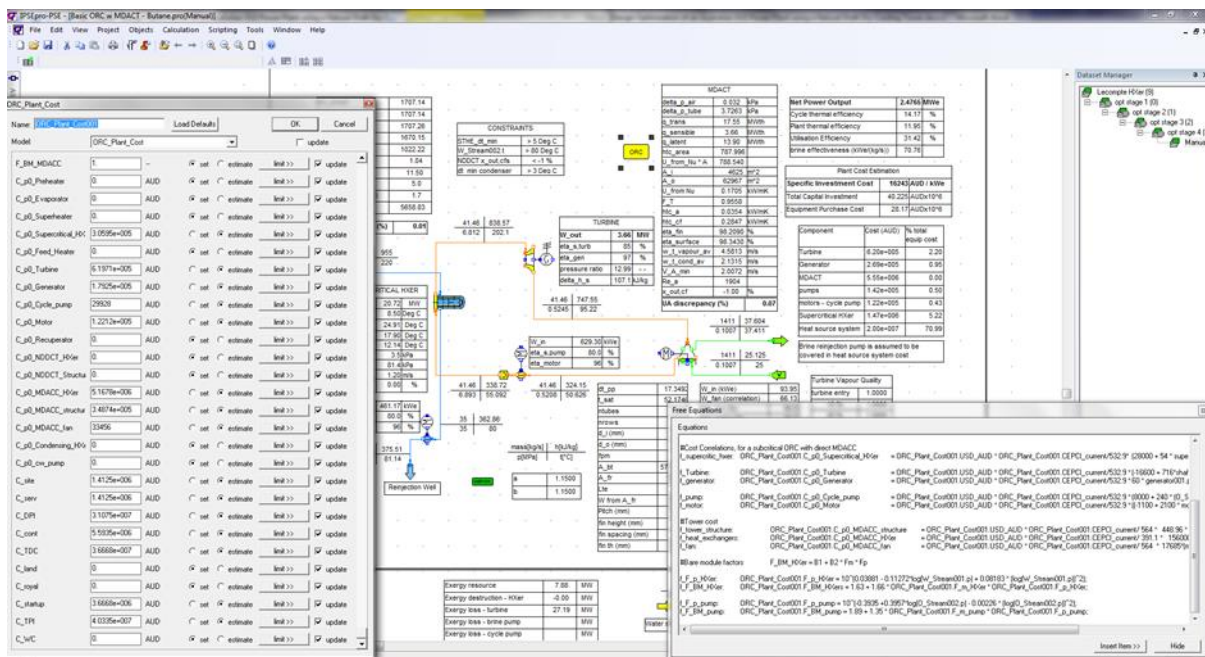
Figure 64: The set up of the ORC_Cost model uses free equations to compile the plant costs.

The equations for the components of capital investment as presented in Table 11 are implemented within the ORC_Cost model. This approach allows live calculation of the TCI and SIC which can then be used as the optimisation objective.

5. NDDCT Trade-Off Analysis

The two condensing systems to be considered in this project are an indirect cooling NDDCT system and a direct condensing MDACT. The design process of MDACTs is suitable to be implemented and optimised as part of the detailed cycle design. For NDDCTs on the other hand, it is useful to obtain some level of familiarity with their behaviour prior to the detailed design stage.

In this section the indirect NDDCT condensing system is analysed using the developed NDDCT module. This is to demonstrate that the NDDCT model behaves as expected for various conditions. This section also aims to explore the various trade-offs involved in NDDCT design. Validations of the model are found in Appendix A and Appendix B.

This process begins with an initial sizing optimisation to find a feasible operating point to begin with. From this initial design, the effects of varying key geometric parameters will be investigated. Following this, the NDDCT performance will be analysed for varying ambient temperatures.

The trade-off is between NDDCT performance and cost, as the higher performing systems will likely be the larger, more expensive NDDCT configurations. For the NDDCT geometric investigation process, the optimisation objective will be SIC_{cd} (AUD/kWth), which uses thermal heat rejection, rather than net power generation as is used for the overall cycle.

$$SIC_{cd} = \frac{capital\_cost_{cd}}{\dot{Q}_{out}}$$

<div align="right">**Equation 107**</div>

Once an optimum NDDCT geometry has been determined, the NDDCT model performance will be investigated within cycle model to determine the optimum NDDCT size. The optimisation for this will be the overall cycle SIC as per Equation 20.

5.1 Reference Case

The reference case used for this analysis is the supercritical butene basic ORC case that was found in the preliminary analysis. A basic ORC is selected as the cycle simplicity allows the analysis to focus on the NDDCT, and butene was selected as it is the highest performing basic cycle as per Table 29. The condensing system inlet conditions are summarised below in Table 36.

Variable	Value	Units
Fluid	Butene	-
Heat rejection duty to condense fluid at 50 ºC	17.23	MW$_{th}$
Cycle fluid inlet temperature	96.26	ºC
Cycle fluid inlet pressure – saturation pressure at 50ºC	0.626	MPa
Cycle fluid inlet mass flow rate	41.39	kg/s
Ambient air temperature	25	ºC

The cycle used for the reference case is the basic ORC using supercritical butene shown in Figure 41, in the preliminary analysis. The NDDCT inlet parameters from Figure 41 will be used in this analysis for the condensing system inlet conditions.

The indirect NDDCT condensing system consists of a cooling water loop which is separate from the cycle fluid loop. Heat is transferred to the cooling water loop from the cycle fluid in the condenser; the heated cooling water then circulates through the NDDCT to dump that heat to the atmosphere via the airflow through the tower. A screenshot of the model from IPSEpro is shown below in Figure 65.
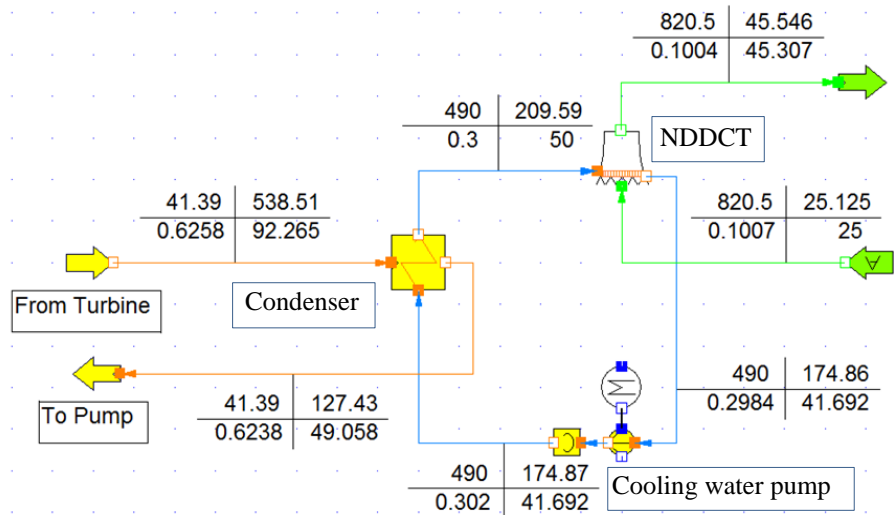
Figure 65: Isolated model of an indirect cooling NDDCT.

In this model the inlet conditions at the "From Turbine" source are set, the cooling water temperature, pressure and mass flow rate are set at the NDDCT inlet in order to facilitate model convergence, and finally the ambient conditions are also set.

5.2 NDDCT Initial Sizing Optimisation

The developed NDDCT IPSEpro model is quite sensitive to initial estimates; it requires the specification of an initial estimate of the air outlet and cycle fluid outlet temperatures within a few °C of the actual solution in order to converge.

To find an initial feasible solution the IPSEpro genetic algorithm optimisation module was used to vary the initial estimate values while searching for feasible tower designs. This approach was used to find a feasible tower design to use as a starting point after which an investigation of varying key NDDCT geometric parameters will be performed. The objective of this initial optimisation is not necessarily to find the optimum tower design immediately, only a few generations and a high population was used in order to generate a search with a wide spread across the decision variables.

Table 37: Optimisation parameters for Genetic Algorithm, for the initial sizing design.

Optimisation Parameter	Value
Population	150
Generations	3
Possibility of crossovers	0.6
Possibility of mutations	0.006

In order to reduce the number of variables manipulated by the optimiser, the NDDCT model was configured to calculate the tower dimensions from a specified number of bundles, aspect ratio and diameter ratio and for a constant assumed A_{e3}/A_3 ratio. The A_{e3}/A_3 ratio represents the coverage of the inlet area by heat exchangers. Similarly, by simply setting the number of bundles, the inlet diameter is calculated and then the other tower dimensions are defined according to the specified aspect ratio and the diameter ratio. The following relationships, listed in Table 38, were used in this process.

Table 38: Geometric relationships used for NDDCT sizing design.

Relationship	Source	Equation Number
$H_3 = d_3/6.5$	From (Zou, 2013)	Equation 108
$n_{ts} = d_3 / \left(\dfrac{82.958}{60}\right)$	Kroger (2004) uses 60 tower supports for a 82.958m base diameter tower	Equation 109
$L_{ts} = \dfrac{15.78}{13.67} H_3$	Kröger (2004) uses tower supports of length 15.78m for a tower of H_3 13.67m	Equation 110

The optimisation objective used was to minimise the SIC_{cd} (AUD/kW$_{th}$) using the cost correlations from Section 2.8.2. The fixed NDDCT parameters are given in Section 4.2.2. The settings used for the decision variables are given below in Table 39.

Table 39: Decision variables used for NDDCT geometry optimisation in direct cooling configuration.

Variable	Minimum	Maximum	Bit / Interval
Aspect ratio (H_5/d_3)	0.8	1.2	6 / 0.00625
Diameter ratio (d_5/d_3)	0.8	1.0	5 / 0.00625
Number of bundles, n_b	22	38	4 / 1.0
Cooling water flow rate, $\dot{m}_{cf}$ (kg/s)	380	700	6 / 10.0
T_{a4} initial estimate	35	60	7 / 0.391
$T_{cf,out}$ initial estimate	35	60	7 / 0.391

It is not expected that the solution found will be the global optimum design as the requirement of the temperature initial estimates would result in many potentially feasible solutions failing during the optimisation. It will however, give a feasible tower design which can form the starting point of the investigation into the effects of varying certain aspects of the tower geometry. The results of the initial optimisation are given below in Table 37.

Table 40: Results for the initial optimisation of the NDDCT geometry.

Variable	Value	Unit
H_5	29.95	m
d_5	31.71	m
H_3	7.00	m
d_3	35.24	m
n_b	29	-
r_a	0.85	-
r_d	0.90	-
A_{fr}/A_3	0.85	-

The ratio A_{fr}/A_3 is the frontal area of the heat exchangers over the total inlet area of the NDDCT. The value of this ratio can be changed by either changing the number of, or the dimensions of the heat exchanger bundles for constant inlet area.

5.3 NDDCT Geometry Variation Investigation

During the NDDCT geometry variation investigation the effects of varying NDCCT parameters are investigated. Throughout this process the starting values given in Table 40 will be refined and by the end of the process an optimum set of tower geometry will be selected. Following this the effects of varying cooling fluid inlet and ambient conditions are investigated. The first characteristic investigated is the aspect ratio. The following figure shows the effect of varying tower aspect ratio, which results in increasing the tower height while keeping all else the same.
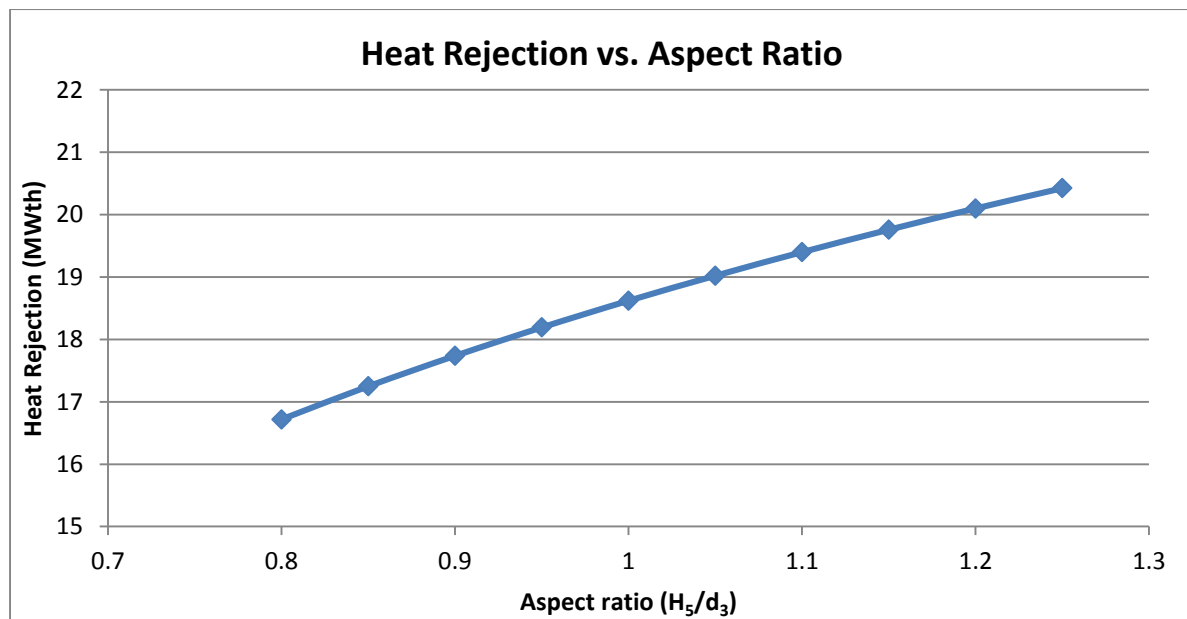
Figure 66: Heat rejection vs. aspect ratio for fixed inlet conditions, diameter ratio fixed at 0.9 and n_b fixed at 29.

Figure 66 shows that heat rejection rate increases approximately linearly with aspect ratio, i.e., increasing tower height. This is due to the increase in air mass flow rate with increasing aspect ratio as illustrated in Figure 67.
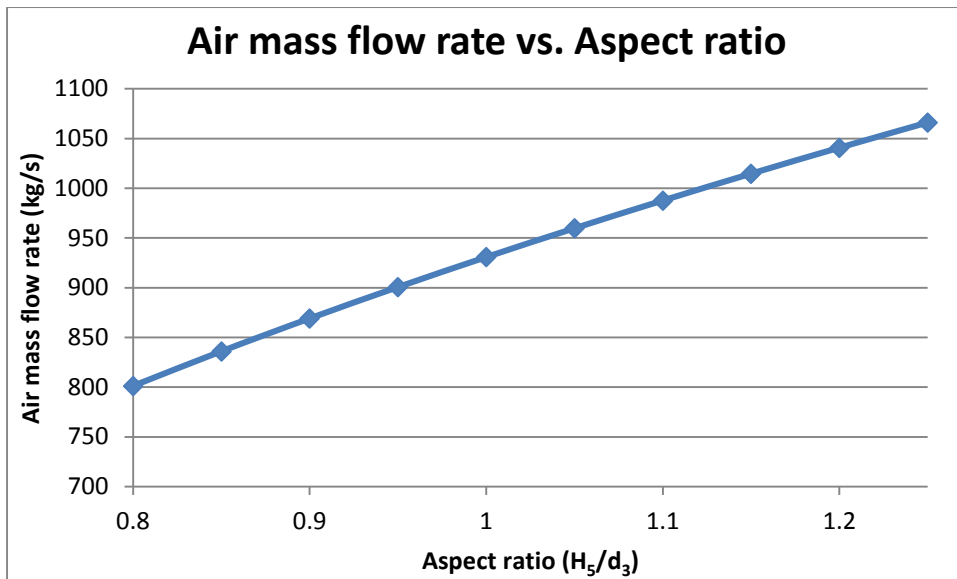
Figure 67: Air mass flow rate vs. aspect ratio for fixed inlet conditions, diameter ratio fixed at 0.9 and n_b fixed at 29.

Next the effect of varying the diameter ratio, r_d, (tower outlet diameter / tower base diameter) is considered, for fixed aspect ratio. As can be seen from Figure 66 and Figure 67 the aspect ratio of 0.85 given in Table 40 is sub optimal. For the purposes of investigating the effect of diameter ratio on NDDCT performance an aspect ratio of 1.2 is selected. The optimum aspect ratio will be investigated following this. The effect of varying diameter ratio is shown below in Figure 68.
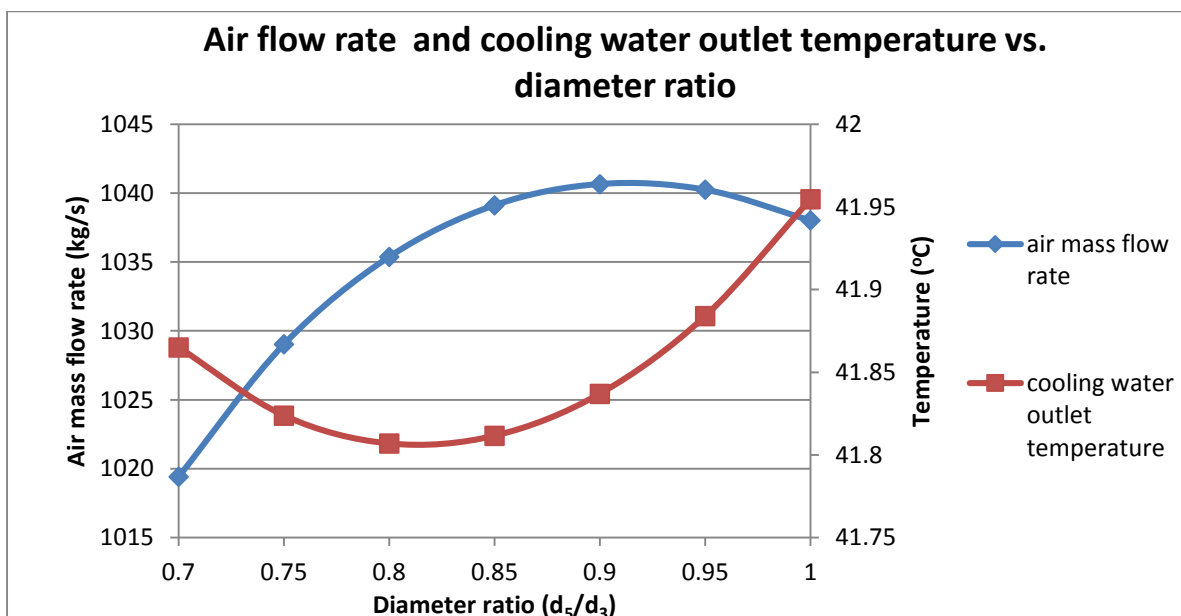
Figure 68: Air mass flow rate and cooling water outlet temperature vs. diameter ratio for aspect ratio = 1.2 and n_b = 29.

The diameter ratio also affects the performance of the tower; however, this time there seems to be an optimum diameter ratio. In order to determine whether this is a constant optimum,

112

the heat rejection is plotted against diameter ratio for a range of aspect ratios, as is shown below in Figure 69.
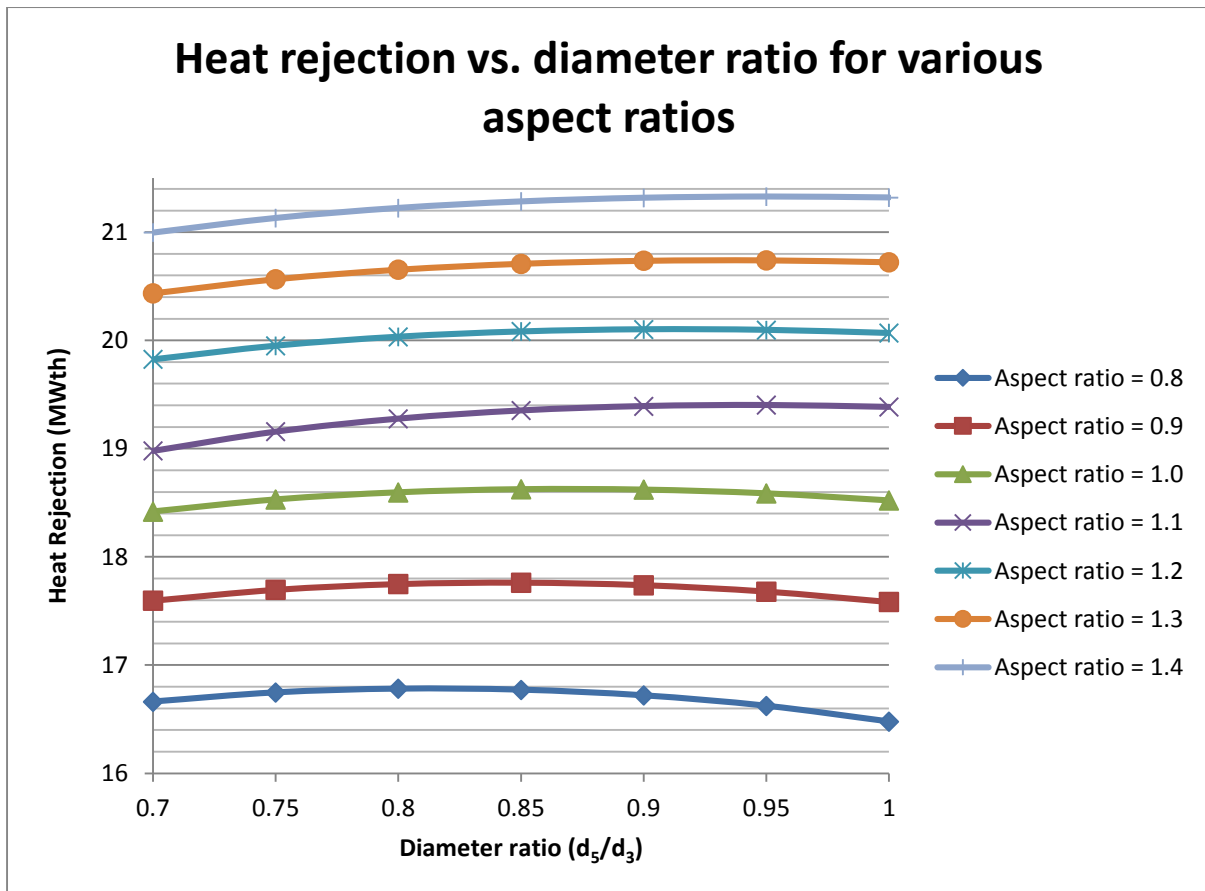
Figure 69: Heat rejection from NDDCT vs. diameter ratio for various aspect ratios.

As depicted in Figure 69, the diameter ratio influences the heat transfer. However the optimum diameter ratio appears to be dependent on the aspect ratio. The peak heat transfer for $r_a = 0.8$ occurs between $r_d = 0.8$ to 0.85, whereas the peak heat transfer for $r_a = 1.4$ is higher; at approximately r_d of 0.95 to 1. Another observation is that an increase in the aspect ratio increases the heat rejection to a much more significant degree than changing the diameter ratio.
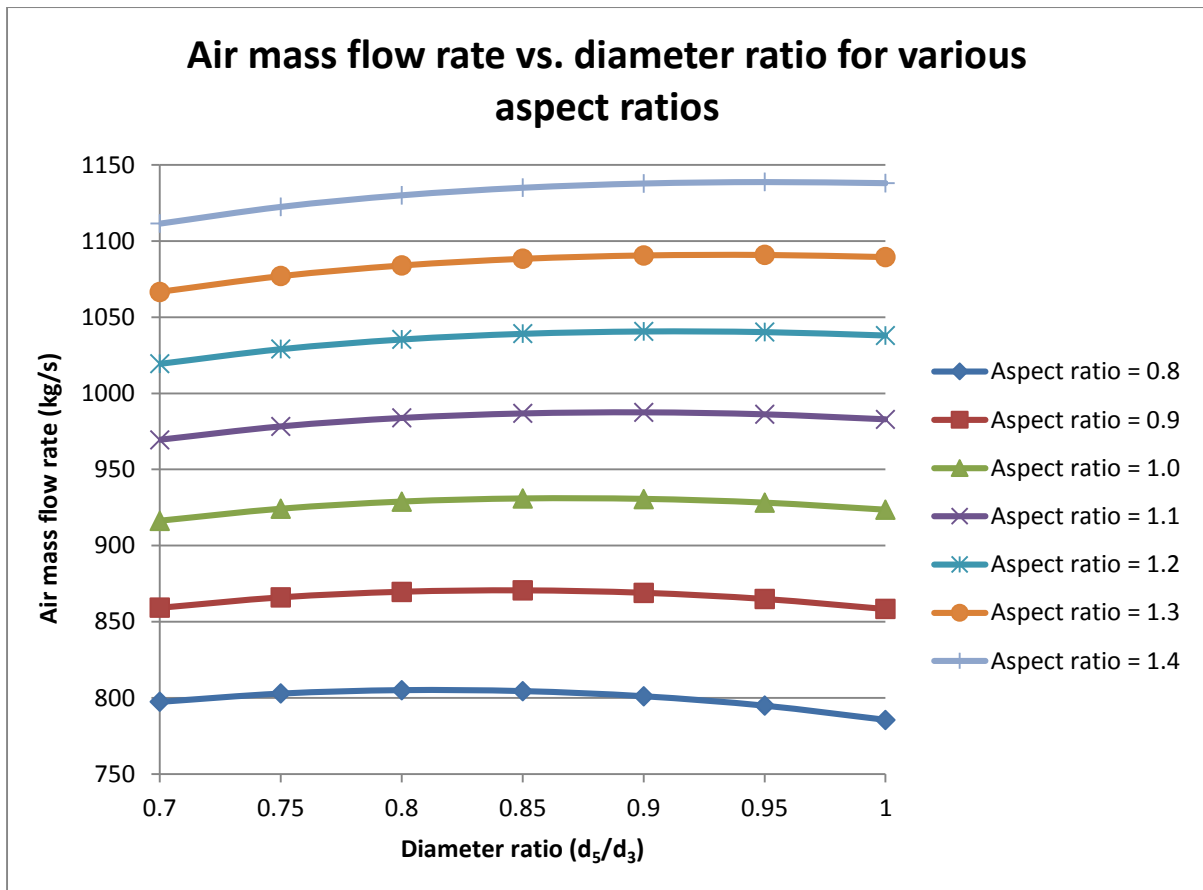
Figure 70: Air mass flow rate of NDDCT vs. diameter ratio for various aspect ratios.

Figure 70 shows that the air mass flow rate follows a similar trend to the heat rejection plot shown in Figure 69, indicating that the air mass flow rate achieved through the tower is directly proportional to the heat rejection load achieved. This is in accordance with the operating principle of the tower.

A key conclusion to be drawn from the above is that increasing tower height results in increased heat rejection, however this will come with the increased cost of the tower structure. Presumably there is an economic limit at which increasing the tower height is no longer beneficial. In order to analyse this, the diameter ratio is plotted against the SIC_{cd} of heat rejection, for various aspect ratios.
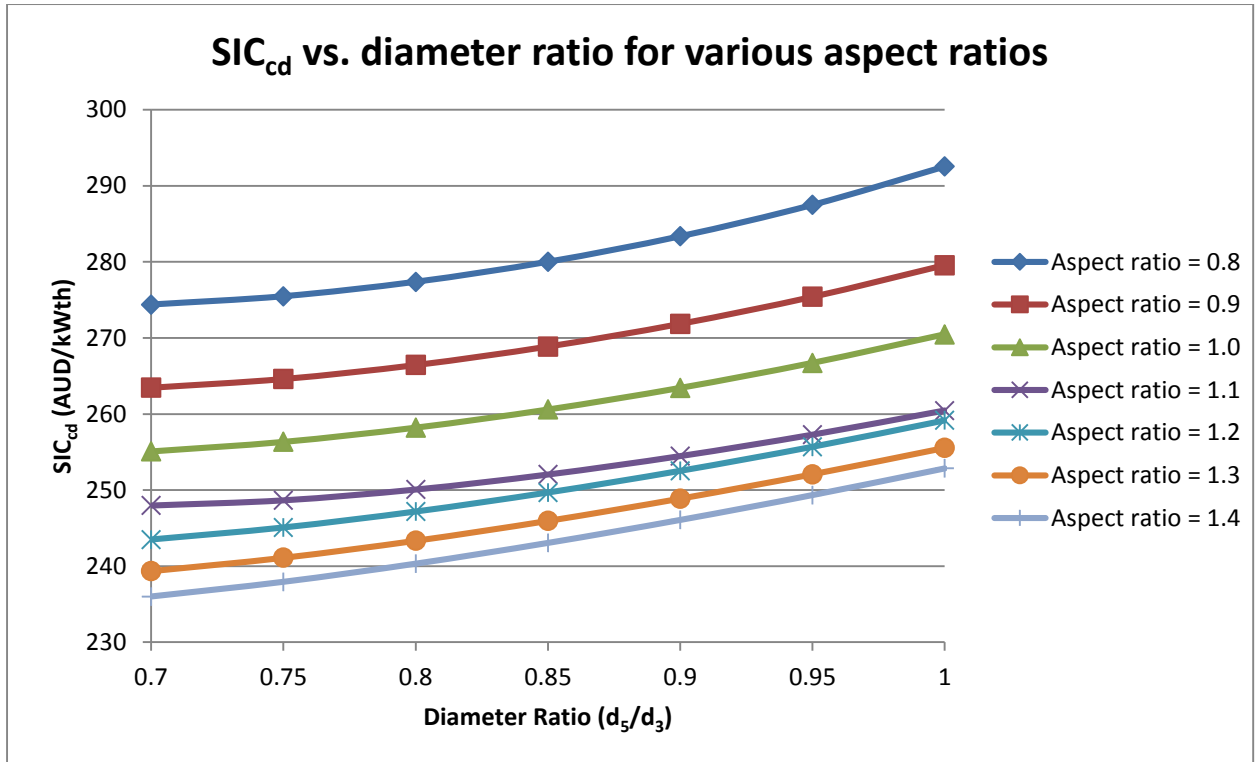
Figure 71: Specific investment cost of heat rejection for the NDDCT vs. aspect ratio.

Figure 71 shows that the optimum diameter ratio for SIC_{cd} is at low diameter ratios for all aspect ratios. There appear to be diminishing gains for increasing the aspect ratio, and presumably for the increasing aspect ratio there will be additional structural design complications due to the tall narrow structure. From Figure 71 the NDDCT configuration that gives the optimum SIC_{cd} value would be tall and narrow with a large diameter ratio.

With this optimised tower geometry the heat rejection is significantly higher than required for the reference case, at about 21 MWth, as shown above in Figure 69, where only about 17 MWth is required to condense the cycle fluid for the reference cycle. Thus far the NDDCT analysis has used the initial guess value of 29 bundles and the associated tower dimensions. As this tower size results in significantly higher heat rejection than is required, the next step is to find the most economic tower size which can achieve the required heat rejection rate. In order to do this n_b is varied with a fixed aspect ratio and diameter ratio of r_a =1.4 and r_d = 0.7, as these ratios give the best performance in terms of SIC_{cd}, as shown in Figure 71, to find the range of tower size that is more appropriate to the heat rejection rate required.

For this stage of the analysis the cycle fluid inlet conditions are those shown in the reference cycle (Figure 41), and the cooling water temperature at the inlet to the NDDCT is fixed, while the cooling water mass flow rate is used to find the conditions at which the indirect

cooling system, for each number of bundles considered, condenses the cycle fluid while maintaining a pinch point temperature difference of at least 3 °C.
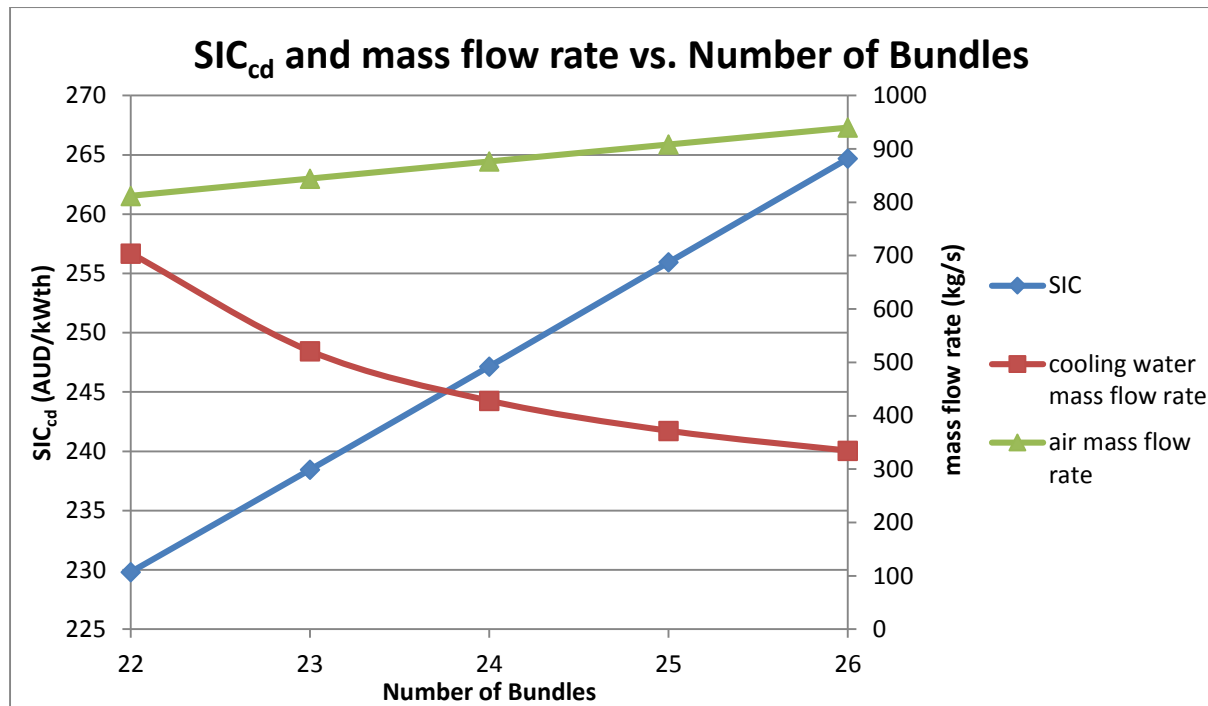
Figure 72: Specific Investment cost and mass flow rate vs. number of bundles, for NDDCT with $r_a = 1.4$ and $r_d = 0.7$, sized to provide sufficient heat rejection to meet the condensing load in the reference cycle, in Error! Reference source not found.**.**

As might be expected the SIC_{cd} decreases linearly with decreasing n_b, due to decreasing tower size. However, the trade-off for decreasing tower size is that approach temperatures between air and water outlets are reduced. Increasing the water mass flow rate, which is necessary in order to utilise a smaller tower results in a reduced ΔT_{cw} and there is a cutoff for when ΔT_{cw} is less than the required temperature rise in the condensing heat exchanger. This occurs at n_b = 21. No solution was found for a 21 bundle tower with cooling water at inlet at 50 °C due to insufficient temperature drop for the water at the elevated cooling water mass flow rate, which is in excess of 1000 kg/s for 21 bundles. Figure 73 illustrates the decrease in temperature approaches for the range of bundles from 22 to 26.
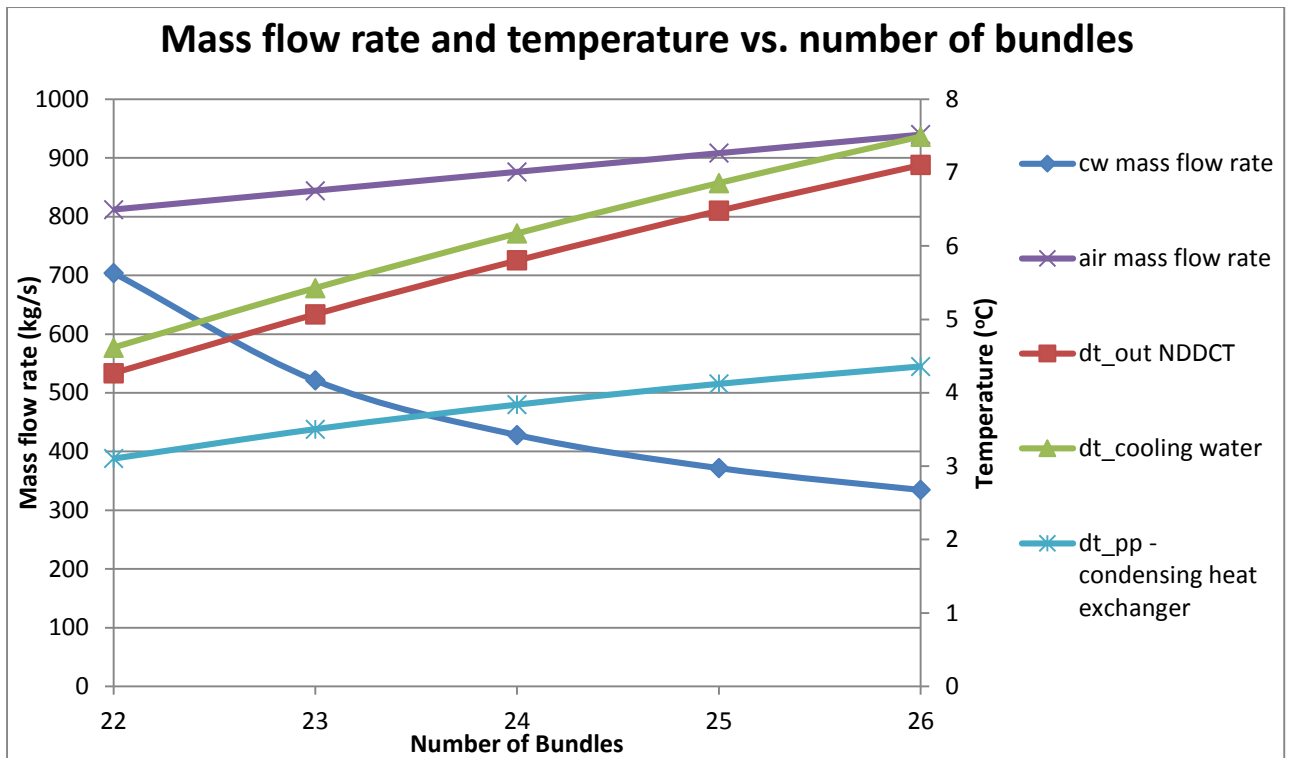
Figure 73: Mass flow rate and temperature difference vs number of bundles.

For the analysis thus far, constant inlet temperatures were used and the cooling water mass flow rate was varied to give the subcooled liquid at the outlet of the condenser. Figure 73 shows that towers with less than the 29 bundle tower previously considered may be used. However, to go any lower than 22 bundles would require an increase in cycle condensing temperature; already it can be seen that the ΔT_{pp} in the condensing heat exchanger decreases with decreasing tower size, due to the required increase in cooling water mass flow rate. When this ΔT_{pp} gets too low the only option is to increase the condensing temperature and pressure of the cycle, which results in a decreased net power generation. This implies that the smaller towers will be further penalised at higher ambient temperatures. In order to determine the optimum, the performance of each tower size should be considered at various ambient temperatures.

The analysis thus far has been done with A_{fr}/A_3 of 0.85, the effect of this parameter is now investigated.
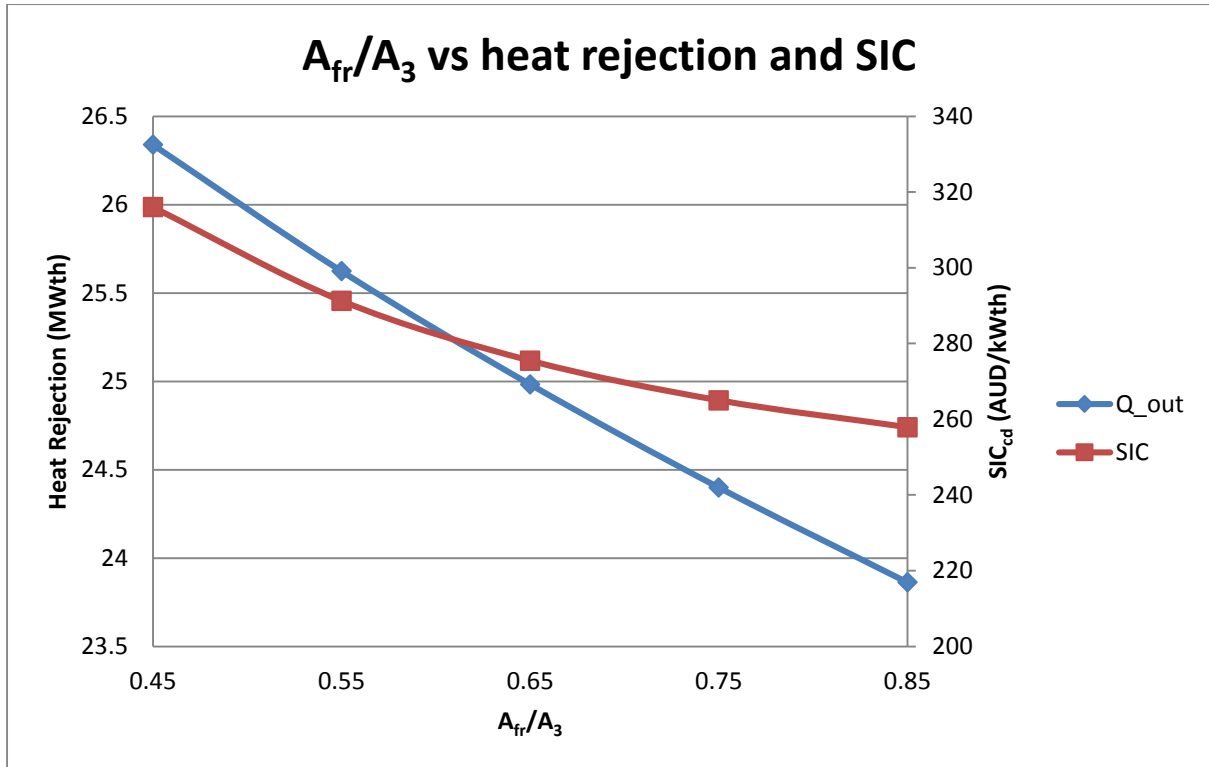
Figure 74: Ratio of the tower inlet area covered by heat exchangers vs heat rejection and *SIC_cd* for fixed number of bundles and constant inlet conditions.

The SIC value increases with decreasing A_{fr}/A_3 due to the increase in heat rejection being outweighed by the cost of the tower structure. The upper limit for the A_{fr}/A_3 depends on the heat exchanger layout and additional space required for heat exchanger supports. Y. Lu et al. (2013) use a value of approximately 0.65 for A_{fr}/A_3 and this will be used in this work.

5.4 Ambient Temperature Variation

The NDDCT behaviour for varying cooling fluid and ambient conditions is investigated in this section. A tower with 23 bundles is used for this analysis, with an aspect ratio of 1.4 and diameter ratio of 0.7 as per the findings of the previous section. The influence of the tower size on the performance at a range of ambient temperatures is shown Figure 75.
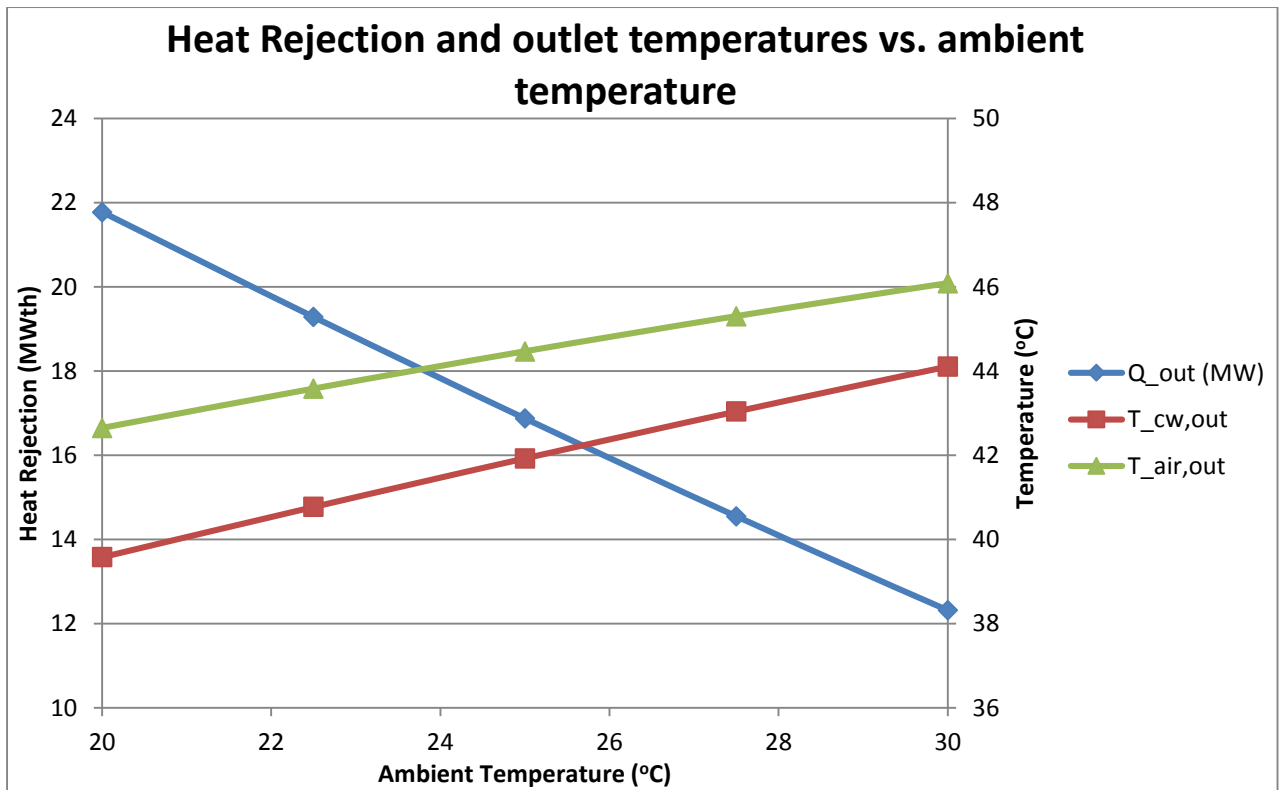
Figure 75: Heat rejection and outlet temperatures vs. ambient temperature for constant cooling water flow rate and inlet temperature.

Changes in ambient temperature cause significant deviations in heat rejection rate for the same cooling water inlet conditions, as shown in Figure 75. Almost 10MWth differential results from a change in ambient temperature of 10°C. Figure 75 also shows that as the ambient temperature increases the $T_{cw,out}$ line is approaching the $T_{air,out}$, alluding to a reduced capacity for heat rejection at increasing ambient temperature. This is shown for constant cooling water mass flow rate.

The amount of heat rejected can be controlled via the cooling water mass flow rate. This capacity for control is illustrated below in Figure 76, which shows the NDDCT performance for varying cooling water mass flow rate at constant ambient temperature and water inlet temperature.
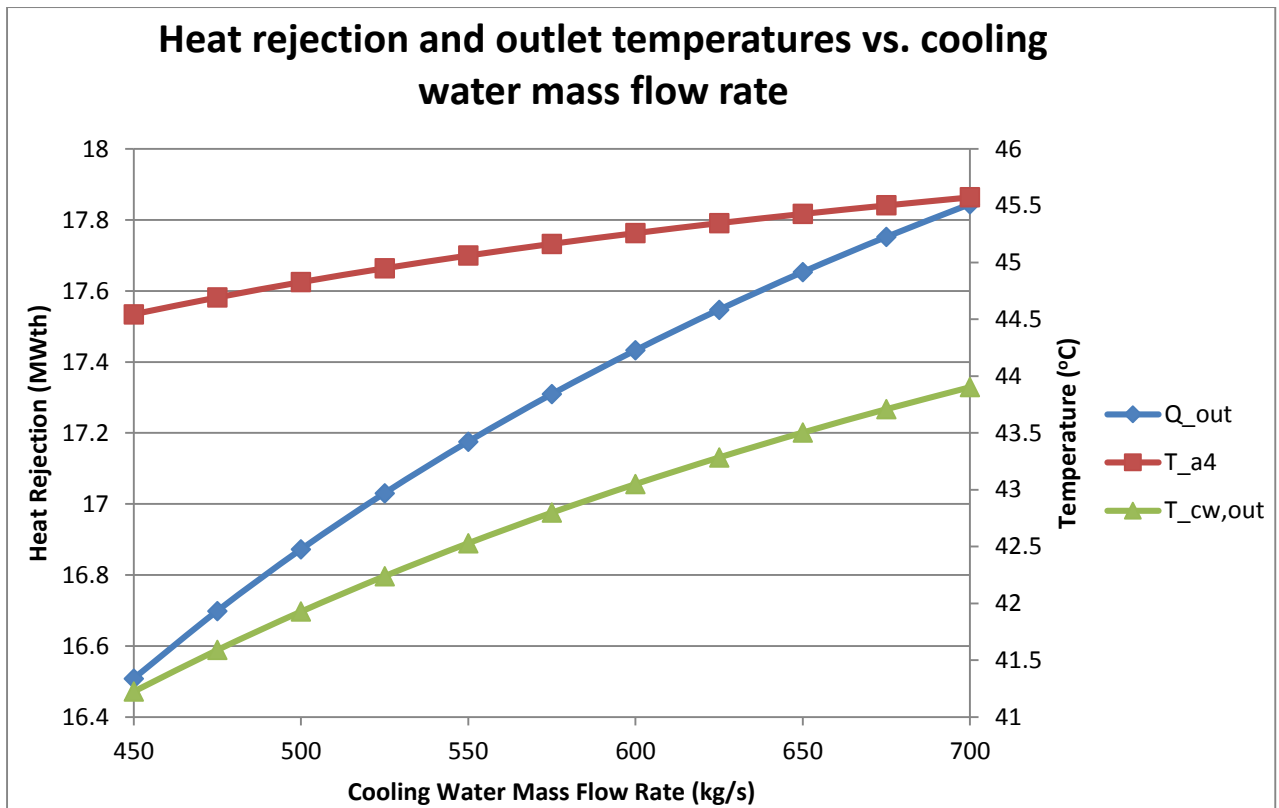
Figure 76: Heat rejection and water and air outlet temperatures vs. cooling water mass flow rate for constant tower geometry and constant inlet temperature.

The heat rejected can be controlled by varying the cooling water mass flow rate. However, as the cooling water flow rate increases the water outlet temperature approaches the air outlet temperature, signifying that the water is achieving a lower temperature drop through the NDDCT due to the increased water flow rate, despite the increased air flow rate through the tower. This increase in water outlet temperature also means that the ΔT_{pp} in the condenser will decrease. Hence there is a limitation to how much additional heat can be rejected with variation of the water inlet mass flow rate. Beyond this limit the cooling water inlet temperature will need to be increased, and as a result the condensing temperature of the cycle will need to be increased. This effect must now be analysed in the cycle model to infer the economic size of the NDDCT in terms of SIC.

5.5 In-Cycle Performance Analysis

In this section the NDDCT will be analysed in the reference cycle model and the number of bundles considered will be varied to determine the extent of the influence cycle performance. This analysis will use the design assumptions and constraints as specified in Section 6.1.
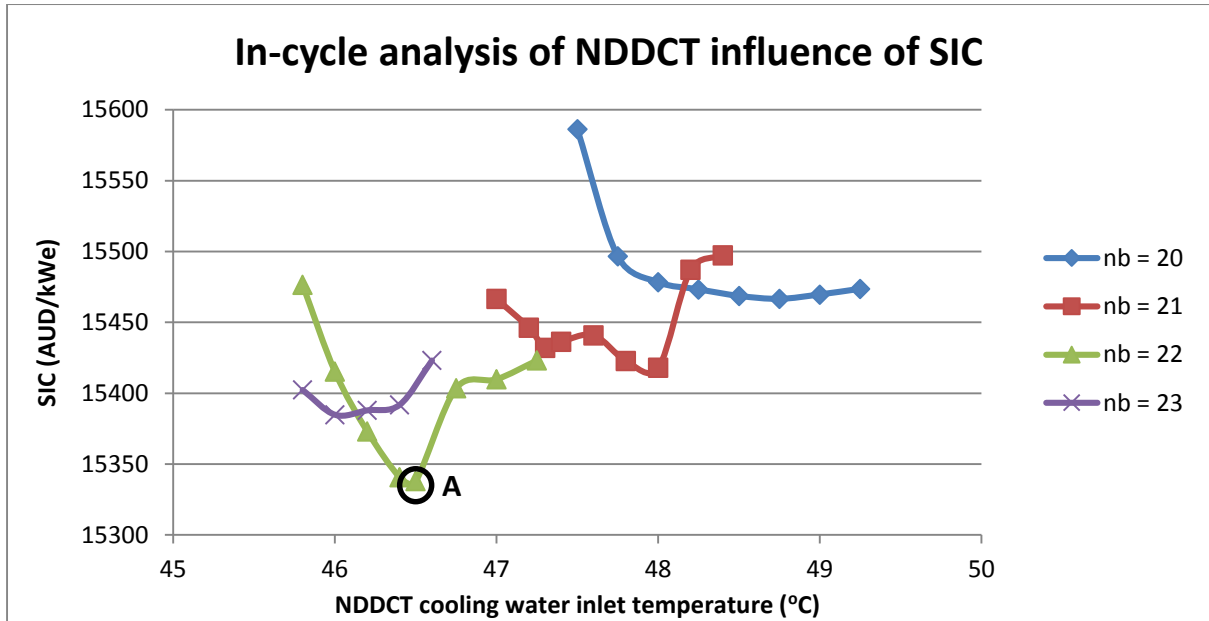
Figure 77: Tower size (specified by number of bundles) and the corresponding cooling water inlet temperature vs. plant Specific Investment Cost.

According to this modelling the optimum tower size for the reference case considered is the point A in Figure 77. As the number of bundles increases and the tower gets larger, the achievable cooling tower inlet temperature decreases, due to the increased capacity for a higher air mass flow rate through the tower. The NDDCT parameters at the optimum, point A, as shown in Figure 77 are presented below in Table 41.

Table 41: Optimum NDDCT selected for the supercritical Butene basic ORC.

Variable	Value	Unit
H_5	52.45	m
d_5	26.23	m
H_3	5.76	m
d_3	37.46	m
n_{ts}	27.10	-
L_{ts}	6.65	-
n_b	22.00	-
r_a	1.40	-
d_5/d_3	0.70	-
A_{e3}/A_3	0.65	-
$T_{cw,in}$	46.5	ºC
$\dot{m}_{cw}$	750	kg/s

This is the optimum for the reference case of supercritical Butene basic ORC, and as all of the considered cycles are designed for a similar condensing temperature and heat rejection rate, the above NDDCT design will be used for each of the detailed designs.

6. Detailed Cycle Design

In the next phase of the project the top performing candidate cycles that were selected from the results of the preliminary analysis were subject to a detailed cycle analysis to optimise the cycle and component design for minimum Specific Investment Cost.

6.1 Component Design Constraints

This section covers the component specific detailed design constraints that were used throughout the detailed cycle design.

6.1.1 MDACT

The MDACT has an additional degree of control that is provided by the control of the air flow rate via the control of the fan. With the outlet cycle fluid stream vapour quality set to saturated liquid and the cycle fluid saturation temperature set, the required air flow rate is calculated based on the specified pinch point temperature difference and MDACT design to give the power consumed by the fan motor. The heat transfer area and air mass flow rate determine the air-side pressure drop and therefore the power demand on the fan. Larger heat transfer surface area results in a lower air velocity through the heat exchanger and lower pressure drop at the expense of higher MDACT cost.

In order to perform the MDACT design a number of design assumptions are used:

- Fan efficiency is 60% (Daniel Walraven et al., 2015),
- Cycle fluid outlet vapour quality is set to -1%,
- The tubes used are as per Lecompte et al. (2013), with the tube geometry summarised below in Table 42, and
- Single tube pass, A-frame heat exchanger arrangement is used, as was shown in Figure 26.

Table 42: Fixed condenser geometric parameters, (Lecompte et al., 2013), dimensions correspond to Figure 60.

Parameter	Description	Value
d_i	Tube inner diameter	12.85 mm
d_o	Tube outer diameter	15.88 mm
P_t	Tube pitch	35.00 mm
d_f	Fin diameter	33.66 mm
t_f	Fin thickness	0.5 mm

Parameter	Description	Value
P_f	Fin pitch	2.8 mm
k_t	Tube thermal conductivity, for A214 mild steel	50 W/m K
k_{fin}	Fin thermal conductivity, for 6063 aluminium	204 W/m K
2θ	Apex angle of angle of A-frame heat exchangers	60 °

The MDACT optimisation variables are presented in Table 44.

6.1.2 Heat Exchanger Design

The cycle detailed design involves the design and optimisation of the heat exchangers. In this process there are a number of design decisions to be addressed. Key constraints are as follows:

- Maintain the same ΔT_{pp} limits as were used in the preliminary analysis, as this is a heat exchanger performance capability limitation; 5 °C is used for STHEs and 3 °C is used for PHEs.

- The minimum limitation on LMTD is no longer necessary as the effect of LMTD is captured in the cost of the heat exchanger, i.e., lower LMTD results in larger UA required, and therefore higher cost.

- Maximum unit length of 12.4 m to be able to be transported on a standard semi-trailer, therefore maximum tube length of 11.5 m is used.

- Minimum tube pitch is 1.15 x d_o and staggered tube layout is used as it is found by Walraven et al. (2014) to be the most effective for ORC.

- Minimum tube d_i of 5mm as used in Schröder et al. (2014) and Daniel Walraven et al. (2015).

- An assumed heat transfer coefficient is used for the condensing heat exchanger of 3 kW/m²K, which is in the typical value range given in the VDI Heat Atlas (2010) for a spiral plate heat exchanger condensing vapour to liquid.

- Thermal conductivity of the tubes for STHEs is assumed to be 40 W/m K.

The calculated heat transfer coefficient depends on the tube thickness which is a significant consideration for mechanical design. Annaratone (2007) gives the tube thickness required for a long thin cylinder under external pressure as:

$$t = \frac{pD_o}{2f}$$

Equation 111

where f = design tensile strength; at 250 °C the range for carbon steels is 126 – 317 MPa, according to AS1210 (2010),

p = design pressure; 35 MPa for the case where cycle side is not pressurised, and

D_o = tube outer diameter.

The tube diameter is an optimisation variable as it affects the heat transfer coefficient and the cycle fluid side pressure drop. Applying a safety factor and corrosion allowance, c, Equation 111 becomes

$$t = SF \frac{pD_o}{2f} + c$$

<div align="right">**Equation 112**</div>

A safety factor of 1.5 and a corrosion allowance of 1 mm will be used. Equation 112 will be utilised in the IPSEpro flow sheet using free equations to calculate required thickness for the specified inner diameter.

6.2 Cycle Design Point Selection Procedure

The process used for the design point optimisation is presented in this section. The design point selection involved two stages: the model setup, and the optimisation. The optimisation used the same multiple stage approach as was used in the preliminary analysis. The first stage involved a high population, single generation search to span the search space to find the approximate region of the optimum. In subsequent stages, the population was decreased and generations increased while the decision variable ranges were narrowed and the bit numbers increased to increase the resolution. The process was continued until subsequent optimisations find no further improvement in SIC.

6.2.1 Model Setup

The cycle operating points from the preliminary analysis were used to initially set up the detailed cycle model. The detailed models for the heat exchangers and condensers were set up in the cycle, with the NDDCT geometry set to the optimum found in Section 5.5 or the MDACT geometry set to the values given in Table 44.

The detailed design flow sheet is shown below in Figure 78 for the supercritical butane regenerative ORC with NDDCT.
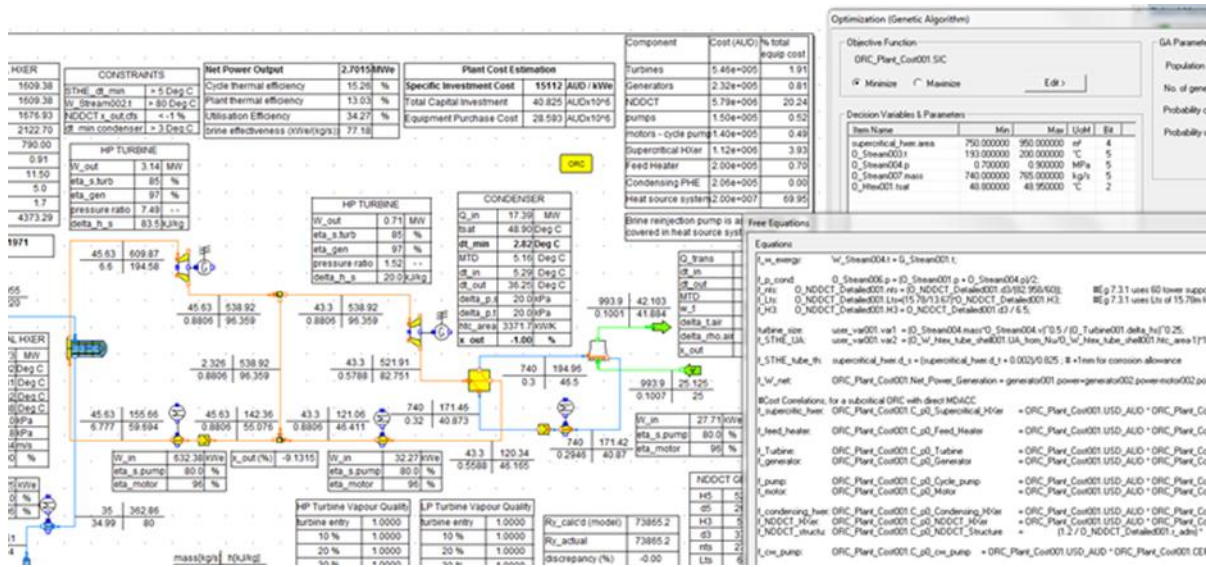
Figure 78: IPSEpro model flowsheet used for detailed cycle design of supercritical butene basic ORC, showing the optimisation window and the free equations window used to set up the cost correlations.

The heat exchanger geometry was manually iterated to achieve a UA value within 5% of the required value. Free variables and free equations were used to ensure the actual UA is greater than or equal to the required UA value. The cost correlations and the ORC cost model are set up for the components relevant to the cycle, as was described in Section 4.6. When cycle model functionality was ensured through the manual iterative design the optimisation module was set up.

6.2.2 NDDCT Cycle Optimisation

The NDDCT design is set as per Section 5.5, so the optimisation of the NDDCT condensed cycles focused on the STHE and cycle parameters. The values for turbine inlet temperature and pressure found in the preliminary analysis were used as the initial values, and a fairly narrow search range assigned. The NDDCT optimisation in Section 5.5 is for a specific condensing temperature, $T_{cd,cf}$, the optimum for other cycle fluids was expected to be of a similar value, hence a narrow range was used for $T_{cd,cf}$. The decision variables for the basic ORC with NDDCT are given in Table 43 below, where *pa* is used to denote the value found in the preliminary analysis.

Table 43: Decision variables used for NDDCT geometry optimisation in indirect cooling configuration, *pa* denotes the value found in the preliminary analysis.

Variable	Minimum	Maximum	Bit / Interval
Cooling water mass flow rate, $\dot{m}_{cw}$ [kg/s]	730	780	5 / 1.563
Cycle fluid condensing temperature, $T_{cd,cf}$ [ºC]	46	50	5 / 0.125

126

Variable	Minimum	Maximum	Bit / Interval
Turbine inlet temperature, $T_{turb,i}$ [°C]	*pa* - 2	*pa* +2	5 / 0.125
Turbine inlet pressure, $P_{turb,i}$ [MPa]	*pa* – 0.25	*pa* + 0.25	4 / 0.0156
Heat exchanger heat transfer surface area, A_{hts} [m^2]	750	1200	6 / 7.03
Tube length, L_{te} [m]	~8	11.5	7 / ~0.03
Tube inner diameter, d_i [mm]	5.0	~20.0	6 / ~0.23
Tube pitch, P_t [-]	1.15d$_o$	1.5d$_o$	5 / 0.011

Similarly to the preliminary analysis these values were the default starting values, however if during the manual design stage it was found that other values may be more suitable then these starting values were adjusted slightly to provide better targeting, according to the findings of manual design prior. Table 43 shows the decision variables used for the basic ORC.

The recuperated cycle only requires a single additional cycle variable to be included as a decision variable, which is the recuperator outlet temperature on the high pressure side. The value found in the preliminary analysis was used with the range set to be ∓ 5 °C. The recuperator geometry is also the scope of the optimisation. However, the overall size of the recuperator is much smaller than the brine heat exchanger(s); the design point heat transfer rate is about 2 MWth, compared to 20.7 MWth for the brine heat exchanger(s). Therefore, it was decided that as the recuperator design optimisation adds a significant degree of computational effort for a relatively insignificant effect on the overall cycle performance, the strategy was used that manual recuperator optimisation stages were interspersed between the GA optimisation stages. This was found to be an effective strategy.

The regenerative cycle only requires the addition of the regeneration pressure as an optimisation variable and the mixed stream after the feed fluid heater has the vapour quality limit set to a maximum of -1% to provide sufficient sub-cooling at the high pressure pump inlet, as per Section 2.7.2. The value found for the regeneration pressure in the preliminary analysis is used as the initial value and the range is set to be ∓ 0.2 MPa, with 5 bits, to give a search interval of 0.0125 MPa.

6.2.3 MDACT Cycle Optimisation

The same optimisation approach was used as for the NDDCT condensed cycles, with the addition of the decision variables for MDACT geometry optimisation.

Variable	Minimum	Maximum	Bit / Interval
Pinch point temperature difference, ΔT_{pp} [°C]	5	20	7 / 0.117
Cycle fluid condensing temperature, $T_{cd,cf}$ [°C]	45	55	6 / 0.156
Tube length, $L_{te,MDACT}$ [m]	10	20	6 / 0.156
Number of tubes, $n_{t,,MDACT}$ [-]	4,000	10,000	8 / 27.4
Number of rows, $n_{rows,,MDACT}$ [-]	3	6	2 / 1
Turbine inlet temperature, $T_{turb,i}$ [°C]	pa - 2	pa +2	5 / 0.125
Turbine inlet pressure, $P_{turb,i}$ [MPa]	$pa - 0.25$	$pa + 0.25$	4 / 0.0156
Heat exchanger heat transfer surface area, A_{hts} [m²]	750	1,200	6 / 7.03
Tube length, $L_{te,he}$ [m]	~8	11.5	7 / ~0.03
Tube inner diameter, $d_{i,he}$ [mm]	5.0	~20.0	6 / ~0.23
Tube pitch, $P_{t,he}$ [-]	1.15d_o	1.5d_o	5 / 0.011

The same approach was used for the optimisation of the recuperated cycles as was described above for the NDDCT condensed cycles. Similarly to the NDDCT condensed cycles, the optimisation of the regenerative cycle sees the addition of regeneration pressure to the decision variables, with the same settings used. The MDACT condensed regenerative cycles also require the feed fluid heater outlet vapour quality to be set and this is used as an optimisation variable with the range of -5% to -1% and 5 bits, to give a search interval 0.125%.

6.3 Summary of Results & Discussion

The minimum SIC results found by the above process for each of the cycles in the detailed design point analysis are summarised below in Table 45. The values of the decision variables that deliver these minimum SIC results are given in Table 46.

Table 45: Design point values for selected cycles.

Cycle Fluid	Cycle type	Sub- or Super-critical	Condensing system	$\eta_{th,cycle}$ (%)	η_u (%)	$\dot{W}_{net}$ (MWe)	TCI (AUDx10⁶)	SIC (AUD /kWe)
Butane	Recuperated	Super	NDDCT	15.40	34.65	2.731	42.156	15,436
			MDACT	14.83	32.96	2.598	41.991	16,163
Butene	Recuperated	Super	NDDCT	15.34	34.48	2.717	41.851	15,401
			MDACT	14.64	32.48	2.560	41.979	16,397

Cycle Fluid	Cycle type	Sub- or Super-critical	Condensing system	$\eta_{th,cycle}$ (%)	η_u (%)	$\dot{W}_{net}$ (MW$_e$)	TCI (AUDx10^6)	SIC (AUD /kWe)
Isobutene	Recuperated	Super	NDDCT	15.45	34.77	2.741	42.112	15,366
			MDACT	14.60	32.55	2.565	41.892	16,331
R152a	Recuperated	Super	NDDCT	15.17	34.03	2.682	42.184	15,727
			MDACT	14.57	32.29	2.545	41.934	16,477
Butene	Regenerative	Super	NDDCT	15.28	34.32	2.705	42.570	15,739
			MDACT	14.24	31.59	2.490	41.290	16,583
Butane	Regenerative	Super	NDDCT	15.24	34.22	2.697	42.430	15,732
			MDACT	14.58	32.48	2.560	41.583	16,243
R152a	Regenerative	Super	NDDCT	15.14	33.95	2.676	42.860	16,017
			MDACT	14.26	31.64	2.494	41.608	16,684
Isobutene	Regenerative	Super	NDDCT	15.10	33.86	2.669	42.830	16,046
			MDACT	14.51	32.30	2.546	41.826	16,430
Butene	Basic	Super	NDDCT	15.10	33.85	2.668	41.830	15,680
			MDACT	14.26	31.64	2.494	41.001	16,439
R152a	Basic	Super	NDDCT	14.96	33.49	2.640	41.961	15,897
			MDACT	13.85	30.63	2.409	39.924	16,570
Isobutene	Basic	Super	NDDCT	14.99	33.57	2.646	42.031	15,886
			MDACT	14.16	31.39	2.474	40.589	16,406
Butane	Basic	Super	NDDCT	14.87	33.24	2.620	41.655	15,901
			MDACT	14.17	31.40	2.476	41.124	16,612
Isobutane	Recuperated	Super	NDDCT	15.43	33.64	2.651	42.478	16,023
			MDACT	14.81	31.75	2.503	42.493	16,980
R123	Basic	Sub	NDDCT	14.90	33.48	2.626	42.009	15,995
			MDACT	13.45	31.41	2.325	41.928	18,033
Isopentane	Regenerative	Sub	NDDCT	15.09	33.83	2.667	42.392	15,897
			MDACT	14.36	31.90	2.514	41.832	16,637

The above results show that all of the NDDCT condensed cycle results in a higher TCI value than for their respective MDACT cycles. However, as the NDDCT cycles achieve significantly higher net power generation, they achieve lower SIC values.

There are two main factors that contribute to the reduction in $\dot{W}_{net}$ of the MDACT condensed cycles; the first and more obvious cause is the parasitic power consumption by the fan motor

in the MDACT, the other main cause of reduction in $\dot{W}_{net}$ for the MDACT cycles is the higher condensing temperature, as is shown below in Table 46 through Table 48, which results in a lower turbine shaft work due to the reduction in pressure ratio.

The recuperated MDACT cycles have similar SIC values to the basic cycles with the same fluid, whereas the SIC value for the NDDCT condensed cycle is notably lower for the recuperated cycle. This seems to be due to a higher MDACT cost for the recuperated cycles as compared to for the other cycles, as is shown below in Figure 79. Decreasing the MDACT inlet temperature through recuperation of the sensible heat from the turbine exhaust stream increases the proportion of latent heat to be rejected for the same overall heat rejection rate and decreases the mean temperature difference in the MDACT. In order to address this one or more of the following is required: increase the cycle fluid condensing temperature in order to increase the mean temperature difference, increase the MDACT heat transfer area, or increase the air mass flow rate through the MDACT resulting in increased fan motor power consumption, all of which have a negative effect on the SIC value. This effect does not seem so pronounced for the indirect condensing NDDCT, which may be due to the indirect condensing system arrangement.

The MDACT condensed basic R123 cycle has a significantly higher SIC value than the other cycles considered, due to the effect mentioned above – higher latent heat rejection in the MDACT leading to a larger heat transfer surface area and a higher condensing temperature for the cycle. The combination of which is a more expensive cycle which generates lower net power than predicted in the preliminary analysis due to a higher turbine exhaust pressure. Similarly to above, the NDDCT condensed R123 basic cycle does not seem to be affected to the same extent and still achieves a comparable SIC value to the other basic cycles.

The values for the decision variables which give the results in Table 45 as well as the equipment cost data is presented in the following pages.

Table 46: Values of the decision variables for detailed design optimisation of the basic ORCs, corresponding to the results given in Table 45, NDDCT values as shown in Table 41.

Component / Stream	Variable	Basic Butane with NDDCT	Basic Butene with NDDCT	Basic Isobutene with NDDCT	Basic R152a with NDDCT	Basic R123 with NDDCT	Basic Butane with MDACT	Basic Butene with MDACT	Basic Isobutene with MDACT	Basic R152a with MDACT	Basic R123 with MDACT
Turbine inlet	T [°C]	202.5	201.0	205.0	208.9	162.7	202.1	200.9	201.3	206.9	162.3
Turbine inlet	P [MPa]	6.80	6.80	8.00	10.00	2.46	6.81	7.21	7.41	10.00	2.45
Condenser inlet	P [MPa]	0.48	0.58	0.59	1.14	0.21	0.52	0.63	0.63	1.21	0.25
Condenser inlet	T_{sat} [°C]	48.85	48.80	48.70	48.76	49.30	52.17	52.29	51.39	51.07	54.75
Cooling Water	$\dot{m}$ [kg/s]	765.0	751.0	755.0	755.9	771.2	-	-	-	-	-
Preheater	A [m^2]	-	-	-	-	780.00	-	-	-	-	810.00
	L_t [m]	-	-	-	-	10.90	-	-	-	-	11.50
	d_i [mm]	-	-	-	-	6.00	-	-	-	-	5.00
	P_t [-]	-	-	-	-	1.15	-	-	-	-	1.15
Evaporator	A [m^2]	-	-	-	-	245.00	-	-	-	-	255.00
	L_t [m]	-	-	-	-	7.90	-	-	-	-	6.85
	d_i [mm]	-	-	-	-	14.5	-	-	-	-	12.0
	P_t [-]	-	-	-	-	1.15	-	-	-	-	1.15
Supercritical Heat Exchanger	A [m^2]	820	895	950	920	-	1022	978	756	887	-
	L_t [m]	11.5	11.5	11.5	11.5	-	11.5	11.5	11.5	11.5	-
	d_i [mm]	5.20	5.00	5.20	5.00	-	5.00	5.00	5.00	5.00	-
	P_t [-]	1.15	1.15	1.15	1.15	-	1.15	1.15	1.15	1.15	-

Component / Stream	Variable	Basic Butane with NDDCT	Basic Butene with NDDCT	Basic Isobutene with NDDCT	Basic R152a with NDDCT	Basic R123 with NDDCT	Basic Butane with MDACT	Basic Butene with MDACT	Basic Isobutene with MDACT	Basic R152a with MDACT	Basic R123 with MDACT
MDACT	n_{tubes} [-]	-	-	-	-	-	5937	5661	5706	5063	6700
	n_{rows} [-]	-	-	-	-	-	3	3	3	3	4
	L_t [m]	-	-	-	-	-	19.3	20.0	20.0	19.3	20.0
	ΔT_{pp} [°C]	-	-	-	-	-	17.35	17.28	16.76	17.35	20.10
	W_{fan} [kWe]	-	-	-	-	-	94.81	103.13	106.39	170.05	150.63

*Fan motor work is not a decision variable, but is of interest as the ΔT_{pp} determines the air mass flow rate which in turn determines the fan motor power consumption, which has considerable effect on overall cycle performance.

Table 47: Values of the decision variables for detailed design optimisation of the recuperated ORCs, corresponding to the results given in Table 45, NDDCT values as shown in Table 41.

Component / Stream	Variable	Recuperated Butane with NDDCT	Recuperated Butene with NDDCT	Recuperated Isobutane with NDDCT	Recuperated Isobutene with NDDCT	Recuperated R152a with NDDCT	Recuperated Butane with MDACT	Recuperated Butene with MDACT	Recuperated Isobutane with MDACT	Recuperated Isobutene with MDACT	Recuperated R152a with MDACT
Turbine inlet	T [°C]	192.4	191.4	197.7	190.9	195.2	193.8	191.4	194.1	190.5	197.9
Turbine inlet	P [MPa]	6.43	6.52	8.28	6.33	8.90	6.57	6.57	8.00	6.62	9.59
Condenser inlet	P [MPa]	0.51	0.61	0.67	0.61	1.17	0.51	0.64	0.71	0.62	1.20
Condenser inlet	T_{sat} [°C]	49.50	49.64	48.95	49.29	49.33	50.39	51.76	50.30	50.28	50.36
Cooling Water	$\dot{m}$ [kg/s]	732.0	736.0	619.5	730.5	744.0	-	-	-	-	-
Supercritical Heat	A [m^2]	875	812	920	864	814	768	883	852	805	886

Component / Stream	Variable	Recuperated Butane with NDDCT	Recuperated Butene with NDDCT	Recuperated Isobutane with NDDCT	Recuperated Isobutene with NDDCT	Recuperated R152a with NDDCT	Recuperated Butane with MDACT	Recuperated Butene with MDACT	Recuperated Isobutane with MDACT	Recuperated Isobutene with MDACT	Recuperated R152a with MDACT
Exchanger	L_t [m]	11.5	11.5	11.5	11.5	11.5	11.5	11.5	11.5	11.5	11.5
	d_i [mm]	5.0	5.0	5.0	5.0	5.0	5.2	5.0	5.0	5.5	5.0
	P_t [-]	1.15	1.15	1.15	1.15	1.15	1.15	1.15	1.15	1.15	1.15
Recuperator	A [m²]	250	167	200	100	190	150	150	300	110	140
	L_t [m]	3.3	2.5	4	2.3	2.9	2.55	2.5	4	2.75	2.25
	d_i [mm]	8.0	9.0	8.0	9.0	9.0	9.0	9.0	7.0	9.0	9.0
	P_t [-]	1.25	1.25	1.5	1.5	1.25	1.25	1.25	1.25	1.5	1.25
MDACT	n_{tubes} [-]	-	-	-	-	-	6217	6030	6200	6345	6140
	n_{rows} [-]	-	-	-	-	-	3	3	3	3	3
	L_t [m]	-	-	-	-	-	20.0	20.0	20.0	19.2	19.3
	ΔT_{pp} [ºC]	-	-	-	-	-	18.00	18.50	17.80	18.37	18.16
	W_{fan}* [kWe]	-	-	-	-	-	118.66	98.30	107.25	144.80	133.14

*Fan motor work is not a decision variable, but is of interest as the ΔT_{pp} determines the air mass flow rate which in turn determines the fan motor power consumption, which has considerable effect on overall cycle performance.

Table 48: Values of the decision variables for detailed design optimisation of the regenerative ORCs, corresponding to the results given in Table 45, NDDCT values as shown in Table 41.

Component / Stream	Variable	Regenerative Butane with NDDCT	Regenerative Butene with NDDCT	Regenerative Isobutene with NDDCT	Regenerative R152a with NDDCT	Regenerative Isopentane with NDDCT	Regenerative Butane with MDACT	Regenerative Butene with MDACT	Regenerative Isobutene with MDACT	Regenerative R152a with MDACT	Regenerative Isopentane with MDACT
Turbine inlet	T [ºC]	196.0	194.1	202.3	200.9	167.3	196.6	193.7	200.4	203.1	164.5
Turbine inlet	P [MPa]	6.82	6.60	8.00	9.75	2.48	6.85	6.69	8.26	9.40	2.36
Condenser inlet	P [MPa]	0.48	0.58	0.59	1.14	0.20	0.51	0.63	0.62	1.21	0.22
Condenser inlet	T_{sat} [ºC]	48.93	49.10	48.80	48.81	49.10	51.19	52.54	50.83	50.97	51.80
Cooling Water	$\dot{m}$ [kg/s]	740.0	739.0	747.0	743.6	758.4	-	-	-	-	-
LP Turbine inlet	P [MPa]	0.65	0.82	1.00	1.50	0.31	0.69	0.78	0.78	1.44	0.30
LP Turbine inlet	T [ºC]	90.3	93.2	99.7	95.5	103.3	92.6	89.4	86.4	99.3	102.5
Preheater	A [m²]	-	-	-	-	615	-	-	-	-	875
	L_t [m]	-	-	-	-	11.5	-	-	-	-	11.5
	d_i [mm]	-	-	-	-	5.25	-	-	-	-	5.0
	P_t [-]	-	-	-	-	1.15	-	-	-	-	1.15
Evaporator	A [m²]	-	-	-	-	235	-	-	-	-	259
	L_t [m]	-	-	-	-	5.0	-	-	-	-	6.0
	d_i [mm]	-	-	-	-	15.0	-	-	-	-	15.0
	P_t [-]	-	-	-	-	1.15	-	-	-	-	1.15
Supercritical Heat Exchanger	A [m²]	665	745	815	800	-	939	880	931	952	-
	L_t [m]	11.5	11.5	11.5	11.5	-	11.5	11.5	11.5	11.5	-

Component / Stream	Variable	Regenerative Butane with NDDCT	Regenerative Butene with NDDCT	Regenerative Isobutene with NDDCT	Regenerative R152a with NDDCT	Regenerative Isopentane with NDDCT	Regenerative Butane with MDACT	Regenerative Butene with MDACT	Regenerative Isobutene with MDACT	Regenerative R152a with MDACT	Regenerative Isopentane with MDACT
	d_i [mm]	5.25	5.15	5.25	5.0	-	5.0	5.0	5.0	5.0	-
	P_t [-]	1.15	1.15	1.15	1.15	-	1.15	1.15	1.15	1.15	-
MDACT	n_{tubes} [-]	-	-	-	-	-	5376	5289	5486	5320	5684
	n_{rows} [-]	-	-	-	-	-	3	4	3	3	3
	L_t [m]	-	-	-	-	-	20.0	20.0	20.0	20.0	20.0
	ΔT_{pp}[°C]	-	-	-	-	-	17.1	17.8	16.7	16.9	17.9
	W_{fan}* [kWe]	-	-	-	-	-	130.0	148.2	134.0	123.9	113.6

*Fan motor work is not a decision variable, but is of interest as the ΔT_{pp} determines the air mass flow rate which in turn determines the fan motor power consumption, which has considerable effect on overall cycle performance.
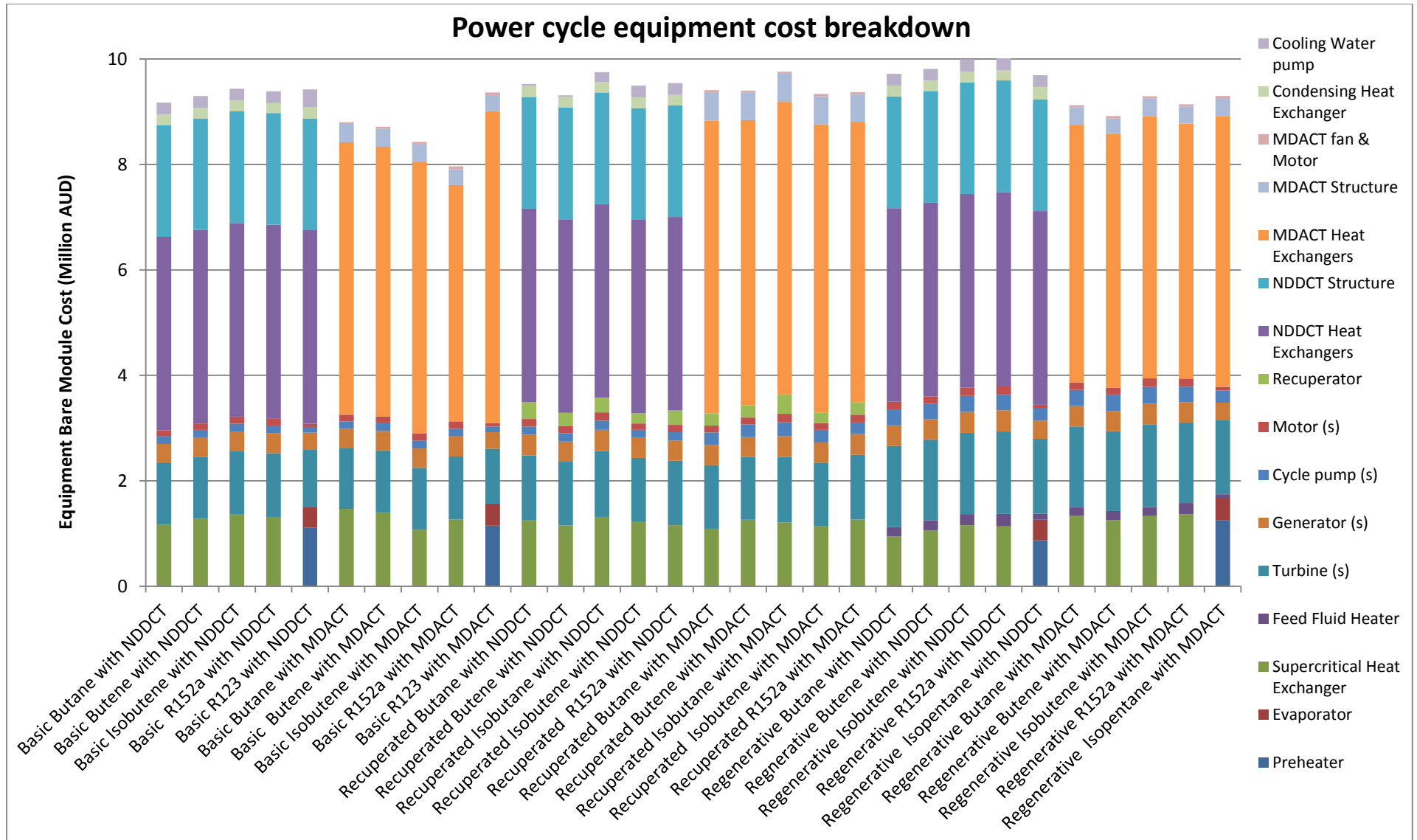
Figure 79: Power cycle bare module equipment cost breakdown by equipment item for each cycle, corresponding to the results given in Table 45.

Table 49: Equipment bare module cost values found in the detailed design optimisation, for basic ORCs, in 2014 AUD.

	Basic Butane with NDDCT	Basic Butene with NDDCT	Basic Isobutene with NDDCT	Basic R152a with NDDCT	Basic R123 with NDDCT	Basic Butane with MDACT	Basic Butene with MDACT	Basic Isobutene with MDACT	Basic R152a with MDACT	Basic R123 with MDACT
Brine Heat Exchanger(s)	1,166,910	1,277,810	1,360,330	1,315,190	1,509,064	1,470,140	1,402,630	1,073,800	1,266,330	1,564,320
Turbine	1,167,370	1,178,000	1,199,620	1,208,080	1,077,400	1,156,930	1,175,370	1,173,860	1,196,610	1,043,810
Generator	365,235	369,614	378,506	381,984	328,076	360,937	368,531	367,908	377,270	314,145
Cycle pump	140,962	140,961	147,212	143,768	107,038	142,172	147,455	149,193	146,182	109,888
Motor	119,941	120,000	133,389	138,128	62,673	122,088	128,365	129,514	140,648	65,415
Indirect NDDCT System	6,214,043	6,210,690	6,218,662	6,200,810	6,337,816	-	-	-	-	-
MDACT	-	-	-	-	-	5,550,029	5,494,053	5,533,723	4,834,908	6,267,619

Table 50: Equipment bare module cost values found in the detailed design optimisation, for recuperated cycles, in 2014 AUD.

	Recuperated Butane with NDDCT	Recuperated Butene with NDDCT	Recuperated Isobutane with NDDCT	Recuperated Isobutene with NDDCT	Recuperated R152a with NDDCT	Recuperated Butane with MDACT	Recuperated Butene with MDACT	Recuperated Isobutane with MDACT	Recuperated Isobutene with MDACT	Recuperated R152a with MDACT
Brine Heat Exchanger(s)	1,248,050	1,155,060	1,315,430	1,232,170	1,157,820	1,091,650	1,260,430	1,213,410	1,144,290	1,264,400
Recuperator	316,338	244,863	279,784	191,026	273,705	230,946	230,959	370,855	199,420	232,668
Turbine	1,233,020	1,208,500	1,251,430	1,202,980	1,222,290	1,206,250	1,191,850	1,239,890	1,201,530	1,230,600
Generator	390,477	382,158	399,776	379,888	387,823	381,231	375,311	395,047	379,292	391,233
Cycle pump	157,724	154,702	174,380	150,530	152,838	239,492	244,981	264,683	242,404	221,277

	Recuperated Butane with NDDCT	Recuperated Butene with NDDCT	Recuperated Isobutane with NDDCT	Recuperated Isobutene with NDDCT	Recuperated R152a with NDDCT	Recuperated Butane with MDACT	Recuperated Butene with MDACT	Recuperated Isobutane with MDACT	Recuperated Isobutene with MDACT	Recuperated R152a with MDACT
Motor	146,054	144,718	156,061	123,005	139,299	130,204	129,618	157,027	128,609	146,012
Indirect NDDCT System	6,033,275	6,021,729	6,174,067	6,214,874	6,211,059	-	-	-	-	-
MDACT	-	-	-	-	-	6,129,900	5,967,816	6,120,468	6,044,423	5,883,810

Table 51: Equipment bare module cost values found in the detailed design optimisation, for regenerative cycles, in 2014 AUD.

	Regenerative Butane with NDDCT	Regenerative Butene with NDDCT	Regenerative Isobutene with NDDCT	Regenerative R152a with NDDCT	Regenerative Isopentane with NDDCT	Regenerative Butane with MDACT	Regenerative Butene with MDACT	Regenerative Isobutene with MDACT	Regenerative R152a with MDACT	Regenerative Isopentane with MDACT
Brine Heat Exchanger(s)	944,295	1,058,030	1,159,590	1,137,680	1,263,589	1,344,300	1,255,470	1,331,710	1,363,300	1,664,493
Feed Fluid Heater	177,884	194,769	208,535	237,419	113,584	153,536	173,019	170,377	215,286	80,196
Turbines	1,539,640	1,527,950	1,543,620	1,563,110	1,421,610	1,532,450	1,512,860	1,562,280	1,527,210	1,403,710
Generators	392,167	388,230	396,894	402,042	344,099	389,239	379,712	400,561	385,349	335,307
Cycle pumps	301,373	294,792	302,420	300,996	225,559	304,906	306,806	319,235	295,124	226,011
Motors	145,168	141,039	157,308	163,778	75,821	145,368	140,218	160,018	151,550	72,020
Indirect NDDCT System	6,216,832	6,210,377	6,228,939	6,212,999	6,245,948	-	-	-	-	-
MDACT	-	-	-	-	-	5,253,894	5,150,565	5,349,999	5,203,236	5,516,586

Table 52: Equipment cost as a percentage of total equipment cost (excluding heat source subsystem cost) for each cycle, corresponding to the results given in Table 45.

	Brine Heat Exchanger(s) (%)	Feed Fluid Heater (%)	Recuperator (%)	Turbine(s) (%)	Generator(s) (%)	Cycle pump(s) (%)	Motor(s) (%)	Indirect NDDCT System (%)	MDACT (%)
Basic Butane with NDDCT	12.7	-	-	12.7	4.0	1.5	1.3	67.7	-
Basic Butene with NDDCT	13.7	-	-	12.7	4.0	1.5	1.3	66.8	-
Basic Isobutene with NDDCT	14.4	-	-	12.7	4.0	1.6	1.4	65.9	-
Basic R152a with NDDCT	14.0	-	-	12.9	4.1	1.5	1.5	66.1	-
Basic R123 with NDDCT	16.0	-	-	11.4	3.5	1.1	0.7	67.3	-
Basic Butane with MDACT	16.7	-	-	13.1	4.1	1.6	1.4	-	63.1
Basic Butene with MDACT	16.1	-	-	13.5	4.2	1.7	1.5	-	63.0
Basic Isobutene with MDACT	12.7	-	-	13.9	4.4	1.8	1.5	-	65.7
Basic R152a with MDACT	15.9	-	-	15.0	4.7	1.8	1.8	-	60.7
Basic R123 with MDACT	16.7	-	-	11.1	3.4	1.2	0.7	-	66.9
Recuperated Butane with NDDCT	13.1	-	3.3	12.9	4.1	1.7	1.5	63.3	-
Recuperated Butene with NDDCT	12.4	-	2.6	13.0	4.1	1.7	1.6	64.7	-
Recuperated Isobutane with NDDCT	13.5	-	2.9	12.8	4.1	1.8	1.6	63.3	-
Recuperated Isobutene with NDDCT	13.0	-	2.0	12.7	4.0	1.6	1.3	65.5	-
Recuperated R152a with NDDCT	12.1	-	2.9	12.8	4.1	1.6	1.5	65.1	-
Recuperated Butane with MDACT	11.6	-	2.5	12.8	4.1	2.5	1.4	-	65.1
Recuperated Butene with MDACT	13.4	-	2.5	12.7	4.0	2.6	1.4	-	63.5
Recuperated Isobutane with MDACT	12.4	-	3.8	12.7	4.0	2.7	1.6	-	62.7
Recuperated Isobutene with MDACT	12.3	-	2.1	12.9	4.1	2.6	1.4	-	64.7

	Brine Heat Exchanger(s) (%)	Feed Fluid Heater (%)	Recuperator (%)	Turbine(s) (%)	Generator(s) (%)	Cycle pump(s) (%)	Motor(s) (%)	Indirect NDDCT System (%)	MDACT (%)
Recuperated R152a with MDACT	13.5	-	2.5	13.1	4.2	2.4	1.6	-	62.8
Regenerative Butane with NDDCT	9.7	1.8	-	15.8	4.0	3.1	1.5	64.0	-
Regnerative Butene with NDDCT	10.8	2.0	-	15.6	4.0	3.0	1.4	63.3	-
Regenerative Isobutene with NDDCT	11.6	2.1	-	15.4	4.0	3.0	1.6	62.3	-
Regenerative R152a with NDDCT	11.4	2.4	-	15.6	4.0	3.0	1.6	62.0	-
Regenerative Isopentane with NDDCT	13.0	1.2	-	14.7	3.6	2.3	0.8	64.5	-
Regenerative Butane with MDACT	14.7	1.7	-	16.8	4.3	3.3	1.6	-	57.6
Regenerative Butene with MDACT	14.1	1.9	-	17.0	4.3	3.4	1.6	-	57.8
Regenerative Isobutene with MDACT	14.3	1.8	-	16.8	4.3	3.4	1.7	-	57.6
Regenerative R152a with MDACT	14.9	2.4	-	16.7	4.2	3.2	1.7	-	56.9
Regenerative Isopentane with MDACT	17.9	0.9	-	15.1	3.6	2.4	0.8	-	59.3

The results given in Table 45 show that the NDDCT condensed cycles achieve an SIC value that is 2% to 6% lower than for their respective MDACT condensed cycles for all cases except the basic R123 cycle, for which the NDDCT cycle is 11% lower. The MDACT system is much lower in cost than the indirect NDDCT system, for the basic and regenerative cycles. However, as mentioned earlier the MDACTs for the recuperated cycles require somewhat larger heat transfer surface area due to the increased latent heat transfer incurred by recuperating the sensible heat from the turbine exhaust stream. This brings the MDACTs for the recuperated cycles up to a similar cost as the indirect NDDCT systems. The NDDCT condensed cycles achieve significantly higher $\dot{W}_{net}$ than the MDACT condensed cycles, so even with the higher TCI values, the NDDCT cycles achieve lower SIC values in all cases considered.

Figure 79 shows that the condensing system forms the largest proportion of the power cycle equipment cost, i.e., not including heat source subsystem cost, at an average of about 60% across the cycles considered, with heat exchangers and turbine(s) forming the next largest, both at about 13%. Equipment cost as a percentage of total cost is also presented below in Figure 80.

As shown above in Figure 79, the preheater cost is higher than the evaporator cost for the subcritical cycles considered; this is due to a much higher heat load in the preheater.

In many cases the brine heat exchanger(s) cost is noticeably different for the NDDCT and MDACT versions of the same cycle. These cases may be due to the lower condensing temperature for NDDCTs, which results in a lower brine heat exchanger cycle fluid inlet temperature, which gives a higher MTD allowing less heat transfer surface area; they may also be due to the optimisation resulting in selection of dissimilar operating turbine inlet temperatures, or a combination of the two.

The power cycle equipment cost data is summarised below in Figure 80 with sub-system costs grouped and represented as a percentage of the total equipment cost, excluding the heat source subsystem cost.

Figure 80: Percentage of total equipment bare module cost for each sub-system of the power cycle. This excludes the heat source subsystem cost.

The majority of selected design points have a reduced turbine inlet temperature as compared to the preliminary analysis. This suggests that it's more economical to reduce the turbine inlet temperature from the thermodynamic optimum found in the preliminary analysis in order to increase the MTD and thereby decrease the heat transfer surface area required and the cost of the heat exchangers. As a small reduction in turbine inlet temperature doesn't significantly affect the net power generation but reducing the heat exchanger area has a non-negligible effect on TCI and therefore SIC, because as is shown above, heat exchangers form a significant portion of system cost.

For supercritical cycles the turbine inlet pressure is not as influential on cycle performance, as compared to sub-critical cycles, where the evaporation pressure determines the pinch point temperature difference and small changes in pressure can have a significant influence on the $\dot{W}_{net}$ and the heat transfer area required.

As shown in Table 45, the highest performing cycle in terms of SIC is the recuperated cycle; the basic and regenerative cycles have only slightly lower SIC values. The five cycles with the lowest SIC value are selected to progress to the annual performance analysis stage, these consist of four recuperated cycles and a basic cycle. The next two highest ranked cycles are regenerative cycles which are also considered for comparison. Finally, to compare the performance with varying ambient temperature of NDDCTs versus MDACTS one of each cycle is also considered with MDACT. Butene is the only fluid with a finalist cycle of each cycle type, so this will be used for the MDACT comparison. The 10 cycles being considered in the next stage are given in Table 53.

Table 53: The cycles being considered in the annual performance analysis.

Cycle	SIC (AUD /kWe)
Recuperated isobutene with NDDCT	15,366
Recuperated butene with NDDCT	15,401
Recuperated butane with NDDCT	15,436
Basic butene with NDDCT	15,739
Recuperated R152a with NDDCT	16,017
Regenerative butane with NDDCT	15,732
Regenerative butene with NDDCT	15,739
Basic butene with MDACT	16,439
Recuperated butene with MDACT	16,397
Regenerative butene with MDACT	16,583

7. Plant Performance Variation with Ambient Temperature

The aim of this section is to determine the variation of plant performance with changing ambient temperatures. Each of the selected cycles were analysed in IPSEpro across the range of ambient temperatures expected at Innamincka, South Australia. These results were then used to predict the annual performance variation of each power cycle based on historical temperature data. The climate data used in this analysis was sourced from the Australian Bureau of Meteorology (BOM), and is given in Appendix D. This section also compares the performance variation with changing ambient temperature of each of the finalist cycle types as well as for NDDCT versus MDACT condensed cycles. Diurnal, seasonal and annual performance variation is investigated, and the mean annual net power generation calculated. This was used to find the annualised SIC for each of the finalist cycles, the measure by which the optimum cycle for the conditions given in Table 1 is selected.

7.1 Performance Variation with Ambient Temperature

Each of the selected cycles were analysed at intervals of 5°C across the expected range of ambient temperatures, the results are summarised here in Figure 81.
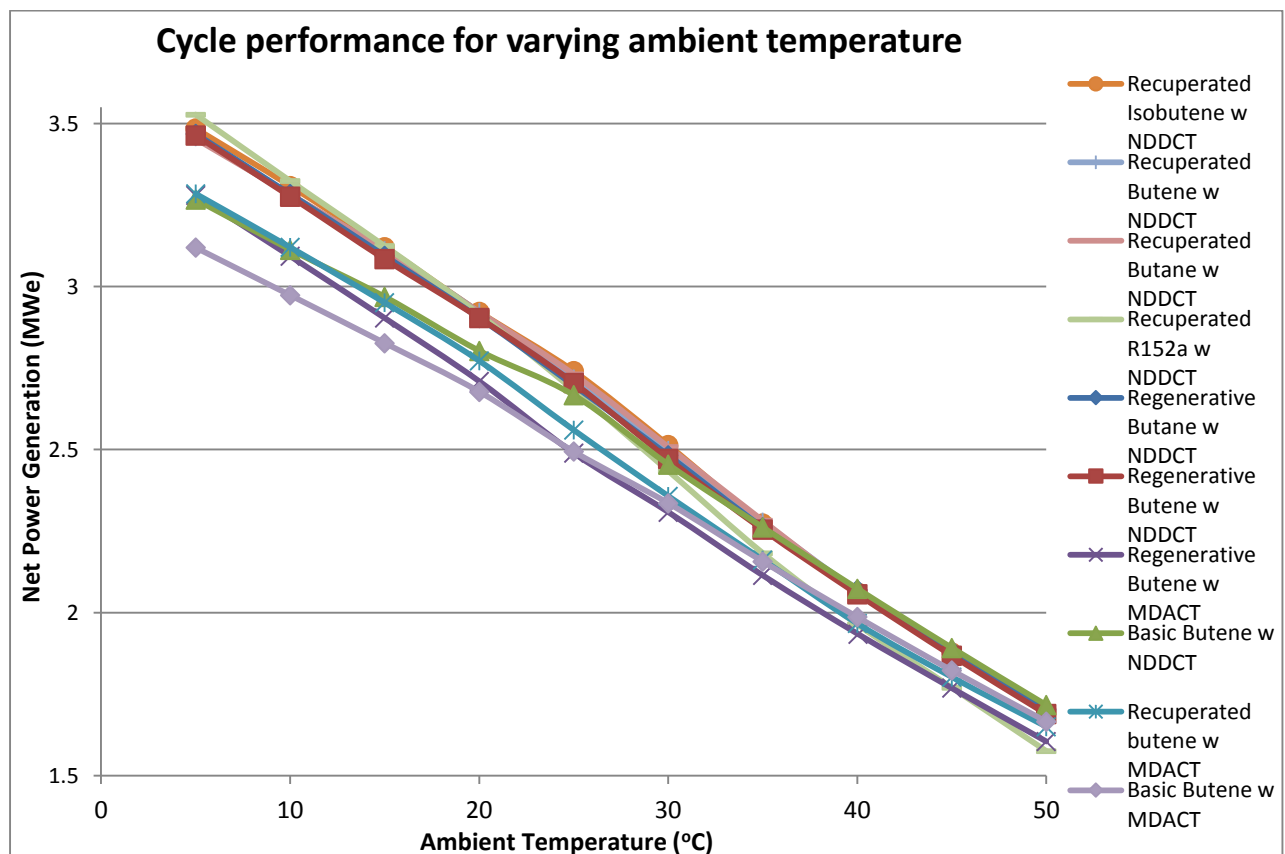
Figure 81: Net power generation vs ambient temperature.

144

The recuperated and regenerative cycles show an approximately linear dependence on ambient temperature, whereas the basic cycle shows a change in gradient at the design point. The change in gradient for the basic cycle at ambient temperatures below the design point, shown below in Figure 82, indicates that the basic ORC lacks the capacity to exploit the lower condensing temperature afforded by lower ambient temperatures, as the recuperated and regenerative cycle are able to. At ambient temperatures above the design point the basic cycle exhibits a similar performance curve to the other cycles, indicating that all cycles are similarly limited by increasing ambient temperature.

Net power generation vs ambient temperature for butene basic ORC with NDDCT

$y = -0.03021x + 3.41710$

$y = -0.03788x + 3.59796$
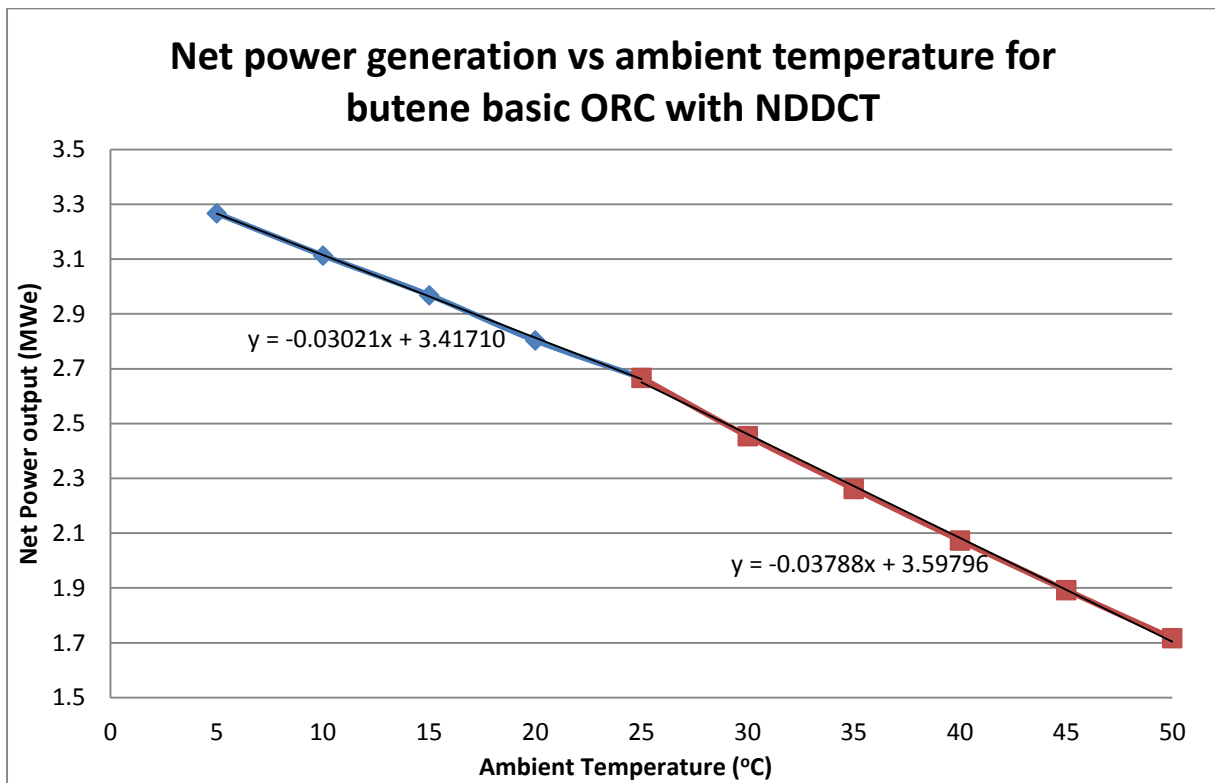
Figure 82: Variation of net power generation with changing ambient temperature for the basic butene cycle, showing the slight change in gradient at the design point of 25 °C ambient temperature.

In order to compare the performance variation of each of the cycle configurations considered, the $\dot{W}_{net}$ across the range of ambient temperatures is plotted below in Figure 83 for NDDCT and MDACT for each of the cycle types using butene as the cycle fluid.
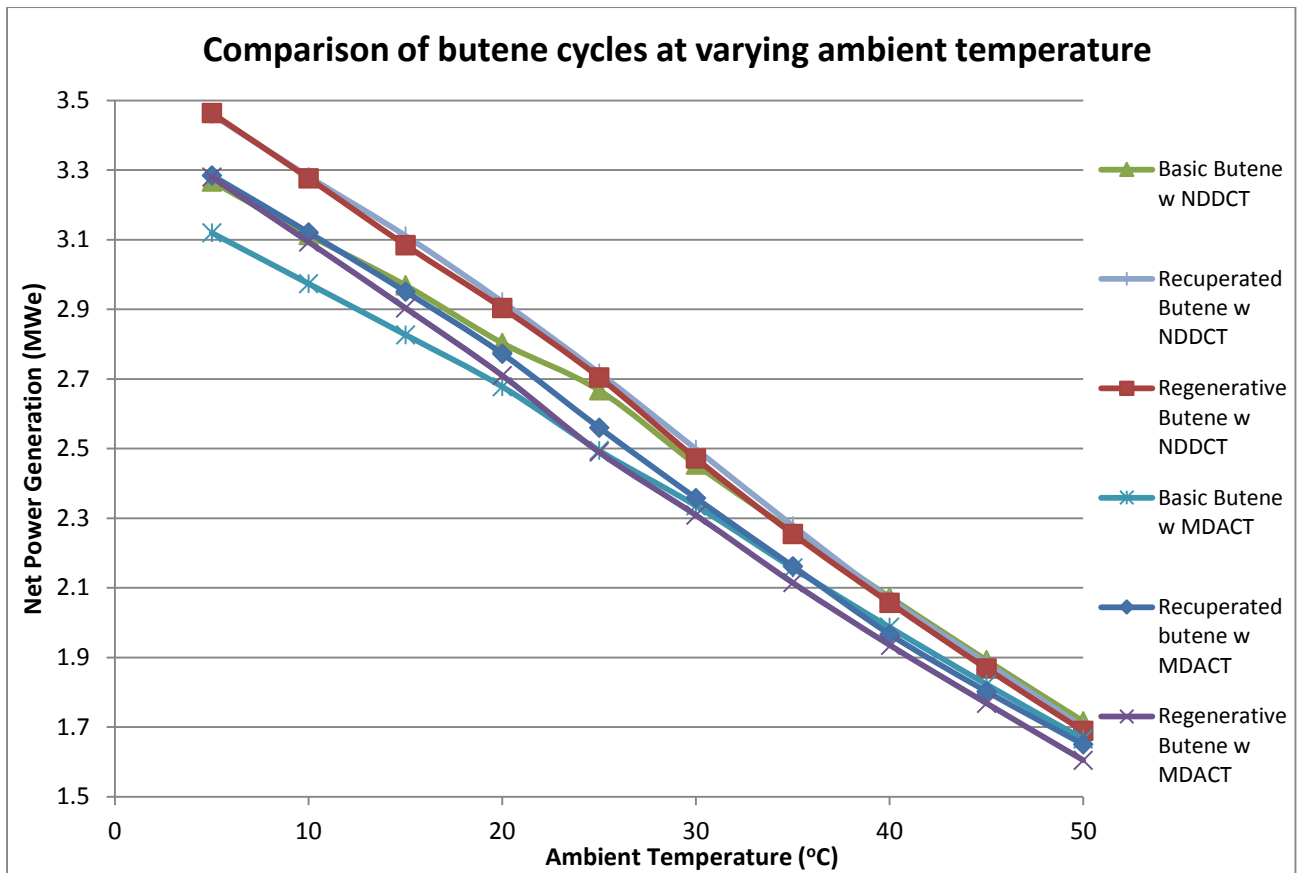
Figure 83: Comparison of the cycle types and of NDDCT vs. MDACT using butene as the cycle fluid, for varying ambient temperature.

Figure 83 illustrates the benefit of the recuperated and regenerative cycles over the basic cycle, which is quite significant at lower ambient temperatures. The recuperated cycle achieves this by maintaining an elevated brine heat exchanger inlet temperature for decreasing condensing temperature, through recuperating sensible heat at the turbine exhaust. This has the disadvantage of increasing the MDACT size, as was shown in Section 6.3.

The regenerative cycle allows control of the regeneration rate, which can be varied to control the brine heat exchanger inlet temperature to maintain the design point heat transfer for reduced ambient temperatures. This increases cycle efficiency, because as regeneration rate is increased the mass flow rate to the condenser decreases, resulting in less heat being rejected to the atmosphere. This capacity comes at the expense of the feed fluid heater, which is a relatively low cost, and the higher cost of turbines, but does not however negatively affect MDACT size as the inlet temperature remains the same, and only the mass flow rate changes for decreasing ambient temperature.

At ambient temperatures higher than the design point the performance curve of the basic cycle converges with the recuperated and regenerative cycles, signifying the end of the

beneficial range of the recuperator and of regeneration. This occurs as the rising condensing temperature approaches the recuperator outlet and feed fluid heater outlet temperature and the recuperator and feed fluid heater can no longer be of benefit.

The MDACT cycles appear to follow the same trend as their respective NDDCT cycles, but at a lower $\dot{W}_{net}$. Interestingly, this modelling shows that with increasing ambient temperature the MDACT cycles performance curves seem to approach that of the NDDCT cycles.

7.2 Diurnal Performance Variation

To investigate the influence of seasonal variation on the $\dot{W}_{net}$ on a diurnal basis, a sample set of typical temperatures for each season were used. Temperature data from BOM for 2012 was used and the sample temperatures were taken from the third week of January, April, July and October to represent the seasons. The diurnal and seasonal variation is illustrated below in Figure 84.
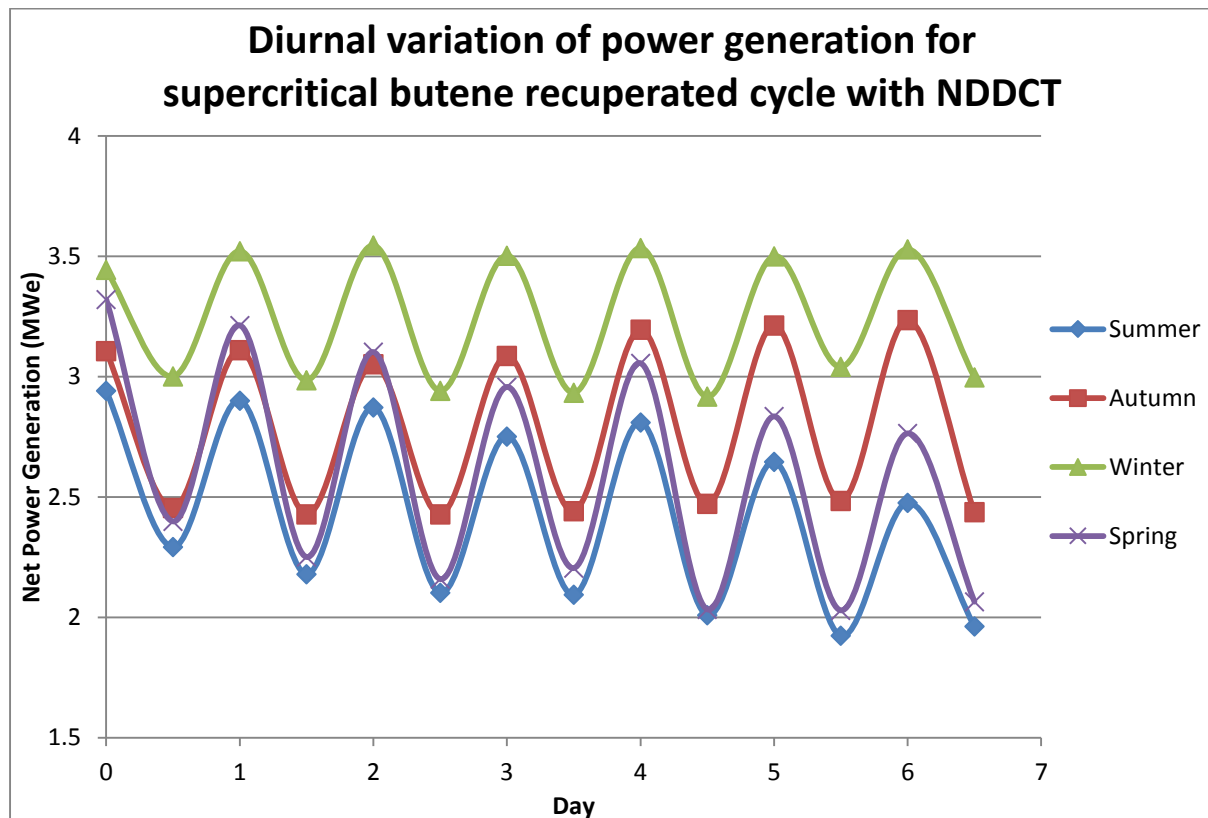
Figure 84: Diurnal variation of power plant performance for a sample week of each season from 2012. Sample temperatures for the third week of January, April, July and October of 2012, data taken from BOM.

As can be seen from Figure 84, there is significant variation in $\dot{W}_{net}$ on a daily basis as well as a seasonal basis due to the changing ambient temperature. The diurnal variability in winter is notably lower than for the other seasons, which in this case is due to the lower variation in

temperature for the sample week. A comparison of typical $\dot{W}_{net}$ ranges for each of the selected cycles is presented below in Figure 85 for the sample week of summer used above.
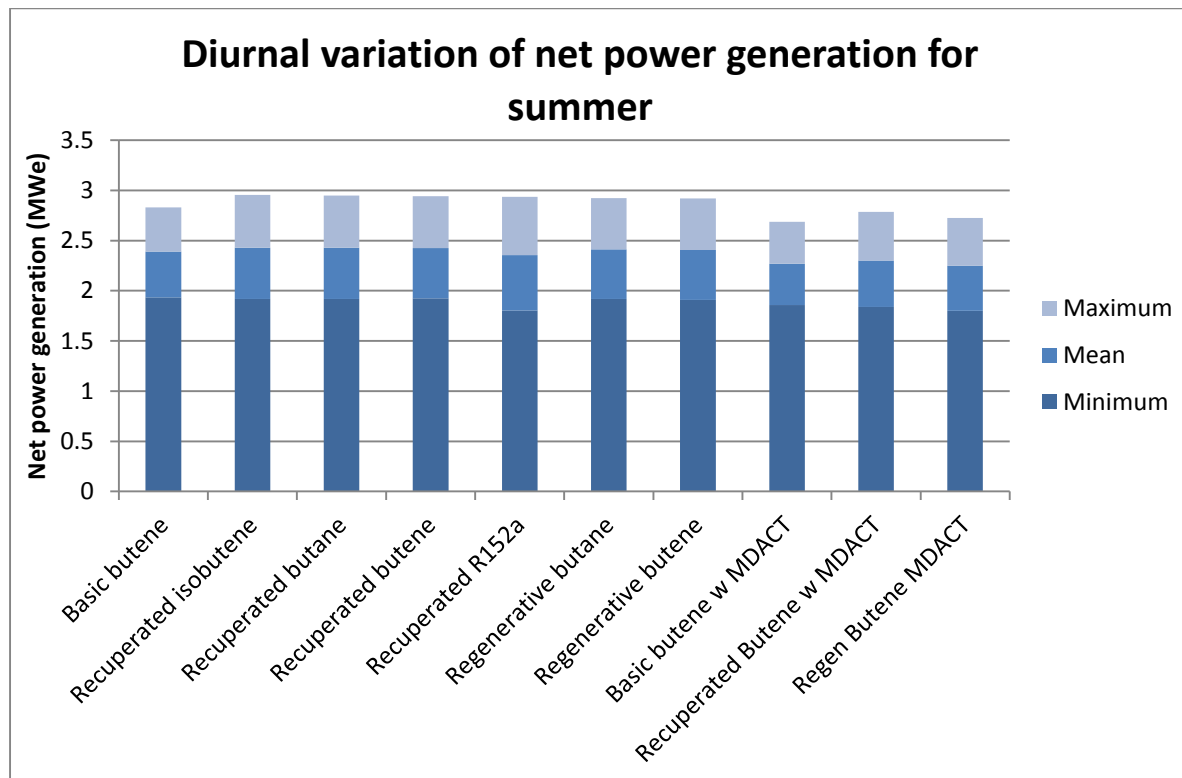
Figure 85: Range of net power generation for the sample week of summer, the third week of January 2012, for each of the selected cycles.

The above figure shows the degree of $\dot{W}_{net}$ variability changes for each fluid and cycle type. Recuperated R152a has a high range but a lower mean $\dot{W}_{net}$, when compared to some other cycles, such as recuperated butene which has a higher mean and lower range of $\dot{W}_{net}$. The latter is presumably the advantageous scenario as it gives a consistently higher power generation. The seasonal variation data is presented numerically in Table 54 through Table 57.

Table 54: Diurnal analysis over the sample week of summer 2012, with mean temperature of 31.7 °C. The same sample data as per Figure 84 is used.

	Min. $\dot{W}_{net}$ (MWe)	Mean. $\dot{W}_{net}$ (MWe)	Max. $\dot{W}_{net}$ (MWe)	Range $\dot{W}_{net}$ (MWe)	Min. $\dot{W}_{net}$ relative to mean (%)	Max. $\dot{W}_{net}$ relative to mean (%)
Basic butene	1.935	2.390	2.831	0.896	-19.0	18.4
Recuperated isobutene	1.918	2.430	2.955	1.037	-21.1	21.6
Recuperated butane	1.920	2.428	2.947	1.028	-20.9	21.4
Recuperated butene	1.923	2.426	2.942	1.018	-20.7	21.3

148

	Min. $\dot{W}_{net}$ (MWe)	Mean. $\dot{W}_{net}$ (MWe)	Max. $\dot{W}_{net}$ (MWe)	Range $\dot{W}_{net}$ (MWe)	Min. $\dot{W}_{net}$ relative to mean (%)	Max. $\dot{W}_{net}$ relative to mean (%)
Recuperated R152a	1.803	2.357	2.934	1.131	-23.5	24.5
Regenerative butane	1.920	2.413	2.923	1.004	-20.4	21.2
Regenerative butene	1.908	2.406	2.921	1.013	-20.7	21.4
Basic butene with MDACT	1.859	2.271	2.688	0.830	-18.1	18.4
Recuperated butene with MDACT	1.838	2.300	2.786	0.948	-20.1	21.1
Regenerative butene with MDACT	1.800	2.250	2.726	0.926	-20.0	21.1

Table 55: Diurnal analysis over the sample week of autumn 2012, with mean temperature of 22.7 ºC. The same sample data as per Figure 84 is used.

	Min. $\dot{W}_{net}$ (MWe)	Mean. $\dot{W}_{net}$ (MWe)	Max. $\dot{W}_{net}$ (MWe)	Range $\dot{W}_{net}$ (MWe)	Min. $\dot{W}_{net}$ relative to mean (%)	Max. $\dot{W}_{net}$ relative to mean (%)
Basic butene	2.401	2.704	3.064	0.663	-11.2	13.3
Recuperated isobutene	2.433	2.807	3.255	0.822	-13.3	15.9
Recuperated butane	2.432	2.800	3.237	0.805	-13.1	15.6
Recuperated butene	2.429	2.796	3.235	0.806	-13.1	15.7
Recuperated R152a	2.355	2.771	3.270	0.915	-15.0	18.0
Regenerative butane	2.413	2.782	3.227	0.814	-13.3	16.0
Regenerative butene	2.407	2.777	3.223	0.816	-13.3	16.0
Basic butene with MDACT	2.275	2.573	2.929	0.654	-11.6	13.9
Recuperated butene with MDACT	2.296	2.648	3.071	0.775	-13.3	16.0
Regenerative butene with MDACT	2.245	2.597	3.029	0.784	-13.6	16.6

Table 56: Diurnal analysis over the sample week of winter 2012, with mean temperature of 10.7 ºC. The same sample data as per Figure 84 is used.

	Min. $\dot{W}_{net}$ (MWe)	Mean. $\dot{W}_{net}$ (MWe)	Max. $\dot{W}_{net}$ (MWe)	Range $\dot{W}_{net}$ (MWe)	Min. $\dot{W}_{net}$ relative to mean (%)	Max. $\dot{W}_{net}$ relative to mean (%)
Basic butene	2.813	3.093	3.369	0.556	-9.1	8.9
Recuperated isobutene	2.930	3.263	3.574	0.643	-10.2	9.5
Recuperated butane	2.923	3.239	3.529	0.606	-9.8	9.0
Recuperated butene	2.917	3.243	3.545	0.628	-10.0	9.3

	Min. $\dot{W}_{net}$ (MWe)	Mean. $\dot{W}_{net}$ (MWe)	Max. $\dot{W}_{net}$ (MWe)	Range $\dot{W}_{net}$ (MWe)	Min. $\dot{W}_{net}$ relative to mean (%)	Max. $\dot{W}_{net}$ relative to mean (%)
Recuperated R152a	2.906	3.279	3.625	0.718	-11.4	10.6
Regenerative butane	2.899	3.244	3.572	0.673	-10.7	10.1
Regenerative butene	2.896	3.238	3.560	0.664	-10.6	10.0
Basic butene with MDACT	2.669	2.942	3.201	0.533	-9.3	8.8
Recuperated butene with MDACT	2.763	3.077	3.369	0.606	-10.2	9.5
Regenerative butene with MDACT	2.702	3.058	3.403	0.701	-11.6	11.3

Table 57: Diurnal analysis over the sample week of spring 2012, with mean temperature of 27.4 ºC. The same sample data as per Figure 84 is used.

	Min. $\dot{W}_{net}$ (MWe)	Mean. $\dot{W}_{net}$ (MWe)	Max. $\dot{W}_{net}$ (MWe)	Range $\dot{W}_{net}$ (MWe)	Min. $\dot{W}_{net}$ relative to mean (%)	Max. $\dot{W}_{net}$ relative to mean (%)
Basic butene	2.038	2.534	3.139	1.102	-19.6	23.9
Recuperated isobutene	2.026	2.607	3.343	1.317	-22.3	28.2
Recuperated butene	2.029	2.599	3.321	1.292	-21.9	27.8
Recuperated butane	2.027	2.601	3.320	1.293	-22.1	27.6
Recuperated R152a	1.916	2.552	3.369	1.452	-24.9	32.0
Regenerative butane	2.023	2.588	3.319	1.296	-21.8	28.3
Regenerative butene	2.012	2.581	3.314	1.302	-22.1	28.4
Basic butene with MDACT	1.948	2.412	3.002	1.054	-19.2	24.4
Recuperated butene with MDACT	1.931	2.465	3.154	1.224	-21.7	28.0
Regenerative butene with MDACT	1.892	2.417	3.125	1.233	-21.7	29.3

According to the above results, the variability in winter is lower, at roughly $\mp$ 10%, whereas summer and spring see variability of greater than $\mp$ 20%. The basic butene cycle shows lower variability but also a lower mean $\dot{W}_{net}$ than the other cycles. The recuperated R152a cycle shows the highest mean $\dot{W}_{net}$ in winter; however, is not the highest for the other seasons. The recuperated isobutene cycle shows the highest mean $\dot{W}_{net}$ in the other seasons and also exhibits a fairly low variability. The MDACT cycles show a similar degree of variability to their respective NDDCT cycles.

7.3 Annual Performance Variation

150

The annual performance variation analysis used daily temperature data from the Bureau of Meteorology (BOM) for 2012, to calculate the annual mean $\dot{W}_{net}$ of each of the cycles. The results for the supercritical butene recuperated cycle are shown below in Figure 86, comparing the net power generation for the NDDCT and MDACT. These two cycle configurations are selected for comparison to illustrate the effect of NDDCT versus MDACT on cycle performance.
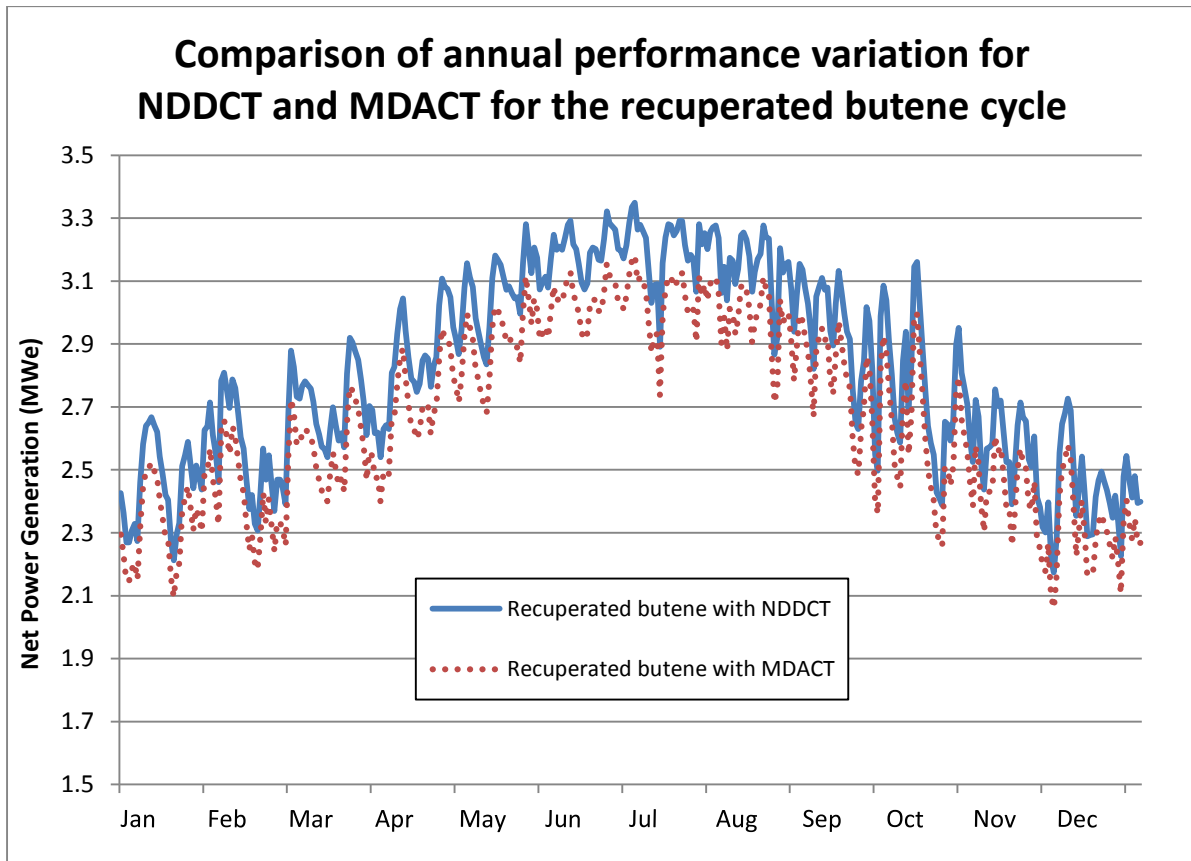
Figure 86: Comparison of the annual performance variation in net power generation of recuperated butene cycle with NDDCT and with MDACT calculated for daily temperatures for 2012.

Figure 86 is for mean daily temperature data for a specific year. The limits of upper and lower expected $\dot{W}_{net}$ were also calculated based on historical monthly data from BOM for the highest maximum, lowest maximum, highest minimum and lowest minimum for the period of 1972 to 1999, this is shown below in Figure 87.
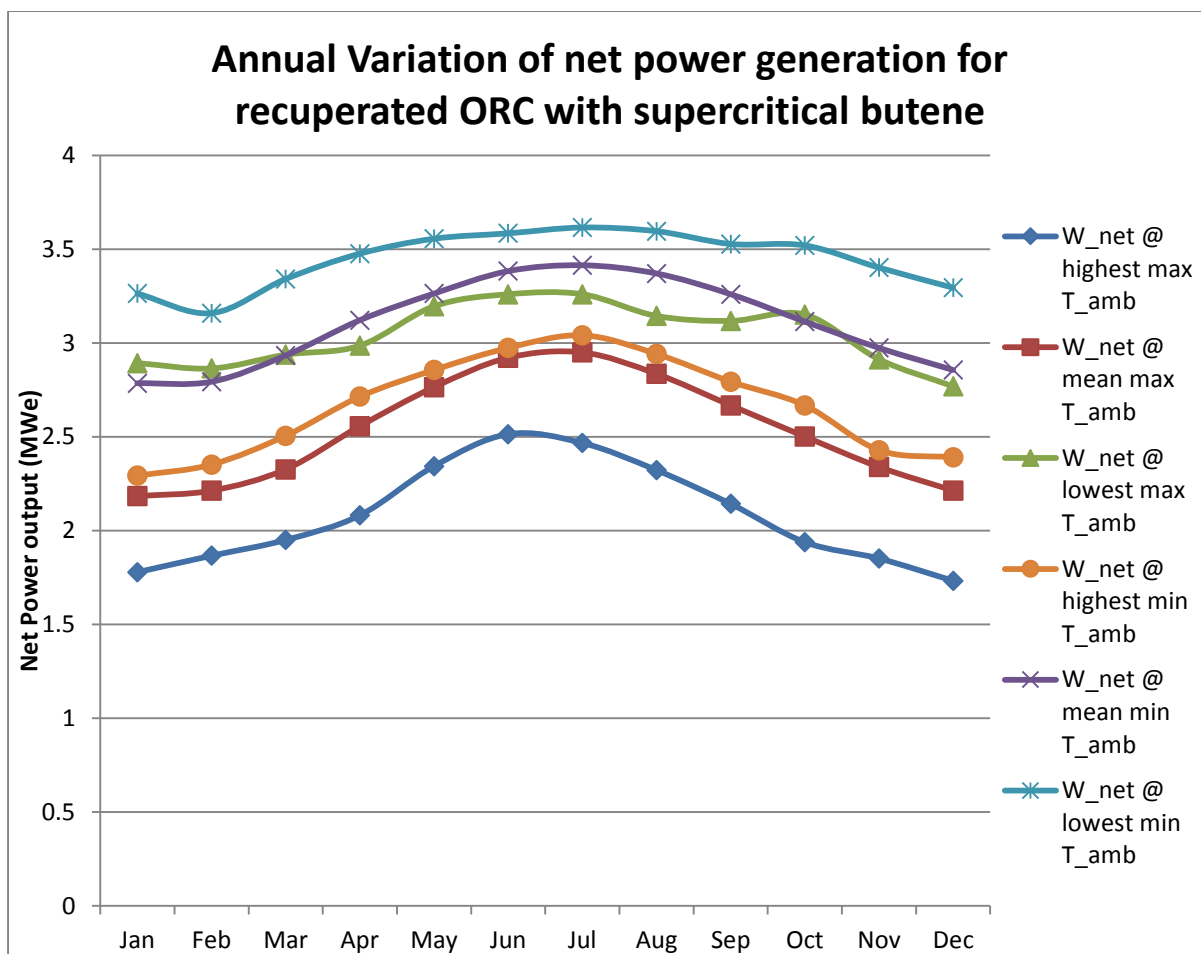
Figure 87: Upper and lower limits of expected annual variation of net power generation calculated from monthly temperature data from BOM for 1972 to 1999.

Figure 87 shows that in the extreme case $\dot{W}_{net}$ can vary by over 1.5 MWe. The range between the mean maximum and mean minimum temperatures is 0.5 MWe to 0.6 MWe, this is likely to be a more representative range for a typical year. From the daily temperature data, a mean annual $\dot{W}_{net}$ was calculated for each cycle, and from this and the TCI value found in the design point analysis the annualised SIC was calculated. The results are given below in Table 58.

Table 58: Mean annual net power generation and annualised SIC for each of the finalist cycles, calculated using 2012 temperature data from BOM.

	Mean Annual $\dot{W}_{net}$ (MWe)	TCI (AUDx10⁶)	Annualised SIC (AUD/kWe)
Recuperated isobutene with NDDCT	2.832	42.112	14,870
Recuperated butene with NDDCT	2.821	41.851	14,838
Recuperated butane with NDDCT	2.825	42.156	14,925
Recuperated R152a with NDDCT	2.798	42.184	15,075

	Mean Annual $\dot{W}_{net}$ (MWe)	TCI (AUDx10^6)	Annualised SIC (AUD/kWe)
Basic butene with NDDCT	2.729	41.830	15,327
Regenerative butane with NDDCT	2.805	42.430	15,125
Regenerative butene with NDDCT	2.801	42.570	15,196
Basic butene with MDACT	2.592	41.001	15,819
Recuperated butene with MDACT	2.671	41.979	15,715
Regenerative butene with MDACT	2.618	41.290	15,771

Interestingly, the recuperated butene cycle mean annual $\dot{W}_{net}$ increased more than that for the isobutene recuperated cycle from the design point, as was shown in Table 45. As the recuperated butene has a slightly lower TCI and a similar mean annual $\dot{W}_{net}$, it ends up with a lower annualised SIC.

8. Conclusion

The aim of this project was to identify the optimum power cycle configuration for an Australian EGS power plant using a binary ORC and NDDCT. This was performed over several stages, starting with a preliminary analysis of a wide range of organic fluids in several cycle configurations, optimising cycles for maximum net power generation, $\dot{W}_{net}$. The highest performing cycles were designed to a more detailed stage using one-dimensional condenser and heat exchanger models, and using cost correlations to optimise the cycles for the SIC. At this stage each cycle was designed separately with an NDDCT and MDACT as the condenser to compare the impact on cycle performance. Following this a selection of cycles were analysed at the range of ambient temperatures expected. This data was then used in calculating diurnal and annual performance variation of each of the cycles. Finally, a mean annual net power generation was calculated from daily temperature data for 2012 and an annualised SIC was calculated for each cycle, the measure by which final selection of the optimum cycle is made.

8.1 Preliminary Analysis

The preliminary analysis began with searching REFPROP for all fluids with critical temperature in the range of 50 to 250 ºC, and these formed the candidate fluid list. Relevant physical properties, health, safety and environmental data was collected where available. These fluids were then analysed in a range of cycle configurations: basic ORC, ORC with recuperator, regenerative ORC and dual fluid ORC, optimising for maximum $\dot{W}_{net}$.

There were a number of fluids that were analysed although REFPROP states their upper temperature limit is below the brine inlet temperature of 220 ºC, because the stated limit is the applicability limits of the correlations used in the software, not necessarily the thermal stability limit of the fluid. There were a number of fluids this situation applied to and which were found to achieve a high $\dot{W}_{net}$, but they were not progressed to the detailed design stage as the thermal stability limit needs to be verified before any further consideration is given to these fluids.

The preliminary analysis found that the 15 cycles with the highest $\dot{W}_{net}$ were the basic, recuperated and regenerative ORC configurations, with the highest three being recuperated cycles. The highest performing fluids were butane, butene, isobutene, R152a, R123 and isopentane. The dual fluid cycle underperformed as compared to the other cycles.

The highest performing cycles from the preliminary analysis were found to be supercritical cycles, with the highest performing subcritical cycle generating about 5% less net power than the highest supercritical cycles. The critical temperatures of the highest performing supercritical fluids are in the range of 110 ºC to 170ºC. The high performing subcritical fluids have higher critical temperatures, ranging from 170 ºC to 190 ºC.

8.2 NDDCT Analysis

As part of this thesis a detailed NDDCT model was developed in IPSEpro based on the Kroger (2004) method. This model was analysed in Chapter 5, first in isolation to investigate the effects of varying key geometric parameters, and then in a reference case basic cycle to investigate how NDDCT size affects cycle performance.

The results of the independent NDDCT analysis found that increasing tower height for constant base diameter and heat exchanger area significantly increases heat rejection, and decreases SIC_{cd}, which is the specific investment cost of the condensing system in AUD/kWth of heat rejection; an aspect ratio of 1.4 was selected. Decreasing the outlet diameter relative to the base diameter was found to slightly decrease the heat rejection rate but to improve SIC_{cd} due to the lower tower structure cost, and a diameter ratio of 0.7 was selected. The proportion of heat exchanger coverage of the tower inlet was also investigated and it was found that decreasing the heat exchanger coverage increased the heat rejection, for constant heat exchanger area, but also increased the SIC_{cd} value, decreasing cost effectiveness, as the increased cost of the tower structure outweighed the benefit to the additional heat rejection. The proportion of the tower inlet that can be utilised depends on the heat exchanger configuration and is also limited by the additional space required for heat exchanger supports; a value of 0.65 was used.

The NDDCT design configuration found above was then used to determine the optimum overall NDDCT size for the cycle used in the reference case. Four tower sizes were investigated, specified by the number of bundles and the three geometric ratios identified above. Increasing the tower size allows a lower condensing temperature for the cycle, which results in a higher $\dot{W}_{net}$, but results in increasing the NDDCT cost. It was found that the tower with 22 bundles, and a tower height of 52.5 m provided the lowest SIC value for the cycle. This NDDCT design was then used in the design point calculations

8.3 Detailed Cycle Design

Each of the selected finalist cycles were optimised separately for minimum SIC using an indirect condensing NDDCT and direct condensing MDACT, at the design point ambient temperature of 25 °C. A detailed STHE model was used so the heat transfer surface area could be accurately calculated. This analysis found in all cases that the NDDCT condensed cycles, despite their higher TCI, gave significantly lower SIC values, due to the increased $\dot{W}_{net}$. An additional benefit of NDDCT condensing is found due to the lower condensing temperature and fixed brine outlet temperature, a smaller heat transfer area is required due to the increase in mean temperature difference, resulting in cheaper heat exchangers. The condensers formed the majority of the power cycle equipment cost, at about 60% of the total power cycle equipment cost, i.e., excluding the heat source subsystem cost. The heat exchangers and turbines were the next highest proportion, both at approximately 13% of total equipment cost.

The highest performing cycles in ascending order of SIC were the recuperated cycles with isobutene, butene and butane, the basic butene cycle, the recuperated R152a and the regenerative butene and regenerative butane cycles. These are all supercritical cycles, the subcritical cycles considered in this stage underperformed due to lower $\dot{W}_{net}$ and higher TCI. These cycles were selected to progress to the annual performance variation analysis along with one of each cycle type with an MDACT condenser, in order to allow comparison of NDDCT and MDACT performance variation with changing ambient temperature. Butene was used as the cycle fluid for the MDACT cases, as it is the only fluid selected for each cycle and so will allow direct comparison of NDDCT and MDACT performance.

8.4 Annual Performance Analysis

The selected cycles were first analysed at intervals of 5 °C across the range of ambient temperatures expected at Innamincka, South Australia. The recuperated and regenerative cycles showed approximately linear dependence on ambient temperature, the basic ORC showed linear dependence but with a change of gradient after the design point of 25 °C. This is due to the inability of the basic cycle to effectively exploit the lower condensing temperature as the recuperated and regenerative cycles can. The brine heat exchanger heat transfer profiles for the basic butene cycle are very well matched at the design point, however as the condensing temperature, and therefore the brine heat exchanger inlet temperature is reduced, the heat transfer profiles are no longer ideally matched. This results in a higher

MTD and allows the heat exchanger outlet temperature to be increased, but the benefit in terms of $\dot{W}_{net}$ is not as high as maintaining the design point heat transfer, as in the cases of the recuperated and regenerative cycles.

The cycle performance data at various ambient temperatures was used to determine the diurnal variability of $\dot{W}_{net}$ of each cycle for a sample week of each of the four seasons. The results showed a strong variation with season, with the mean $\dot{W}_{net}$ for the regenerative butene ORC in winter being 3.247 MWe as compared to 2.404 MWe for summer. The results also found that the diurnal variation in summer was higher than in the winter, at about $\mp$ 20% and $\mp$ 10% respectively.

Next, the mean annual $\dot{W}_{net}$ for each cycle was calculated from daily temperature data for 2012. The results found that the NDDCT condensed cycles generated a mean annual $\dot{W}_{net}$ of 5.3% to 7% higher than their respective MDACT condensed cycles. The cycle found to have the highest mean annual $\dot{W}_{net}$ value was the recuperated isobutene cycle at 2.832 MWe. The mean annual $\dot{W}_{net}$ values were used to calculate the annualised SIC, for which the recuperated supercritical butene cycle has the lowest value and is therefore selected as the optimum cycle configuration.

8.5 Recommendations for Future Work

This thesis uses a comprehensive approach to the detailed cycle design and off-design analysis of ORC using NDDCTs and MDACTs. The results of this work are based on assumptions and cost correlations suitable for a feasibility level study. In order to provide a higher level of accuracy further work is required. The areas for further work are:

- Account for quantity of fluid required, availability and cost.
- Quantify cost of additional plant safety measures required for use of flammable cycle fluids as this may have a non-negligible effect on the overall plant cost.
- Acquire supplier quotes to validate the equipment cost models used. Especially cooling tower cost models as they form the largest proportion of the equipment cost.
- Determine turbine isentropic efficiency for each cycle fluid considered and characterise off-design performance.
- Implement a more detailed analysis of supercritical heat transfer process, utilising a stepwise calculation method of fluid properties and local heat transfer coefficient.
- Implement a detailed PHE model to model the condenser.

- A number of fluids such as R245fa and R245ca were identified in the preliminary analysis as thermodynamically promising fluids for this heat source temperature; however, the temperature upper limit stated in REFPROP is lower than the brine inlet temperature. As stated in Section 3.2 this is not necessarily the thermal stability limit of the fluid, but the validity limit of the correlation used in REFPROP. Further investigation into the actual thermal stability limits of these fluids is recommended.

- Further investigation of the geothermal brine properties to determine the effect of lowering the brine outlet temperature on the rate of fouling and perform a trade-off analysis on the cost of increased maintenance and downtime vs the higher net power output. Walraven et al. (2013) found that constraint of the brine outlet temperature from the heat exchangers greatly decreases the power output of the system.

9. References

Akers, W. W., & Rosson, H. F. (1960). Condensation inside a horizontal tube. *Chemical Engineering Progress Symposium Series, 56*(30), 145-149.

AlfaLaval. (n.d.). Compabloc - the new laser welded heat exchanger series.   Retrieved 15/03/2014, from http://www.alfalaval.com/solution-finder/products/compabloc/Documents/PPM00033EN.pdf

Angelino, G., & Colonna di Paliano, P. (1998). Multicomponent Working Fluids For Organic Rankine Cycles (ORCs). *Energy, 23*(6), 449-463. doi: http://dx.doi.org/10.1016/S0360-5442(98)00009-7

Annaratone, D. (2007). *Pressure Vessel Design*

Annaratone, D. (2010). Handbook for Heat Exchangers and Tube Banks Design.

ASHRAE. (2009). Chapter 29 - Refrigerants *ASHRAE Handbook: Fundamentals*. Atlanta, GA: American Society of Heating, Refrigeration and Air-Conditioning Engineers, Inc.

Astolfi, M., Xodo, L., Romano, M. C., & Macchi, E. (2011). Technical and economical analysis of a solar–geothermal hybrid plant based on an Organic Rankine Cycle.

Atrens, A. D., Gurgenci, H., & Rudolph, V. (2011). Economic Optimization of a CO2-Based EGS Power Plant. *Energy & Fuels, 25*(8), 3765-3775. doi: Doi 10.1021/Ef200537n

Augustine, C., Field, R., DiPippo, R., Gigliucci, G., Fastelli, I., & Tester, J. (2009). Modeling and Analysis of Sub- and Supercritical Binary Rankine Cycles for Low- to Mid-Temperature Geothermal Resources. *Geothermal Resources Council Transactions, 33*, 689-694.

Bao, J., & Zhao, L. (2013). A review of working fluid and expander selections for organic Rankine cycle. *Renewable and Sustainable Energy Reviews, 24*, 325-342. doi: 10.1016/j.rser.2013.03.040

Bertani, R. (2015, 19-25 April 2015). *Geothermal Power Generation in the World - 2010–2015 Update Report.* Paper presented at the World Geothermal Congress 2015, Melbourne, Australia.

Branan, C. R. (2005). *Rules of Thumb for Chemical Engineers - A Manual of Quick, Accurate Solutions to Everyday Process Engineering Problems*

Brown, D. (2009). Hot Dry Rock Geothermal Energy; Important Lessons from Fenton Hill.

Bureau of Meterology, A. G. (2015). Climate statistics for Australian locations - Summary statistics MOOMBA. from http://www.bom.gov.au/climate/averages/tables/cw_017096.shtml

California Energy Commission. (2015). Geothermal Energy in California.   Retrieved 24/03/15, from http://www.energy.ca.gov/geothermal/background.html

Calise, F., Capuozzo, C., Carotenuto, A., & Vanoli, L. (2014). Thermoeconomic analysis and off-design performance of an organic Rankine cycle powered by medium-temperature heat sources. *Solar Energy, 103*, 595-609. doi: DOI 10.1016/j.solener.2013.09.031

Calise, F., Capuozzo, C., & Vanoli, L. (2013). Design and parametric optimization of an organic rankine cycle powered by solar energy. *American Journal of Engineering and Applied Sciences*, 178-204.

Campos Rodríguez, C. E., Escobar Palacio, J. C., Venturini, O. J., Silva Lora, E. E., Melián Cobas, V., Marques dos Santos, D., . . . Gialluca, V. (2013). Exergetic and economic comparison of ORC and Kalina cycle for low temperature enhanced geothermal system in Brazil. *Applied Thermal Engineering, 52*.

Chen, H., Goswami, D. Y., & Stefanakos, E. K. (2010). A review of thermodynamic cycles and working fluids for the conversion of low-grade heat. *Renewable and Sustainable Energy Reviews, 14*(9), 3059-3067. doi: http://dx.doi.org/10.1016/j.rser.2010.07.006

Clean Energy Action Project. (2012). Geothermal Energy Case Studies: Landau EGS Geothermal CHP Plant.   Retrieved 15/02/2014, from http://www.cleanenergyactionproject.com/CleanEnergyActionProject/Geothermal_Technologies_Case_Studies.html

Cooling Towers: Overhaul of two natural draft cooling towers in celsa ostrowiec steelworks (2007).   Retrieved 10/02/15, from http://www.uniserv.com.pl/en/Celsa.html

Delgado-Torres, A. M., & García-Rodríguez, L. (2007). Preliminary assessment of solar organic Rankine cycles for driving a desalination system.

DiPippo, R. (2004). Second Law assessment of binary plants generating power from low-temperature geothermal fluids. *Geothermics, 33*(5), 565-586. doi: 10.1016/j.geothermics.2003.10.003

DiPippo, R. (2008). *Geothermal Power Plants: Principles, Applications, Case Studies and Environmental Impact* (2nd ed.).

DiPippo, R. (2012). *Geothermal Power Plants: Principles Applications, Case Studies and Environmental Impact* (3rd ed.).

Drescher, U., & Brüggemann, D. (2006). Fluid selection for the Organic Rankine Cycle (ORC) in biomass power and heat plants. *Applied Thermal Engineering*.

Erbas, M., & Biyikoglu, A. (2013). *Design of low temperature Organic Rankine Cycle and turbine*. Paper presented at the 4th International Conference on Power Engineering, Energy and Electrical Drives, Istanbul, Turkey.

Fernández, F. J., Prieto, M. M., & Suárez, I. (2011). Thermodynamic analysis of high-temperature regenerative organic Rankine cycles using siloxanes as working fluid. *Energy*.

Forooghi, P., & Hooman, K. (2014). Experimental analysis of heat transfer of supercritical fluids in plate heat exchangers. *International Journal of Heat and Mass Transfer, 74*, 448-459. doi: DOI 10.1016/j.ijheatmasstransfer.2014.03.052

Franco, A., & Villani, M. (2009). Optimal design of binary cycle power plants for water-dominated, medium-temperature geothermal fields. *Geothermics, 38*(4), 379-391. doi: 10.1016/j.geothermics.2009.08.001

Gabbrielli, R. (2012). A novel design approach for small scale low enthalpy binary geothermal power plants. *Energy Conversion and Management, 64*, 263-272. doi: DOI 10.1016/j.enconman.2012.04.017

Ganjehsarabi, H., Gungor, A., & Dincer, I. (2012). Exergetic performance analysis of Dora II geothermal power plant in Turkey. *Energy*.

Geodynamics Limited. (2012). Enhanced Geothermal Systems Technology FAQ.   Retrieved 4/03/2015, from http://www.geodynamics.com.au/Resource-Centre/Geothermal-FAQ.aspx

Goodarzi, M. (2010). A proposed stack configuration for dry cooling tower to improve cooling efficiency under crosswind. *Journal of Wind Engineering and Industrial Aerodynamics, 98*(12), 858-863. doi: http://dx.doi.org/10.1016/j.jweia.2010.08.004

Goodarzi, M., & Keimanesh, R. (2013). Heat rejection enhancement in natural draft cooling tower using radiator-type windbreakers. *Energy Conversion and Management, 71*(0), 120-125. doi: http://dx.doi.org/10.1016/j.enconman.2013.03.031

Greenhut, A. D., Tester, J. W., DiPippo, R., Field, R., Love, C., Nichols, K., . . . Fastelli, I. (2010). *Solar-Geothermal Hybrid Cycle Analysis for Low Enthalpy Solar and Geothermal Resources.* Paper presented at the World Geothermal Congress 2010 Bali, Indonesia.

Gu, Z., & Sato, H. (2001). Optimisation of cyclic parameters of a supercritical cycle for geothermal power generation.

Gu, Z., & Sato, H. (2002). Performance of supercritical cycles for geothermal binary design.

Gupta, H. K., & Roy, S. (2006). *Geothermal Energy : An Alternative Resource for the 21st Century*

Guzovic, Z., Raskovic, P., & Blatari, Z. (2014). The comparision of a basic and a dual-pressure ORC (Organic Rankine Cycle): Geothermal Power Plant Velika Ciglena case study. *Energy, 76*, 175-186. doi: DOI 10.1016/j.energy.2014.06.005

He, S., Gurgenci, H., Guan, Z., & Alkhedhair, A. M. (2013). Pre-cooling with Munters media to improve the performance of Natural Draft Dry Cooling Towers. *Applied Thermal Engineering, 53*(1), 67-77. doi: 10.1016/j.applthermaleng.2012.12.033

Heberle, F., & Brüggemann, D. (2010). Exergy based fluid selection for a geothermal Organic Rankine Cycle for combined heat and power generation. *Applied Thermal Engineering*.

Huijuan Chen, D. Yogi Goswami, Muhammad M. Rahman, & Stefanakos, E. K. (2010). A supercritical Rankine cycle using zeotropic mixture working fluids for the conversion of low-grade heat into power.

Hung, T.-C. (2001). Waste heat recovery of organic Rankine cycle using dry fluids.

Imran, M., Park, B. S., Kimb, H. J., Lee, D. H., Usmana, M., & Heo, M. (2014). Thermo-economic optimization of Regenerative Organic Rankine Cycle for waste heat recovery applications. *Energy Conversion and Management, 87*, 107-118. doi: DOI 10.1016/j.enconman.2014.06.091

Invernizzi, C. M. (2013). Closed Power Cycles; Thermodynamic Fundamentals and Applications. London: Springer.

Jalilinasrabady, S., Itoi, R., Valdimarsson, P., Fujii, H., & Tanaka, T. (2011). Energy and Exergy Analysis of Sabalan Binary Geothermal Power Plant. *Journal of the Geothermal Research Society of Japan, 33*(3), 113-121. doi: 10.11367/grsj.33.113

Kang, S. H. (2012). Design and experimental study of ORC (organic Rankine cycle) and radial turbine using R245fa working flui. *Energy, 41*.

Kanoglu, M. (2002). Exergy analysis of a dual-level binary geothermal power plant. *Geothermics, 31*(6), 709-724.

Kanoglu, M., & Bolatturk, A. (2008). Performance and parametric investigation of a binary geothermal power plant by exergy. *Renewable Energy, 33*(11), 2366-2374. doi: DOI 10.1016/j.renene.2008.01.017

Karellas, S., & Schuster, A. (2008). Supercritical Fluid Parameters in Organic Rankine Cycle Applications.

Kranz, S. (2009). Market Study - Germany, Low-Bin project.   Retrieved 23/02/2015, from http://www.lowbin.eu/public/GFZ-LowBin_marketsituation.pdf

Kröger, D. G. (2004). *Air-Cooled Heat Exchangers and Cooling Towers*. Tulsa, Okl: Pennwell Corp.

Lai, N. A., Wendland, M., & Fischer, J. (2011). Working fluids for high-temperature organic Rankine cycles. *Energy, 36*(1), 199-211. doi: http://dx.doi.org/10.1016/j.energy.2010.10.051

Le, V. L., Feidt, M., Kheiri, A., & Pelloux-Prayer, S. (2014). Performance optimization of low-temperature power generation by supercritical ORCs (organic Rankine cycles) using low GWP (global warming potential) working fluid. *Energy, 67*, 513-526.

Le, V. L., Kheiri, A., Feidt, M., & Pelloux-Prayer, S. (2014). Thermodynamic and economic optimizations of a waste heat to power plant driven by a subcritical ORC (Organic Rankine Cycle) using pure or zeotropic working fluid. *Energy, 78*.

Lecompte, S., Huisseune, H., van den Broek, M., De Schampheleire, S., & De Paepe, M. (2013). Part load based thermo-economic optimization of the Organic Rankine Cycle (ORC) applied to a combined heat and power (CHP) system. *Applied Energy, 111*, 871-881. doi: DOI 10.1016/j.apenergy.2013.06.043

161

Lemmon, E. W., Huber, M. L., & McLinden, M. O. (2013). NIST Standard Reference Database 23: Reference Fluid Thermodynamic and Transport Properties-REFPROP, Version 9.1, National Institute of Standards and Technology, Standard Reference Data Program, Gaithersburg.

Li, M., Wang, J., Hea, W., Gaob, L., Wang, B., Maa, S., & Dai, Y. (2013). Construction and preliminary test of a low-temperature regenerative Organic Rankine Cycle (ORC) using R123. *Renewable Energy, 57*.

Li, M., Wang, J., Li, S., Wang, X., He, W., & Dai, Y. (2013). Thermo-economic analysis and comparison of a CO2 transcritical power cycle and an organic Rankine cycle. *Geothermics, 50*, 101-111.

Li, T. L., Wang, Q. L., Zhu, J. L., Hu, K. Y., & Fu, W. C. (2015). Thermodynamic optimization of organic Rankine cycle using two-stage evaporation. *Renewable Energy, 75*, 654-664. doi: DOI 10.1016/j.renene.2014.10.058

Liu, Q., Duan, Y., & Yang, Z. (2013). Performance analyses of geothermal organic Rankine cycles with selected hydrocarbon working fluid. *Energy*.

Lu, Y., Guan, Z., Gurgenci, H., & Zou, Z. (2013). Windbreak walls reverse the negative effect of crosswind in short natural draft dry cooling towers into a performance enhancement. *International Journal of Heat and Mass Transfer, 63*(0), 162-170. doi: http://dx.doi.org/10.1016/j.ijheatmasstransfer.2013.03.075

Lu, Y. S., Guan, Z. Q., Gurgenci, H., Hooman, K., He, S. Y., & Bharathan, D. (2015). Experimental study of crosswind effects on the performance of small cylindrical natural draft dry cooling towers. *Energy Conversion and Management, 91*, 238-248. doi: DOI 10.1016/j.enconman.2014.12.018

Lu, Y. S., Gurgenci, H., Guan, Z. Q., & He, S. Y. (2014). The influence of windbreak wall orientation on the cooling performance of small natural draft dry cooling towers. *International Journal of Heat and Mass Transfer, 79*, 1059-1069. doi: DOI 10.1016/j.ijheatmasstransfer.2014.09.012

Madhawa Hettiarachchi, H. D., Golubovic, M., Worek, W. M., & Ikegami, Y. (2007). Optimum design criteria for an Organic Rankine cycle using low-temperature geothermal heat sources. *Energy, 32*(9), 1698-1706. doi: 10.1016/j.energy.2007.01.005

Mago, P. J., Chamra, L. M., Srinivasan, K., & Somayaji, C. (2007). An examination of regenerative organic Rankine cycles using dry fluid.

Massoud, M. (2005). *Engineering Thermofluids; Thermodynamics, Fluid Mechanics and Heat Transfer*: Springer Berlin Heidelberg.

Meinel, D., Wieland, C., & Spliethoff, H. (2014). Economic comparison of ORC (Organic Rankine cycle) processes at different scales. *Energy, 74*.

Mills, T., & Humphreys, B. (2013). *Habanero Pilot Project - Australia's First EGS Power Plant*. Paper presented at the 2013 Australian Geothermal Energy Conference, Brisbane Australia.

Muñoz de Escalona, J. M., Sánchez, D., Chacartegui, R., & Sánchez, T. (2012). Part-load analysis of gas turbine & ORC combined cycles. *Applied Thermal Engineering*.

Naterer, G. F. (2003). Ch 10: Heat ExchangersHeat Transfer in Single and Multiphase Systems.

Peters, M. S., Timmerhaus, K., & West, R. E. (2003). *Plant Design and Economics for Chemical Engineers* (5th ed. ed.). Dubuque, IA: McGraw-Hill.

Petr, V., & Kolovratnik, M. (2013). *Wet steam energy loss and related Baumann rule in low pressure steam turbines*.

Quoilin, S., Declaye, S., Legros, A., Guillaume, L., & Lemort, V. (2012). *Working fluid selection and operating maps for Organic Rankine Cycle expansion machines.* Paper presented at the International Compressor Engineering Conference, Purdue.

Quoilin, S., Declaye, S., Tchanche, B. F., & Lemort, V. (2011). Thermo-economic optimization of waste heat recovery Organic Rankine Cycles. *Applied Thermal Engineering, 31*(14-15), 2885-2893. doi: DOI 10.1016/j.applthermaleng.2011.05.014

Quoilin, S., Van den Broek, M., Declaye, S., Dewallef, P., & Lemort, V. (2013). Techno-economic survey of Organic Rankine Cycle (ORC) systems. *Renewable & Sustainable Energy Reviews, 22*, 168-186. doi: DOI 10.1016/j.rser.2013.01.028

Ravagnani, M. A. S. S., Silva, A. P., Arroyo, P. A., & Constantino, A. A. (2005). Heat exchanger network synthesis and optimisation using genetic algorithm. *Applied Thermal Engineering, 25*(7), 1003-1017. doi: 10.1016/j.applthermaleng.2004.06.024

Rayegan, R., & Tao, Y. X. (2010). A procedure to select working fluids for Solar Organic Rankine Cycles (ORCs).

Rettig, A., Lagler, M., Lamare, T., Li, S., Mahadea, V., McCallion, S., & Chernushevich, J. (2011). Application of ORC.

Saadat, A., Frick, S., Kranz, S., & Regenspurg, S. (2010). Chapter 6; Energetic Use of EGS Reservoirs. In E. Huenges (Ed.), *Geothermal Energy Systems: Exploration, Development, and Utilization*. Weinheim, Germany: Wiley-VCH Verlag GmbH & Co. KGaA.

Sauret, E., & Rowlands, A. S. (2011). Candidate radial-inflow turbines and high-density working fluids for geothermal power systems. *Energy, 36*(7), 4460-4467. doi: 10.1016/j.energy.2011.03.076

Schröder, E., Neumaier, K., Nagel, F., & Vetter, C. (2014). Study on Heat Transfer in Heat Exchangers for a New Supercritical Organic Rankine Cycle

Schuster, A., Karellas, S., & Aumann, R. (2010). Efficiency optimization potential in supercritical Organic Rankine Cycles. *Energy, 35*(2), 1033-1039. doi: 10.1016/j.energy.2009.06.019

Shah, R. K., & Sekulic, D. P. (2003). *Fundamentals of heat exchanger design*.

Simtech. (2014). Manual: IPSEpro Process Simulator - Process Simulation Environment.

Smith, R. (2005). *Chemical Process Design and Integration*. Chichester: Wiley.

SPX. (2014). 800 class natural draft counterflow cooling tower. Overland Park, Kansas: SPX Cooling Technologies Inc.

Stewart, S. W. (2003). *Enhanced finned-tube condenser design and optimization.* (Doctoral Thesis), Georgia Institute of Technology.

Tempesti, D., & Fiaschi, D. (2013). Thermo-economic assessment of a micro CHP system fuelled by geothermal and solar energy. *Energy*.

Thulukkanam, K. (2013). *Heat Exchanger Design Handbook* (2nd ed.).

Toshiba. (n.d.). Totally enclosed fan cooled premium efficiency heavy duty electric motors.

Towler, G., & Sinnott, R. (2013). Chapter 7 - Capital Cost Estimating. In G. Towler & R. Sinnott (Eds.), *Chemical Engineering Design (Second Edition)* (pp. 307-354). Boston: Butterworth-Heinemann.

Turton, R., Bailie, R. C., Whiting, W. B., & Shaeiwitz, J. A. (2009). *Analysis, synthesis, and design of chemical processes*. Upper Saddle River, N.J: Prentice Hall.

VDI. (1980). *Wärmetechnische Arbeitsmappe* (12th ed. ed.).

VDI. (1988). *Wärmeatlas* (5th ed.). Düsseldorf, Germany: VDI-Gesellschaft Verfahrenstech.

VDI. (2010). *VDI Heat Atlas*

Vélez, F., Segovia, J. J., Martín, M. C., Antolín, G., Chejne, F., & Quijano, A. (2012). Comparative study of working fluids for a Rankine cycle operating at low

temperature. *Fuel Processing Technology, 103*(0), 71-77. doi: http://dx.doi.org/10.1016/j.fuproc.2011.09.017

Vetter, C., Wiemer, H.-J., & Kuhn, D. (2013). Comparison of sub- and supercritical Organic Rankine Cycles for power generation from low-temperature/low-enthalpy geothermal wells, considering specific net power output and efficiency. *Applied Thermal Engineering, 51*(1–2), 871-879. doi: http://dx.doi.org/10.1016/j.applthermaleng.2012.10.042

Walraven, D., Laenen, B., & D'haeseleer, W. (2013). Comparison of thermodynamic cycles for power production from low-temperature geothermal heat sources. *Energy Conversion and Management, 66*, 220-233. doi: DOI 10.1016/j.enconman.2012.10.003

Walraven, D., Laenen, B., & D'haeseleer, W. (2015). Economic system optimization of air-cooled organic Rankine cycles powered by low-temperature geothermal heat sources. *Energy, 80*, 104-113. doi: DOI 10.1016/j.energy.2014.11.048

Walraven, D., Laenen, B., & D'haeseleer, W. (2015). Minimizing the levelized cost of electricity production from low-temperature geothermal heat sources with ORCs: Water or air cooled? *Applied Energy, 142*, 144-153. doi: DOI 10.1016/j.apenergy.2014.12.078

Walraven, D., Laenen, B., & D'haeseleer, W. (2014). Optimum configuration of shell-and-tube heat exchangers for the use in low-temperature organic Rankine cycles.

Wang, J., Yan, Z., Zhao, P., & Dai, Y. (2014). Off-design performance analysis of a solar-powered organic Rankine cycle. *Energy Conversion and Management, 80*, 150-157. doi: DOI 10.1016/j.enconman.2014.01.032

Watson, A. (2013). *Geothermal Engineering; Fundamentals and Applications*. New York: Springer.

Wurtz, W., & Peltier, R. (2008). Air-cooled condensers eliminate plant water use. from http://www.powermag.com/air-cooled-condensers-eliminate-plant-water-use/

Xu, J., & Liu, C. (2013). Effect of the critical temperature of organic fluids on supercritical pressure Organic Rankine Cycles. *Energy, 63*(0), 109-122. doi: http://dx.doi.org/10.1016/j.energy.2013.09.068

Xu, R.-J., & He, Y.-L. (2011). A vapor injector-based novel regenerative organic Rankine cycle. *Applied Thermal Engineering, 31*(6–7), 1238-1243. doi: http://dx.doi.org/10.1016/j.applthermaleng.2010.12.026

Yanga, M.-H., & Yeh, R.-H. (2015). Economic performances optimization of the transcritical Rankine cycle systems in geothermal application. *Energy Conversion and Management, 95*, 20-31.

Yari, M. (2010). Exergetic analysis of various types of geothermal power plants. *Renewable Energy, 35*(1), 112-121. doi: http://dx.doi.org/10.1016/j.renene.2009.07.023

Yasuo, K. (2009). Thermodynamics/Power Cycles *Nuclear Engineering Handbook* (pp. 713-726): CRC Press.

Yildirim, D., & Ozgener, L. (2012). Thermodynamics and exergoeconomic analysis of geothermal power plants. *Renewable and Sustainable Energy Reviews*.

Zarrouk, S. J., & Moon, H. (2014). Efficiency of geothermal power plants: A worldwide review. *Geothermics, 51*(0), 142-153. doi: http://dx.doi.org/10.1016/j.geothermics.2013.11.001

Zhai, Z., & Fu, S. (2006). Improving cooling efficiency of dry-cooling towers under cross-wind conditions by using wind-break methods. *Applied Thermal Engineering, 26*(10). doi: http://dx.doi.org/10.1016/j.applthermaleng.2005.10.016

Zhang, F.-Z., & Jiang, P.-X. (2012). Thermodynamic analysis of a binary power cycle for different EGS geofluid temperatures. *Applied Thermal Engineering, 48*, 476-485. doi: DOI 10.1016/j.applthermaleng.2012.04.028

Zou, Z. (2013). *Development, Modelling and Optimisation of Solar Enhanced Natural Draft Dry Cooling Tower.* (PhD), University of Queensland.

Appendix A – NDDCT Model Validation - Comparison with Results from Kroger

The IPSEpro NDDCT model is compared to the results presented in Kroger Example 7.3.1 for validation. Item names are as denoted in Figure 88.
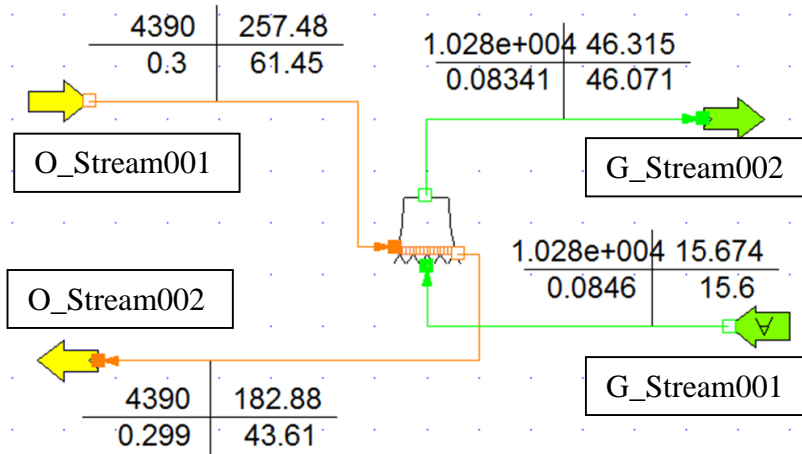
Figure 88: NDDCT IPSEpro model item names

The results of the validation are given for the key parameters presented in Kroger (2004).

Table 59: Comparison of IPSEpro model results against results from Kroger (2004) for validation

IPSEpro NDDCT Model values				Kroger Values			Discrepancy (%)
Item Name	Variable	Value	Units	Variable	Value	Units	
O_Stream002	T	43.6103	ºC	T_{wo}	43.59495	ºC	0.0352
O_NDDCT_Detailed001	q_trans	327512	kW	Q	327490	kW	0.0067
O_NDDCT_Detailed001	T_a4	320.239	K	T_{a4}	320.2471	K	-0.0025
O_NDDCT_Detailed001	T_a34	304.428	K	T_{a34}	304.4319	K	-0.0013
O_NDDCT_Detailed001	MTD_overall	20.4852	ºC	ΔT_{LM}	20.474	ºC	0.0547
O_NDDCT_Detailed001	F_T	0.95435	--	F_T	0.954265	--	0.0089
O_NDDCT_Detailed001	UA	16752.5	kW/K	UA	16762.2	kW/K	-0.0578

IPSEpro NDDCT Model values				Kroger Values			Discrepancy (%)
Item Name	Variable	Value	Units	Variable	Value	Units	
O_NDDCT_Detailed001	K_to	-0.70476	--	K_{to}	-0.70446	--	0.0422
O_NDDCT_Detailed001	K_tshe	0.424853	--	K_{tshe}	0.42466	--	0.0454
O_NDDCT_Detailed001	K_cthe	1.58863	--	K_{cthe}	1.5886	--	0.0019
O_NDDCT_Detailed001	K_ctche	1.23598	--	K_{ctche}	1.2359	--	0.0065
O_NDDCT_Detailed001	K_ctehe	1.27306	--	K_{ctehe}	1.27308	--	-0.0016
O_NDDCT_Detailed001	K_he_normal	28.974	--	K_{he}	28.9729	--	0.0038
O_NDDCT_Detailed001	K_he_theta	35.3186	--	$K_{he\theta}$	35.3175	--	0.0031
O_NDDCT_Detailed001	htc_t	6.92232	kW/m^2	h_w	69487.6	W/m^2	-0.3805

Appendix B – NDDCT Model Validation - Comparison with MATLAB Code based on Kroger

The IPSEpro NDDCT model was analysed in isolation with identical inlet conditions specified and then compared against the results found by the MATLAB code utilised in (He, Gurgenci, Guan, & Alkhedhair, 2013). The largest magnitude of discrepancy was 0.84% with most values being significantly less.
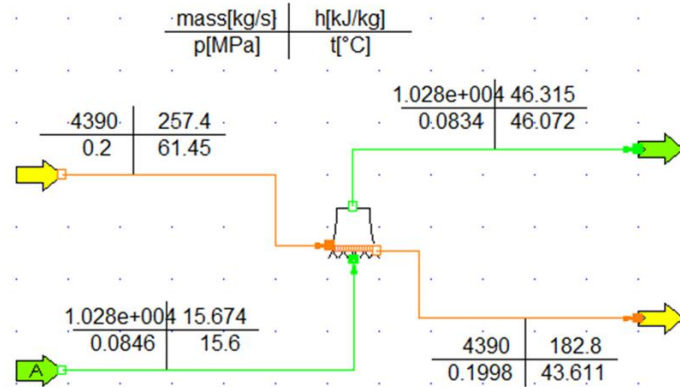
Figure 89: Screenshot of the NDDCT model being analysed in isolation

Table 60: Model Performance Validation by comparison of results with MATLAB Code

IPSEpro NDDCT model results		Largest discrepancy		0.8412 %	Suoying HE's MATLAB code results		
		Largest negative discrepancy		-0.4741 %			
Object	Variable	Value	Units	% Discrepancy	Name	Value	Units
O_NDDCT_Detailed001	A_cfs	21368.4		-0.0028	Aw	21369	
O_NDDCT_Detailed001	A_fr	4625.34		-0.0963	Afr	4629.8	
O_NDDCT_Detailed001	A_ti	0.06786		-0.0619	Ati	0.0679	
O_NDDCT_Detailed001	A_ts	0.00037		0.0000	Ats	0.00036644	
O_NDDCT_Detailed001	A3	5410.61		0.0002	A3	5410.6	
O_NDDCT_Detailed001	A5	2642.08		-0.0008	A5	2642.1	
O_NDDCT_Detailed001	Ae3	2364.9		-0.0972	Ae3	2367.2	
O_NDDCT_Detailed001	Apex_semi_angle	30.75	Deg	-0.0021	ApexAngle	0.5367	rad
O_NDDCT_Detailed001	C_Dts	2		0.0000	Cdts	2	
O_NDDCT_Detailed001	Cp_a34	1007.13		0.0030	Cpa	1007.1	
O_NDDCT_Detailed001	Cp_cfsm	4181.66		0.0421	cpw	4179.9	
O_NDDCT_Detailed001	Cp_da34	1007.12		0.0020	Cpav	1007.1	

168

| IPSEpro NDDCT model results | | Largest discrepancy | 0.8412 % | Suoying HE's MATLAB code results | | |
| | | Largest negative discrepancy | -0.4741 % | | | |
Object	Variable	Value	Units	% Discrepancy	Name	Value	Units
O_NDDCT_Detailed001	Cp_wv34	1890.17		-0.0016	Cpwv	1890.2	
O_NDDCT_Detailed001	d3	83		0.0000	d3	83	
O_NDDCT_Detailed001	d5	58		0.0000	d5	58	
O_NDDCT_Detailed001	de	0.0216		0.0000	de	0.0216	
O_NDDCT_Detailed001	DE_A	0.98882					
O_NDDCT_Detailed001	delta_p_hot	0.002					
O_NDDCT_Detailed001	df	0.0572		0.0000	df	0.0572	
O_NDDCT_Detailed001	draft_Eqn_LHS	103.044		-0.0326	leftside	103.0776	
O_NDDCT_Detailed001	draft_Eqn_RHS	103.044		-0.0329	rightside	103.0779	
O_NDDCT_Detailed001	dt_in	28.1435					
O_NDDCT_Detailed001	dt_out	14.3608					
O_NDDCT_Detailed001	dts	0.5		0.0000	dts	0.5	
O_NDDCT_Detailed001	f_Dt	0.02272		0.0797	fDw	0.0227	
O_NDDCT_Detailed001	F_T	0.95435		0.0052	FT	0.9543	
O_NDDCT_Detailed001	h_aeA_a	18892.1	kW/K	-0.0999	heaAa	18911000	W/K
O_NDDCT_Detailed001	h_cf_out_init_est	184.509					
O_NDDCT_Detailed001	h_cfs	6.92231	kW/m^2	-0.3697	hw	6948	W/m^2
O_NDDCT_Detailed001	H3	13.67		0.0000	H3	13.67	
O_NDDCT_Detailed001	H4	15.614		-0.0115	H4	15.6158	
O_NDDCT_Detailed001	H5	120		0.0000	H5	120	
O_NDDCT_Detailed001	inv_Fr_D	3.41944					
O_NDDCT_Detailed001	k_a34	0.02656		-0.1380	ka	0.0266	
O_NDDCT_Detailed001	k_cfsm	0.64351		-0.3236	kw	0.6456	
O_NDDCT_Detailed001	K_ci	0.05		0.0000	Kci	0.05	
O_NDDCT_Detailed001	K_ct	2.28994		0.0017	Kct	2.2899	
O_NDDCT_Detailed001	K_ctche	1.23594		-0.0049	Kctche	1.236	
O_NDDCT_Detailed001	K_ctehe	1.27507		0.1469	Kctehe	1.2732	
O_NDDCT_Detailed001	K_cthe	1.58655		-0.1919	Kcthe	1.5896	

IPSEpro NDDCT model results		Largest discrepancy		0.8412 %	Suoying HE's MATLAB code results		
		Largest negative discrepancy		-0.4741 %			
Object	Variable	Value	Units	% Discrepancy	Name	Value	Units
O_NDDCT_Detailed001	K_d	4.1886		0.0000	Kd	4.1886	
O_NDDCT_Detailed001	k_da34	0.02656		-0.1372	kav	0.0266	
O_NDDCT_Detailed001	K_he	28.974					
O_NDDCT_Detailed001	K_he_theta	35.3186					
O_NDDCT_Detailed001	K_to	-0.70452					
O_NDDCT_Detailed001	K_tshe	0.42421		-0.1391	Ktshe	0.4248	
O_NDDCT_Detailed001	k_wv34	0.01903		0.1595	kwv	0.019	
O_NDDCT_Detailed001	Lt	15		0.0000	Lt	15	
O_NDDCT_Detailed001	Lte	14.4		0.0000	Lte	14.4	
O_NDDCT_Detailed001	Lts	15.78		0.0000	Lts	15.78	
O_NDDCT_Detailed001	m_A_5_sq	15.1494					
O_NDDCT_Detailed001	m_A_fr_sq	4.94312					
O_NDDCT_Detailed001	MTD	20.4851		0.0352	delta_Tlm	20.4779	
O_NDDCT_Detailed001	mu_a34	1.87E-05		-0.0011	ua	0.000018672	
O_NDDCT_Detailed001	mu_cfsm	0.00052		0.4758	uw	0.00052165	
O_NDDCT_Detailed001	mu_da34	1.87E-05		-0.0005	uav	0.000018672	
O_NDDCT_Detailed001	mu_wv34	1.02E-05		0.0000	uwv	0.000010182	
O_NDDCT_Detailed001	nb	142		0.0000	nb	142	
O_NDDCT_Detailed001	nfp	2		0.0000	nwp	2	
O_NDDCT_Detailed001	nr	4		0.0000	nr	4	
O_NDDCT_Detailed001	ntb	154		0.0000	ntb	154	
O_NDDCT_Detailed001	nts	60		0.0000	nts	60	
O_NDDCT_Detailed001	Ny	174748		-0.0069	Ny	174760	
O_NDDCT_Detailed001	p_a6	0.834	bar	-0.0072	Pa6	83406	Pa
O_NDDCT_Detailed001	P_l	0.058					
O_NDDCT_Detailed001	p_w	0.17725					
O_NDDCT_Detailed001	p_ws	1772.48					
O_NDDCT_Detailed001	phi_c	0.6877		0.0138	fi2	0.6876	

IPSEpro NDDCT model results		Largest discrepancy	0.8412 %	Suoying HE's MATLAB code results		
		Largest negative discrepancy	-0.4741 %			
Object	Variable	Value	Units	% Discrepancy	Name	Value	Units
O_NDDCT_Detailed001	phi_cf	0.44549		0.0429	fi3	0.4453	
O_NDDCT_Detailed001	phi_h	0.38796		-0.1382	fi1	0.3885	
O_NDDCT_Detailed001	pi	3.14159					
O_NDDCT_Detailed001	Pr_a34	0.70793		0.0040	Pra	0.7079	
O_NDDCT_Detailed001	Pr_cfs	3.40591		0.8412	Prw	3.3775	
O_NDDCT_Detailed001	q_trans	327511	kW	-0.0912	Q1	327810000	W
O_NDDCT_Detailed001	Re_cfs	45153.9		-0.4741	Rew	45369	
O_NDDCT_Detailed001	relative_ roughness	0.00052		0.0000	relative_ roughness	0.000524	
O_NDDCT_Detailed001	rho_a1	1.0206		0.0000	roav1	1.0206	
O_NDDCT_Detailed001	rho_a3	1.02104		0.0039	roav3	1.021	
O_NDDCT_Detailed001	rho_a34	0.96801		0.0009	Meanroav34	0.968	
O_NDDCT_Detailed001	rho_a4	0.92022		0.0016	roav4	0.9202	
O_NDDCT_Detailed001	rho_a4_init_est	0.93508					
O_NDDCT_Detailed001	rho_a5	0.91006		-0.0049	roav5	0.9101	
O_NDDCT_Detailed001	rho_a6	1.0102		-0.0099	roav6	1.0103	
O_NDDCT_Detailed001	Ry	119074		-0.0050	Ry	119080	
O_NDDCT_Detailed001	sigma	0.433		0.0000	sigma	0.433	
O_NDDCT_Detailed001	sigma_c	0.6314		0.0000	sigma_c	0.6314	
O_NDDCT_Detailed001	T_a1	288.75		0.0000	Ta1	288.75	
O_NDDCT_Detailed001	T_a3	288.617		0.0001	Ta3	288.6167	
O_NDDCT_Detailed001	T_a34	304.428		0.0007	MeanTa34	304.4259	
O_NDDCT_Detailed001	T_a4	320.239		0.0012	Ta4	320.2351	
O_NDDCT_Detailed001	T_a5	319.221		0.0011	Ta5	319.2174	
O_NDDCT_Detailed001	T_a6	287.58		0.0000	Ta6	287.58	
O_NDDCT_Detailed001	theta_m	26.7247	Deg	0.0073	sida_m	0.4664	rad
O_NDDCT_Detailed001	UA	16752.5	kW/K	-0.1282	UA	16774000	W/K
O_NDDCT_Detailed001	W	1.30E-05			W1	0	
G_Stream001	p	0.846	bar	0.0000	Pa1	84600	Pa

IPSEpro NDDCT model results		Largest discrepancy		0.8412 %	Suoying HE's MATLAB code results		
		Largest negative discrepancy		-0.4741 %			
Object	Variable	Value	Units	% Discrepancy	Name	Value	Units
G_Stream001	t	15.6	Deg C				
G_Stream001	h	15.6743					
G_Stream001	s	6.8794					
G_Stream001	v	0.97968					
G_Stream001	mass	10283.6	kg/s	-0.1010	ma	10294	
G_Stream002	p	0.834					
G_Stream002	t	46.0714					
G_Stream002	h	46.3149					
G_Stream002	s	6.98433					
G_Stream002	v	1.09865					
G_Stream002	mass	10283.6	kg/s				
O_Sink001	mass	4390	kg/s				
O_Sink001	p	2.998					
O_Sink001	t	43.6102					
O_Source001	mass	4390	kg/s				
O_Source001	p	3					
O_Source001	t	61.45	Deg C	0.0000	Twi	334.6	K
O_Stream001	p	3					
O_Stream001	t	61.45					
O_Stream001	h	257.484					
O_Stream001	s	0.84932					
O_Stream001	v	0.00102					
O_Stream001	rho	982.531		-0.4496	Densityw	986.9682	
O_Stream001	mass	4390	kg/s				
O_Stream001	x	-0.14049					
O_Stream002	p	2.998					
O_Stream002	t	43.6102		0.0562	Two	316.7357	
O_Stream002	h	182.88					

| IPSEpro NDDCT model results | | Largest discrepancy | | 0.8412 % | Suoying HE's MATLAB code results | | |
| | | Largest negative discrepancy | | -0.4741 % | | | |
Object	Variable	Value	Units	% Discrepancy	Name	Value	Units
O_Stream002	s	0.62019					
O_Stream002	v	0.00101					
O_Stream002	rho	990.875					
O_Stream002	mass	4390	kg/s				
O_Stream002	x	-0.17492					

Appendix C – Aspen HYSYS v IPSEpro LTP Lib Results Comparison

The performance of R152a in a simple binary cycle was calculated in Aspen HYSYS and IPSEpro LTP_Lib over a range of operating points using the same assumptions. The results of the analysis can be seen in Figure 90.
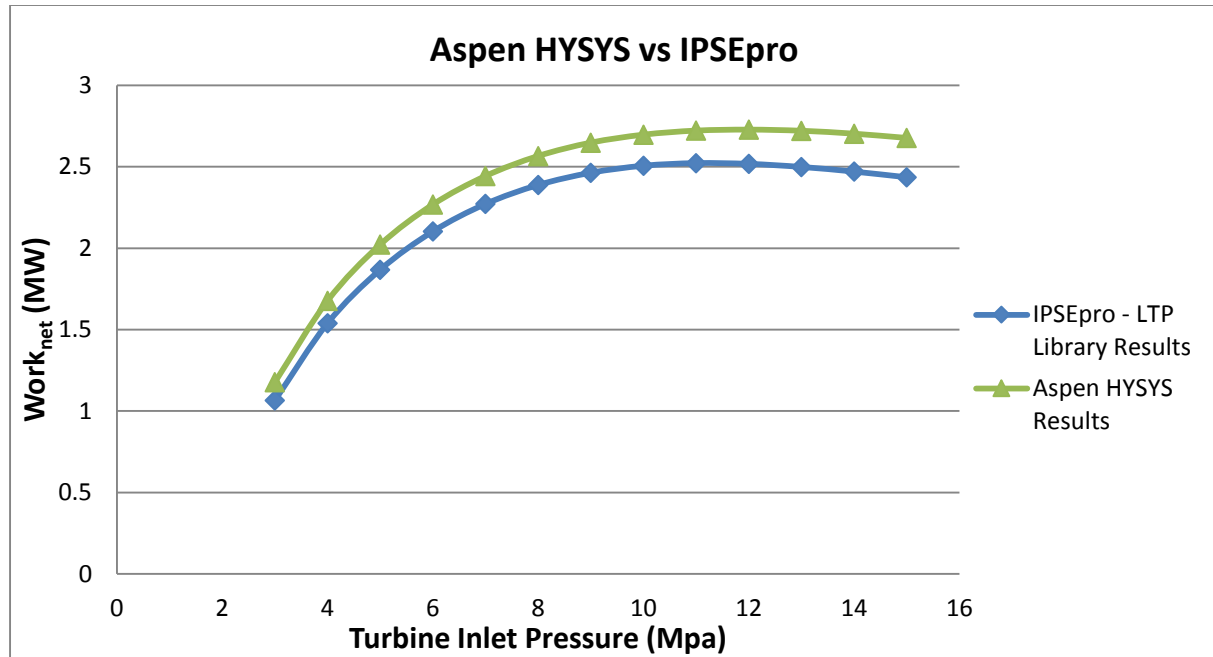
Figure 90: Aspen HYSYS vs IPSEpro LTP_Lib for a simple binary cycle with R152a as working fluid

The shape of the performance curves are in fair agreement but there is a discrepancy of 7-10% across the calculated range of turbine inlet pressure.

A detailed comparison of each point in the cycle of a single case was performed in an attempt to identify the source of the discrepancy, 11 MPa turbine inlet pressure was selected. However the issue with this comparison is that from the outset the mass flow rate is 6% different. The mass flow rate is calculated based on the required flow through the brine heat exchanger to achieve the specified output conditions. This shows that there is disagreement between the two software heat exchange calculations.

In order to more clearly compare the two software packages, each component was analysed in isolation with the same inlet conditions so that the difference in the outlet conditions could be clearly observed. The heat exchanger was found to be the source of the errors. The calculated Q_{in} was found to be 4% different and since Q_{in} is calculated from the brine side, since that is fully specified, it must be the fluid properties referenced in the software. IPSEpro refers to the REFPROP 9.1 for fluid properties, whereas Aspen HYSYS was compared using

the Peng-Robinson database. Aspen HYSYS guides the user through setup and suggests which fluid property database is most appropriate for the application, and for the power generation the Peng-Robinson database was suggested. REFPROP uses the most accurate equations of state worldwide (Lemmon et al., 2013).

The subscripts in the following tables refer to the points in Figure 12.

Table 61: Comparison of brine side heat transfer calculation in Aspen HYSYS vs IPSEpro LTP_Lib

	Aspen HYSYS	IPSEpro	Discrepancy
Mass Flow Rate (kg/s)	35	35	-
T_a (Deg C)	80	80	-
P_a (MPa)	30	30	-
h_a (kJ/kg)	-15000	952.99	-
T_b (Deg C)	220	220	-
P_b (MPa)	29.98	29.98	-
h_b (kJ/kg)	-15620	358.78	-
Δh_{a-b} (kJ/kg)	620	594.21	4.16%
$\dot{Q}_{in}$ (MW)	21700	20797.35	4.16%

Table 62: Comparison of pump calculation in Aspen HYSYS vs IPSEpro LTP_Lib

	Aspen HYSYS	IPSEpro	Discrepancy
Mass Flow Rate (kg/s)	62.89	62.89	-
T_1 (Deg C)	50	49.749	-
P_1 (MPa)	1.170	1.170	-
h_1 (kJ/kg)	-7466	290.5	-
x_1	0	0	-
$W_{in,pump}$ (MW)	0.991	0.9723	1.89%
ΔP_{pump} (Mpa)	9.850	9.850	-
ΔT_{pump} (Deg C)	9.990	13.141	-31.54%
T_2 (ºC)	59.99	62.89	-4.83%
P_2 (MPa)	11.02	11.02	-
h_2 (kJ/kg)	-7450	305.47	-
Δh_{2-1} (kJ/kg)	16	14.97	6.44%

The pump calculation shows some discrepancy in the outlet conditions for the same ΔP_{pump}, this is could be due to using the different fluid properties resulting in a different Δh_{2-1}. The isolated comparison of the turbines however showed only minor discrepancies which again could be attributed to the fluid properties used.

Table 63: Comparison of turbine calculation in Aspen HYSYS vs IPSEpro LTP_Lib

	Aspen HYSYS	IPSEpro	Discrepancy
Mass Flow Rate (kg/s)	62.89	62.89	-
T_3 (Deg C)	210.00	210.00	-
P_3 (MPa)	11.00	11.00	-
h_3 (kJ/kg)	-7100	659.12	-
$\dot{W}_{out}$ (MW)	4.431	4.441	-0.23%
$\Delta P_{turbine}$ (Mpa)	9.810	9.810	-
$\eta_{s,\ turbine}$	0.85	0.85	-
T_4 (Deg C)	86.81	87.648	-0.97%
P_4 (MPa)	1.19	1.19	-
h_4 (kJ/kg)	-7171	588.51	-
Δh_{4-3} (kJ/kg)	71	70.61	0.55%

The main source of the discrepancies is the different source of fluid properties used in Aspen HYSYS and IPSEpro LTP. Since IPSEpro is using the more accurate source of fluid properties there can be high confidence in the results obtained with IPSEpro LTP library.

Appendix D – Site Climate Data

There are two sets of site climate data from BOM used in this project:

Historical Monthly Temperature Data

Table 64: Monthly mean temperature data from 1972 to 1999 (Bureau of Meterology, 2015)

Month	Jan	Feb	Mar	Apr	May	Jun	Jul	Aug	Sep	Oct	Nov	Dec
Highest temperature (ºC) for years 1972 to 1999	47.8	45.4	43.2	39.9	33.6	29.6	30.7	34.1	38.4	43.5	45.8	49.1
Mean maximum temperature (ºC) for years 1972 to 1999	37.4	36.7	34.0	28.6	23.7	19.9	19.2	22.0	26.0	29.9	33.7	36.7
Lowest maximum temperature (ºC) for years 1972 to 1999	20.6	21.3	19.5	18.3	12.8	11.0	11.0	14.2	14.9	14.0	20.1	23.6
Highest minimum temperature (ºC) for years 1972 to 1999	34.8	33.4	29.8	24.9	21.5	18.6	16.9	19.4	23.0	26.0	31.6	32.5
Mean minimum temperature (ºC) for years 1972 to 1999	23.2	23.0	19.6	14.8	10.9	7.3	6.3	7.7	11.0	15.0	18.6	21.5
Lowest temperature (ºC) for years 1972 to 1999	10.9	13.8	8.6	4.2	1.2	0.0	-1.4	-0.5	2.3	2.6	6.7	10

Daily temperature data for 2012

Bureau of Meteorology Station Number: 17123

Product Code: IDCJAC0011

Month	Day	Minimum temperature (Degree C)	Maximum temperature (Degree C)
1	1	22.4	40.9
1	2	23.7	42.6
1	3	27	43.7
1	4	28.1	42.6
1	5	28.7	40.2
1	6	26.1	41.8
1	7	24.8	45.7
1	8	27.8	33.9
1	9	22.2	33.8
1	10	20.6	32.7
1	11	20.6	32.2
1	12	19.8	32.2
1	13	18.7	34.5
1	14	19.4	34.8
1	15	20.4	37.5
1	16	21.1	39.4
1	17	24	39.6
1	18	22.6	41.7
1	19	26.5	43.9
1	20	30.5	42.9
1	21	28.9	40.6
1	22	28.2	39.6
1	23	22.7	36.6
1	24	22.5	35.2
1	25	21.7	34
1	26	23	36
1	27	25.4	37.2
1	28	23.5	35.7
1	29	24	36.6

Month	Day	Minimum temperature (Degree C)	Maximum temperature (Degree C)
1	30	23.6	39.2
1	31	22.1	31.8
2	1	20.6	32.8
2	2	17.4	32.4
2	3	18.7	36
2	4	19.4	38
2	5	25.8	35.9
2	6	18	28.5
2	7	15	30.3
2	8	16.7	31.3
2	9	16.9	33.7
2	10	17.2	29.1
2	11	16.2	31.4
2	12	17	34.4
2	13	18.1	36.9
2	14	17.8	38.9
2	15	20.7	40.7
2	16	23.3	42.4
2	17	21.8	41.8
2	18	24.3	43.6
2	19	24.7	44.2
2	20	27.6	36.1
2	21	20	36.7
2	22	23.9	37.4
2	23	19.8	37.9
2	24	22.2	39.7
2	25	27.5	38.5
2	26	22.7	38.6
2	27	27.5	33.8
2	28	25.7	36.8

179

Month	Day	Minimum temperature (Degree C)	Maximum temperature (Degree C)
2	29	26.9	38.1
3	1	23.3	27.9
3	2	18.8	23.1
3	3	20	24.4
3	4	19.8	29.1
3	5	19.4	29.8
3	6	18.8	28.5
3	7	16.9	29.7
3	8	17.9	29.3
3	9	16.9	30.8
3	10	16.6	33.1
3	11	18.5	34.5
3	12	20.4	34.2
3	13	20.6	35.8
3	14	20.7	36.1
3	15	21.1	36.9
3	16	22.6	31.1
3	17	19.5	31
3	18	20.5	32.7
3	19	22	33.5
3	20	20.4	34
3	21	21.4	35.1
3	22	17.4	28
3	23	14.1	25.8
3	24	14.3	26.3
3	25	13.6	28.4
3	26	14.5	28.8
3	27	15.3	31.1
3	28	16.8	32.8
3	29	20.5	34.2

Month	Day	Minimum temperature (Degree C)	Maximum temperature (Degree C)
3	30	16.1	34.2
3	31	15.9	35
4	1	18.4	36
4	2	17.9	36.4
4	3	18.5	39.5
4	4	18.3	35.5
4	5	18.2	35
4	6	17.6	36.2
4	7	18.3	27
4	8	16.8	27.6
4	9	13.3	26
4	10	12.7	22.6
4	11	9.7	23.9
4	12	10.7	28
4	13	12.7	30.2
4	14	15.2	31
4	15	15.1	31.6
4	16	16.6	31.6
4	17	15.7	31.3
4	18	12.8	30.6
4	19	12.3	30.3
4	20	11.7	31.4
4	21	14	33.4
4	22	20.1	24.1
4	23	16.3	26.6
4	24	12.9	21.8
4	25	8.8	21.5
4	26	8.7	23
4	27	8.7	23.3
4	28	8.6	24.8

Month	Day	Minimum temperature (Degree C)	Maximum temperature (Degree C)
4	29	10.8	27.4
4	30	11.7	28.3
5	1	11.6	30.8
5	2	12.3	26.2
5	3	10.7	21.1
5	4	5.8	21.9
5	5	7.7	22.4
5	6	6.9	24.8
5	7	9	27.8
5	8	8.3	30.5
5	9	8.6	32.4
5	10	10.2	32.7
5	11	12.8	31.2
5	12	13.5	24.7
5	13	9.3	20.9
5	14	5.7	20.7
5	15	6.1	21
5	16	5	23
5	17	5.1	25
5	18	5.5	26.7
5	19	6.5	25.1
5	20	7.9	24.8
5	21	8.3	25.3
5	22	6.7	26.7
5	23	6.7	29.4
5	24	10.2	17.4
5	25	3.8	17
5	26	3.7	21.2
5	27	7.5	21.9
5	28	6.2	18.8

Month	Day	Minimum temperature (Degree C)	Maximum temperature (Degree C)
5	29	6.6	20.2
5	30	7.4	24.7
5	31	11.9	19
6	1	13.8	16.2
6	2	13.8	18
6	3	9.2	17.7
6	4	5.9	16.8
6	5	9.1	16.3
6	6	7.9	16.9
6	7	6.8	18.6
6	8	5.4	17.9
6	9	4.4	16.5
6	10	3.4	16.7
6	11	4.7	19.7
6	12	4.5	20.8
6	13	5.4	22.4
6	14	7.2	23.8
6	15	9	23.1
6	16	9.3	21.8
6	17	4.5	21.4
6	18	4.8	20.2
6	19	4.6	20.7
6	20	5.3	21.8
6	21	3.3	24
6	22	8	15.5
6	23	2	16.4
6	24	3.5	17.1
6	25	2.7	18.5
6	26	3.3	18.5
6	27	5.9	19.4

Month	Day	Minimum temperature (Degree C)	Maximum temperature (Degree C)
6	28	4	21.5
6	29	5	21.9
6	30	6.4	18.2
7	1	3.6	16.9
7	2	1.9	15.7
7	3	0.8	15.9
7	4	3.5	18.3
7	5	3.6	17.3
7	6	3.5	18.6
7	7	2.1	21.2
7	8	5.2	24.1
7	9	11.1	23.2
7	10	10.1	21.3
7	11	7.4	23.8
7	12	15.1	26.2
7	13	7.7	20
7	14	5.3	17.9
7	15	2.5	18.3
7	16	1.6	19.4
7	17	3.2	19.6
7	18	2	20
7	19	3.3	16.9
7	20	2.2	18
7	21	5.2	19.4
7	22	7.2	20.1
7	23	4.9	21.4
7	24	4.2	22.8
7	25	7.6	24.9
7	26	3.5	17.3
7	27	6.6	17.8

Month	Day	Minimum temperature (Degree C)	Maximum temperature (Degree C)
7	28	4.7	17.7
7	29	5.5	19.8
7	30	5.1	17.1
7	31	3.6	17.8
8	1	1.4	19.6
8	2	1.4	21.9
8	3	8.3	24.4
8	4	5.5	22.8
8	5	7.9	26
8	6	5.5	21.3
8	7	4.2	23.1
8	8	4.6	26.6
8	9	8.2	20.5
8	10	3.7	19.1
8	11	4.1	18.2
8	12	4.2	19.4
8	13	3	23.5
8	14	6.3	26.2
8	15	5.5	23.7
8	16	3.2	23.8
8	17	7.8	18.3
8	18	3.2	17.8
8	19	3.3	19.9
8	20	2.4	21
8	21	6.8	27.6
8	22	8.2	34.3
8	23	16.8	23.2
8	24	2.3	22.8
8	25	6.1	23.2
8	26	6	21.9

Month	Day	Minimum temperature (Degree C)	Maximum temperature (Degree C)
8	27	4.3	23.2
8	28	4.4	27.7
8	29	9.8	29.1
8	30	11.7	21.5
8	31	7	20.8
9	1	5.1	23.7
9	2	5.6	26.2
9	3	6.4	28
9	4	7.4	31.3
9	5	13.1	31.6
9	6	6.6	26.7
9	7	10.4	21.3
9	8	7.8	22.4
9	9	8.1	24.1
9	10	5.4	26.4
9	11	9.2	29.6
9	12	8.8	32.3
9	13	12.3	22.1
9	14	6.3	22.7
9	15	6.6	25.9
9	16	9.3	26.9
9	17	11.2	27.7
9	18	9.2	30.9
9	19	12.6	35.3
9	20	14.2	38.7
9	21	21.6	32.2
9	22	13.5	33.1
9	23	15.8	27.7
9	24	11.1	23.9
9	25	8.6	28.6

Month	Day	Minimum temperature (Degree C)	Maximum temperature (Degree C)
9	26	10.8	33.9
9	27	18.8	38.8
9	28	24.1	35.9
9	29	13.1	23.4
9	30	8.2	23.3
10	1	8.7	25.2
10	2	11.5	28.8
10	3	12.1	33.4
10	4	16.6	35.6
10	5	17.1	37.2
10	6	17.1	38.7
10	7	15.2	28.2
10	8	8.6	30.3
10	9	16.4	34.3
10	10	15.4	28.8
10	11	8.4	19.9
10	12	4.7	22.8
10	13	7.5	26.9
10	14	9.2	32.3
10	15	12.3	35.8
10	16	15.3	38
10	17	19	36.9
10	18	16.5	41.1
10	19	22	41.2
10	20	23.7	40.3
10	21	27	38.1
10	22	17.6	35.1
10	23	17	36.1
10	24	14.7	40.8
10	25	19.6	32.8

Month	Day	Minimum temperature (Degree C)	Maximum temperature (Degree C)
10	26	19.9	21.1
10	27	10.6	27.7
10	28	14	31.3
10	29	13.8	33.8
10	30	13.6	36.5
10	31	15.8	39.4
11	1	22.2	36.5
11	2	18.5	30.9
11	3	16.7	35.2
11	4	17.7	41.2
11	5	19.9	42.9
11	6	23.7	33
11	7	22.2	34.3
11	8	21.9	34.1
11	9	19.7	28.1
11	10	17.5	32.8
11	11	14.4	35.1
11	12	15.6	38.5
11	13	21.1	37.6
11	14	18.9	39.8
11	15	21.3	43.7
11	16	24.2	35.6
11	17	20.8	32.4
11	18	15.5	34.3
11	19	16.8	35.2
11	20	14.7	37.9
11	21	19.4	38.9
11	22	22.7	36.7
11	23	15.4	39.5
11	24	22.8	41.2

Month	Day	Minimum temperature (Degree C)	Maximum temperature (Degree C)
11	25	22.2	43.2
11	26	23.1	45.3
11	27	26.8	42.4
11	28	22.6	42.1
11	29	27.6	45.7
11	30	29.6	45.7
12	1	29.1	41
12	2	24	33.3
12	3	19.3	33.7
12	4	20.3	31.1
12	5	17.8	31.4
12	6	15.1	35.9
12	7	18.1	40.4
12	8	23.8	42.9
12	9	26.4	36.3
12	10	20.8	37.1
12	11	21.3	41.7
12	12	27.3	42.5
12	13	27.4	42.2
12	14	25.8	43.7
12	15	26.6	37.3
12	16	22.7	38.7
12	17	22.9	37.2
12	18	22.2	39.3
12	19	25.6	37.3
12	20	25.4	39.4
12	21	26.3	40.7
12	22	22.9	40.8
12	23	23.4	44.1
12	24	28.1	44.7

Month	Day	Minimum temperature (Degree C)	Maximum temperature (Degree C)
12	25	24.1	36.8
12	26	20.9	36.9
12	27	21.6	39.8
12	28	24.4	39.6
12	29	21.9	38.9
12	30	24	40.8
12	31	23.6	41